

UNIVERSITY OF BELGRADE
FACULTY OF TECHNOLOGY AND METALLURGY

Vuk V. Radmilović

**TRANSPARENT NANOCOMPOSITE
FILMS FOR PLASTIC ELECTRONICS
APPLICATIONS**

Doctoral Dissertation

Belgrade, 2016

UNIVERZITET U BEOGRADU
TEHNOLOŠKO-METALURŠKI FAKULTET

Vuk V. Radmilović

**TRANSPARENTNI NANOKOMPOZITNI
FILMOVI ZA PRIMENU U PLASTIČNOJ
ELEKTRONICI**

Doktorska Disertacija

Beograd, 2016

Podaci o mentoru i članovima komisije

Mentor:

Dr **Petar Uskoković**, redovni profesor,
Univerzitet u Beogradu, Tehnološko-metalurški fakultet

Članovi komisije:

Akademik Dr **Zoran Popović**, naučni savetnik,
Institut za Fiziku, Beograd

Dr **Dorđe Janačković**, redovni profesor,
Univerzitet u Beogradu, Tehnološko-metalurški fakultet

Dr **Vesna Radojević**, redovni profesor,
Univerzitet u Beogradu, Tehnološko-metalurški fakultet

Dr **Erdmann Spiecker**, redovni profesor,
Univerzitet Erlangen-Nirnberg, Institut za Mikro i Nanostrukturna
Istraživanja

Datum odbrane: _____

Acknowledgements

First and foremost, I would like to thank Professor Velimir R. Radmilović for his help, guidance, constant mentoring, committed to the highest standard and excellence in education and science, which extended far beyond my work on this project.

I would also like to thank the members of the committee of this PhD thesis, Professors Petar Uskoković, Djordje Janačković, Vesna Radojević, Erdmann Spiecker, and academician Zoran Popović, for their useful suggestions and their expeditious feedback after the thesis submission.

I am in debt to Professors Erdman Spiecker and Christoph Brabec of Erlangen-Nuremberg University, as well as Silke Christiansen from the Max Planck Institute for the Science of Light, who have been instrumental in the completion of this work by having their labs and staff available to assist me in training and producing a significant portion of the results presented in this thesis. I am grateful for the aid, advice, and encouragement I received during my stay at the Center for Nanoanalysis and Electron Microscopy (CENEM), University of Erlangen-Nuremberg, Germany.

A number of other collaborators deserve special thanks for their contributions: Drs. Colin Ophus, Peter Ercius, Jim Ciston, Josh Kacher and Andrew Minor, from the National Center for Electron Microscopy (NCEM), Molecular Foundry, Lawrence Berkeley National Laboratory (LBNL), University of California, Berkeley, California, USA, Carlo Carraro of the Department of Chemical Engineering, University of California at Berkeley, as well as professor Evica Ivanović from the Faculty of Agriculture, University of Belgrade, Serbia.

I would like to thank the members of the Department of Materials Engineering, as well as all colleagues from the Faculty of Technology and Metallurgy and the Innovation Center of the Faculty of Technology and Metallurgy, University of Belgrade, Serbia, who help me in various ways during the course of this thesis.

Last, but not least, I would like to thank my parents, girlfriend, family and friends for all the support and constant encouragement during my PhD project.

Transparent Nanocomposite Films for Plastic Electronic Applications

ABSTRACT

As solar cell technology gains more and more attraction every year, research keeps up with trends by an exponential number of published papers every year. These papers cover a wide range of topics regarding solar cells and the individual components of which they are comprised, which is the subject of this thesis. Different topics of research have been addressed in order to better understand and optimize individual solar cell components (layers) such as silver nanowires (AgNWs), AgNW based nanocomposite and Ag dendrites for the application as transparent electrodes, polymer nanocomposites (PNC) for the possible application as protective layers (encapsulants) as well as organic tandem solar cells as a whole device, utilizing AgNWs as the transparent electrode.

The first part of the thesis concentrates on AgNWs and an AgNW based nanocomposite. These AgNWs were synthesized by a simple polyol reduction process. The main focus of this research was elucidating the solid-state wetting and subsequently welding mechanisms that occur during annealing of AgNWs before a layer of aluminum doped zinc oxide (AZO) is deposited on them, for the enhancement of properties essential for an electrode in a solar cell. Microstructural characterization using scanning electron microscopy (SEM) and transmission electron microscopy (TEM) revealed that solid-state wetting and subsequent welding occurred only between nanowires whose contact geometry is characterized by an enormous difference in radii of curvature. Results also indicated that, for two AgNWs in contact, during annealing, the AgNW in contact through a smaller radius of curvature dissolves, Ag atoms diffuse and are incorporated in a welded zone between the AgNWs whose crystallographic orientation is inherent from the AgNW in contact through a large radius of curvature. Wetting angle between two welded AgNWs was measured to be below 4.8° , indicating almost complete wetting. Direct atomic column measurements were performed in order to elucidate crystal lattice distortion. Tomography was employed to better understand the morphology of the welded zone and confirmed the welding mechanism based on cross

sectional transmission electron microscopy imaging. Electron diffraction orientation and strain mapping were performed in order to elucidate possible strain fluctuation across the AgNWs as well as confirm crystallographic orientation of the welded zone. Crystal lattice distortion, directly measured by atomic column displacements in drift corrected cross-sectional atomic resolution scanning transmission electron microscopy images of an AgNW, prepared by focused ion beam (FIB), demonstrated non-uniform distribution of strain in five twin segments of the nanowire.

The second part of the thesis is focused on tandem bulk heterojunction (BHJ) organic solar cells, precisely a double and a triple junction tandem BHJ solar cell, as well as pristine AgNWs used as transparent electrodes in these solar cells. The double junction tandem BHJ organic solar cell was processed entirely from solution while in the case of the triple junction tandem BHJ organic solar cell, all layers were processed from solution with the exception of the bottom and top electrodes. SEM and TEM characterization gave insight in the microstructure of all layers present in the cells both, organic (intermediate polymer layers and polymer nanocomposite active layers) and inorganic (intermediate metal oxide layers and electrodes). Conventional and scanning transmission electron microscopy (CTEM and STEM) in tandem with energy dispersive X-ray spectroscopy (EDS) gave insight into the elemental distribution inside the solar cells and allowed precise analysis of layer thickness and morphology. AgNWs used as transparent electrodes were characterized for sheet resistance and optical transmittance and both exhibited linear decrease with the increase of layer thickness in the range between 50 and 160 nm. Area coverage calculations of AgNWs were performed using SEM imaging in tandem with a dedicated code written in MatLab for image analysis, as the degree of coverage greatly influences the performance of the electrode and, with it, the performance of the entire solar cell device.

The third part of the thesis deals with Ag dendrites produced by a simple electrochemical method. The emphasis of the study was on the detailed analysis of defect structure evolution during dendrite formation, which includes randomly distributed twins and stacking faults on $\{111\}$ crystallographic planes. This was discovered using orientation imaging microscopy (OIM), based on electron-backscattered diffraction (EBSD). It was also shown that the broad faces of the dendrites are of $\{111\}$ type. The main trunks grow in the $[\bar{1}1\bar{2}]$ direction while the

branches grow from the main trunk in $[\bar{2}\bar{1}\bar{1}]$ and $[12\bar{1}]$ directions. All these directions are of $\langle 112 \rangle$ type, since dendrite facets are broken into stable 111 and 200 steps and ledges. Another important result is related to elucidation of two types of in-plane randomly distributed 60° rotational twins in the broad dendrite surface plane.

The fourth part of the thesis is focused on polymer nanocomposites processed from solution, with polyvinyl butyral (PVB) as the polymer matrix and carbonaceous materials like multi-walled carbon nanotubes (MWCNTs), single-walled carbon nanotubes (SWCNTS) and graphene as the nanofillers. It was found that, with the addition of 1 wt.% of carbonaceous nanofillers in the polymer matrix, mechanical properties, obtained using nanoindentation, greatly improve with practically no expense to optical properties. Highest improvement of $\sim 66\%$ for reduced modulus and $\sim 50\%$ for hardness exhibited the PVB/graphene nanocomposite which had the lowest optical transparency of all nanocomposites at 84%. Raman spectroscopy confirmed the intimate connection between matrix and nanofiller, which led to enhanced properties compared to the pristine polymer.

Key words: *silver nanowires, organic solar cells, tandem solar cells, silver dendrites, twinning, polymer nanocomposites, polyvinyl butyral, carbon nanotubes, graphene, transmission electron microscopy*

Scientific area: Technological Engineering

Scientific sub-area: Materials Engineering

UDC number: 66.017:620.3]:621.38(043.3)

Transparentni Nanokompozitni Filmovi za Primenu u Plastičnoj Elektronici

APSTRAKT

S obzirom na porast interesovanja za solarnim tehnologijama, istraživanja idu u korak sa takvim trendovima što se manifestuje eksponencijalnim rastom broja objavljenih naučnih radova svake godine. Ovi radovi pokrivaju širok spektar tema vezanih za solarne ćelije i individualne slojeve od kojih su one sačinjene, što je i predmet proučavanja ove teze. Istraživanja su se odvijala u nekoliko pravaca kako bi se bolje razumeli i optimizovali individualni slojevi (komponente) solarnih ćelija kao što su nano-žice srebra, nanokompoziti na bazi nano-žica srebra i dendriti srebra, za primenu kao transparentne elektrode, polimerni nanokompoziti za primenu kao zaštitni slojevi (enkapsulanati) kao i kompletne organske tandem solarne ćelije koje koriste nano-žice srebra kao transparentne elektrode.

Prvi deo teze fokusiran je na nano-žice srebra i nanokompozite na bazi nano-žica srebra. Nano-žice su sintetisane jednostavnom metodom poliol redukcije. Osnova ovog istraživanja bila je razumevanje mehanizama kvašenja u čvrstom stanju i zavarivanja do kojih dolazi prilikom zagrevanja nano-žica, pre nego što je sloj cink oksida dopiran aluminijumom nanešen radi poboljšanja svojstava, od suštinskog značaja za elektrodu u solarnoj ćeliji. Mikrostrukturna karakterizacija korišćenjem skenirajuće elektronske mikroskopije (SEM) i transmisione elektronske mikroskopije (TEM) otkrila je da se kvašenje i zavarivanje odvijaju samo između nano-žica čiji su poluprečnici zakrivljenja u tački dodira veoma različiti. Rezultati su takođe pokazali da, kod dve nano-žice u kontaktu, prilikom zagrevanja, atomi srebra iz područja nano-žice u kontaktu malog poluprečnika zakrivljenja difunduju i ugrađuju se u zonu zavarenog spoja, koja povezuje dve nano-žice. Kristalografska orijentacija zavarenog spoja nasleđena je od nano-žice u velikog poluprečnika zakrivljenja u tački dodira. Ugao kvašenja između dve nano-žice manji je od 4.8° , što je indikator potpunog kvašenja. Tomografija je korišćena kako bi se bolje razumela morfologija zavarenog spoja i potvrdio mehanizam zavarivanja, ustanovljen na osnovu rezultata transmisione elektronske mikroskopije poprečnih preseka nano-žica. Mapiranje orijentacije i

naprezanja elektroskom difrakcijom urađeno je kako bi se utvrdila raspodela naprezanja u nano-žicama i potvrdila kristalografska orijentacija zavarene zone. Distorzija kristalne rešetke direktno je merena mapiranjem pomeranja atomskih kolona na slikama skenirajuće transmisionne elektronske mikroskopije poprečnih preseka nano-žica, pripremljenih fokusiranim jonskim snopom (FIB metodom). Ustanovljena je neravnomerna raspodela naprezanja u dvojnikovanim segmentima nano-žica.

Drugi deo teze bavi se organskim tandem solarnim ćelijama na bazi heterospoja (dvostrukim i trostrukim) kao i netretiranim nano-žicama srebra koje su korišćene kao elektrode u ovim solarnim ćelijama. Solarna ćelija na bazi dvostrukog heterospoja je kompletno procesirana iz rastvora dok su u solarnoj ćeliji na bazi trostrukog heterospoja svi slojevi procesirani iz rastvora, osim gornje i donje elektrode. SEM i TEM karakterizacija dala je uvid u mikrostrukturu svih slojeva ćelije, kako organskih - polimerni međuslojevi i aktivni sloj polimernog nanokompozita, tako i neorganskih - međuslojevi metalnih oksida i elektrode. Konvencionalna i skenirajuća transmisiona elektronska mikroskopija (CTEM i STEM) u tandemu sa spektroskopijom na bazi disperzije energije X-zraka, korišćene su kako bi se dobila raspodela elemenata u solarnim ćelijama i omogućila precizna analiza debljine slojeva i njihova morfologija. Nano-žice srebra, korišćene kao transparentna elektroda, karakterisane su radi utvrđivanja električne otpornosti i optičke transmisije i ustanovljeno je da se obe smanjuju sa povećanjem debljine sloja u opsegu od 50 do 160 nm. Merenja pokrivenosti površine vršena na bazi SEM slika, u tandemu sa MatLab kodom, posebno napisanim za analizu prikazanu u ovoj tezi. Ova merenja su vršena s obzirom da stepen pokrivenosti utiče na učinak elektrode a samim tim i stepen iskorišćenosti cele solarne ćelije.

Treći deo teze vezan je za dendrite srebra proizvedene jednostavnom elektrohemijomskom metodom. Posebna pažnja u ovom istraživanju stavljena je na detaljnu analizu nastanka defekata strukture tokom formiranja dendrita, što uključuje proizvoljno raspodeljene dvojnike i greške u redosledu na kristalografskim ravnima tipa $\{111\}$. Ovo je utvrđeno korišćenjem slika dobijenih orijentacionom mikroskopijom (OIM), difrakcijom elektrona rasejanih unazad (EBSD). Pokazano je da je osnovna frontalna ravan dendrita tipa $\{111\}$. Ustanovljeno je da osnovno stablo dendrita raste u pravcu $[\bar{1}1\bar{2}]$, dok grane dendrita rastu u pravcima $[\bar{2}\bar{1}\bar{1}]$ i $[12\bar{1}]$. Svi navedeni pravci

su <112> tipa pošto su facete dendrita razložene na stabilne 111 i 200 stepenice i ledževe. Još jedan važan rezultat ovih istraživanja odnosi se na ustanovljeno prisustvo dva tipa dvojnika proizvoljno raspoređenih u osnovnoj frontalnoj ravni dendrita, koji su međusobno rotirani za 60°.

Četvrti deo teze se odnosi na polimerne nanokompozite procesirane iz rastvora, sa polivinil butiralom (PVB) kao matricom i ugljeničnim materijalima, kao što su višezidne ugljenične nanocevi (MWCNT), jednozidne ugljenične nanocevi (SWCNT) i grafín, kao nanopuniocima. Rezultati su pokazali dadodatkom 1 mas.% ugljeničnih nanopunioca u polimernu matricu, mehanička svojstva, dobijena nanoindentacijom, znatno se poboljšavaju ali ne na uštrb optičkih svojstava. Najveće poboljšanje od ~66% za redukovan modul i ~50% za tvrdoću pokazao je nanokompozit sa grafínom kao nanopuniocem iako je, u odnosu na ostale kompozite, pokazao manju optičku transmisiju, koja je iznosila 84%. Ramanova spektroskopija je potvrdila uspostavljanje spoja na graničnoj površini između matrice i nanopunioca koje je rezultiralo poboljšanim svojstvima.

Ključne reči: *nanožice srebra, organske solarne ćelije, tandem solarne ćelije, dendriti srebra, dvojnikovanje, polimerni nanokompoziti, polivinil butiral, ugljenične nanocevi, grafín, transmisiona elektronska mikroskopija.*

Naučna oblast: Tehnološko inženjerstvo

Uža naučna oblast: Inženjerstvo materijala

UDK broj : 66.017:620.3]:621.38(043.3)

Table of Contents

List of Symbols and Abbreviations.....	xiii
List of Images.....	xviii
List of Tables.....	xxxi
1. Introduction.....	1
References.....	6
2. Theoretical Background.....	9
2.1. Silver nanostructures.....	9
2.1.1. Crystal Defects.....	10
2.1.2. Silver Nanowires.....	13
2.1.3. Silver Dendrites.....	24
2.2. Organic Solar Cells.....	26
2.3. Carbonaceous materials.....	42
2.3.1. Polymer Nanocomposites with Carbonaceous Nanofillers.....	49
2.3.2. Polyvinyl Butyral based nanocomposites.....	55
References.....	56
3. Experimental.....	70
3.1. Synthesis and Processing Methods.....	70
3.2. Characterization Methods.....	75
3.2.1. UV-Vis Spectroscopy.....	75
3.2.2. Raman Spectroscopy.....	76
3.2.3. Mechanical Characterization by Nanoindentation.....	77
3.2.4. Structural Characterization.....	81
3.2.4.1. Scanning Electron Microscopy.....	81
3.2.4.2. Transmission Electron Microscopy.....	87
3.3. AgNWs and AgNW based Nanocomposite - Experimental Procedure...	100
3.4. Tandem Organic Solar Cell - Experimental Procedure.....	104
3.5. Ag Dendrites - Experimental Procedure.....	107
3.6. Polymer Nanocomposites - Experimental Procedure.....	111
References.....	115
4. Results.....	118
4.1. AgNWs and AgNWs/AZO Nanocomposite.....	118
4.1.1. Electron Tomography of Thin AgNWs.....	135
4.1.2. Diffraction Orientation and Strain Mapping of AgNWs.....	137
4.2. Tandem Organic Solar Cells.....	140
4.2.1. AgNWs Used as Electrodes in Tandem Organic Solar Cells.....	140
4.2.2. Double junction Tandem OSC.....	150
4.2.3. Triple junction Tandem OSC.....	158
4.3. Ag Dendrites.....	164
4.4. Polymer Nanocomposites.....	174

References.....	184
5. Discussion.....	185
5.1. AgNWs and AgNWs/AZO Nanocomposite.....	185
5.1.1. Electron Tomography of Thin AgNWs.....	192
5.1.2. Diffraction Orientation and Strain Mapping.....	192
5.2. Tandem Organic Solar Cells.....	194
5.2.1. AgNWs Used as Electrodes in Tandem Organic Solar Cells.....	194
5.2.2. Double Junction Tandem OSC.....	195
5.2.3. Triple Junction Tandem OSC.....	198
5.3. Ag Dendrites.....	200
5.4. Polymer Nanocomposites.....	203
References.....	207
6. Conclusions and Future Outlook.....	211

Biography

List of Symbols and Abbreviations

1D – one dimensional	ω – angular velocity
2D – two dimensional	\vec{a}_1, \vec{a}_2 – hexagonal lattice vectors
3D – three dimensional	A – absorbance
α – optical absorption coefficient	A₁₀₀ – free surface area of (100) facet section
β – coefficient which depends on dominant scattering (thermal or Rutherford)	ABX₃ – perovskite type structure
γ_{100} – surface energy of free surface (100) facet	ADF – annular dark field
γ_T – surface energy of twin boundary	AgNW – silver nanowire
γ_w – surface energy of nanoweld	ALD – atomic layer deposition
ϵ_{xx} – horizontal strain	AMI.5 – standard solar spectra at Earth's surface
ϵ_{xy} – shear strain	APCE – absorbed photon to current efficiency
ϵ_{yy} – vertical strain	A_{TNW} – twin interface area of nanowire
ϵ – molar absorptivity of species (extinction coefficient)	A_{tw} – area of twin boundary in nanoweld
η_A – absorption efficiency	A_w – surface area of nanoweld
η_{ED} – exciton diffusion efficiency	AZO – aluminum doped zinc oxide
η_{CT} – charge transfer efficiency	BCC – body centered cubic
η_{CC} – charge collection efficiency	BF – bright field
η – power conversion efficiency	BHJ – bulk heterojunction
θ – rotational angle	BKD – backscatter Kikuchi diffraction
ν_{sample} – Poisson's coefficient of sample	BP – back-projection
ν – frequency of photon	BSE – backscattered electrons
ν_i – Poisson's coefficient of indenter	c – concentration of the species
ρ – density of final deposited film	C – amplitude contrast
σ_{DC} – direct current conductivity	CBED – conversion beam electron diffraction
σ_{OP} – optical conductivity	C_c – chromatic aberration coefficient
σ_{NW} – strain energy of nanowire	CdTe – Cadmium telluride
σ_w – strain energy of nanoweld	

CE – counter electrode
 \vec{C}_h – chirality vector
CIGS – copper indium gallium selenide
CIS – copper indium selenide
CL – condenser lens
(CN)₂ – cyanogen
CNT – carbon nanotubes
CTEM – conventional transmission electron microscopy
CVD – chemical vapor deposition
C_s – spherical aberration coefficient
D – distance of sample from top of objective lens
D-A – donor acceptor
DC – direct current
DEZ – diethyl zinc
DFEH – dark field electron holography
DI – deionized
DLA – diffusion-limited aggregation
DPP – diketopyrrolopyrrole
DSSC – dye sensitized solar cells
DWCNT – double-walled carbon nanotube
d_y – resolution along y axis
e – unit electronic charge
E – the mean energy
ΔE – the energy width of the beam
EBSD – electron back-scattered diffraction
EDS – energy dispersive x-ray spectroscopy
EELS – electron energy loss spectroscopy
EFTEM SI – energy filtered transmission electron microscopy spectrum imaging
EG – ethylene glycol
E_{HOMO(D)} – Energy level of highest occupied molecular orbital of donor
E_{LUMO(D)} – energy level of lowest unoccupied molecular orbital of donor
EMI – electromagnetic interference
E_{ph} – energy of photon
EQE – external quantum efficiency
E_r – reduced modulus
E_{sample} – elastic modulus of sample
ESD – electrostatic dissipation
ETL – electron transporting layer
e_{xz} – factor of stretching along z direction
FCC – face centered cubic
FF – fill factor
FFT – fast Fourier transform
FIB – focused ion beam
FoM – figure of merit
FOV – field of view
FTO – fluorine tin oxide
GB – grain boundary
GDMS – glow discharge mass spectrometry
GEN-2 – Merck proprietary material (properties and chemical structures)

not available)	<i>Kα</i> – emitted x-ray from K electron shell
<i>GIS</i> – gas injection system	<i>L</i> – pathlength
<i>GO</i> – graphene Oxide	<i>Lα</i> – emitted x-ray from L electron shell
<i>GPA</i> – geometric phase analysis	<i>LAADF</i> - low angle annular dark field
<i>h</i> – Planck’s constant	<i>LD</i> - exciton diffusion length
<i>HAADF</i> – high angle annular dark field	<i>LUMO</i> – lowest unoccupied molecular orbital
<i>HCP</i> – hexagonal close packed	<i>M</i> – power of magnification
<i>HF</i> – hydrofluoric acid	<i>M</i> – spectral mismatch factor
<i>HIPL</i> – high intensity pulsed light	<i>M9/2</i> – two-layer PNC with PVB as the matrix and MWCNT as the nanofiller
<i>hkl</i> – lattice indices	<i>M9/4</i> – four-layer PNC with PVB as the matrix and MWCNT as the nanofiller
<i>HOMO</i> – highest occupied molecular orbital	<i>M9/8</i> – eight-layer PNC with PVB as the matrix and MWCNT as the nanofiller
<i>HTL</i> – hole transporting layer	<i>M⁺</i> – metal ion
<i>HRTEM</i> - high resolution transmission electron microscopy	<i>Micro-D</i> - micro-electron diffraction
<i>I</i> – transmitted intensity of light	<i>MO</i> – metal oxide
<i>I₀</i> – incident intensity of light	<i>MWCNT</i> – multi-walled carbon nanotubes
<i>I₁</i> and <i>I₂</i> – intensities of two adjacent areas	<i>n</i> – order of reflection
<i>ICBA</i> – indene-C ₆₀ bisadduct	<i>N</i> – number of 2D projections
<i>IDB</i> – inversion domain boundary	<i>Nano-D</i> – nano-electron diffraction
<i>IPCE</i> – incident photon to current efficiency	<i>NBED</i> – nano-beam electron diffraction
<i>IQE</i> – internal quantum efficiency	<i>NIR</i> – near infrared
<i>I_{sc}</i> – short circuit current (photocurrent)	<i>N-PEDOT</i> – neutral poly(3,4-ethylenedioxythiophene):poly(styrenesulfonate)
<i>ITO</i> – indium tin oxide	
<i>j</i> – diffusion current density	
<i>J_{MP}</i> – current density at maximum power	
<i>J_{SC}</i> – short circuit current density	
<i>J_{SC1}, J_{SC2}, J_{SC3}</i> - short circuit current densities of individual sub-cells	

NS – nanostructures
n-type – donor semiconductor
OA - objective aperture
OIM – orientation imaging microscopy
OL – objective lens
OLED – organic light emitting diode
OPV – organic photovoltaic
OSC – organic solar cell
OTEC – ocean thermal energy conversion
PC₆₁BM – [6,6]-phenyl-C₆₁-butyric acid methyl ester
PC₇₁BM – [6,6]-phenyl-C₇₁-butyric acid methyl ester
PCDTBT - poly(2,7-carbazole-*alt*-4,7-dithienyl-2,1,3-benzothiadiazole)
PCE – power conversion efficiency
pDPP5T-2 – diketopyrrolopyrrole–quinquethiophene
PEDOT:PSS – poly(3,4-ethylenedioxythiophene):poly(styrene sulfonate)
PET – polyethylene terephthalate
P_{ideal} – power of ideal device
P_{in} – input light power
PL – projector lens
P_{MP} – point of maximum power
PNC – polymer nanocomposites
P_{out} – output electrical power
PS – polystyrene
P_{source} – light intensity incident on the device
p-type – acceptor semiconductor
PVA – polyvinyl alcohol
PVAc – polyvinyl acetates
PVB – polyvinyl Butyral
PVP – polyvinylpyrrolidone
PVB+M – *PNC* with *PVB* as the matrix and MWCNT as the nanofiller
PVB+S – *PNC* with *PVB* as the matrix and SWCNT as the nanofiller
PVB+G – *PNC* with *PVB* as the matrix and graphene as the nanofiller
PVD – physical vapor deposition
R – reflectance
R – goodness of fit
R_a – average surface roughness
RBM – radial breathing mode
r_c – chromatically limited resolution
RE – reference electrode
r-GO – reduced graphene oxide
R_q or *RMS* – root mean square surface roughness
R_p – parallel resistance
RPM – rounds per minute
r_s – spherically limited resolution
R_S – sheet resistance
SAD – selected area diffraction
SADP – selected area diffraction pattern
SE - secondary electrons
SEM – scanning electron microscopy
SERS – surface enhanced Raman spectroscopy
SF – stacking fault

SFE – stacking fault energy
STD – standard deviation
SWCNT – single-walled carbon nanotubes
T – transmittance
T₁-T₅ – twin segments
TEM – transmission electron microscopy
TLD – through lens detector
T_m – melting temperature
TMA – trimethylaluminium
TP – twin plane
TPRE – twin plane reentrant edge
UV-VIS – ultraviolet – visible
V_{MP} – voltage at maximum power
V_{OC} – open circuit voltage
V_{OC1}, V_{OC2}, V_{OC3} – open circuit voltages
of individual sub-cells
V_{NW} – strained volume of nanowire
V_w – volume of nanoweld
WBP – weighted back-projection
WE – working electrode
WHS – Wagner, Hamilton and Seidensticker
Z – atomic number
Z-contrast – atomic number contrast microscopy

List of Figures

Figure 1.1. Total reserves (in TWy) for finite energy resources – coal, uranium, petroleum and natural gas (top) and yearly potential (in TWy/y) for renewable energies – wind, waves, OTEC (ocean thermal energy conversion), biomass, hydro, geothermal and tidal. For the pie chart, maximum values in presented value range were considered; After [3,5].....	2
Figure 1.2. Optical transparency at 550nm wavelength as a function of electrical sheet resistance of various metallic films, ITO, AgNWs, SWCNTs, graphene and PEDOT:PSS [44].....	4
Figure 2.1. Schematic representation of stacking sequence of FCC structures: purple plane of atoms (A), green plane of atoms (B) and yellow plane of atoms (C) form the ABC stacking sequence.....	12
Figure 2.2. Schematic of a) perfect and b) twinned FCC crystal lattice. Atom planes A, B and C noted. Arrows indicate twin planes.....	13
Figure 2.3. A) Polyol synthesis of AgNS where EG reduces Ag^+ into fluctuating nuclei which grow into multiply twinned, singly twinned or single crystalline seeds from which various structures can be grown like B) spheres [28], C) cubes, D) truncated cubes, E) right bipyramids, F) bars, G) spheroids, H) triangular plates and I) wires [29]; red lines represent twin planes, dark facets are of $\{100\}$ orientation while light facets are of $\{111\}$ orientation [30].....	15
Figure 2.4. Mechanism of AgNW growth, A) Multiply twinned seed grows with confinement of $\{100\}$ facets by PVP in noted $[110]$ growth direction, B) Diffusion of Ag atoms on both ends of AgNW, on facets with $\{111\}$ orientations where there is weak interaction with PVP; Arrows indicate flux of Ag atoms toward $\{111\}$ planes; Red lines represent twin boundaries (planes) while the red plane represents one twin plane [33].....	16
Figure 2.5. Cross-section of an AgNW. Five twin segments are noted by numbers 1-5. Shown in image is a wedge angle of a single twin segment as well as the angle of missing gap. Twin boundaries separating twin segments are of $\{111\}$ orientation.....	17

Figure 2.6. Optical transparency as a function of sheet resistance for graphene (black squares), SWCNTs (red circles), AgNWs (green triangles) and ITO (blue circles). Also noted are the iso-value lines of FoM [97].....22

Figure 2.7. Schematic of a solar cell showing the cycle of electrons. Photon induced excitation of electrons from valence to conduction band. Contact selective to the conduction band delivers electrons to the external circuit after which they are returned to the valence band by a contact selective to the valence band; electrons are depicted as black circles [145].....26

Figure 2.8. Simplified schematic diagram of a bilayer device noting appropriate layers.....30

Figure 2.9. Simplified schematic diagram of a BHJ device noting appropriate layers. Active layer consist of an electron donor acceptor (D/A) blend.....31

Figure 2.10. Schematic showing the working principle of the BHJ OSC: excitation of electron in donor and creation of exciton (1), diffusion of exciton to D/A interface (2), exciton dissociation (3) and charge collection (4); full circles and arrows represent electrons and electron diffusion paths, respectively, while hollow circles and arrow represent holes and hole diffusion paths; numbers indicate steps in the working procedure.....32

Figure 2.11. a) Schematic of regular stacked architecture of OSCs, b) Schematic of inverted stacked architecture of OSCs; HTL and ETL denote hole and electron transporting layers, respectively.....35

Figure 2.12. Typical current versus voltage curves in the dark and under illumination; Green rectangle corresponds to value of maximum power and white rectangle corresponds to value of power of ideal device. Open circuit voltage is noted by (3), point of maximum power is noted by (2) and short circuit current density is noted by (1).....40

Figure 2.13. Eight allotropic modifications of carbon: a) diamond, b) graphite (comprised of many graphene planes), c) lonsdaleite, d) C₆₀, e) C₅₄₀ fullerite, f) C₇₀, g) amorphous carbon, h) carbon nanotubes (pictured is a SWCNT).....42

Figure 2.14. Schematic of ways the hexagonal carbon sheet can be rolled into a tube. This is an example of forming (3,2) type CNTs [213].....43

Figure 2.15. CNT closed with a half of a C ₆₀ molecule at each side resulting in a: a) zig-zag structure of (9,0) type, b) armchair structure of (5,5) type [213].....	44
Figure 2.16. a) Schematic illustration of a graphene sheet, b) reconstructed micrograph of exit electron wave acquired by TEM; model showing two hexagonal rings of an ideal graphene lattice with noted bond length [223].....	47
Figure 2.17. Dispersing scenarios of laminated graphene material in polymer matrix, a) separated, b) intercalated, c) exfoliated; black platelets represent graphene material, while blue lines represent polymer chains [296].....	54
Figure 3.1. Working procedure of spin coating films, a) The ink is drop cast onto substrate, b) elimination of excess material during rotation, c) even ink distribution during rotation, d) solvent evaporation; Grey arrows represent motion of spinning while orange arrows represent evaporation of solvent; After [3].....	71
Figure 3.2. Doctor blading setup, a) Side view, b) Frontal view; The arrow indicates direction of blade movement; Width of film is dependent on the width of blade frame.....	72
Figure 3.3. Schematic of electrodeposition set-up consisting of three electrodes: working electrode (WE), reference electrode (RE) and counter electrode (CE) immersed in metal ion (M ⁺) containing electrolyte; Flow of current (A) and potential (V) are marked in the schematic.....	73
Figure 3.4. Atomic layer deposition cycle consisting of 4 steps, a) pulse of organometallic precursor, b) chamber purging, c) pulse of second precursor, d) chamber purging.....	74
Figure 3.5. Schematic presentation of the Berkovich indenter tip.....	78
Figure 3.6. Typical loading-unloading curve, shown as load versus displacement (depth).....	80
Figure 3.7. Schematic presentation of the loading - unloading cycle geometric parameters characterizing the indenter - sample contact; After [25].....	80
Figure 3.8. Interaction volume between the electron beam and the sample. Note that the BSE can leave the sample from a greater depth than the SE.....	83
Figure 3.9. Schematic of FIB/SEM dual beam system. Noted are the electron and ion columns, at 52° with respect to each other, as well as the gas injection system (GIS).....	86

Figure 3.10. Effects occurring during interaction of high energy electron beam with the sample; After [38].....	87
Figure 3.11. Different operation modes in TEM/STEM.....	88
Figure 3.12. Two main modes in TEM: a) forming of BF image and b) forming of diffraction image [39].....	89
Figure 3.13. Diagram of formation of a SAD image [38].....	90
Figure 3.14. Diagram of role of objective aperture and forming of: a) BF image, b) DF image, c) high resolution phase contrast image [38], d) and e) are BF and DF images, respectively, of a Al ₃ Sc-Al ₃ Zr core-shell precipitate in aluminum alloy, f) HRTEM image of Al ₃ Zr shell [40].....	90
Figure 3.15. a) Typical experimental setup for STEM imaging: STEM beam (1), sample (2), ADF detector (3), BF detector (4) and convergent beam electron diffraction image (5); After [42], b) HAADF image of Al ₃ Zr shell between Al ₃ Sc core and aluminum matrix; note the strongest contrast is in the region containing zirconium; After [43].....	94
Figure 3.16. Schematic representation of two axial aberrations: a) spherical, b) chromatic; discs of least confusion are indicated by black arrows; blue lines indicate no energy loss; green and red lines indicate energy loss electrons, of energies E- ΔE_1 and E- ΔE_2 , respectively [47].....	96
Figure 3.17. Sequence of the FIB sample preparation procedure of AgNWs encapsulated with AZO, a) carbon deposition, b) trench milling, c) Lamella lift-out and attachment to half-grid by carbon deposition, with nanomanipulator, d) high magnification image of lamella attached to half grid for final thinning; note the nanowire cross-section is perpendicular to the electron beam.....	102
Figure 3.18. a) Polarization curve of Ag electrodeposition, b) Current density as a function of time, at an overpotential of 100 mV [8].....	108
Figure 3.19. Schematic representation of the Ag dendrite sample preparation and EBSD based OIM analysis: a) Sample surface is parallel to the ion beam after tilting of stage by 7°; b) Sample surface is perpendicular to electron beam; c) Sample surface is 70° with respect to incident electron beam for EBSD analysis [9].....	110
Figure 3.20. Sequence of the FIB sample preparation procedure of Ag dendrites, a) Selection of a typical Ag nanodendrite, b) carbon and platinum protection layer	

deposition, c) lamella lift-out by nanomanipulator, after trench milling after initial thinning, d) lamella attachment on Cu grid poles, followed by final thinning.....	110
Figure 3.21. Gold contact pads as electrodes on the nanocomposite film; noted are size of pads and spacing in between them.....	112
Figure 3.22. Four point probe electrical measurements on PVB nanocomposite films with gold contact pads as electrodes. Numbers 1 - 4 represent electrodes on which conductivity was measured.....	112
Figure 3.23. Image of BioTek Synergy 4 Plate with numerous samples characterized simultaneously.....	113
Figure 3.24. Graph depicting load as a function of time. Experimental indentation parameters for all sample measurements are: Initial load 0 μN , loading/unloading rate 200 μNs^{-1} , maximum load 2000 μN , and hold time, at maximum load, 2 s.....	114
Figure 4.1. a) Scanning electron micrograph of as synthesized AgNWs, b) Histogram of diameter distribution.....	118
Figure 4.2. a) Scanning electron micrograph AgNWs after annealing, b-d) High magnification scanning electron micrographs of random welded junctions; After [1]; Circles denote welded junctions.....	118
Figure 4.3. X-ray diffraction analysis of investigated AgNWs.....	119
Figure 4.4. a) Scanning electron micrograph AgNWs on silicon after annealing and AZO deposition, b) Histogram of diameter distribution.....	119
Figure 4.5. a) Scanning electron micrograph AgNWs with AZO encapsulation, b-d) High magnification scanning electron micrographs of random welded junctions; Circles denote welded junctions.....	120
Figure 4.6. a) HAADF STEM image of AgNWs encapsulated with AZO in plain view, b) CTEM image of an AgNW encapsulated with AZO.....	120
Figure 4.7. a) Conventional transmission electron micrograph of AZO, taken with inserted selected area diffraction pattern; b) Selected area diffraction (SAD) pattern of area shown in a); c) simulated ring diffraction pattern for ZnO wurtzite structure, d) rotational average line profile of experimental SADP shown in b).....	121
Figure 4.8. a) High resolution phase contrast image of AZO taken close to [100] zone axis; insets present Fast Fourier Transforms (FFTs) of grains shown in white squares; Inversion domain boundary (IDB) noted by white arrows; b) Enlarged FFT taken from	

AZO grain 1; c) Simulated ZnO wurtzite structure in [100] zone axis with noted reflections; d-f) Composite FFTs of grains 1 + 2, 1 + 3 and 2 + 3, respectively; Simulated structures are presented below each FFT composite; Red circles represent $\sim 5^\circ$ difference in rotation between grains 1 and 3.....122

Figure 4.9. a) HAADF image of AgNWs encapsulated with AZO and energy dispersive spectroscopy (EDS) maps of silver (yellow), aluminum (red), zinc (blue) and oxygen (orange) [1], b) EDS spectrum (given as intensity as a function of energy) taken from the area shown in the HAADF image a).....123

Figure 4.10. Low magnification ADF scanning transmission electron micrograph of a cross-section of AgNWs/AZO nanocomposite; note the pentagonal cross-section of AgNWs and columnar growth of AZO nano-grains.....124

Figure 4.11. a) ADF micrograph of single AgNW encapsulated with AZO; b) HAADF micrograph of same NW; c) integrated line profile across AgNW/AZO interface within white rectangle in b); d) ADF image of a different AgNW with appropriate EDS maps for silver, zinc, oxygen, and aluminum [2], e) integrated line profile across AZO/black pentagonal region interface within white rectangle in aluminum map.....125

Figure 4.12. Low magnification ADF scanning transmission electron microscopy cross-sectional image of welded Ag NWs a) before tilting; b) after tilting, where welded regions are indicated by white arrows; After [1].....126

Figure 4.13. a) High resolution ADF STEM cross-sectional image of welded region between two Ag NWs; left inset: low magnification image with black square showing analyzed region; right inset: FFT from the red square region; b) enlarged region indicated by red square in a); c) moiré pattern obtained using 111 reflection indicated by yellow circle in FFT inset in a); Dotted red line represents twin plane, extending from the top NW into the welded region; After [1].....127

Figure 4.14. a) High resolution ADF STEM cross-sectional image of welded region between two Ag NWs; bottom left inset: low magnification image with black square showing analyzed region; upper left inset: FFT from the red square region; top right inset: FFT from the center of the welded region, b) image of enlarged region indicated by red square in a) with noted twin planes by white arrows, c) moiré pattern obtain using 111 reflection indicated by yellow circle in left middle inset FFT in a).....128

Figure 4.15. a) High resolution ADF STEM cross-sectional image of the right-hand side welded region between two Ag NWs; left inset: low magnification image with black square showing analyzed region; right inset: FFT from the red square region, b) enlarged region indicated by red square in a) with white dashed line noting twin plane, c) moiré pattern obtain using 111 and 200 reflections indicated by yellow circle in FFT inset in a).....	129
Figure 4.16. a) HRSTEM HAADF image of AgNW with twin segments indicated by numbers 1-5; inset is an FFT from twin segment 1; Displacement maps: b) Horizontal; c) Vertical; d) Radial; e) Annular; Strain maps: f) Horizontal (ϵ_{xx}), g) Shear (ϵ_{xy}), h) Vertical (ϵ_{yy}), i) rotational (θ).....	130
Figure 4.17. ADF scanning transmission electron micrograph of AgNWs encapsulated in AZO; White arrows indicate twin planes and red circle indicates formation of neck region [1].....	131
Figure 4.18. a) HRSTEM image of AgNW corner and b) enlarged region indicated by red square in a) showing a reentrant angle of $\sim 141^\circ$ at the corners of pentagonal cross-section where two twin segments meet; red dots illustrate FCC unit cells in neighboring AgNW twin segments.....	132
Figure 4.19. Roughness measurement for AgNWs/AZO nanocomposite presented as height as a function of distance.....	132
Figure 4.20. Optical transmittance of various electrodes in the UV-VIS/NIR spectra: 100 nm thick AZO film (red line), AgNWs (orange line), heated AgNWs (blue line), AgNWs encapsulated by 100 nm thick AZO film (green line), heated AgNWs and subsequently encapsulated by 100 nm thick AZO film (pink line). Bare glass substrate is represented by a black line; After [2].....	133
Figure 4.21. Current density as a function of voltage for silicon based solar cells with various top electrodes; After [2].....	134
Figure 4.22. STEM image of welded AgNWs. Disconnected welded junctions are indicated by red circles while welded junctions with preserved integrity are indicated by blue circles. Background corresponds to lacey carbon grid.....	135
Figure 4.23. HAADF STEM image of welded junction between two AgNWs. White arrows indicate NW diameters.....	136

Figure 4.24. 3D structure of the reconstructed welded junction between two AgNWs. White dashed line indicated central ridge of thinner NW interrupted at nanoweld.....136

Figure 4.25. 3D volume renderings of welded AgNWs, shown from different viewpoints; Cartesian coordinates are indicated in both images.....137

Figure 4.26. a) HAADF STEM image of welded AgNWs with indicated thicknesses, b) NBED pattern taken close to $[\bar{1}12]$ zone axis from the region indicated by red circle in a).....138

Figure 4.27. Orientation maps for various sections of both AgNWs and the welded zone; a) and b) are maps of thinner NW and the welded zone; c) and d) are maps of left and right sections of the thicker NW, below the welded zone; e) Map of left section of thicker NW above the welded zone; light blue color indicates area where diffraction signal > 0 , black color depicts area with no diffraction signal, white color represents area with highest signal; Insets represent NBED patterns with noted orientations.....138

Figure 4.28. Color-coded maps of coherent strain (ϵ_{xx} , ϵ_{yy} , ϵ_{xy}) and lattice rotation angle (θ) distribution within AgNWs and the welded zone; black color indicates contour of investigated sample; Insets represent NBED patterns corresponding to indicated color-coded areas. Also noted are Cartesian coordinates.....139

Figure 4.29. Optical transmittance of AgNW samples: 1 (red line), 2 (blue line), 3 (green line), 4 (black line) and 5 (pink line).....141

Figure 4.30. Surface roughness (height as a function of distance) of AgNWs: a) Sample 1, b) Sample 2, c) Sample 3, d) Sample 4 and e) Sample 5.....142

Figure 4.31. a) SEM image of an undesirable structure which includes oxide particles and charged patches, b) Histogram of intensities with fit double Gaussian function showing a peak corresponding to the background (left) and a peak corresponding to the AgNWs (right).....143

Figure 4.32. a) Up-sampled SEM image using a factor of 2, smoothed slightly, after applying threshold value, indicated in histogram in Figure 4.31b, b) Skeleton SEM image with all non-NW features removed.....144

Figure 4.33. Correction of skeleton image from Figure 4.32b.....145

Figure 4.34. Correction of image in Figure 4.33. Note that all non-NW features are successfully removed from the final image used for statistical analysis.....146

Figure 4.35. a) BF image of AgNWs, b) Intensity line profile averaged along yellow rectangle in shown in a).....	146
Figure 4.36. a) BF image of an AgNW network, b) Histogram of diameter size distribution of AgNWs; Analysis of AgNW network was performed based on the average diameter of AgNWs (Figure 4.36b), calculated by measuring NW diameters by intensity line profile averaging, as shown in Figure 4.35a and b.....	147
Figure 4.37. Effects of a) AgNW network thickness and b) area coverage on optical transmittance (blue squares) and sheet resistance (red circles) of AgNWs.....	148
Figure 4.38. Relationship between of AgNW network thickness and the total area coverage.....	149
Figure 4.39. a) Selected area ring diffraction pattern; b) Intensity line profile showing, besides FCC Ag rings, the presence of Ag ₂ O surface oxide film on AgNWs, given in red.....	149
Figure 4.40. Schematic of layout of tandem double-junction BHJ organic solar cell [3].....	150
Figure 4.41. a) Low magnification scanning electron micrograph of tandem double-junction organic solar cell cross-section after cleaving; b) higher magnification of image in a), c) top view of solar cell.....	151
Figure 4.42. Scanning transmission electron micrograph of tandem double-junction organic solar cell cross-section after FIB milling. The layers 1-10 are as follows: glass (1), PEDOT:PSS (2), printed Ag (3), PEDOT:PSS (4), GEN-2:PC ₆₁ BM (5), ZnO (6), N-PEDOT (7), pDPP5T-2:PC ₆₁ BM (8), ZnO (9), AgNWs (10).....	151
Figure 4.43. a) BF CTEM micrograph of tandem double-junction organic solar cell cross-section acquired using FIB lamella prepared by lift-out method; Layers 1-10 correspond to the ones in Figure 4.42; After [3].....	152
Figure 4.44. a) Low magnification BF image of glass/P_Ag interface structure; b) and c) HRTEM images of Ag nanoparticles in P_Ag electrode; inset is FFT of Ag particle in c).....	153
Figure 4.45. High magnification transmission electron micrograph of AgNW electrode in a) low thickness area, b) area of high thickness.....	154

Figure 4.46. HAADF STEM micrograph of tandem double-junction organic solar cell cross-section acquired by FIB lift-out lamella [3]; Layers 1-10 correspond to the ones in Figure 4.42.....155

Figure 4.47. HAADF scanning transmission electron micrograph of tandem double-junction organic solar cell and EDS maps of silver (red), zinc (yellow), oxygen (blue), sulfur (pink) and nitrogen (orange) taken from the HAADF STEM image [3].....157

Figure 4.48. Current density as a function of voltage for the tandem double-junction organic solar cell processed on glass; After [3].....158

Figure 4.49. Schematic of layout of tandem triple-junction BHJ organic solar cell [4].....158

Figure 4.50. Scanning transmission electron micrograph of tandem triple junction organic solar cell cross-section after FIB milling. Numbers 1-14 correspond to the following layers: glass (1), ITO (2), PEDOT:PSS (3), DPP:PC₆₁BM (4), ZnO (5), N-PEDOT (6), DPP:PC₆₁BM (7), ZnO (8), N-PEDOT (9), AgNWs (10), ZnO (11), PCDTBT:PC₇₁BM (12), MoO_x (13) and Ag (14).....159

Figure 4.51. a) BF transmission electron micrograph of tandem triple junction organic solar cell cross-section acquired by FIB lamella lift-out; After [4]; Layers 1-14 correspond to the ones in image 4.50.....160

Figure 4.52. a) HAADF STEM image of tandem triple junction organic solar cell cross-section acquired by FIB lamella lift-out; After [4]; Layers 1-14 correspond to the ones in image 4.50.....160

Figure 4.53. HAADF scanning transmission electron micrograph of tandem triple junction organic solar cell and EDS maps of silver (orange), zinc (pink), oxygen (blue), indium (yellow), tin (green), sulfur (turquoise) and molybdenum (purple) taken from HAADF STEM image; After [4].....162

Figure 4.54. Current density as a function of voltage for the tandem triple junction organic solar cell; After [4].....163

Figure 4.55. Scanning electron micrograph of Ag dendrites on silicon substrate.....164

Figure 4.56. Scanning electron micrographs of Ag nanodendrites on silicon substrate taken at different tilt angles [5].....165

Figure 4.57. a) and b) Scanning electron micrographs of an Ag dendrite taken at different tilts, c) cross-section of Ag dendrite, d) enlarged area indicated by white rectangle in c) [5].....	166
Figure 4.58. a) HAADF transmission electron micrographs of an Ag dendrite showing white spherical islands along the trunk, b) enlarged area indicated by white rectangle in a); white arrows indicate numerous white lines perpendicular to branch axis [5].....	167
Figure 4.59. a) BF transmission electron micrograph of an Ag dendrite, b) SAD pattern of dendrite shown in a) after tilting into two-beam condition; c) SAD pattern of dendrite taken close to $[\bar{1}11]$ zone axis; black arrows indicate numerous black lines/stripes perpendicular to branch axis; Growth directions of type $\langle 112 \rangle$ of trunk and branches are given in square brackets.....	167
Figure 4.60. a) Transmission electron micrograph of an Ag dendrite, b) High resolution phase contrast image of enlarged area indicated by white rectangle in a); left inset: FFT of Ag_2O ; right inset: FFT of Ag twins.....	168
Figure 4.61. a) HRTEM image of an Ag dendrite arm; the dotted white line indicates traces of $\{111\}$ planes, b) moiré pattern obtain using 200 and 111 reflections, c) lattice rigid rotation angle map with the look up color table given in radians [5].....	169
Figure 4.62. a) Scanning electron micrograph of an Ag dendrite, b) orientation map of dendrite with the lookup stereographic triangle and white lines which indicate twin boundaries, c) the orientation imaging color coded map showing two twin variants; d-e) The 100 and 111 pole figures constructed from the orientation data [5].....	170
Figure 4.63. a) High resolution transmission electron micrograph of twins in the zone between the dendrite trunk and arm; inset is a FFT taken from the area indicated by the white square, b) schematic illustration of twin planes with respect to growth directions and distinctive angles [5].....	171
Figure 4.64. Scanning electron micrograph of an Ag dendrite taken at two different tilt angles.....	172
Figure 4.65. Optical micrograph of a drop cast Ag dendrite on glass; note uniform distribution of dendrites.....	172
Figure 4.66. Current as a function of voltage of 250 μL drop cast Ag dendrites before (blue) and after heating 3 minutes at 250°C (beige).....	173

Figure 4.67. Transmittance as a function of wavelength for various volumes of Ag dendrites deposited on glass: 50 μL (blue), 150 μL (dark grey) and 250 μL (red).....173

Figure 4.68. Optical micrograph of a) PVB nanocomposite with MWCNTs, b) PVB nanocomposite with SWCNTs, c) PVB nanocomposite with graphene.....174

Figure 4.69. High resolution transmission electron micrographs of as received a) MWCNTs, b) SWCNT, and c) graphene [6].....175

Figure 4.70. a) Low magnification transmission electron micrograph of nanocomposite PVB with MWCNTs, b) High resolution transmission electron micrograph of individual MWCNT embedded in PVB matrix [6], c) MWCNT exhibiting tearing inside the PVB matrix.....176

Figure 4.71. Raman shift (as a function of intensity) of pristine MWCNTs (pink), PVB polymer (blue) and nanocomposite PVB with MWCNTs (red) in the range of 1200-1700 cm^{-1} (a), and 2500-3000 cm^{-1} (b); Characteristic D, G, D' and 2D peaks are noted [6].....177

Figure 4.72. Raman shift (as a function of intensity) of pristine SWCNTs (pink), PVB polymer (blue) and nanocomposite PVB with SWCNTs (red) in the range of 100-400 cm^{-1} (a), and 1200-1700 cm^{-1} (b) and 1200-1700 cm^{-1} (c); Characteristic RMB, D, G and 2D peaks are noted [6].....178

Figure 4.73. Raman shift (as a function of intensity) of pristine graphene (pink), PVB polymer (blue) and nanocomposite PVB with graphene (red) in the range of 1200-1700 cm^{-1} (a), and 2500-3000 cm^{-1} (b); Characteristic D, G and 2D peaks are noted [6]....179

Figure 4.74. a) Transmittance as a function of wavelength for samples processed under identical conditions, b) transmittance as a function of wavelength for nanocomposite samples PVB with MWCNTs for different sample thicknesses, c) transmittance as a function of thickness at two different wavelengths, 360 nm (circles) and 550 nm (squares), for nanocomposite samples PVB with MWCNTs [6].....180

Figure 4.75. Typical load – displacement curves for pure PVB (black line), PVB with MWCNTs (blue line), PVB with SWCNTs (red line), and PVB with graphene (green line).....181

Figure 4.76. Reduced modulus (red circles) and hardness values (blue squares) for pure PVB film, PVB with SWCNTs (PVB+S), PVB with MWCNTs (PVB+M), and PVB with graphene (PVB+G) nanocomposites; Also displayed are the standard deviations;

After [6].....	182
Figure 4.77. Electrical resistivity of pure PVB, PVB with SWCNTs (PVB+S), PVB with MWCNTs (PVB+M), and PVB with graphene (PVB+G) nanocomposites [6].....	183
Figure 5.1. Proposed model of solid-state wetting and subsequent welding of two AgNWs during annealing; a) before the formation of a neck region, b) after the formation of a neck region, c) neck expansion; d) two NW in contact along 100 facet, where the formation of a neck region is significantly delayed [13].....	189
Figure 5.2. HRSTEM ADF image illustrating atomic layer nucleation; yellow arrows indicate 100 facets while white arrow indicates growth direction of 111 planes. This image is modified from Figure 4.13a with inset representing low magnification image with red square showing analyzed region.....	191

List of Tables

Table 2.1. Properties of SWCNTs, MWCNTs and Graphite [219,220,221].....	45
Table 2.2. Properties of single layer graphene and GO [237].....	48
Table 3.1. Processing parameters of doctor bladed AgNWs.....	105
Table 4.1. Various solar cell working parameters with respect to type of top electrode used; After [2].....	134
Table 4.2. Various AgNW networks with differing processing parameters.....	141
Table 4.3. Statistical analysis of AgNW surface coverage.....	147
Table 4.4. Thicknesses measured by profilometer [3] and by line profile from TEM and STEM images of layers in the tandem double-junction organic solar cell.....	156
Table 4.5. Thicknesses measured by profilometer [4] and by line profile from TEM and STEM images of layers in the tandem triple junction organic solar cell	161
Table 4.6. Displacement before and after hold at maximum load P_{max} as well as final displacement of pure PVB, PVB with MWCNTs, PVB with SWCNTs and PVB with graphene. Values obtained from Figure 4.75.....	181
Table 4.7. Hardness and reduced modulus values of pristine PVB, PVB with MWCNTs, PVB with SWCNTs and PVB with graphene; After [6].....	183

1. Introduction

It is fairly obvious that, as we proceed well into the 21st century, one of the main concerns of the human race, if not the main one, is solving the energy problem i.e. providing sustainable energy for ~7.5 billion people on earth (2016 data [1]) and their ever rising need for energy. Keeping in mind the amounts of finite energy resource reserves, along with their environmental drawbacks such as radiation for uranium and atmosphere pollution for fossil fuels, drastic measures have to be taken in order to balance energy production and prevention of environmental disasters of global proportions like nuclear meltdowns or the greenhouse effect. This is the reason why, in the near future, global infrastructure has to run exclusively on renewably generated energy. Fortunately, there is more than enough available renewable energy to meet global needs, if it can be harnessed. Based on the REN21 2016 report [2] renewable energy accounted for ~19% of global energy consumption in 2014 with a rising trend in 2015 as a consequence of rising capacity and generation.

Among all renewable energy sources, the sun, as a practically unlimited source of energy, shows the most potential for dealing with the energy issue of global energy dependence as solar technology perfectly fits the profile of supporting environmental trends of reducing harmful emission of substances which pollute the atmosphere. Figure 1.1 shows, in terawatt years (TWy) and terawatt years per year (TWy/y), total recoverable reserves for finite energy resources (fossil fuels and uranium) and yearly potentials for renewables.

Potential of solar energy is not included in the chart presented in Figure 1.1 as it has a value of nearly 23000 TWy/y [3], more than 200 times the amount of all other resources combined. Coupled with the fact that the total global energy consumption in 2015 was ~18.5 TWy [4], it is evident that the path of solar technology is the predominant one to take if humanity plans to match global energy supply with its demands.

Solar energy is harnessed through solar cells, also called solar photovoltaic (PV) devices. In these multi-layer structures, whose purpose is to collect solar energy and convert it into electricity, besides the active layers where the photoconversion actually occurs, electrode layers serve a very important function. Electrodes form differences in potentials which help split electron-hole pairs (excitons) during photoconversion and

guide the charge carriers (electrons and holes) to their respective electrodes, thereby forming electron current. Solar cells, through electrodes, are connected to external circuits, i.e. applications which utilize produced electricity.

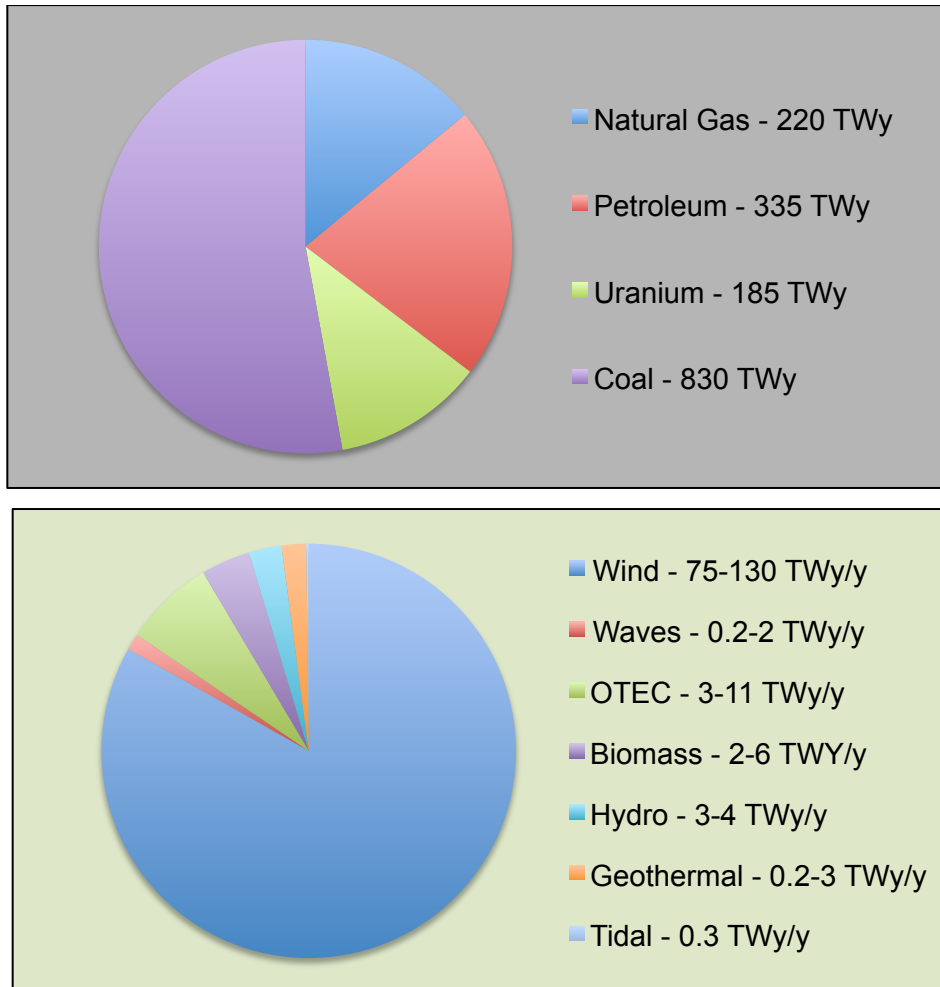


Figure 1.1. Total reserves (in TWy) for finite energy resources – coal, uranium, petroleum and natural gas (top) and yearly potential (in TWy/y) for renewable energies – wind, waves, OTEC (ocean thermal energy conversion), biomass, hydro, geothermal and tidal. For the pie chart, maximum values in presented value range were considered; After [3,5].

Indium tin oxide (ITO), a degenerately doped n-type semiconductor, is the most frequently used material for electrodes in new generations of solar cells and optoelectronic devices in general. Its composition is usually 74 wt.% of indium, 18 wt.% of oxygen and 8 wt.% of tin as indium (III) oxide (In_2O_3) is doped with tin dioxide (SnO_2) in order to increase charge carrier density and convert it from a p-type to

a n-type semiconductor [6,7]. The optical transmittance of ITO films is in the ~90% range with electrical resistivity below 10^{-4} Ωcm [8]. These properties make ITO an excellent choice for the transparent electrode in optoelectronic devices. However, numerous drawbacks of this material include [9]:

- High prices of indium, as a result of very limited global resources;
- Expensive and demanding processing methods, like physical vapor deposition (PVD) either by pulsed laser deposition or by sputtering, which require complex high-temperature, high-vacuum and inert conditions [10];
- High diffusivity of indium during photoconversion, which negatively impacts other layers and thus, the solar cell as a whole;
- Insufficient chemical stability which in time can lead to corrosion;
- Toxicity [11];
- Brittleness i.e. lack of mechanical flexibility [12].

Next generation solar cells require electrodes which, besides excellent optical and electrical properties, exhibit flexibility, light weight and are cheap solutions, compatible with large scale manufacturing methods like roll-to-roll printing [13]. A wide range of materials have come into consideration as alternatives for replacing ITO as the transparent electrode in solar cells as well as optoelectronic devices in general:

- *Metal Oxides* like aluminum doped zinc oxide (AZO) [14] and fluorine doped tin oxide (FTO) [15];
- *Conductive Polymers* like poly(3,4 - ethylene - dioxy - thiophene) poly(styrenesulfonate) - PEDOT:PSS [16,17] and *Polymer Nanocomposites* like CNT/epoxy resin [18] or PEDOT:PSS/r-GO [19];
- *Thin Metallic Films* of nickel [20], gold [21], silver [22], copper and aluminum [23];
- *Carbonaceous Nanomaterial films* of graphene (including r-GO) [24,25,26,27] and CNT [28,29,30];
- *Nanowire Networks* of metals like copper [31,32,33,34], gold [35,36] or even metal alloys like cupronickel [37].

The most extensively studied nanowire network for transparent electrodes is that of silver (Ag). In Figure 1.2 silver nanowires – AgNWs [38,39] are compared to conventional ITO [39,40] as well as carbon nanotubes (CNTs) [38,39,40], graphene [38,39], various metals and metal oxides [20,21,23,41,42] and PEDOT:PSS polymer [43]. Keeping in mind that materials with the best performances are found closest to the upper left part of the diagram (dotted rectangle), it is evident that AgNWs prove to be the most promising candidate to replace conventional ITO as transparent electrodes for optoelectronic devices.

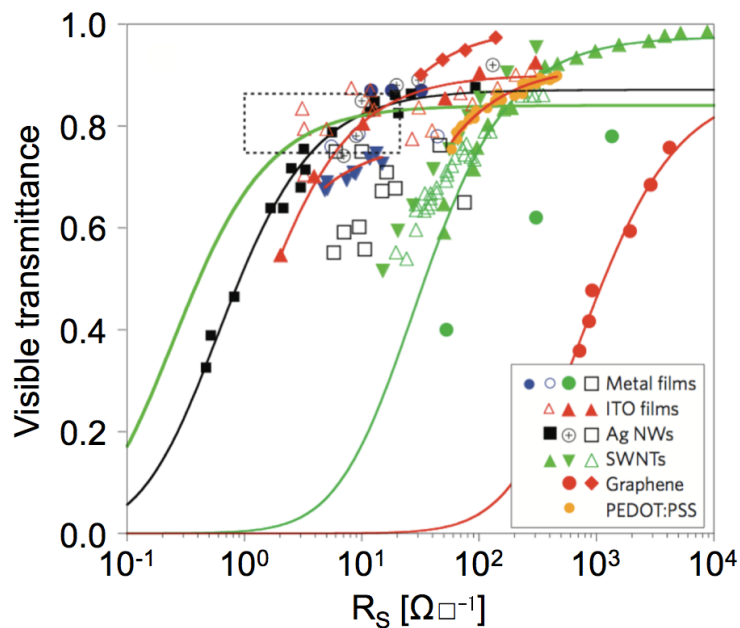


Figure 1.2. Optical transparency at 550nm wavelength as a function of electrical sheet resistance of various metallic films, ITO, AgNWs, SWCNTs, graphene and PEDOT:PSS [44].

With this in mind, this thesis deals with the structural characterization of pristine AgNWs and the AgNWs/AZO composite as well as the phenomenology of solid-state wetting and subsequent welding occurring during AgNW annealing for the purpose of decreasing sheet resistance without optical transmittance deterioration. Also, in this thesis, Ag dendrites are proposed as a novel transparent electrode solution, primarily because of the ease and cost of their manufacturing i.e. synthesis and processing. Structural characterization of Ag dendrites was performed with an emphasis on defect formation during their growth. Results obtained from aforementioned structural

analyses of AgNWs and Ag dendrites provide an understanding of material structure and can therefore lead to future tailoring of that structure in order to achieve desired properties of the material.

Organic solar cells utilize organic semiconductors like conductive polymers or small organic molecules to absorb light and convert it into electricity. This third generation of solar cells with unique properties, has high potential for various novel optoelectronic applications where the material demands for low thickness and high mechanical flexibility are ever-rising. Although, presently, these solar cells exhibit low efficiency and a short life-time, beneficial properties like mechanical flexibility and light weight, abundance and relatively low price of materials, high optical absorption at low thicknesses as well as simple processing methods and hence cheap large scale production rank them at the top of the solar cell industry of the near future. One of the most important areas of research in organic solar cells is the multi-junction (tandem) concept, which is the most relevant way of overcoming the Shockley–Queisser limit of power conversion efficiency for single bandgap solar cells. This tandem solar cell concept consists of stacking multiple photoactive layers for the purpose absorbing light in a broader range of wavelengths of the solar spectrum. This thesis deals with processing and structural characterization of organic tandem bulk heterojunction solar cells where the results give insight in the morphology of individual layers present in these cells.

One of the most common problems facing solar cells is degradation, which shortens their life-times. Environmental factors like humidity, oxygen, temperature and light intensity can lead to insulating thin oxide barriers on metal electrodes or the breakup of polymer conjugation, which results in the decrease of electrical conductivity. The concept of encapsulation has been employed in order to protect the solar cell from environmental factors which hinder its performance. This thesis deals with processing and characterization of polymer nanocomposite films which have superior optical and mechanical properties needed for a protective layer for solar cells.

Aim of this work was to utilize characterization methods, primarily scanning electron microscopy (SEM) and transmission electron microscopy (TEM) in order to elucidate the microstructure of AgNWs, AgNW/AZO nanocomposite, Ag dendrites and individual layers comprising organic tandem bulk heterojunction solar cells as well as

the role of morphology in the solid-state wetting and welding processes which occur during annealing of AgNWs. With obtained results, a correlation between microstructure and properties can be made which can lead to future material tailoring for the application as transparent electrodes in solar cells. The aim of this work also included characterization of polymer nanocomposites, with polyvinyl butyral (PVB) as the matrix and multi-walled carbon nanotubes (MWCNTs), single-walled carbon nanotubes (SWCNTs) and graphene as the nanofiller, in order to justify how even very small loading of nanofiller can enhance properties essential for the application of these nanocomposites as protective layers (encapsulants) for solar cells.

REFERENCES

-
- [1] <http://www.census.gov/popclock/>
- [2] Renewables 2016 Global Status Report, Renewable Energy Policy Network for the 21st Century.
- [3] Perez, R. and M. Perez, The International Energy Agency SHC Programme Solar Update, 50 (2009) 2-3.
- [4] International Energy Agency 2016 Report – Key World Energy Statistics.
- [5] The Solar Heating and Cooling Programme (SHC) Update, November 2015.
- [6] O. P. Agnihotri, A. K. Sharma, B. K. Gupta, and R. Thangaraj, Journal of Physics D: Applied Physics, 11 (1978) 643–648.
- [7] M. Sikora, D. Adam, P. M. Korczyk, A. Prodi-Schwab, P. Szymczak, and M. Cieplak, Langmuir, 28 (2012) 1523–1530.
- [8] S. Sohn and H-M. Kim, In *Organic Light Emitting Diode - Material, Process and Devices*, S. H. Ko Ed., InTech, Rijeka, Croatia, 2011, p. 233.
- [9] M. Geoghegan and G. Hadziioannou, *Polymer Electronics*, Oxford University Press, Oxford, UK, 2013, p. 95.
- [10] B. L. Gehman, S. Jonsson, T. Rudolph, M. Scherer, M. Weigert, and R. Werner, Thin Solid Films, 220 (1992) 333-336.
- [11] K. Nagano, T. Nishizawa, Y. Umeda, T. Kasai, T. Noguchi, K. Gotoh, N. Ikawa, Y. Eitaki, Y. Kawasumi, T. Yamauchi, H. Arito and S. Fukushima, Journal of Occupational Health, 53 (2011) 175-87.
- [12] Z. Chen, B. Cotterell, W. Wang, E. Guenther, S-J. Chua, Thin Solid Films, 394 (2001) 202-206.
- [13] R. Sondergaard, M. Hosel, D. Angmo, T. T. Larsen-Olsen, F. C. Krebs, Materials Today, 15 (2012) 36–49.
- [14] K. Schulze, C. Urich, R. Schueppel, K. Leo, M. Pfeiffer, E. Brier, E. Reinhold, and P. Baeuerle, Applied Physics Letters, 91 (2007) 073521-073523.
- [15] Z. Y. Banyamin, P. J. Kelly, G. West and J. Boardman, Coatings, 4 (2014) 732-746.
- [16] J. Saghaei, A. Fallahzadeh and T. Saghaei, Organic Electronics, 24 (2015) 188–194.

-
- [17] J. Ouyang, C-W. Chu, F-C. Chen, Q. Xu, and Y. Yang, *Advanced Functional Materials*, 15 (2005) 203–208.
- [18] Z. Yang, T. Chen, R. He, H. Li, H. Lin, L. Li, G. Zou, Q. Jia and H. Peng, *Polymer Chemistry*, 4 (2013) 1680-1684.
- [19] Y. G. Seol, T. Q. Trung, O. J. Yoon, I-Y. Sohn and N. E. Lee, *Journal of Materials Chemistry*, 22 (2012) 23759-23766.
- [20] L. Martínez, D. S. Ghosh, S. Giurgola, P. Vergani and V. Pruneri, *Optical Materials*, 31 (2009) 1115–1117.
- [21] E. J. Gillham, J. S. Preston and B. E. Williams, *Philosophical Magazine*, 46 (1955) 1051–1071.
- [22] N. Kim, H-D. Um, I. Choi, K-H. Kim, and K. Seo, *ACS Applied Materials & Interfaces*, 8 (2016) 11412–11417.
- [23] M-G. Kang and L. J. Guo, *Advanced Materials*, 19 (2007) 1391–1396.
- [24] P. Blake, P. D. Brimicombe, R. R. Nair, T. J. Booth, D. Jiang, F. Schedin, L. A. Ponomarenko, S. V. Morozov, H. F. Gleeson, E. W. Hill, A. K. Geim and K. S. Novoselov, *Nano Letters*, 8 (2008) 1704–1708.
- [25] G. Eda, G. Fanchini and M. Chhowalla, *Nature Nanotechnology*, 3 (2008) 270–274.
- [26] S. Bae, H. Kim, Y. Lee, X. Xu, J- S. Park, Y. Zheng, J. Balakrishnan, T. Lei, H. R. Kim, Y. I. Song, Y-J. Kim, K. S. Kim, B. Ozyilmaz, J-H. Ahn, B. H. Hong and S. Iijima, *Nature Nanotechnology*, 5 (2010) 574–578.
- [27] A. Reina, X. Jia, J. Ho, D. Nezich, H. Son, V. Bulovic, M. S. Dresselhaus and J. Kong, *Nano Letters*, 9 (2009) 30–35.
- [28] R. A. Hatton, A. J. Miller and S. R. P. Silva, *Journal of Materials Chemistry*, 18 (2008) 1183–1192.
- [29] T. M. Barnes, J. D. Bergeson, R. C. Tenent, B. A. Larsen, G. Teeter, K. M. Jones, J. L. Blackburn, and J. van de Lagemaat, *Applied Physics Letters*, 96 (2010) 243309.
- [30] R. Ulbricht, X. Jiang, S. Lee, K. Inoue, M. Zhang, S. Fang, R. Baughman and A. Zakhidov, *Physica Status Solidi*, 243 (2006) 3528–3532.
- [31] A. R. Rathmell, S. M. Bergin, Y-L. Hua, Z-Y. Li and B. J. Wiley, *Advanced Materials*, 22 (2010) 3558–3563.
- [32] A. R. Rathmell and B. J. Wiley, *Advanced Materials*, 23 (2011) 4798–4803.
- [33] H. Wu, L. Hu, M. W. Rowell, D. Kong, J. J. Cha, J. R. McDonough, J. Zhu, Y. Yang, M. D. McGehee and Y. Cui, *Nano Letters*, 10 (2010) 4242–4248.
- [34] D. Zhang, R. Wang, M. Wen, D. Weng, X. Cui, J. Sun, H. Li and Y. Lu, *Journal of American Chemical Society*, 134 (2012) 14283–14286.
- [35] P. E. Lyons, S. De, J. Elias, M. Schamel, L. Philippe, A. T. Bellew, J. J. Boland and J. N. Coleman, *Journal of Physical Chemistry Letters*, 2 (2011) 3058–3062.
- [36] A. Sanchez-Iglesias, B. Rivas-Murias, M. Grzelczak, J. Perez-Juste, L. M. Liz-Marzan, F. Rivadulla and M. A. Correa-Duarte, *Nano Letters*, 12 (2012) 6066–6070.
- [37] A. R. Rathmell, M. Nguyen, M. Chi and B. J. Wiley, *Nano Letters*, 12 (2012) 3193–3199.
- [38] S. De, P. J. King, P. E. Lyons, U. Khan, and J. N. Coleman, *ACS Nano*, 4 (2010) 7064–7072.
- [39] F. Bonaccorso, Z. Sun, T. Hasan, A. C. Ferrari, *Nature Photonics*, 4 (2010) 611–622.

-
- [40] T. M. Barnes, M. O. Reese, J. D. Bergeson, B. A. Larsen, J. L. Blackburn, M. C. Beard, J. Bult and J. van de Lagemaat, *Advanced Energy Materials*, 2 (2012) 353–360.
- [41] T. Dimopoulos, G. Z. Radnoczi, B. Pécz and H. Bruckl, *Thin Solid Films*, 519 (2010) 1470–1474.
- [42] L. Holland and G. Siddall, *British Journal of Applied Physics*, 9 (1958) 359–361.
- [43] Y. H. Kim, C. Sachse, M. L. Machala, C. May, L. M. Meskamp and K. Leo, *Advanced Functional Materials*, 21 (2011) 1076–1081.
- [44] K. Ellmer, *Nature Photonics*, 6 (2012) 809–817.

2. Theoretical Background

2.1. Silver Nanostructures

Nanostructured materials, exhibiting dimensions (at least one) in the nano-scale (less than 100 nm) can be isolated, substrate-supported or embedded nanosized particles, thin wires or thin films [1,2]. These nanostructures (NS) exhibit high surface-to-volume ratios, manifested through high surface energy. Also present are quantum effects, which apply for structures with very small dimensions and are the result of confinement of electron movement. For these reasons, NS present good models for investigations of various phenomena, as they exhibit very different properties compared to the properties of the bulk material. This is especially true for metallic NS where a property like optical transmittance is dependent on absorption in the visible spectrum, the plasmon band, which relies on factors like size and shape of NS, metal species, surrounding medium, etc. [3]. As the metallic NS size and shape greatly influence their properties, tailoring these factors for desired results is very important. During synthesis of metallic NS (crystals), their morphology is dependent on the thermodynamic equilibrium i.e. how close or far the crystal is from it [4,5]. Driving force for crystallization is a key factor here as its variation leads to the formation of a wide range of shapes [6] ranging from polyhedrons to hierarchical structures like dendrites [7]. This is, of course, very challenging as precise control of driving force, and therefore tuning of distance from equilibrium, is not a simple task.

Control of the driving force and distance from thermodynamic equilibrium i.e. control of the synthesis process of silver nanostructures (AgNS) has become a hot topic as silver is a metal of particular interest, as its electrical and thermal conductivities [8] are the highest among metals and the third highest among all elements, after CNTs and graphene, carbon allotropes. Various methods of AgNS synthesis have been developed including, among others [9]:

- Chemical reduction of salts;
- Photochemical, thermal or sonochemical decomposition of organometallics;
- Electrochemical synthesis.

Chemical reduction method stands out as the most commonly used technique as its advantages include reproducibility and the ability to produce AgNS with controlled size and in large quantities. It is also interesting because of the fact that stabilization of NS, for the purposes of passivation and deagglomeration, is easy to apply. In this case, steric stabilization is the most common method used, where a polymeric layer acts as a surface barrier. This method of synthesis will be discussed in more detail in the section on AgNW structures.

Synthesis of AgNS via electrochemical method is also commonly employed [10]. It consists of passing an electric current between two or more electrodes in an electrolyte medium. As the electrode potential, which is the driving force of the synthesis, can be controlled, as well as the fact that no secondary species are produced during the process, this method is very promising and in some instances superior to the chemical reduction method.

For AgNS to be utilized in optoelectronics as transparent electrodes, the emphasized application in this thesis, several routes have to be taken in order to assure the required properties, high optical transmittance and high electrical conductivity, will be exhibited. The reason for this is that, although highly conductive in the bulk, Ag exhibits highest reflectivity of all metals, 98% in infrared (IR) region and 75.6-96.9% in visible (Vis) region [11]. As this property is a function of Ag film thickness, ultra thin films can exhibit high optical transparency [12]. Films can also be patterned into grids [13] where spacing between the AgNS would increase the optical transparency of the whole structure.

2.1.1 Crystal Defects

Crystal perfection is an unachievable concept as it is not found in nature. A structure where the arrangement of atoms matches the hypothetical perfectness does not exist as all crystals have some sort of defects. This is a very beneficial fact with regards to materials engineering as, with the presence of defects, material properties can be tuned in various combinations according to the requirement of the materials applications. On the other hand, perfect crystals, limited by their structure and

composition, would not have the possibility to have their properties altered. Regarding the dimensions of crystal defects, they can be classified as [14]:

- *0- dimensional (point) defects*: singular isolated defects in the crystal structure, can be either intrinsic, like a vacancy or interstitial or extrinsic, like interstitial or substitutional dopants (solutes) or impurities;
- *1- dimensional (linear) defects – dislocations*: line defects depicting linear irregularity in crystal structure characterized by the Burgers vector which describes magnitude and direction of distortion (irregularity); dislocations can be edge, screw, mixed and partial;
- *2- dimensional (planar) defects*: free surfaces – interfaces between solid and vapor/liquid (structure and energy determine shape and properties), grain boundaries (misorientation of grain dictates structure), phase boundaries (differences in phase properties dictate structure) as well as twin boundaries and stacking faults, which will be discussed in details in the following text;
- *3- dimensional (bulk) defects*: precipitates, pores, voids and inclusions of second-phase particles, pores.

Stacking Faults

Hexagonal close packed (HCP) and body centered cubic (BCC) structures have a stacking sequence ABABABAB, where A is the first plane of atoms, B the second plane whose atoms are directly above interstitial sites of the first plane, the second A is the third plane where atoms are directly above the atoms of the first plane, and so forth. In face centered cubic (FCC) structures, the stacking sequence is ABCABCABC, meaning that the third plane of atoms (C) in sequence does not have atoms located above atoms of planes A or B (Figure 2.1).

A stacking fault (planar defect) is a single plane interruption in the sequence of atom plane stacking i.e. it occurs where the sequencing pattern is broken. An extrinsic stacking fault occurs when an additional plane of atoms is introduced to the structure which changes from ABCABC to ABC|B|ABC where |B| is the added plane.

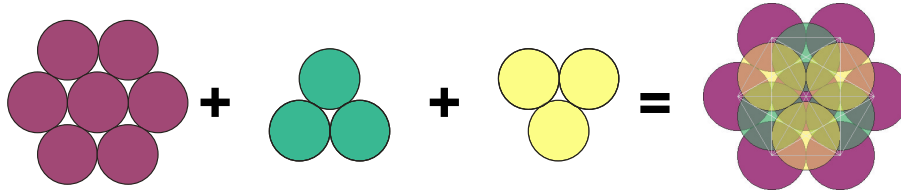


Figure 2.1. Schematic representation of stacking sequence of FCC structures: purple plane of atoms (A), green plane of atoms (B) and yellow plane of atoms (C) form the ABC stacking sequence.

These stacking faults are a result of numerous interstitials, which gather on close-packed planes. An intrinsic stacking fault occurs when a plane of atoms is removed from the structure, changing the sequence from ABCABC to ABC||BCABC, where || indicates removed A plane. These stacking faults are the result of condensation of vacancies onto close-packed planes as well as partial slips of crystals caused by dislocation motion [14,15].

Twin Boundaries (Planes)

When a stacking fault continues for numerous atomic spaces, it produces another stacking fault – a twin of the original. This twin plane boundary separates parts of the crystal with mirror lattice symmetry as shown in Figure 2.2. Perfect crystal structure has the sequence of ABCABCABC while the twinned structure has the sequence ABC|A|CBACB|A|BCABCA, where |A| atomic planes are twin boundaries (planes) with the twin in between them. Twin planes usually occur during crystal growth. In the case from Figure 2.2b, when the crystal grows, an extrinsic stacking fault develops on plane C (to the right of |A|), fault energy is minimized if the next added plane of atoms is B instead of A. Stacking fault energy (SFE) of the material (crystal) is the main factor that determines force required for formation of twins. In FCC metals with low SFE like silver, twinning is a detrimental mode of plastic deformation, which occurs by shear stress on the (111) plane in $[11\bar{2}]$ direction [16] since the crystallographic plane and direction depend on the crystal structure.

Atomic displacements that result in twins can be a consequence of either mechanical shear force, resulting in mechanical twins, or annealing, resulting in annealing twins.

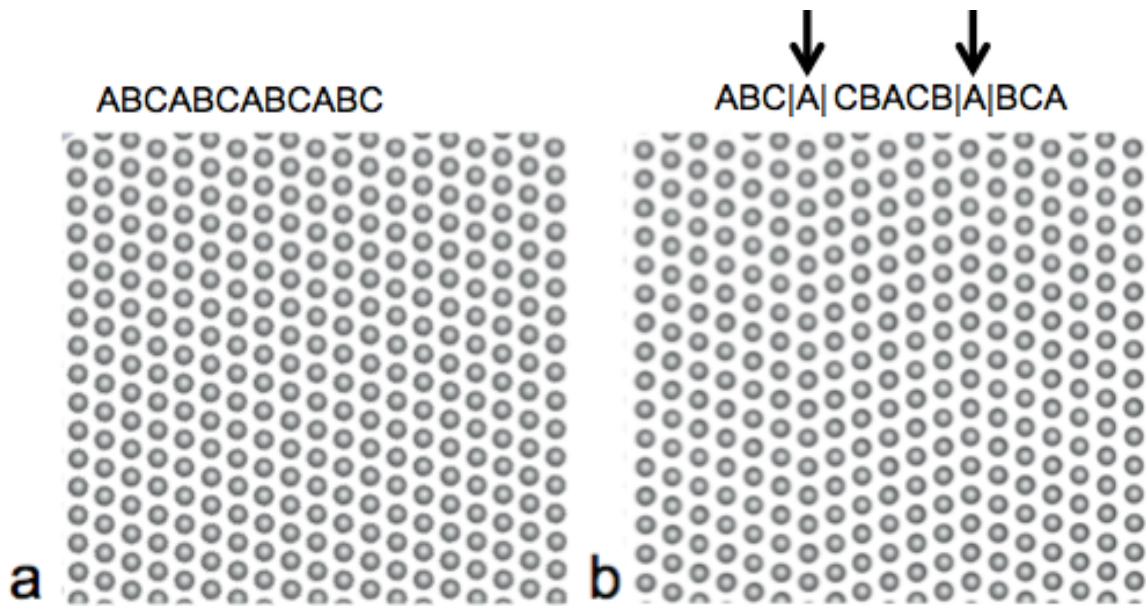


Figure 2.2. Schematic of a) perfect and b) twinned FCC crystal lattice. Atom planes A, B and C noted. Arrows indicate twin planes.

Deformation twinning is one of the two types of plastic deformation in metals, the other being slip deformation and both are a consequence of movement of dislocations with large Burgers vectors. Lattice reconfiguration during slip deformation is gradual, with five independent slip systems required in order for deformation to occur while generation and growth of slip bands during deformation is poorly coordinated. Deformation twins are formed by simple shear force with highly coordinated atom displacements, reconfiguration of structure occurs suddenly and produces additional slip systems in crystals with a limited number of slip systems [17,18].

2.1.2. Silver Nanowires

An alternative to Ag grids can be networks of AgNWs, which adopt the same concept of gaps (spacing) between Ag, resulting in high transparency. The advantage of the AgNW concept is that they can be processed from solution which is much simpler, more cost efficient and scalable, a fact very important for mass production. Simple and scalable processing of AgNW networks from dispersion can be achieved by spin coating [19], rod coating [20], doctor blading [21], air spraying [22] and even drop

casting [23], processes which are scalable and compatible with the roll-to-roll concept of production of flexible optoelectronics.

Although various methods have been used to synthesize AgNWs, polyol reduction [24] shows the most promise, as it is a simple, low-energy and large-scale synthesis method of production of AgNWs with narrow size distribution and high aspect ratios of length-to-diameter. This method has also been used for synthesis of AgNS with various sizes and shapes [25,26], shown in Figures 2.3B-I. During synthesis, by varying reaction parameters like temperature, reagent concentration, etc. high degree of control over nucleation and growth can be achieved i.e. morphology of the structure can be tuned [26].

Polyols are compounds with multiple reactive hydroxyl functional groups. For AgNW synthesis, ethylene glycol (EG), a monomeric polyol is most commonly used as the reducing agent and solvent because of two key factors: it can solvate both, the salt used as the precursor and the surfactant, and it has a high boiling point of 196 °C, allowing synthesis at high temperatures [27]. By adding AgNO₃ (silver nitrate), commonly used as a precursor, to EG, silver ions (Ag⁺) reduce to nuclei (Ag atoms), which are highly volatile i.e. prone to fluctuation which is dependent on size and available thermal energy. As these nuclei grow, they form larger clusters, fluctuations disappear (structure becomes static) and they adopt the role of seeds from which various structures can be grown. These seeds can be multiply twinned (as in the case of AgNWs), single twinned or single crystalline (no boundary defects). This is depicted in Figure 2.3A. Addition of atoms and the formation of aggregates are fuelled by mechanisms of surface diffusion and surface energy minimization, which is why controlling the kinetics of each step (nucleation, evolution of nuclei and growth of seeds) can lead to the control of nanocrystal morphology, as explained above.

For multiply twinned seeds, their growth is more rapid at active sites - defect (twin) locations, which in turn leads to the formation of NWs with a pentagonal cross-section. These types of seeds are the most abundant type of morphology because they exhibit low surface energy (at twin boundaries) as a result of high concentration of defects and are the most reactive as Ag atoms preferentially are attached to the twin defects, which leads to anisotropic uniaxial elongation of the structure.

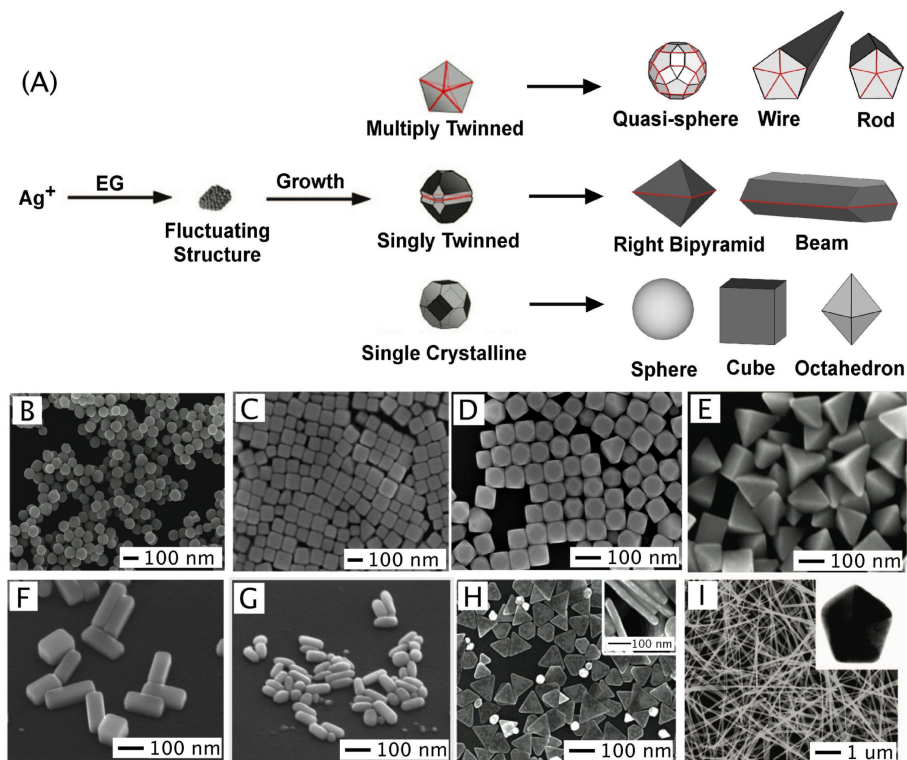


Figure 2.3. A) Polyol synthesis of AgNS where EG reduces Ag^+ into fluctuating nuclei which grow into multiply twinned, singly twinned or single crystalline seeds from which various structures can be grown like B) spheres [28], C) cubes, D) truncated cubes, E) right bipyramids, F) bars, G) spheroids, H) triangular plates and I) wires [29]; red lines represent twin planes, dark facets are of $\{100\}$ orientation while light facets are of $\{111\}$ orientation [30].

Surfactant commonly used in this procedure is polyvinylpyrrolidone (PVP), a polymer which controls the shape of AgNWs during synthesis. Utilizing a surfactant prevents the coalescence of nuclei during initial growth of NWs [31] as it binds to $\{100\}$ NW facets, passivating them through interaction of oxygen atoms from the carboxyl group in the PVP with the surface Ag atoms [32]. This enables growth only of $\{111\}$ facets in the $[110]$ direction [33,34,35,36] resulting in a one-dimensional (1D) structure. This is graphically shown in Figure 2.4. In order to prove that binding of PVP is preferential to $\{100\}$ planes, Sun et al. [33] employed attachment of gold particles to AgNWs through dithiol linkage. Gold particles were attached to the tips of AgNWs while side $\{100\}$ facets were strongly passivated so no replacement of PVP with dithiol molecules occurred.

It was already mentioned that the formation of multiply twinned particles (in this case pentagonally twinned) is energetically favorable and that twin planes are high energy sites. These nanoparticles grow rapidly in an anisotropic manner with Ag diffusing to $\{111\}$ facets on the tip. Some authors suggested that Ostwald ripening is the mechanism of growth of the AgNWs [33] while others claim that AgNW growth is surface reduction-rate limited on all facets, dismissing nanoparticle aggregation and Ostwald ripening processes [37].

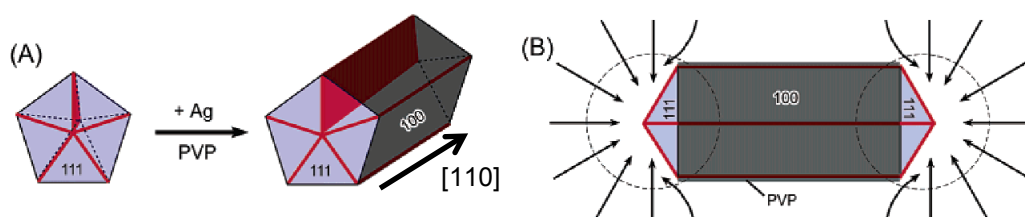


Figure 2.4. Mechanism of AgNW growth, A) Multiply twinned seed grows with confinement of $\{100\}$ facets by PVP in noted $[110]$ growth direction, B) Diffusion of Ag atoms on both ends of AgNW, on facets with $\{111\}$ orientations where there is weak interaction with PVP; Arrows indicate flux of Ag atoms toward $\{111\}$ planes; Red lines represent twin boundaries (planes) while the red plane represents one twin plane [33].

Numerous studies on nucleating agents have been explored [38,39,40] with chlorides producing good results. These agents can be added during synthesis in order to promote AgNW formation as they affect the morphology of seeds during initial formation [27]. Their role is to attach on the Ag pentagonally twinned seeds thereby preventing agglomeration and performing electrostatic stabilization [29, 41, 42]. Addition of metal halides such as sodium chloride (NaCl) or copper (II) chloride (CuCl_2) leads to the formation of silver chloride (AgCl), thereby reducing the concentration of free cationic ions during initial seed formation. This, in turn, slows down reaction conditions, which results in the formation of thermodynamically stable multiply twinned Ag seeds [27].

The cross-section of the AgNW is essentially comprised of five tetrahedrons, which form a pentagon. These tetrahedrons are actually five $\{111\}$ twinned sub-crystals separated by $\{111\}$ planes, with the wedge-angle of one tetrahedron being 70.53° . With 5 tetrahedrons, each with a 70.53° angle, the structure falls short of producing 360° , a

full structure, by 7.35° [43], as shown in Figure 2.5. The structure therefore has to strain in order to compensate for the missing gap of 7.35° . For very small crystals, the gap is compensated by coherent elastic strain. For larger crystals, stacking faults [35,44] and/or single wedge disclinations, produce inhomogeneous strain which can be eased by opening up the gap, which can lead to crack formation around the five-fold axis [45].

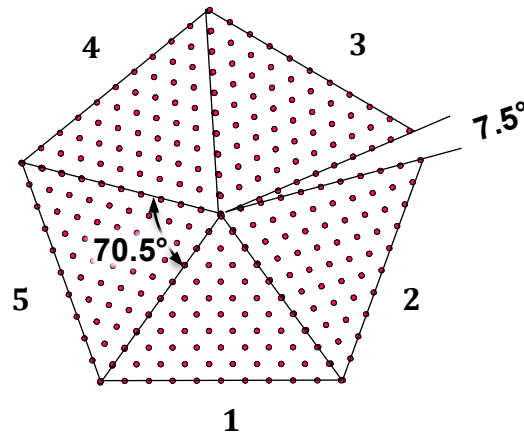


Figure 2.5. Cross-section of an AgNW. Five twin segments are noted by numbers 1-5. Shown in image is a wedge angle of a single twin segment as well as the angle of missing gap. Twin boundaries separating twin segments are of $\{111\}$ orientation.

Although shown as such in graphical depictions, especially in Figure 2.5, the cross-section of the AgNW isn't exactly an ideal pentagonal shape [46,47], exhibiting slight deviations. The 5 corners (tips) of the pentagonally twinned cross-section are actually rounded (truncated) [48] which is a result of surface energy minimization [49,50].

Properties of AgNWs

Besides enhanced optoelectronic properties of AgNWs, which are primary requirements for application in the field of flexible transparent electronics, mechanical properties are very important as well. For AgNWs with low thicknesses of $\sim 30\text{nm}$, Young's modulus is 20% higher than 83 GPa of bulk Ag [51] while yield strength can be higher ~ 50 times than 54 MPa, that of bulk Ag [52]. This is due to the strain intrinsic from NW formation [53]. Concerning their deformation behavior, AgNWs exhibit the following: superelastic, almost no plastic and very little brittle failure [51]. Factors

which influence this behavior are NW thickness, aspect ratio and partial dislocation nucleation at NW surface [54,55].

Optical transmittance of AgNWs, although high because of empty gaps between the NWs, exhibits losses due to reflective scattering of light by the metal [56]. The ratio of diffuse transmittance (passage of light through an object which redirects it in a diffusive manner) and direct transmittance (no change in direction/quality of light when going through an object) can be a very important factor for AgNWs for their application in optoelectronics. This ratio is called the haze factor and it is very dependent on the method of synthesis and processing of AgNWs and can range from <2% to >30%, with thinner AgNWs exhibiting less fluctuations of the haze factor across the absorption spectrum [57]. The haze factor is essentially an indicator of the degree of how the transmitted light is scattered. For optoelectronic display applications, low values of haze factor are desired but for applications like photovoltaics, high values of the haze factor mean enhancement of depth of light passage into the active (absorbing) layer, improving the efficiency of the device [58].

Electrical properties present a function of individual AgNW dimensions as well as the morphology of the NW network. Resistance increases with the decrease in length and diameter (thickness) of the NWs which is attributed to surface scattering of electrons [59]. This means that surface scattering is dominant, causing reduction of the mean free path of electrons and an increase of resistivity above the resistivity of the bulk material [27]. For an AgNW of ~40nm in diameter and a length of ~20 μm , Sun et al. obtained the electrical resistivity of $1.25 \times 10^{-5} \Omega\text{cm}$, about 8 times greater than that of bulk Ag [60]. Although resistance increases with diameter decrease, it has been reported that significant thickness decrease to values below 18nm can result in conductivity increase as the system would function in the bulk and not the percolative regime [61]. Dependence of NW length on electrical properties is a complex relation as the percolation of the entire network plays a very important role. When two NWs are touching, they are in contact with each other through a junction, extending the percolation of the network but increasing resistance as junctions exhibit enormous resistances of up to $1\text{G}\Omega$ [20], several orders higher than individual AgNWs. From this, it can be concluded that longer NWs need less junctions for creating conduction paths (percolation), explained by Hecht et al. [62], where it has been stated that the minimum

number of NWs required to produce a conductive path across the network is proportional to the square of the NW lengths [27]. Besides the dimensions of the NWs, their density or area coverage (a) is very important as it influences both, conductivity ($R_S \sim 1/a$) and transmittance ($T \sim -a$). Spalleck in her PhD thesis [63] presented several methods of total area coverage calculations utilizing scanning and transmission electron microscopy (in phase contrast or Z-contrast mode):

- *The threshold method*, where a fixed threshold is applied, meaning the histogram of the image is divided by the application of a cutoff value into two areas - one containing NWs and the other containing the background area;
- *High magnification – low magnification method*: combination of two magnifications for same area is used with low magnification image acquired in order to preserve charging and inhomogeneous contamination after which a convenient threshold is applied to the high magnification image using the threshold method described above;
- *Morphological line segmentation method*: NWs are identified as one pixel wide crossing lines and subsequently widened to the experimentally determined average diameter. This method was used in the research presented in this thesis.
- *Histogram analysis method*: based on the analysis of the contributions of the grey value histograms, histogram is fitted while allowing for a transition region, where contributions overlap.

As previously mentioned, junction resistance is very high, unequivocally affecting the resistance of the entire network. Morphology of the junction is the key factor for its resistance so various post-processing methods have been implemented in order to modify the junction morphology thereby reducing the resistance of the entire network without affecting optical properties, including:

- Thermal annealing [23];
- Plasmonic welding, inducing local melting and solidification [64,65,66];
- High intensity pulsed light technique (HIPL) [67];
- Plasma sintering at elevated [68] and room temperatures [69];

- Cold rolling [70,71,72];
- Chemical approach by ion exchange [73].

Nanojoining of AgNW through modification of junction morphology, also called welding or coupling, besides conductivity, enhances bonding strength and fracture resistance. This leads to higher mechanical durability [74] of NW networks, a very important property for flexible optoelectronic devices.

In the case of thermal annealing, thermal activation occurs at relatively low temperatures like 0.2 - 0.4 T_m i.e. well below melting temperature. This leads to surface diffusion of Ag atoms and the formation of NW welded junctions, due to very low activation energy, 0.3-0.4 eV [75], for diffusion on (100) surfaces. Decrease of the total free energy of the junction, as a result of surface decrease of high energy surfaces, is the driving force for the local enhanced diffusion [76,77,78]. This process is essentially sintering and can occur, presuming certain criteria are met, even at room temperatures [79,80,81]. Joining of AgNWs consists of several steps:

- Solvent desorption (between 30 and 140 °C);
- Organic molecule (PVP) desorption (around 150 °C); displacement of these molecules can also occur spontaneously, due to surface atom diffusion [82];
- Local sintering (above 200 °C) if sufficient time is provided [83].

Stated temperature intervals are not exact as it is difficult to determine their precise values. However, Langley in his PhD thesis, while studying the effects of thermal annealing on the electrical resistance of AgNWs by measuring resistance in-situ during a thermal ramp in air [27], found a generally acceptable sequence:

- *Reduction* – drop of resistance with desorption of solvent and capping agent as NWs gain a more intimate contact between each other;
- *Stabilization* – increase in number of welded junctions decreases resistance of network;
- *Spheroidization* – if temperatures are too high or time of annealing is long at moderate temperatures, NW exhibit morphological instability, known as

Rayleigh instability [84] the origin of which is the reduction of surface energy. This phenomenon leads to the reduction of percolation in the network leading to the increase in resistance, as NW are fragmented into sequences of nanospheres [85,86].

Applications of AgNWs

Although AgNS have a wide range of applications including bioengineering [87], catalysis [88] and even textile engineering [89], AgNWs have mostly found their place in the field of optoelectronics, most notably solar cells or photovoltaics. As with other optoelectronic devices like displays (liquid crystal, flat panel or plasma), touch panels, or light emitting diodes (LED), solar cells require materials with high electrical conductivity and optical transparency for creating high performance transparent electrodes. Conventional material used for this purpose is tin doped indium oxide, commonly called indium tin oxide or ITO [90,91]. Although with high optical transparency at relatively low resistances, ITO has numerous drawbacks, as explained in the Introduction chapter of this thesis. As the optoelectronic industry requires materials which exhibit high efficiency in their applications along with long lifetimes and cost effectiveness [92,93], alternatives to ITO are explored in order elucidate materials with performances equal to or greater than ITO and deposition techniques which are simple, cheap and reproducible. In the Introduction chapter of this thesis, a few of the most promising candidates were stated. Among them, AgNWs draw particular interest because of their figures of merit compared to ITO as well as other prominent alternatives like graphene and SWCNT. Figure of merit (FoM) is defined as the ratio of direct current (DC) conductivity σ_{DC} and optical conductivity σ_{OP} [94]. It essentially provides quantitative information on the balance between conductivity and transparency and it is, along with the haze factor, an indicator of the potential of a material to efficiently serve as an electrode in solar cells. Graph in Figure 2.6. depicts optical transparency as a function of sheet resistance of ITO and most promising alternative materials, with respect to their FoM, which in this case is presented as the ratio of optical transparency (at 550nm wavelength) to sheet resistance [95,96].

Even with dispersion of data, observed are general trends that ITO still exhibits best optoelectronic properties compared to AgNWs, CNTs (high resistance at the junctions) and graphene (high sheet resistances). It is clear that AgNWs are the first in line to replace ITO as they exhibit values of optoelectronic properties closest to the upper left part of the graph i.e. most desired area of high transparency and low sheet resistance, with FoM in some cases exceeding 20000.

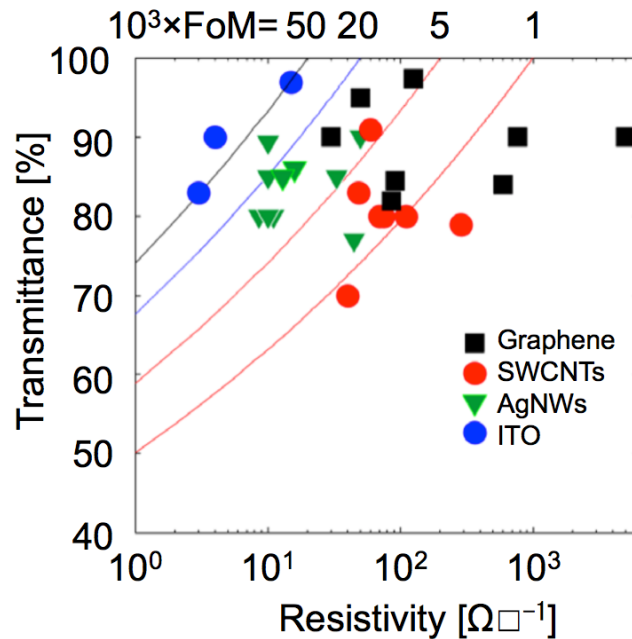


Figure 2.6. Optical transparency as a function of sheet resistance for graphene (black squares), SWCNTs (red circles), AgNWs (green triangles) and ITO (blue circles). Also noted are the iso-value lines of FoM [97].

Additional advantages of AgNWs over other electrodes include:

- Low cost of material - although Ag is expensive, very small amounts of material are needed for processing since electrodes consist of networks, not continuous films;
- The ability to be processed from solution via simple, fairly inexpensive and reproducible methods.

As with all electrodes, AgNW networks exhibit certain drawbacks, which include:

- *Degradation*: similar to bulk Ag, AgNWs are prone to sulfidation and oxidation

- at ambient conditions as high density of surface defects promotes corrosion [98];
- *Instability due to electromigration*: when an electric field is applied, forced surface diffusion of atoms/ions can occur. This hinders the conductive path in the NW network and greatly shortens the lifetime of an optoelectronic device [99,100] and like with bulk materials, it is humidity and temperature sensitive. Bora et al. [101] proposed that crystallinity and defect density affect the stability i.e. susceptibility to electromigration. They concluded that thinner NWs exhibit intra-granular diffusion, which is slower than diffusion along defects and as a result, it makes them more stable than NWs with larger diameters;
 - *Surface roughness*: as it is a network, AgNWs exhibit high surface roughness, as they are not aligned, with some NWs protruding out of the surface while others are piled on top of each other. As this network exhibits high surface to volume ratio, surface roughness is an important factor. In solar cells, especially organic solar cells (OSC), high surface roughness leads to shorting (short circuiting) as active layers (absorbers) can have smaller thicknesses than the roughness values of the electrodes [102,103]. This problem can be resolved by laminating the AgNW networks with a polymer coating [20,104] or by mechanical pressing, which not only reduces shorting problems, but can lead to a decrease in sheet resistance [105,106].

To address these shortcomings, various materials have been paired up with AgNWs in order to create nanocomposites where synergy occurs between multiple phases. These combinations include the aforementioned AgNWs/polymer, AgNWs/graphene [107], AgNWs/CNTs [108], AgNWs/metal oxides (MO) [109,110] as well as hybrids like AgNWs/MO/polymer [111]. One of the most interesting combinations studied so far is AgNWs/AZO (aluminum doped zinc oxide) [112,113,114].

Zinc oxide (ZnO) has become a very interesting option for coupling together with AgNWs because of its optical properties, non-toxicity and low cost, but because of its high electrical resistance it has to be degenerately doped with aluminum, which acts as an electron donor, in order for it to be effectively utilized as an electrode in solar cells [115,116]. Not just a wide band gap semiconductor, AZO, when paired up with

AgNWs, exhibits better charge carrier collection, improved chemical and mechanical stability and a decrease in surface roughness. Of course, this comes with the expense of optical transmittance decrease and reflection increase due to scattering of light from AgNWs into the AZO [117].

2.1.3. Silver Dendrites

The etymology of the word dendrite is the Greek word *dendron* (*δένδρον*) meaning *tree*. In material science, dendrites are crystals with tree-like structures consisting of a trunk (main branch) from which primary branches grow, and possibly secondary branches growing from primary branches. This is the reason why they are considered highly symmetric and hierarchical structures [118,119]. Dendrites are often referred to as fractal structures as they exhibit repeating patterns in their morphology.

It has been well established in material science that, by adjusting size and shape, the physical and chemical properties of NS can be controlled. This is especially true during synthesis of dendrites where the driving force of crystallization influences shape and size by varying the distance from thermodynamic equilibrium. When reaction conditions are far from thermodynamic equilibrium, nucleation and growth are fast which results in the instability of the growing surface and formation of hierarchical morphologies [120,121]. This is the reason why dendrites, especially Ag dendrites, due to the extraordinary properties of Ag, can provide a natural framework for the theoretical studies of disordered systems [122,123].

Various methods have been employed for the synthesis of Ag dendrites including:

- Electrochemical deposition [124];
- Galvanic replacement reaction [125];
- Electroless deposition [126];
- Wet chemical route [127];
- UV irradiation [118].

Most of these methods exhibit drawbacks such as the use of hazardous materials, time consuming processes, complicated equipment, introduction of impurities, low yield or poor reproducibility. As already mentioned, electrochemical synthesis of various Ag nanostructures (dendrites) has an advantage over other synthesis methods because the overpotential (electrochemical driving force) can be easily controlled [128]. With this method, dendrites can be fabricated with high purity and yield [129] in a very reproducible manner by keeping the voltage constant during deposition.

Although several mechanisms explaining Ag dendritic growth have been proposed, including: diffusion-limited aggregation (DLA) [130], oriented attachment [131] and nanoparticle-aggregated self-assembly crystallization [132], dendritic growth during electrochemical deposition has been specifically modeled by Mullins and Sekerka's linear stability analysis [133], Barton and Bockris [134], and by using a twin plane reentrant edge (TPRE) mechanism also known as the Wagner, Hamilton and Seidensticker (WHS) model [135,136]. These models explain the phenomena of how two parallel planes create high aspect ratios in AgNS [137]. According to the TPRE mechanism, crystal growth takes place through the formation of reentrant grooves at the intersections of twin planes. When the grooves are formed, they become favorable sites for further nucleation and growth by the lateral motion of {111} planes. Consequently, the dendrite can be considered as a twinned single crystal with at least one twin boundary, which extends throughout the dendrite while the twinning plane is parallel to the broad dendrite surface [138].

Because of their unique optical and electrical properties, high specific surface area along with numerous active sites and sharp edges (critical for mass transfer) and high potential for network percolation, Ag dendrites have found applications in surface-enhanced Raman spectroscopy (SERS) [139,140], electronics [141], catalysis [140,142], photonics [143], chemical and biological sensing [144] and production of superhydrophobic surfaces [124], to name a few. A novel application for Ag dendrites, proposed in this thesis, are transparent electrodes in solar cells, because of their optoelectronic properties along with a high degree of branching which enhances percolation potential of entire Ag dendrite network.

2.2. Organic Solar Cells

Solar cells are comprised of semiconductors, materials that possess weakly bonded electrons which occupy the valence energy band, for organic semiconductors known as the highest occupied molecular orbital (HOMO). If an energy greater than the band gap energy (gap between valence and conduction bands) is applied to a valence electron, the bonds are broken and the electron is free to move to a higher energy band - the conduction band, for organic semiconductors known as the lowest unoccupied molecular orbital (LUMO). Source of this energy can be supplied by photons - particles of light. When the electrons move to the conduction band, a selective contact (n-type semiconductor) collects such electrons and focuses them to the external circuit, the application to which the solar cell is connected. In this circuit, electrons lose their energy (through work) and are restored to the solar cell by another selective contact (p-type semiconductor) which returns them to the valence band and their initial energy. The whole movement cycle is called electric current, while the creation of electrical current (voltage) upon interaction with light is called the photovoltaic effect. Figure 2.7 presents the ideal relation between energy and spatial boundaries.

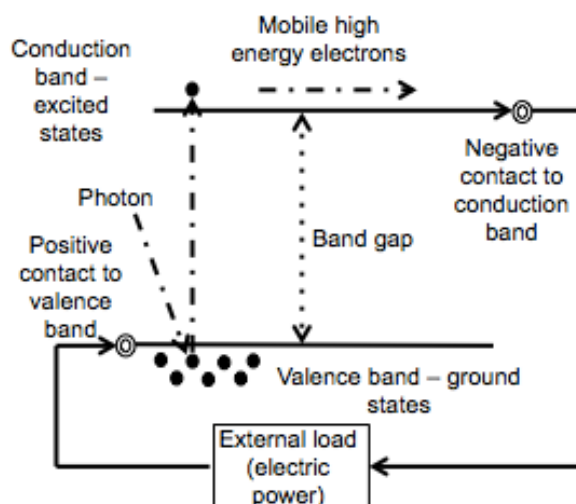


Figure 2.7. Schematic of a solar cell showing the cycle of electrons. Photon induced excitation of electrons from valence to conduction band. Contact selective to the conduction band delivers electrons to the external circuit after which they are returned to the valence band by a contact selective to the valence band; electrons are depicted as black circles [145].

Sunlight is a spectrum of photons with various ranges of energy. Only photons whose energy is greater than the band gap energy (the threshold energy for the photovoltaic effect) can excite electrons from the valence to the conduction band. In the case when photons have insufficient energy, that energy travels through the solar cell and is absorbed at the rear in the form of heat.

In a solar cell, everything revolves around the *p-n junction*, an interface between the p-semiconductor, which contains an excess of holes and the n-semiconductor, which contains an excess of electrons.

Solar cells, with respect to the primary material in the photoconversion, can be:

1) *Inorganic*:

- *Silicon based*: single-crystalline silicon, multicrystalline silicon, thin-film based amorphous silicon and micromorph (tandem combination of crystalline and amorphous silicon);
- *Non – silicon thin-film based*: cadmium-telluride (CdTe), copper-indium-selenide (CIS), copper-indium-gallium selenide (CIGS), quantum dots;

2) *Organic*: based on conductive polymers, conductive polymer blends or conductive polymer nanocomposites;

3) *Hybrid*: dye-sensitized solar cells (DSSC) which utilize organic liquid dyes in combination with titanium dioxide (TiO₂) immersed in an electrolyte solution (catalyst), DSSC which utilize solid-state ABX₃ perovskite type structure as the dye where AB is an organic-inorganic compound like methylammonium lead or tin while X is a halogen.

The highest crystalline silicon based solar cell efficiency up to date, for non-concentrator cells (no lens or mirrors used to focus sunlight), is 25.6% [146]. They are space efficient and have the longest life times which explains why Si-based PV technology still accounts for ~93 % of the total production in 2015 [147]. However,

solar panels based on this technology are the most expensive and are prone to circuit breakdown when covered by dirt or snow.

Highest reported efficiency, so far, for non-silicon based inorganic solar cell, non-concentrator, is 22.3 % [148]. They are less expensive than silicon based solar cells because of their potential for simple mass production. As thin films, they can be produced to be flexible, while retaining high power conversion efficiency of >20% [149], which gives a wider range of application areas, compared to silicon based solar cells. However, thin film inorganic solar cells have short life times and require vast space which in turn increases the cost of auxiliary photovoltaic equipment even though the production of the cells themselves is less expensive than silicon based technology.

Efficiency of DSSCs up to date is 21.1% for perovskite solar cells [150]. They are characterized as cells with good performance in low-light and high temperature conditions, are processed with low energy manufacturing processes and possess versatile product integration (highly flexible, durable and lightweight). However, the liquid electrolyte which is utilized in DSSCs has stability issues, it is expensive while the organic dyes and volatile organic compounds used are hazardous to the environment. Additionally, the perovskite structure is prone to degradation in moist environments.

Types, working principles, layouts and advantages and disadvantages of organic solar cells will be presented in the following text.

Advantages and Disadvantages of Organic Solar Cell Technology

Conducting organic materials, in particular π -conjugated polymers, have emerged as a new class of semiconductors since high conductivity was observed in doped polyacetylene in 1977 [151]. Numerous advantages of this type of photovoltaic include:

- *Environmental impact* – energy consumed during manufacturing is fairly low while utilized organic compounds, including solvents, are not too hazardous to the environment;
- *Inexpensive and versatile materials and processing* – polymers are relatively inexpensive to synthesize, compared to methods of silicon production, and can be processed from solutions into thin films by various simple and inexpensive

methods like coating, printing and roll-to-roll technologies all of which are highly compatible with various substrates and have low energy and temperature requirements;

- *Their intrinsic properties like low weight, flexibility and transparency* due to the molecular nature of the materials, which opens up new market opportunities in applications where these properties are explicitly demanded;
- *Tailoring properties* – functionality of polymers can be tuned through careful molecular design and synthesis in order to fit an application, as organic molecules are easier to handle than inorganic atoms like silicon. Molecular engineering can be used to modify molecular mass, band gap of polymers, length and functional groups of polymers thereby changing charge generation ability, etc. This gives rise to a wide array of multifunctional polymers with specific optical and electrical properties for application in a particular photovoltaic market.

Even with all of these extraordinary possibilities like their intrinsic properties, successful large scale commercialization organic photovoltaics is still not feasible since, out of the three criteria: cost, efficiency and lifetime, only cost is met, which limits them to a niche market [152].

While silicon-based solar cells may last up to 25 years, polymer based devices struggle to last a year [153,154]. Since, conductive polymers are photosensitive, they are reasonably stable in the dark but tend to degrade in the light [155]. The second drawback is the efficiency issue. Highest efficiency reported for polymer based solar cells is 13.2% by Heliatek in 2016 [156], for Helia Film[®], a triple junction cell. Problems of low efficiency, compared to inorganic solar cells, arise from the following:

- *Low dielectric constant* of organic materials means that the electron diffusion lengths are too small;
- *No crystal lattice* – local disorder and impurities are present which leads to low charge carrier mobility of organic materials;
- *Spectral mismatch* between solar spectrum and organic materials which absorb the sunlight – organic materials mostly absorb in the range of visible light in

spectrum while maximum photon density of sunlight is around 700 nm wavelength (between visible and infrared) [152].

Other factors hindering the photovoltaic effect in organic solar cells will be discussed later in this chapter.

Bulk Heterojunction (BHJ) Organic Solar Cells (OSCs)

Heterojunctions, interfaces between two different semiconductors, are common in inorganic devices providing such structures as p-n junctions. The organic analogue to this is the bilayer device, where the semiconductor with higher electron affinity (and ionization potential) is the electron acceptor, while the other is the electron donor. Hence, this structure is also called the donor-acceptor heterojunction. [157,158]. These have been very successful for light emitting diodes (LEDs) producing high quantum efficiencies [159], so the same theory was applied to solar cells. This configuration is ideal for the formation of excitons (electron – hole pairs), which are essential for cell operation, at the interface between the two organic layers. In the case of LEDs, subsequent exciton decay leads to the emission of photons. This is undesirable for solar cells as excitons still need to diffuse to this interface which implies that the light would need to be absorbed within one diffusion length of this interface. An example of this is shown in Figure 2.8. In this configuration, charges are still limited to moving to the respective electron donor and electron acceptor layers. Charge separation can still only occur at the p-n interface i. e. the electron donor/electron (D/A) acceptor interface. The solution to this problem is the bulk heterojunction (BHJ) concept.

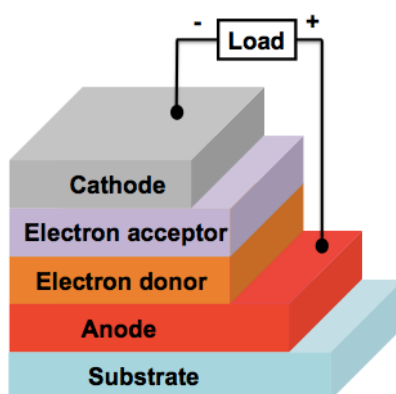


Figure 2.8. Simplified schematic diagram of a bilayer device noting appropriate layers.

Organic materials like polymers (electron donors or p-type materials) and fullerenes – carbonaceous nanostructures (electron acceptors or n-type materials) are generally soluble so they can be blended together in solution. When this solution is processed into a film, it forms an interpenetrating network of materials, both p- and n-type, as a nanocomposite with the polymer as the matrix and the fullerene as the nanofiller. This structure has significant advantages over the bilayer configuration as charge separation can now occur over the entire bulk of the film (wherever there is a polymer/fullerene interface i.e. a heterojunction), effectively removing the problem of exciton diffusion through the entire film thickness. Light absorption can occur throughout the entire film and, as such, charge transport is benefitted. Figure 2.9 shows a schematic of such a configuration.

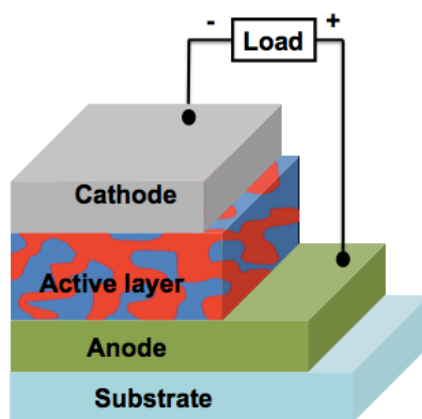


Figure 2.9. Simplified schematic diagram of a BHJ device noting appropriate layers. Active layer consist of an electron donor acceptor (D/A) blend.

Working principle of Bulk Heterojunction Organic Solar Cell

Working principle of organic BHJ solar cells consists of 4 steps [160,161,162,163], depicted in Figure 2.10:

1. Active layer of the cell (BHJ) absorbs a photon and if the energy of that photon is greater than the difference in energies of LUMO (D) and HOMO (D) i.e. the band gap:

$$h\nu \geq E_{\text{LUMO(D)}} - E_{\text{HOMO(D)}}$$

where h is the Planck's Constant and ν is frequency of photon, the photon excites an electron from the HOMO (D) to the LUMO (D), leaving behind a hole. The electron-hole pair is called the exciton, bounded together by electrostatic interactions;

2. The exciton diffuses to the D/A interface;
3. Exciton dissociates, where the electron is transferred from LUMO (D) to LUMO (A) and the hole is left behind;
4. Electrons are collected by the negative electrode (cathode) with work function equal to LUMO (A) while holes are collected by the positive electrode (anode) with work function equal to HOMO (D).

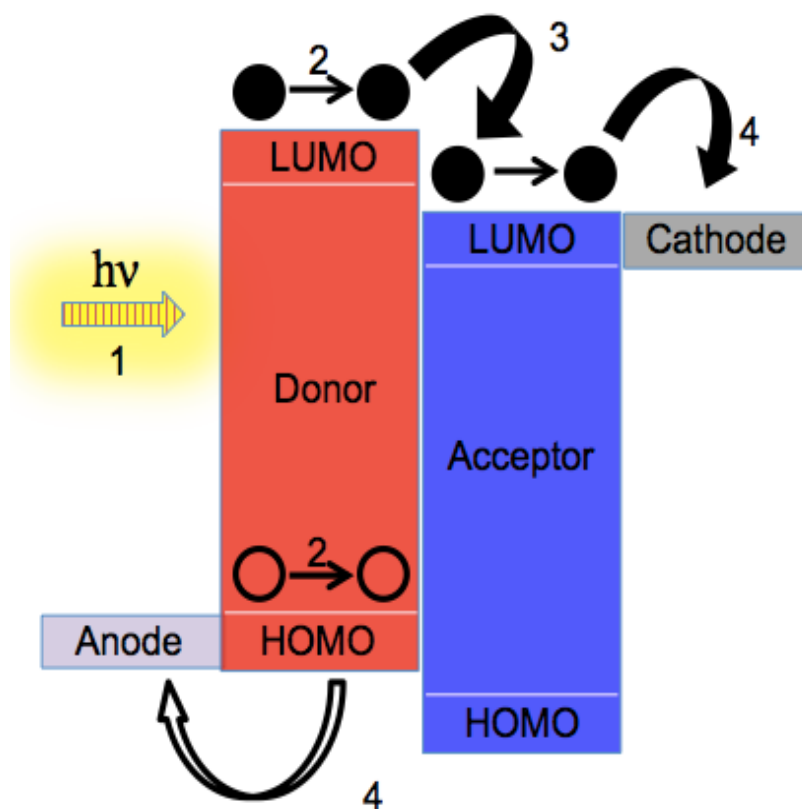


Figure 2.10. Schematic showing the working principle of the BHJ OSC: excitation of electron in donor and creation of exciton (1), diffusion of exciton to D/A interface (2), exciton dissociation (3) and charge collection (4); full circles and arrows represent electrons and electron diffusion paths, respectively, while hollow circles and arrow represent holes and hole diffusion paths; numbers indicate steps in the working procedure.

Hindering Factors for Photoconversion in BHJ Organic Solar Cells

A fact has to be taken into account that not all incident photons get absorbed by the active layer. The active layer semiconductor needs to have a significant band gap in order to generate power and only photons with an energy above the band gap can potentially be absorbed. Losses can also occur due to reflection of light before it reaches the active layer or due to an insufficient extinction coefficient, an intrinsic property which determines how much light is absorbed by a material. Various schemes of light in-coupling can be used to minimize losses. More photons are generally absorbed in materials with lower band gaps but the excess energy of shorter wavelength photons is wasted so there are practical limits on the band gap size [164]. To put things into perspective, crystalline silicon has a band gap of 1.1eV while most polymers have higher band gaps, usually around 1.5 – 2eV. The optimum band gap size depends very much on the additional energy loss mechanisms that are present in the system. A single band gap device has an efficiency limit of around 30% and in order to increase that number, multiple band gaps i.e. multiple absorbers have to be utilized. This will be discussed later in the chapter.

Polymers have efficient optical absorption due to their high optical absorption coefficient ($\alpha \sim 10^5 \text{ cm}^{-1}$) [165]. Majority of photons are absorbed at $1/\alpha$, the penetration depth, so very thin active layers (a few hundred nanometers) are enough for absorption at peak wavelength. However, a relatively narrow absorption band for polymers as well as almost non-existent absorption by fullerenes limit the overall efficiency of these devices. By enhancing optical path length ($1/\alpha$), absorption can be increased but not without decreasing the exciton diffusion length (LD), the average length between exciton generation and recombination. In conjugated polymers LD is very small, <20 nm [166, 167, 168], which implies that a carefully controlled nanostructure, by controlling polymer regioregularity, conjugation length and polydispersity, vapor pressure of the solvent, nanofiller load as well as annealing conditions during solvent evaporation, is required for efficient exciton diffusion and dissociation in a BHJ layer [169].

Optimization of the electrodes is another path in overcoming efficiency-limiting factors for organic PV devices. The low work function (minimum energy required to

remove an electron from the surface of the material) of the cathode is mainly responsible for the built-in potential for optimal charge extraction and Ohmic contact to the photoactive layer [170]. The problem with this layer arises from the incompatibility with other layers. The nature of the polymer/metal interface is very sensitive since defect states originating from chemical reactions and inter-diffusion at the interface can create interfacial barriers and lead to increased series resistance [171].

Some other the factors that obstruct successful conversion of solar into electrical energy in BHJ OSCs include:

- *Photo-oxidation*: Exposure of many conjugated polymers to light and oxygen results in photo-oxidation. Oxidation destroys polymer functional groups, which have a high affinity towards electrons, leading to separated electrons. These electrons stay trapped in the polymer, creating space charges which induce local electrostatic fields that hinder charge transport.
- *Traps*: localized sites in a polymer than can be alternative sites for exciton dissociation. They are a result of structural defects or impurities.
- *Space charges*: formed due to a difference in the charge transport properties of the separated electrons and holes. In this case, an accumulation of one charge species occurs. In most cases, hole mobility is smaller than electron mobility, leading to a build-up of positive charges and increase of hole extraction at the anode while decreasing electron extraction at the cathode, which hinders power conversion.
- *Recombination*: When a semiconductor is taken out of equilibrium by illumination, electron and hole concentrations tend to return to their equilibrium values through recombination. In this process, an electron is returned from the conduction band to the valence band, eliminating a hole i.e. reducing the total number of contributing charge carriers. Recombination may occur after excitation (exciton cannot reach D/A interface during its lifetime), after charge transfer (electron in LUMO (A) recombines with hole in HOMO (D)) or in traps (trapped electron recombines with conduction current hole).

Recombination prevention and improvement of PV device performance can be achieved by optimizing charge transfer by increasing D/A interface and

ensuring transport paths for charges or by optimizing metal/active layer junctions in order for unhindered charge collection [172].

Layout of BHJ Organic Solar Cells

In a typical OSC architecture, the BHJ photoconversion active layer is sandwiched between two electrodes of different work functions, one of which must be transparent. Additionally, intermediate layers like the hole transport (HTL) and electron transport layers (ETL) are used to facilitate the electricity (charge carrier) flow between the BHJ layer and the contacts, forming a circuit. In a standard configuration the transparent conductive electrode is the anode, while in the inverted configuration it is the cathode i.e. in the inverted configuration, electric charges exit the device in the opposite direction because the positions of positive and negative electrodes are reversed. Generally, inverted cells have longer lifetimes but lower efficiencies than regular cells [173,174]. Figure 2.11 depicts the stacking sequences in standard and inverted configurations in OSCs.

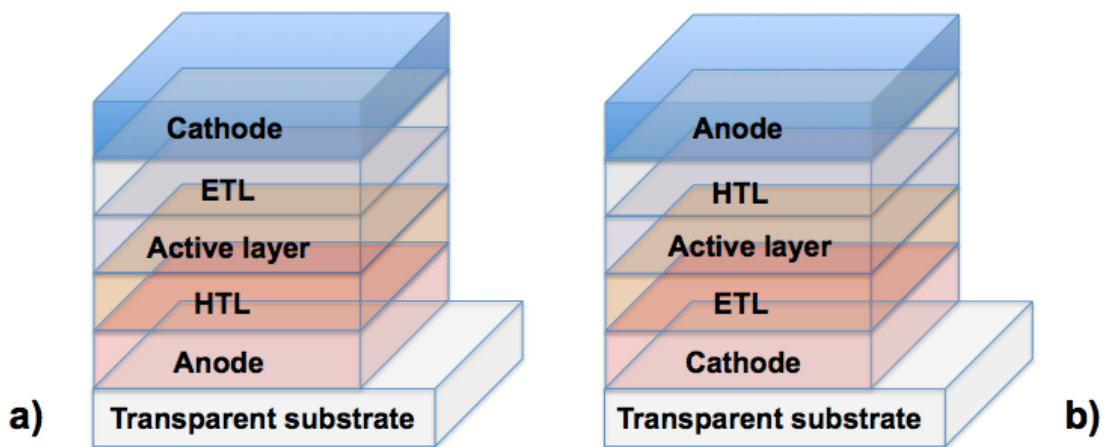


Figure 2.11. a) Schematic of regular stacked architecture of OSCs, b) Schematic of inverted stacked architecture of OSCs; HTL and ETL denote hole and electron transporting layers, respectively.

For the transparent substrate, glass is used, but a flexible alternative can be found in polyethylene terephthalate (PET). The next layer is the transparent electrode, with a high work function (for regular OSC architecture) for the collection of holes. Material

conventionally used for this electrode is indium tin oxide (ITO) [175] although for various reasons already mentioned, extensive research has been undergone to develop alternatives [176]. Intermediate layers like hole transporting layers (HTL) and electron transporting layers (ETL) are positioned around the photoconversion active layer in order to facilitate charge transport. These layers also compensate for the variation in electrode parameters like the work function and surface roughness, as well as improve the absorption within active layer (role of the optical spacer). A wide range of materials can be utilized for this application, from polymers to inorganic compounds like metal oxides [177,178]. The BHJ active layer, as a polymer nanocomposite, consists of a polymer matrix and a nanofiller. The most extensively studied polymer for this purpose is poly(3-hexylthiophene), known as P3HT [179,180], although a wide array of other polymers have been studied for this application [181]. For the nanofiller, the most common materials studied and applied for this purpose are the [6,6]-phenyl-C₆₁-butyric acid methyl ester, known as PC₆₁BM and [6,6]-phenyl-C₇₁-butyric acid methyl ester, known as PC₇₁BM [182], derivatives of C₆₀ and C₇₀ fullerenes [183], respectively. These derivatives have an advantage over their fullerene counterparts because of their joint solubility with polymers in the same solvents. Various other materials have been studied and implemented as electron acceptors, whether they are carbon based like CNTs [184,185] and graphene [186], inorganic like TiO₂, ZnO, CdSe (cadmium selenide), CdS (cadmium sulfide), PbS (lead sulfide), PbSe (lead selenide), SnO₂ (tin dioxide) [187,188] which form hybrid active layers as the polymer matrix is an organic substance, or combinations of multiple acceptors inside the polymer donor like graphene/ZnO [189], PC₆₁BM/C₆₀(CN)₂ [190] or PC₆₁BM/ICBA (indene-C₆₀ bisadduct) [191]. The second contact (electrode) is also a metal layer, which is typically a low work function electrode for the electron collection (for the regular OSCs structure), although alternative materials have been studied for this application, like metal oxides [192].

Tandem BHJ Organic Solar cells

More efficient utilization of absorbed photon energy is one of the best ways to increase solar cell efficiency. Connecting multiple light absorbers (BHJ active layers),

with various band gaps and complementary light absorption spectra, leads to the increase in overall efficiencies of organic solar cells [193,194,195,196]. As of 2016, efficiencies have passed the mark of 10%, specifically 10.4% for a triple-junction OSC [197]. This concept, known as the tandem cell or multi-junction, by utilizing multiple sub-cells (individual active layers accompanied by their immediate HTL, ETL and electrodes) inside a bigger cell, simultaneously addresses absorption and thermalization losses, responsible for more than 55% of the total energy of the solar radiation [198]. By absorbing higher energy photons in a wide band gap absorber (higher voltage and lower photocurrent) and lower energy photons in a smaller band gap absorber (lower voltage and higher photocurrent), this concept can reduce losses and overcome the Shockley–Queisser limit of efficiency for single-junction photovoltaic cells [199].

In the multi-junction OSCs, besides the photoactive layers and the electrodes, the interfacial or intermediate layers are very important as they also have a dual role, as a part of the sub-cell and of the cell as whole. Depending on the tandem architecture, a parallel or a series connection is required to connect the multiple sub-cells.

Conventional series-connected multi-junction cells are most successful in obtaining record power conversion efficiencies. However, a drawback of this configuration is the strict criteria of current matching. This requires elaborate band gap engineering as well as precise control of the thicknesses of the respective sub-cells, which is why some high performance BHJ have limited applicability in this kind of configuration. Contrary to series-connected multi-junction cells, parallel connection configuration requires voltage matching, not current matching, which is an even stricter criteria.

Photovoltaic Characterization: I-V Characteristics

Solar irradiance influences the amount of energy a solar cell produces. Depending on the location and time of day of the measurement, there are significant variations in solar irradiance which is why a standard spectrum has to be used in order for the results to be comparable. For terrestrial based devices the standard spectrum used is AM1.5 which is based on light that has passed through the atmosphere 1.5 times

(thickness and composition of atmosphere specified) and the total irradiance under this spectrum is 1000W/m².

In order to obtain power conversion efficiency (PCE or η), following parameters have to be acquired:

- *Incident photon to conducted electron (IPCE) efficiency* – also called external quantum efficiency (EQE) is the ratio of collected charge carriers to incident photons i.e. amount of produced current by cell when irradiated by light;
- *Absorbed photon to conducted electron (APCE) efficiency* – also called internal quantum efficiency (IQE) is the ratio of collected charge carriers to absorbed photons;
- *Short circuit current density (J_{SC})* - current through the solar cell when the voltage is at 0 value (dependent upon many factors including light intensity, wavelength and material absorption) [200];
- *Open circuit voltage (V_{OC})* - maximum voltage in the solar cell at 0 value of current (dependent on contact materials – electrodes, with their respective work functions [201], as well as materials used for the active layers [202]);
- *Fill factor (FF)* - ratio of maximum power in the solar cell to the product of open circuit voltage and short circuit current density [203].

Power conversion efficiency gives the information on how well a cell performs overall but it is also desirable to know how efficient cells are at individual wavelengths, so that materials can be optimized for light absorption, which is achieved by measuring IPCE. High IPCE or EQE does not guarantee good photovoltaic energy conversion, but it is a prerequisite [204]. It is determined by the four steps of photoconversion and can be presented as a product of different efficiencies:

$$\eta_{EQE} = \eta_A \eta_{ED} \eta_{CT} \eta_{CC}$$

where η_A , η_{ED} , η_{CT} and η_{CC} are the efficiency of absorption, exciton diffusion, charge transfer and charge collection, respectively. In most cases, $\eta_{CT} = 1$ due to the extremely

high charge transfer rate. Therefore, the η_{EQE} of OPV cells is mainly influenced by η_A , η_{ED} , and η_{CC} . The EQE or IPCE efficiency is also defined as:

$$IPCE = \frac{E_{ph} I_{SC}}{P_{in} e}$$

where E_{ph} is the photon energy, I_{sc} is the short circuit current (photocurrent), P_{in} is the input light power and e is the unit electronic charge. This produces a monochromatic efficiency for the device and the information can then be used in conjunction with other measurements such as absorption spectra to optimize device and/or material performance.

The APCE is gained from knowledge of the absorption spectrum of the device and the IPCE. This is then defined as:

$$APCE = \frac{IPCE}{1 - T - R}$$

where T and R are the transmission and reflectance, respectively. This gives the effective internal quantum efficiency for the device.

The current density-voltage (J-V) characteristics are obtained by applying a variable voltage and measuring the current obtained. These characteristics are generally measured in the dark as well as under monochromatic and solar spectrum illuminations. In the dark, the cell displays regular diode-like characteristics with the curve passing through the origin (point 0,0), while under illumination, a non-zero photocurrent (short circuit current) is observed for zero applied voltage (Figure 2.12). Photo-generated electrons move down the band, from the p-type to the n-type semiconductor side, opposite from the forward bias direction. This negative photocurrent is presented as a curve in the fourth quadrant of the J-V diagram.

For tandem devices, where sub-cells are connected in a parallel fashion, V_{OC} is equal to the lowest V_{OC} among the sub-cells. The total J_{SC} in that case equals to the sum of J_{SC} of each sub-cell:

$$J_{SC} = J_{SC1} + J_{SC2} + J_{SC3} \dots$$

For tandem devices, where sub-cells are connected in a series fashion, J_{SC} is equal to the lowest J_{SC} among the sub-cells. The total V_{OC} is equal to the sum of V_{OC} of each sub-cell:

$$V_{OC} = V_{OC1} + V_{OC2} + V_{OC3} \dots$$

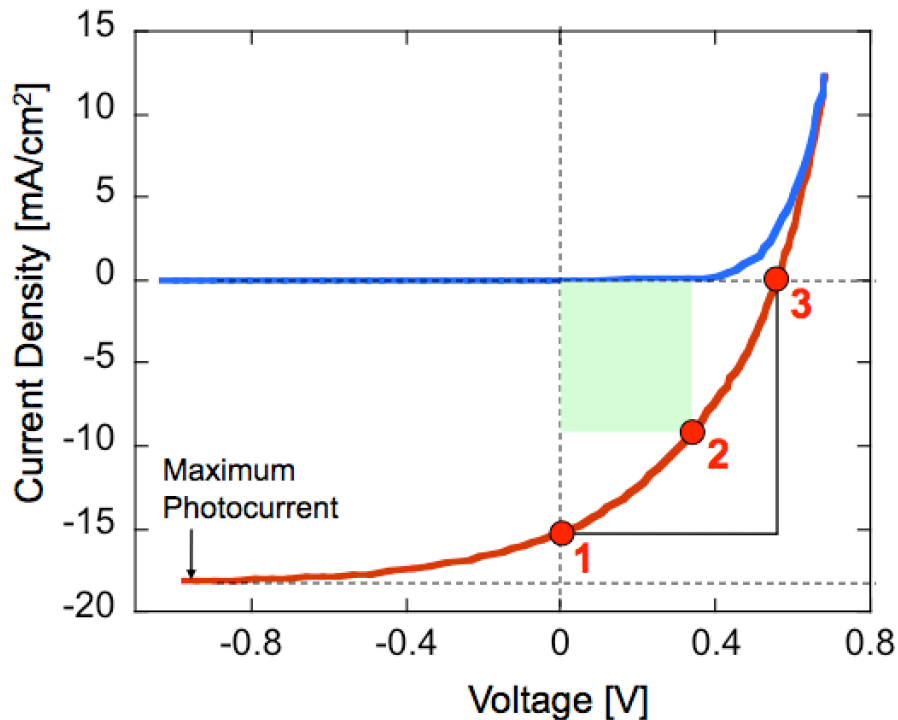


Figure 2.12. Typical current versus voltage curves in the dark and under illumination; Green rectangle corresponds to value of maximum power and white rectangle corresponds to value of power of ideal device. Open circuit voltage is noted by (3), point of maximum power is noted by (2) and short circuit current density is noted by (1).

At any point, the power output of a device is given by the product of the current and voltage at that point. Current density (J_{MP}) and voltage (V_{MP}) are values at point of maximum power (P_{MP}), which corresponds to the area of green square in fourth quadrant in diagram in Figure 2.12. In ideal conditions, when a forward bias is applied and the voltage crosses the V_{OC} point, there would be no photocurrent reduction and the forward bias current should immediately become exponentially large. Power of ideal

device (P_{ideal}), a product of V_{OC} and the J_{SC} corresponds to the area of white square in fourth quadrant of diagram in Figure 2.12. The fill factor (FF) is the ratio of P_{MP} to P_{ideal} :

$$FF = \frac{P_{MP}}{P_{ideal}} = \frac{V_{MP}J_{MP}}{V_{OC}J_{SC}}$$

This quantity is unitless and is actually a measure of how close the solar cell is to an electrically ideal component. It is wavelength dependent since the illuminated J-V characteristics are obtained either under monochromatic illumination or under simulated solar light.

The power conversion efficiency (η), which is the overall efficiency of a solar cell under illumination, is given by:

$$\eta = \frac{P_{MP}}{P_{source}} = \frac{V_{MP}J_{MP}}{P_{source}} = \frac{FFV_{OC}J_{SC}}{P_{source}}$$

This is the efficiency of extracted electrical power for inputted optical power (ratio of output power to incident power). It is also unitless and wavelength dependent. Unlike the FF, η includes not only the quality of device fabrication but also the choice of materials and morphology of the devices.

The AM1.5 conversion power efficiency $\eta_{AM1.5}$ of the photovoltaic devices measured with a solar simulator is given by:

$$\eta_{AM1.5} = \frac{P_{out}}{P_{source}} M = FF \frac{V_{OC}J_{SC}}{P_{source}} M$$

where P_{out} is the output electrical power of the device under illumination, P_{source} is the light intensity incident on the device as measured by a calibrated reference cell and M is the spectral mismatch factor that accounts for deviations in the spectral output of the solar simulator with respect to the standard AM1.5 spectrum and deviations in the spectral response of the device under measurement with respect to that of the reference cell [205].

2.3. Carbonaceous Materials

Carbon is the most abundant non-gaseous element on earth and because of its various properties, carbon based materials have the widest array of applications, depending on the way the carbon atoms are bonded in the structure [206]. For more than 6000 years, carbon is used for the reduction of metal oxides. Graphitic form of carbon was discovered in 1779 while in 1789 diamond was discovered. The following 200 years were spent waiting for the next form of carbon when in 1985 Kroto, Smalley and Curl discovered the fullerene structure [207,208] after which, in 1991, Ijima discovered carbon nanotubes [209] and in 2004 Novoselov and Geim discovered graphene [210].

Figure 2.13 shows eight allotropic modifications of carbon: diamond, graphite (with graphene being a monolayer of basal plane of graphite), diamond with hexagonal lattice called lonsdaleite (in honor of Kathleen Lonsdale), C60 (buckminsterfullerene or bucky-ball), C540 fullerite, C70, amorphous carbon and carbon nanotubes (CNTs). Some of these structures, like CNTs and graphene, possess unique combinations of electrical, thermal, optical and mechanical properties. Because of such properties they have become very attractive as candidates for nanofillers in nanocomposites.

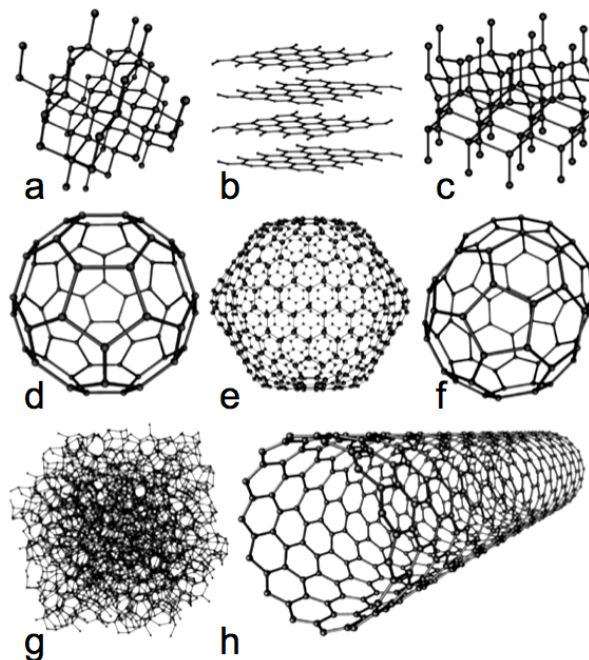


Figure 2.13. Eight allotropic modifications of carbon: a) diamond, b) graphite (comprised of many graphene planes), c) lonsdaleite, d) C60, e) C540 fullerite, f) C70, g) amorphous carbon, h) carbon nanotubes (pictured is a SWCNT).

Carbon Nanotubes

As already mentioned, CNTs were discovered by Ijima [209] in 1991 using transmission electron microscopy. Ijima noticed long cylinders of carbon atoms covalently bonded, of sp^2 type configuration. There are two main types of CNTs: single-walled (SWCNTs) and multi-walled (MWCNTs), where the latter consist of coaxially organized cylinders with distances of 0.34nm between each layer, identical to the distance between basal planes in graphite [211]. A single-walled CNT can be observed as a rolled-up monolayer of a hexagonal network of carbon atoms in sp^2 configuration. There are different ways of how this monolayer can be rolled into a tube, which can be explained by chirality or helicoidal nature of the tubes [212], to be more precise, by the vector chirality vector \vec{C}_h :

$$\vec{C}_h = n\vec{a}_1 + m\vec{a}_2$$

shown in Figure 2.14, where n and m are integers while \vec{a}_1 and \vec{a}_2 are hexagonal lattice vectors.

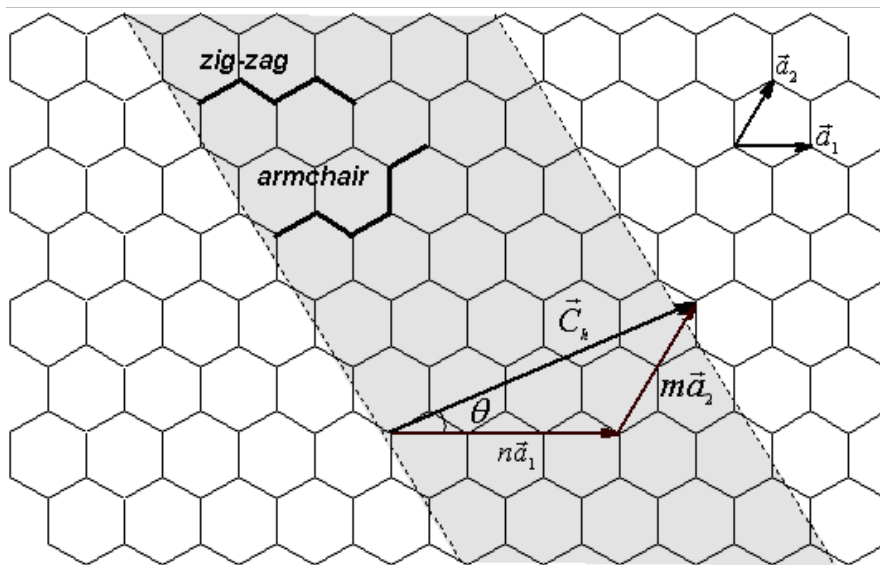


Figure 2.14. Schematic of ways the hexagonal carbon sheet can be rolled into a tube. This is an example of forming (3,2) type CNTs [212].

From an experimental point of view, CNTs are not nearly as perfect as presented in Figure 2.15, where two CNTs are shown to be closed at each side by two halves of a C₆₀ molecule. With the division of this molecule parallel to one of the axes of third order of symmetry, a zig-zag type of CNTs is created, shown in Figure 2.15a. If the division is along the axis of fifth order symmetry, the resulting CNT is of an armchair morphology, shown in Figure 2.15b.

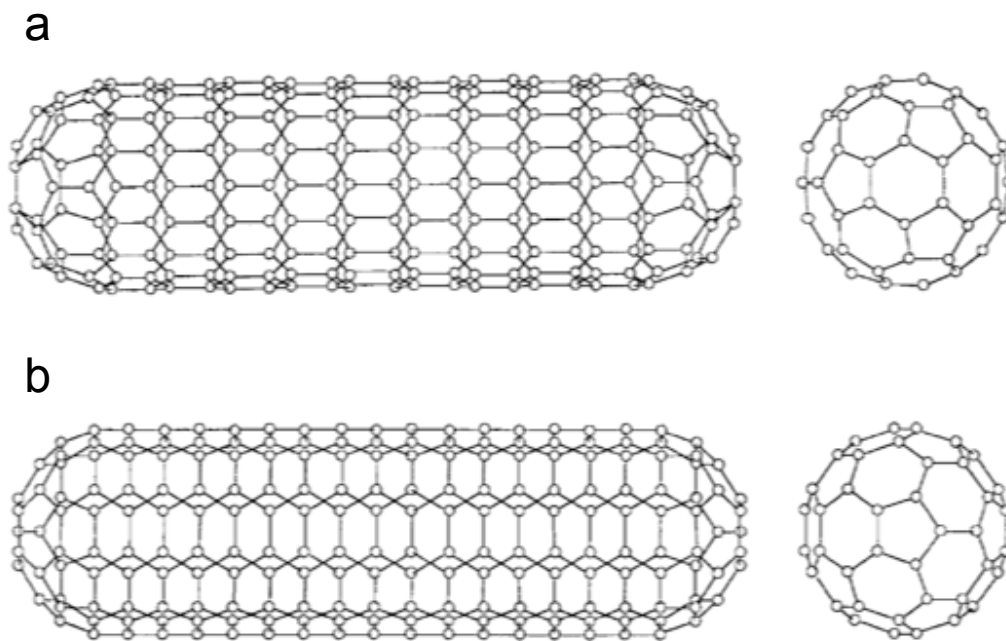


Figure 2.15. CNTs closed with a half of a C₆₀ molecule at each side resulting in: a) zig-zag structure of (9,0) type, b) armchair structure of (5,5) type [213].

It has been reported that CNTs exhibit high elasticity [214] and small specific density [215] as well as a large ratio of length-to-diameter, called the aspect ratio, which is typically in the range of 300 - 1000. They also possess a unique combination of mechanical, electric and thermic properties which qualify them as a suitable candidate for replacing conventional nanofillers during synthesis and processing of nanocomposites, specifically polymer based. Certain types of CNTs can be stronger than steel, lighter than aluminum while having higher electrical conductivity than copper, which is the case with SWCNTs which have a tensile modulus between 640 GPa and 1 TPa [216], tensile strength between 150 and 180 GPa [217], and high thermal

conductivity which can theoretically be higher than 6000 W/mK [218]. Typical properties of SWCNT and MWCNT, compared to graphite are presented in Table 2.1.

Table 2.1. Properties of SWCNTs, MWCNTs and Graphite [219,220,221].

Property	SWCNT	MWCNT	Graphite
Specific gravity	0.8 g/cm	1.8 g/cm	1.9-2.3 g/cm
Elastic modulus	~1 TPa	~0,3-1 TPa	1 TPa (basal plane)
Hardness	50-500 GPa	10-60 GPa	0.2 GPa
Electrical resistivity	5-50 $\mu\Omega\text{cm}$	5-50 $\mu\Omega\text{cm}$	50 $\mu\Omega\text{cm}$ (basal plane)
Electrical conductivity	102-106 S/cm	103-105 S/cm	4000 S/cm (in plane), 3.3 S/cm (c-axis)
Electron mobility	105 cm^2/Vs	104-105 cm^2/Vs	$2 \times 10^4 \text{ cm}^2/\text{Vs}$
Thermal conductivity	3000 W/mK	3000 W/mK	298 W/mK (in plane); 2.2 W/mK (c-axis)
Coefficient of thermal expansion	Insignificant	Insignificant	$-1 \times 10^{-6} \text{ K}^{-1}$ (in plane); $29 \times 10^{-6} \text{ K}^{-1}$ (c-axis)
Thermal stability	>700°C (in air) 2800°C (in vacuum)	>700°C (in air) 2800°C (in vacuum)	450-650°C (in air)
Specific surface area	~400-900 m^2/g	~200-400 m^2/g	Insignificant

For CNT synthesis, various methods have been implemented, of which three are the most widely used [211,212]:

- Arc discharge,
- Laser ablation,
- Chemical vapor deposition (CVD).

The first two methods are based on condensation of carbon atoms from gaseous phase formed by carbon solid phase evaporation. The CVD method is based on the catalytic decomposition of a hydrocarbon or carbon monoxide as a precursor, from which carbon atoms are acquired which secure deposition of CNTs on the substrate or their growth from the substrate. This method produces the best dimension control and CNT structure. In this thesis, CNTs used were synthesized by combustion chemical vapor deposition (CCVD), also known as flame pyrolysis.

Even with all the incredible properties mentioned and intensive research activity yielding many superb publications, dominance of products based on CNT nanocomposites has not been established in the commercial sphere. The reason for this lies in the inconsistency of properties of CNTs as nanofillers in nanocomposites. It is well known that CNT synthesis results in various chirality (rotational symmetry), distribution of dimensions (diameter and length), amounts of impurities and defects present in the same batch. Since these parameters greatly influence CNT properties, it is very difficult to reproduce control experiments with such inconsistent nanofillers and almost impossible to compare experimental results of different research groups.

Graphene

As already mentioned, in 2004 a group of scientists [210] found a way, by the delamination of graphite, to isolate individual graphene sheets using simple scotch tape. Measured electronic properties of these sheets proved to be remarkable [222].

The term graphene is given to a monolayer (1 atom thick) of carbon atoms tightly packed in a two-dimensional hexagonal lattice. It is the basic structure unit for graphitic materials of all dimensions. The source of stability of the monolayer sheet of carbon is the sp^2 carbon configuration. Figure 2.16a represents a schematic of a graphene monolayer and Figure 2.16b represents a reconstructed micrograph of an exit electron wave acquired by TEM. This atomic resolution micrograph shows the graphene layer as a highly ordered structure where individual carbon atoms are represented as bright white dots, organized in hexagonal lattices, with the bond length of 0.142 nm between carbon atoms.

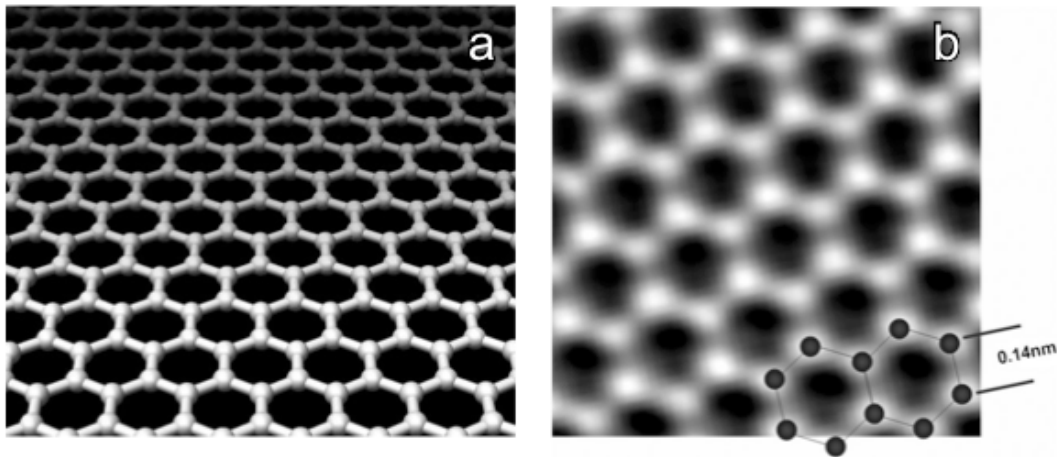


Figure 2.16. a) Schematic illustration of a graphene sheet, b) reconstructed micrograph of exit electron wave acquired by TEM; model showing two hexagonal rings of an ideal graphene lattice with noted bond length [223].

Up until a few years ago, graphene produced from highly oriented pyrolytic graphite was one of the most expensive materials – a sample with a thickness matching a human hair fetched a price of \$1,000 (in 2008) which is translated to \$100,000,000/cm² [224]. From then on, the delamination procedure has been optimized for mass production, allowing companies to produce graphene in very large batches [225]. Today, there is a wide array of methods for synthesizing graphene sheets which include:

- Improved delamination of graphite i.e. exfoliation of graphene sheets from graphite; In this thesis, the graphene used was chemically exfoliated from natural graphite;
- Epitaxial growth on silicon carbide (reduction to graphene) [226] on metal substrates like ruthenium, nickel, etc.;
- Reduction of graphene oxide (GO) with hydrazine;
- Solvothermal synthesis and sonication [227];
- Unzipping and plasma etching of CNTs [228,229,230];
- Production of graphene without a substrate, in a microwave plasma reactor [223,231,232]; This method shows the most promise for mass production of graphene.

Graphene sheets with densities higher than 1 g/cm^3 usually appear in diffraction images as a graphitic layered structure with distances of 0.34 nm between (002) basal planes. This has also been the case for some SWCNT structures [233]. Spray pyrolysis of oxidized and chemically processed graphite in water, in combination with paper treatment methods, yields mono-layered flakes which form a two layered structure with tight bonds. This structure, called graphene oxide (GO) has a tensile modulus of 32 GPa. A characteristic feature of GO are functional groups which are attached to graphene monolayers and can dramatically change the process of polymerization or other chemical processes [234].

At room temperature, thermal conductivity of graphene ranges from $(4.84 \pm 0.44) \times 10^3$ to $(5.30 \pm 0.48) \times 10^3$ W/mK and is characterized by isotropic ballistic thermal conductivity [235]. Thermal conductivity of its three-dimensional version, graphite, is 1000 W/mK (basal plane). In graphite, thermal conductivity in c-axis (outside of basal plane) is up to 100 times smaller than in the basal plane because of the weak bonds and long inter-plane distances between basal planes [236]. Some important properties of single layer graphene and GO are given in Table 2.2.

Nevertheless, graphene separation processes require further development before they can be commercially affordable for use in industrial processes.

Table 2.2. Properties of single layer graphene and GO [237].

Property	Single layer graphene	Graphene oxide
Young's modulus	1000 GPa	220 GPa
Fracture strength	130 GPa	120 MPa
Optical transmittance	97.7%	N/A (Due to defects in functional groups)
Charge carrier concentration	$1.4 \times 10^{13} \text{ cm}^{-2}$	N/A (Due to defects in functional groups)
Room temperature mobility	$\sim 2 \times 10^5 \text{ cm}^2/\text{Vs}$	N/A ($< 1.5 \times 10^4 \text{ cm}^2/\text{Vs}$, due to scattering defect disruption)
Thermal conductivity	$\sim 5000 \text{ W/mK}$	2000 W/mK
Electrical conductivity	10^4 S/cm	10^{-1} S/cm

2.3.1 Polymer Nanocomposites with Carbonaceous Nanofillers

Polymer nanocomposites (PNC) are a part of modern technology, usually known as nanotechnology, globally regarded as one of the most significant areas of technological advances in the 21st century. Polymer nanocomposites are composite materials in which matrices like thermoplastics, thermosetting polymers, elastomers, etc. are reinforced with small quantities (usually less than 5%) of nano-sized particles which exhibit a large length-to-diameter ratio, i.e. $L/d > 300$ [238]. Research suggests that the nanofiller threshold has dropped below 2% [239,240].

Polymer nanocomposites, formed by introducing nanofillers in a polymer matrix, require optimal dispersion for the properties of the nanofiller and the matrix to be synergistically transferred to the nanocomposite. Dispersion at the nanoscale allows the creation of a high interfacial area between the nanofillers and the matrix, which in turn leads to improved properties, compared to the pristine polymer. This has proven to be a difficult task since carbonaceous nanofillers, because of their inert nature, have a tendency to agglomerate as a result of van der Waals forces i.e. if not modified (functionalized) they have poor dispersion in the matrix. Functionalization of these fillers makes them organophilic (tendency of wetting between organic substance and CNTs or graphene), which in turn allows for better dispersion in the polymer matrix.

Processing methods of polymer nanocomposites can also influence nanofiller dispersion. Although latex technology, solid-state shear pulverization and coagulation spinning methods show promise, the most widely used methods to process polymer nanocomposites with carbonaceous nanofillers are [241]:

- *Solution blending*, very amenable to small sample sizes and fairly simple as it involves dispersion of nanofiller in solvent, mixing with polymer and forming of nanocomposite (usually film) by solvent evaporation. High-powered ultrasonication can be used, as it can break up nanofiller agglomerates but can also degrade nanofiller structure, shortening the aspect ratio of the CNTs. Limiting factor of this method can be the solubility of polymer in solvent;
- *Melt blending*, which uses high temperatures and shear force to disperse nanofillers in polymer matrix. Because of high viscosities of nanocomposites

at high nanofiller loadings, it is less effective for dispersion at higher concentrations;

- *In-situ polymerization*, consists of mixing nanofillers with a monomer which is subsequently polymerized. As the polymerization progresses, viscosity of system increases which leads to less effective dispersions.

Carbon Nanotube Based Polymer Nanocomposites

Polymer nanocomposites with CNTs as nanofillers have attracted attention, especially in the last 15 years, due to their excellent potential for exhibiting advanced properties along with their ease and low cost of processability. Properties of CNT based PNCs depend, among other things, on the following factors [241]:

- Type of CNTs (number of walls/layers);
- Chirality i.e. the structure;
- Purity (presence of impurities);
- Defect density;
- Loading of CNT present in the polymer matrix;
- Dispersion and orientation of tubes in the matrix;
- Interface adhesion between tubes and matrix.

Functionalization (modification) of CNTs presents a viable way to control and even improve their dispersion and interfacial properties, which in turn improves nanocomposite properties. Huge progress has been made in the field of functionalization in the last few years, showing great promise for future research [242]. However, many research groups have dealt with pristine (non-functionalized) CNTs as nanofillers in PNCs, because of the simplicity and cost-effectiveness in their production. This thesis follows their example.

As previously mentioned, physical properties of CNT based PNCs are directly related to CNT distribution in the polymer matrix i.e. formed CNT network. This type of structure allows for promotion of various properties, when the percolation threshold is achieved. Generally, properties improve with the increase in CNT content (load), at

small volume fractions but they deteriorate at higher fractions, due to agglomeration. Percolation is dependent on the amount of CNTs per unit of volume (concentration in relation to dispersion and volume), CNT distribution and their mutual correlation i.e. alignment.

A tremendous amount of research has been done in order understand and enhance mechanical properties of PNCs reinforced with CNTs. Qian et al. reported that addition of 1 wt.% of MWCNTs to polystyrene (PS) yielded elastic modulus and break stress increase of 36-42% and ~25%, respectively [243]. Biercuk et al. reported linear increase of Vickers hardness from pristine epoxy to epoxy/SWCNT nanocomposite, by a factor of 3.5, with the addition of 2 wt.% of SWCNTs [244]. Safadi et al. studied PS nanocomposites and reported an almost twofold increase in modulus and strength, with the addition of 2.5 vol.% of MWCNTs [245]. Cadek and Coleman et al. reported an array of results regarding nanocomposites containing poly (vinyl alcohol) and MWCNT. With addition of 1wt.% of nanofiller, hardness was ~1.5 times higher [246], while twofold [247] and fourfold increases [248] were reported with addition of 0.6 vol.% of CNTs.

Research on the electrical properties of CNT based polymer nanocomposites has been just as extensive. In these studies, the percolation threshold i.e. long range connectivity of nanofillers, was a key factor in understanding the role of CNTs nanofiller load in electrical properties of PNCs. The percolation thresholds for CNTs in polymers presented in literature, have shown that, even at small wt.%, electrical conductivity can be achieved in polymer nanocomposites with an insulating polymer matrix. Some examples include:

- MWCNT/epoxy resin nanocomposite with a percolation threshold of 0.0021 wt.% exhibiting maximum conductivity of 10^{-1} S/m at 0.01 wt.% [249];
- SWCNT/epoxy resin nanocomposite with a percolation threshold of 0.023 wt.% exhibiting maximum conductivity of 2×10^{-4} S/m at 0.2 wt.% [250];
- MWCNT/PS nanocomposite with a percolation threshold of 0.8 wt.% exhibiting maximum conductivity of 10^{-2} S/m at 2 wt.% [251];
- SWCNT/PS nanocomposite with a percolation threshold of 0.28 wt.% exhibiting maximum conductivity of 1 S/m at 1.5 wt.% [252];

- MWCNT/PVA nanocomposite with a percolation threshold of 0.2 wt.% exhibiting maximum conductivity of 10 S/m at 5 wt.% [253];
- SWCNT/PVA nanocomposite with a percolation threshold of 0.038 wt.% exhibiting maximum conductivity of 20 S/m at 4 wt.% [254].

Carbon nanotube incorporation in polymer materials has opened up a whole new field of high performance engineering applications where demands can be met by specific properties of PNCs. Targeting electrical conductivity, CNT based PNCs applications include, among others [255]:

- *Electromagnetic interference (EMI) shielding* - prevention of entry/exit electromagnetic radiation from a certain space; Role of CNT based PNCs in this application includes absorption and single reflection i.e. reflection from surface [256,257,258] as well as multiple reflections [259,260];
- *Electrostatic dissipation (ESD)* - reduction of static charge for prevention of discharge, which leads to hazardous situations; Role of CNT based PNCs in this application is to promote dissipation with its surface conductivity [261];
- *Optoelectronics*, such as organic light emitting diodes (OLED) [262,263] and organic solar cells (OSC) where they can be utilized as the electron donor-acceptor photoactive layers [264,265,266,267] or hole transport layers [268];
- *Fuel cells*, from supercapacitors [269,270] to Li-ion batteries [271].

Targeting mechanical properties, especially the high strength/lightweight combination, CNT based PNCs structural applications include, among others: sports and shipbuilding industries, which demand vibrational damping [272,273], aerospace industry [274] and wind power industry [275].

Targeting properties regarding biocompatibility, CNT based PNCs applications include, among others [242]: biosensors [276,277], biocatalytic films [278], gene delivery [279] and implant technology [280].

One of the other important applications of CNT based PNCs is sensing of various gases such as ammonia [281,282,283], methane [284], carbon monoxide [285], nitrous oxide [286], etc.

Graphene Based Polymer Nanocomposites

Along with CNTs, graphene as a nanofiller in polymer nanocomposites caught the attention of many research groups around the world, especially in the last 10 years. Numerous studies have dealt with the fabrication of graphene based PNCs with novel and improved properties such as mechanical, electrical (semi-) conductivity, unique photonic/optical transportation, anisotropic transport, low permeability, fluorescence quenching, etc. [287]. Although some amazing results have been achieved, two challenges, similar to ones for CNTs as the nanofiller, have yet to be bested. The first challenge is related to the dispersion behavior in the polymer matrix, where the large difference in surface energy between graphene and polymer prevents uniform distribution, which leads to agglomeration of particles [288,289]. The second challenge is related to the interfacial interactions between graphene as the nanofiller and the polymer as the matrix, where π -conjugations, although beneficial for advanced properties of graphene, generate surface inertia which can lead to very low interfacial adhesion [290].

As a nanofiller, pristine graphene interacts with the polymer matrix via van der Waals forces, π - π stacking, and hydrophobic interactions, which are weak [287]. To enhance these reactions and reduce effects caused by non-optimal dispersion and surface inertia, modification of graphene is necessary. Fixing these problems will in turn improve properties of the PNC. This can be achieved by GO, the most important derivative of graphene, in combination with innovative ways to exfoliate graphene based materials into single-layer graphene or GO sheets which results in their better dispersion. One way of achieving this is through high shearing produced by ultrasonication of PNC in solution [291,292]. Another way is by process of solution intercalation. In this technique, nanofiller and polymer are soluble in the same solvent. The polymer is firstly adsorbed onto the delaminated nanofiller sheets and when the solvent evaporates, the polymer is sandwiched because of the reassembly of the sheets. Here, efficient exfoliation of stacked laminates, followed by intercalation increases the interfacial area thus leading to stronger PNCs with extraordinary properties [287]. However, this is not an environmentally friendly procedure as it uses large amounts of toxic solvents [293]. PNCs based on graphene materials and various polymers have

been reported [294,295]. Figure 2.17 presents different situations during PNC fabrication with laminated nanofillers by solution intercalation.

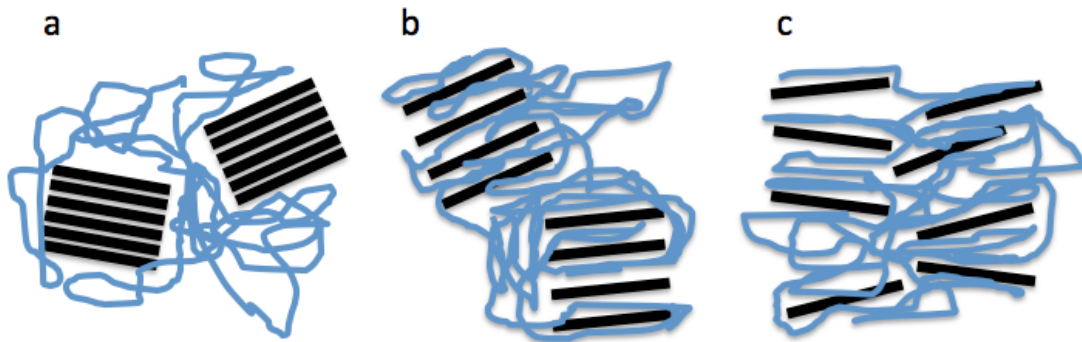


Figure 2.17. Dispersing scenarios of laminated graphene material in polymer matrix, a) separated, b) intercalated, c) exfoliated; black platelets represent graphene material, while blue lines represent polymer chains [296].

Because of their extraordinary properties, graphene and GO based PNCs have a wide array of potential applications. Some of them include:

- Utilizing sensing capabilities for detection of trace levels of toxic metals like lead or cadmium [297], ammonia [298], peroxide [299] or even for biosensing applications, for detection of dopamine [300], nerve cells [301] and proteins and bacteria infected cells [302];
- Utilizing capabilities regarding low permeability for gas barrier applications i.e. preventing gas and moisture from penetrating a structure; as an oxygen barrier [303], as a moisture barrier [304];
- Biomedical applications, which include biomimetics [305], cell based studies [306] and drug delivery [307];
- Utilizing amazing electrical properties for energy storage applications like supercapacitors [308], organic solar cells [309,310] or even EMI shielding [311];
- Utilizing excellent electrocatalytic activity for electrocatalyst applications [312].

2.3.2. Polyvinyl Butyral Based Nanocomposites

Polyvinyl butyral (PVB) is polymer resin with a molecular weight in the range of 30000-100000 g/mol. It is a polyvinyl type polymer comprised of reactive hydrophobic and hydrophilic polymer units, the ratio between which is widely variable. Hydrophobic vinyl butyral units are the part of the polymer that gives it thermoplastic processibility, solubility in numerous solvents, elasticity, as well as compatibility with many resins and plasticizers. Hydrophilic vinyl alcohol units are the part of the polymer responsible for high adhesion to inorganic materials (like glass and metals), high strength, cross-linking ability and anticorrosive properties [313].

Properties which make PVB commercially beneficial include: excellent adhesion and film-forming properties, good water resistance, high bonding power, excellent optical transparency, good elasticity, excellent compatibility with organic solvents and other polymers as well as good thermoplastic processing. These properties make PVB a desired candidate in various fields of applications: coatings and primers, printing inks for packaging, films for laminated safety glass in automotive industry, binders for inorganic powders, adhesives, binders for a wide range of special applications [314] as well as solar cells where PVB can enhance utilization of incident light [315]. One of the most interesting potential industrial applications of PVB reinforced with, for example, CNTs or graphene, which boost mechanical properties of PVB without hindering its optical transparency, stated in the research presented in this thesis, is encapsulation of solar cells (photovoltaic devices). Literature has shown that PVB is a thermoplastic, fairly resistant to heat, UV light and environmental influences and has a high compatibility with module components. Along with strong adhesive properties and the ability to reduce moisture and oxygen permeation, PVB can slow down degradation of solar cells and ensure longer lifetimes [316,317,318].

Among others, a way of synthesizing PVB is as follows: polyvinyl acetates (PVAc), with various molecular weights are the starting material. From there, polyvinyl alcohols (PVA) are produced by trans-esterification. Finally, in a reaction of aqueous polyvinyl alcohol solutions with aldehydes, in the presence of small quantities of mineral acid, polyvinyl butyrals are produced.

Besides CNTs and graphene, fillers used with PVB as the polymer matrix include: barium titanate [319], carbon black [320], montmorillonite clay [321,322], sepiolite [323], indium tin oxide (ITO) [324], titania [325,326], silica [327], alumina [328], magnesium hydroxide [329], zinc oxide [330], etc.

REFERENCES

-
- [1] H. Gleiter, *Acta materialia*, 48 (2000) 1-29; H. Gleiter, *Nanostructured Materials*, 6 (1995) 3-14.
- [2] F. Fathi, PhD thesis, *Ag Nanostructures: from Fabrication to Interaction*, University of Toronto, Toronto, Canada, 2013.
- [3] V. E. Torres Heredia, PhD thesis, *Silver Nanostructures: Chemical Synthesis of colloids and composites nanoparticles, plasmon resonance properties and silver nanoparticles monolayer films prepared by spin-coating*, Polytechnic University of Catalonia, Barcelona, Spain, 2011.
- [4] Y. Oaki and H. Imai, *Crystal Growth & Design*, 3 (2003) 711–716.
- [5] K. Fukami, S. Nakanishi, H. Yamasaki, T. Tada, K. Sonoda, N. Kamikawa, N. Tsuji, H. Sakaguchi and Y. Nakato, *Journal of Physical Chemistry C*, 111 (2007) 1150–1160.
- [6] V. A. Bogoyavlenskiy and N. A. Chernova, *Physical Review E*, 61 (2000) 1629-1633.
- [7] X. K. Meng, S. C. Tang and S. Vongehr, *Journal of Materials Science and Technology*, 26 (2010) 487-522.
- [8] M. H. Rashid and T. K. J. Mandal, *Journal of Physical Chemistry C*, 111 (2007) 16750–16760.
- [9] D. M. Ledwith, D. Aherne and J. M. Kelly, In *Metallic Nanomaterials*, C. S. S. S. Kumar (Ed.), Wiley-VCH, Weinheim, Germany, 2009, pp. 99-149.
- [10] W. Dobbs, J-M. Suisse, L. Douce, and R. Welter, *Angewandte Chemie International Edition*, 45 (2006) 4179 –4182.
- [11] R. G. Chambers, *Proceedings of the Royal Society of London A*, 202 (1950) 378-394.
- [12] G. J. Lee, Y. Lee, B. Y. Jung, S. G. Jung, C. K. Hwangbo, J. H. Kim, and C. S. Yoon, *Journal of the Korean Physical Society*, 51 (2007) 1555–1559.
- [13] J-S. Yu, I. Kim, J.-S. Kim, J. Jo, T. T. Larsen-Olsen, R. R. Sondergaard, M. Hosel, D. Angmo, M. Jorgensen and F. C. Krebs, *Nanoscale*, 4 (2012) 6032-6040.
- [14] J. W. Morris, In *Materials Science and Engineering: An Introduction*. Wiley, Hoboken, USA, 2013, pp. 76–107.
- [15] A. Kelly and K. Knowles, *Crystallography and Crystal Defects*, John Wiley & Sons, Chichester, UK, 2012, pp. 277-279.
- [16] W. S. Hosford, *Mechanical Behavior of Materials*, Cambridge University Press, New York, USA, P. 173
- [17] Y. T. Zhu, X. Z. Liao and X. L. Wu, *Progress in Materials Science*, 57 (2012) 1–62.
- [18] A. G. Froseth, P. M. Derlet, and H. Van Swygenhoven, *Advanced Engineering Materials*, 7 (2005) 16-20.

-
- [19] D-S. Leem, A. Edwards, M. Faist, J. Nelson, D. D. C. Bradley and J. C. Mello, *Advanced Materials*, 23 (2011) 4371–4375.
- [20] L. B. Hu, H. S. Kim, J. Y. Lee, P. Peumans and Y. Cui, *ACS Nano*, 4 (2010) 2955–2963.
- [21] T. Stubhan, J. Krantz, N. Li, F. Guo, I. Litzov, M. Steidl, M. Richter, G. J. Matt, C. J. Brabec, *Solar Energy Materials and Solar Cells*, 107 (2012) 248–251.
- [22] V. Scardaci, R. Coull, P. E. Lyons, D. Rickard, and J. N. Coleman, *Small*, 7 (2011) 2621–2628.
- [23] J-Y. Lee, S. T. Connor, Y. Cui, and P. Peumans, *Nano Letters*, 8 (2008) 689–692.
- [24] Y. Sun and Y. Xia, *Advanced Materials*, 14 (2002) 833–837.
- [25] A. Tao A, P. Sinsermsuksakul P and P. Yang, *Angewandte Chemie International Edition*, 45 (2006) 4597–4601.
- [26] Y. Xia, Y. Xiong, B. Lim, S. E. Skrabalak, *Angewandte Chemie International Edition*, 2009, 48, 60.
- [27] D. Langley, PhD thesis, *Silver nanowire networks: effects of percolation and thermal annealing on physical properties*, University of Grenoble, Grenoble, France, 2015.
- [28] Q. Zhang, C. M. Coble, L. Au, M. McKiernan, A. Schwartz, J. Chen, L. Wen and Y. Xia, *ACS Applied Materials & Interfaces*, 1 (2009) 2044–2048.
- [29] B. Wiley, Y. Sun and Y. Xia, *Accounts of Chemical Research*, 40 (2007) 1067–1076.
- [30] M. Rycenga, C. M. Cobley, J. Zeng, W. Li, C. H. Moran, Q. Zhang, D. Qin and Y. Xia, *Chemical Reviews*, 111 (2011) 3669–3712
- [31] C. Ducamp-Sanguesa, R. Herrera-Urbina and M. J. Figlarz, *Journal of Solid State Chemistry*, 100 (1992) 272-280.
- [32] Y. Gao, P. Jiang, D. F. Liu, H. J. Yuan, X. Q. Yan, Z. P. Zhou, J. X. Wang, L. Song, L. F. Liu, W. Y. Zhou, G. Wang, C. Y. Wang, S. S. Xie, J. M. Zhang and D. Y. Shen, *Journal of Physical Chemistry B*, 108 (2004) 12877–12881.
- [33] Y. Sun, B. Mayers, T. Herricks, and Y. Xia, *Nano Letters*, 2003, 3, 955-960.
- [34] Y. Gao, P. Jiang, L. Song, L. Liu, X. Yan, Z. Zhou and S. Xie, *Journal of Physics D: Applied Physics*, 38 (2005) 1061-1067.
- [35] Y. Gao, L. Song, P. Jiang, L. Liu, X. Yan, Z. Zhou, D. Liu, J. Wang, H. Yuan, Z. Zhang, X. Zhao, X. Dou, W. Zhou, G. Wang, S. Xie, H. Chen, and J. Li, *Journal of Crystal Growth*, 2005 (276) 606–612.
- [36] S. Coskun, B. Aksoy, and H. E. Unalan, *Crystal Growth & Design*, 11 (2011) 4963-4969.
- [37] W. M. Schuette, PhD thesis, *Polyol Synthesis of Silver Nanowires by Heterogeneous Nucleation and Mechanistic Aspects Influencing its Length and Diameter*, Washington University in St. Louis, St. Louis, USA, 2014.
- [38] Y. Sun, Y. Xia, *Advanced Materials*, 14 (2002) 833-837.
- [39] D. Chen, X. Qiao, J. Chen, *Journal of Materials Science: Materials in Electronics*, 22 (2011) 1335-1339.
- [40] C. Chen, L. Wang, G. Jiang, Q. Yang, J. Wang, H. Yu, T. Chen, C. Wang, X. Chen, *Nanotechnology*, 17 (2006) 466-474.
- [41] D. V. Goia, *Journal of Materials Chemistry*, 14 (2004) 451–458.
- [42] L. Gou, M. Chipara, J. M. Zaleski, *Chemistry of Materials*, 19 (2007) 1755-1760.
- [43] J. Monk, J. J. Hoyt, and D. Farkas, *Physical Review B*, 78(2008) 024112.

-
- [44] H. Chen, Y. Gao, H. Zhang, L. Liu, H. Yu, H. Tian, S. Xie, and J. Li, *Journal of Physical Chemistry B*, 108 (2004) 12038–12043.
- [45] S. M. Rupich, E. V. Shevchenko, M. I. Bodnarchuk, B. Lee, and D. V. Talapin, *Journal of the American Chemical Society*, 132 (2010) 289–296.
- [46] H. Hofmeister, S. A. Nepijko, D. N. Ievlev, W. Schulze, and G. Ertl, *Journal of Crystal Growth*, 234 (2002) 773–781.
- [47] H. Chen, Y. Gao, H. Yu, H. Zhang, L. Liu, Y. Shi, H. Tian, S. Xie, and J. Li, *Micron*, 35 (2004) 469–474.
- [48] F. Niekietel, E. Bitzek, and E. Spiecker, *ACS Nano*, 8(2014) 1629–1638.
- [49] V. G. Gryaznov, J. Heydenreich, A. M. Kaprelov, S. A. Nepijko, A. E. Romanov, and J. Urban, *Crystal Research Technology*, 34(1999) 1091–1119.
- [50] A. S. Barnard, *Journal of Physical Chemistry B*, 110 (2006) 24498–24504.
- [51] B. Wu, A. Heidelberg, J. J. Boland, J. E. Sader, X. Sun, and Y. Li, *Nano Letters*, 6 (2006) 468–472.
- [52] Y. Zhu, Q. Qin, F. Xu, F. Fan, Y. Ding, T. Zhang, B. J. Wiley, and Z. L. Wang, *Physical Review B*, 85(2012) 045443.
- [53] A. M. Leach, M. McDowell, and K. Gall, *Advanced Functional Materials*, 17 (2007) 43–53.
- [54] H. S. Park and P. A. Klein, *Journal of Mechanics and Physics of Solids*, 56 (2008) 3144–3166.
- [55] J. H. Yoo, S. I. Oh, and M. S. Jeong, *Journal of Applied Physics*, 107 (2010) 094316.
- [56] C-H. Chung, T-B. Song, B. Bob and R. Zhu and Y. Yang, *Nano Research*, 5 (2012) 805-814.
- [57] C. Preston, Y. Xu, X. Han, J. N. Munday, L. Hu, *Nano Research*, 6 (2013) 461-468.
- [58] T. Chih-Hung, H. Sui-Ying, H. Tsung-Wei, T. Yu-Tang, C. Yan-Fang, Y. H. Jhang, L. Hsieh, W. Chung-Chih, C. Yen-Shan, C. Chieh-Wei, L. Chung-Chun, *Organic Electronics*, 12 (2011) 2003-2011.
- [59] A. Bid, A. Bora and A. K. Raychaudhuri, *Physical Review B*, 74 (2006) 035426.
- [60] Y. Sun, B. Gates, B. Mayers, and Y. Xia, *Nano Letters*, 2(2002) 165–168.
- [61] S. De, P. J. King, P. E. Lyons, U. Khan, and J. N. Coleman, *ACS Nano*, 4 (2010) 7064–7072.
- [62] D. Hecht, L. Hu, G. Gruner, *Applied Physics Letters* 2006, 89, 133112.
- [63] S. Spallek, PhD Thesis, *Electron Microscopy Studies on Structure-property Relationships of Nanoparticulate Transparent Electrodes for Printed Electronics*, Friedrich Alexander University of Erlangen-Nuremberg, Erlangen, Germany, 2016.
- [64] E. C. Garnett, W. Cai, J. J. Cha, F. Mahmood, S. T. Connor, M. G. Christoforo, Y. Cui, M. D. McGehee, M. L. Brongersma, *Nature Materials*, 11 (2012) 241-249.
- [65] S. Han, S. Hong, J. Ham, J. Yeo, J. Lee, B. Kang, P. Lee, J. Kwon, S. S. Lee, M. Y. Yang, *Advanced Materials*, 26 (2014) 5808-5814.
- [66] A. P. Bell, J. A. Fairfield, E. K. McCarthy, S. Mills, J. J. Boland, G. Baffou, D. McCloskey, *ACS Nano*, 9 (2015) 5551-5558.
- [67] Y. Yang, S. Ding, T. Araki, J. Jiu, T. Sugahara, J. Wang, J. Vanfleteren, T. Sekitani, K. Suganuma, *Nano Research*, 9 (2016) 401-414.
- [68] J. H. M. Maurer, L. Gonzalez Garcia, B. Reiser, I. Kanelidis, T. Kraus, *ACS Applied Materials & Interfaces*, 7 (2015) 7838-7842.

-
- [69] S. Zhu, Y. Gao, B. Hu, J. Li, J. Su, Z. Fan, J. Zhou, *Nanotechnology*, 24 (2013) 335202.
- [70] Y. Lu, J. Y. Huang, C. Wang, S. Sun, and J. Lou, *Nature Nanotechnology*, 5 (2010) 218-224.
- [71] T. Tokuno, M. Nogi, M. Karakawa, J. Jiu, T. T. Nge, Y. Aso, K. Suganuma, *Nano Research*, 4 (2011) 1215-1222.
- [72] S. J. Lee, Y-H. Kim, J. K. Kim, H. Baik, J. H. Park, J. Lee, J. Nam, J. H. Park, T-W. Lee, G-R. Yi, and J. H. Cho, *Nanoscale*, 6 (2014) 11828-11834.
- [73] H. Lu, D. Zhang, J. Cheng, J. Liu, J. Mao, W. C. H. Choy, *Advanced Functional Materials*, 25 (2015) 4211-4218.
- [74] K. S. Siow, *Journal of Alloys and Compounds*, 514 (2012) 6-19.
- [75] G. Antczak, G. Ehrlich, *Surface Diffusion: Metals, Metal Atoms, and Clusters*, Cambridge University Press, New York, USA 2010, p. 322.
- [76] R. W. Messler Jr., *Principles of welding: processes, physics, chemistry and metallurgy*, John Wiley & Sons, New York, USA 1999, pp. 115-118.
- [77] M. Brochu, In *Microjoining and nanojoining*, Y. Zhou Ed., Woodhead Publishing Ltd., Cambridge, UK, 2008, p. 749.
- [78] Y. Zhou and A. Hu, *Open Surface Science Journal*, 3 (2011) 32-41.
- [79] S. Magdassi, M. Grouchko, O. Berezin, A. Kamyshny, *ACS Nano*, 2010, 4, 1943.
- [80] M. Grouchko, A. Kamyshny, C. F. Mihailescu, D. F. Anghel, S. Magdassi, *ACS Nano*, 5 (2011) 3354-3359.
- [81] M. Grouchko, I. Popov, V. Uvarov, S. Magdassi, A. Kamyshny. *Langmuir*, 25 (2009) 2501-2503.
- [82] M. Grouchko, P. Roitman, X. Zhu, I. Popov, A. Kamyshny, H. Su, S. Magdassi, *Nature Communications*, 5 (2014) 2994.
- [83] D. P. Langley, M. Lagrange, G. Giusti, C. Jimenez, Y. Brechet, N. D. Nguyen and D. Bellet, *Nanoscale*, 6 (2014) 13535-13542.
- [84] L. Rayleigh, *Proceedings London Mathematical Society*, 1878, s1-10(1), 4.
- [85] M. E. Toimil Molares, A. G. Balogh, T. W. Cornelius, R. Neumann and C. Trautmann, *Applied Physics Letters*, 85 (2004) 5337-5339.
- [86] S. Karim, M. E. Toimil-Molares, A. G. Balogh, W. Ensinger, T. W. Cornelius, E. U. Khan, R. Neumann, *Nanotechnology*, 17 (2006) 5954-5959.
- [87] C. M. Niemeyer, *Angewandte Chemie International Edition*, 40 (2001) 4128-4158.
- [88] Z. J. Jiang, C. Y. Liu, L. W. Sun, *Journal of Physical Chemistry B*, 109 (2005) 1730-1735.
- [89] H. J. Lee, S. H. Jeong, *Textile Research Journal*, 75 (2005) 551-556.
- [90] G. Haacke, *Annual Review of Materials Science*, 7 (1977) 73-93.
- [91] C. G. Granqvist, *Solar Energy Materials and Solar Cells*, 91 (2007) 1529-1598.
- [92] A. Shah, P. Torres, R. Tscharnner, N. Wyrsh and H. Keppner, *Science*, 285 (1999) 692-698.
- [93] C. J. Brabec, *Solar Energy Materials and Solar Cells*, 83(2004) 273-292.
- [94] S. De, T. M. Higgins, P. E. Lyons, E. M. Doherty, P. N. Nirmalraj, W. J. Blau, J. J. Boland and J. N. Coleman, *ACS Nano*, 3 (2009) 1767-1774.
- [95] K. Ellmer, *Nature Photonics*, 6(2012) 809-817.
- [96] T. M. Barnes, M. O. Reese, J. D. Bergeson, B. A. Larsen, J. L. Blackburn, M. C. Beard, J. Bult and J. van de Lagemaat, *Advanced Energy Materials*, 2 (2012) 353-360.
- [97] D. Langley, G. Giusti, C. Mayousse, C. Celle, D. Bellet and J-P. Simonato,

-
- Nanotechnology, 24 (2013) 452001.
- [98] J. L. Elechiguerra, L. Larios-Lopez, C. Liu, D. Garcia-Gutierrez, A. Camacho-Bragado, and M. J. Yacaman, *Chemistry of Materials*, 17(2005) 6042–6052.
- [99] D. G. Pierce and P. G. Brusius, *Microelectronics and Reliability*, 37(1997) 1053–1072.
- [100] B. Stahlmecke, F. J. Meyer zu Heringdorf, L. I. Chelaru, M. Horn-von Hoegen, G. Dumpich, and K. R. Roos, *Applied Physics Letters*, 88 (2006) 053122.
- [101] A. Bora, A. Bid, and A. K. Raychaudhuri, *Journal of Nanoscience and Nanotechnology*, 7(2007) 1831–1835.
- [102] F. Yakuphanoglu and R. S. Anand, *Synthetic Metals*, 160 (2010) 2250–2254.
- [103] Z. Yu, L. Li, Q. Zhang, W. Hu, and Q. Pei, *Advanced Materials*, 23 (2011) 4453–4457.
- [104] B. E. Hardin, W. Gaynor, I. Ding, S. B. Rim, P. Peumans, and M. D. McGehee, *Organic Electronics*, 12 (2011) 875–879.
- [105] T. Tokuno, M. Nogi, J. Jiu, T. Sugahara, K. Suganuma, *Langmuir*, 28 (2012) 9298–9302.
- [106] X.-Y. Zeng, Q.-K. Zhang, R.-M. Yu, C.-Z. Lu, *Advanced Materials*, 22 (2010) 4484–4488.
- [107] R. Chen, S. R. Das, C. Jeong, M. R. Khan, D. B. Janes, and M. A. Alam, *Advanced Functional Materials*, 23 (2013) 5150–5158.
- [108] M-X. Jing, C. Han, M. Li and X.-Q. Shen, *Nanoscale Research Letters*, 9 (2014) 588.
- [109] J-A. Jeong and H.-K. Kim, *Applied Physics Letters*, 104 (2014) 071906.
- [110] A. Kim, Y. Won, K. Woo, C-H. Kim, and J. Moon, *ACS Nano*, 7 (2013) 1081–1091.
- [111] R. Zhu, C-H. Chung, K. C. Cha, W. Yang, Y. B. Zheng, H. Zhou, T.-B. Song, C.-C. Chen, P. S. Weiss, G. Li, and Y. Yang, *ACS Nano*, 5 (2011) 9877–9882.
- [112] Q. Huang, W. Shen, X. Fang, G. Chen, Y. Yang, J. Huang, R. Tan and W. Song, *ACS Appl. Mater. Interfaces*, 7 (2015) 4299–4305.
- [113] Q. Xu, W. Shen, Q. Huang, Y. Yang, R. Tan, K. Zhu, N. Dai and W. Song, *Journal of Materials Chemistry C*, 2 (2014) 3750–3755.
- [114] J-L. Tian, H.-Y. Zhang and H.-J. Wang, *Journal of Electronic Materials*, 45 (2016) 3040–3045.
- [115] S. Hartner, M. Ali, C. Schulz, M. Winterer and H. Wiggers, *Nanotechnology*, 20 (2009) 445701.
- [116] R. Pandey, S. Yuldashev, H. D. Nguyen, H. C. Jeon and T. W. Kang, *Current Applied Physics*, 12 (2012) S56–S58.
- [117] M. Gobelt, R. Keding, S. W. Schmitt, B. Hoffmann, S. Jackle, M. Latzel, V. V. Radmilovic, V. R. Radmilovic, E. Spiecker and S. Christiansen, *Nano Energy*, 16 (2015) 196–206.
- [118] Y. Zhou, S. H. Yu, C. Y. Wang, X. G. Li, Y. R. Zhu and Z. Y. Chen, *Advanced Materials*, 11 (1999) 850–852.
- [119] X. P. Sun and M. Hagner, *Langmuir*, 23 (2007) 9147–9150.
- [120] Y. Oaki and H. Imai, *Crystal Growth & Design*, 3 (2003) 711–716.
- [121] X. K. Meng, S. C. Tang and S. Vongehr, *Journal of Materials Science and Technology*, 26 (2010) 487–522.
- [122] X. Qin, Z. Miao, Y. Fang, D. Zhang, J. Ma, L. Zhang, Q. Chen, and X. Shao,

-
- Langmuir, 28 (2012) 5218–5226.
- [123] Y. Xia and J. Wang, *Materials Chemistry and Physics*, 125 (2011) 267–270.
- [124] C. Gu, T.-Y. Zhang, *Langmuir*, 24 (2008) 12010–12016.
- [125] C. Gu, H. Ren, J. Tu and T.-Y. Zhang, *Langmuir*, 25 (2009) 12299–12307.
- [126] H. P. Ding, G-Q. Xin, K.-C. Chen, M. Zhang, Q. Liu, J. Hao and H.-G. Liu, *Colloids and Surfaces A: Physicochemical and Engineering Aspects*, 335 (2010) 166-171.
- [127] L. Wang, H. Li, J. Tian and X. Sun, *ACS Applied Materials & Interfaces*, 2 (2010) 2987-2991.
- [128] X. K. J. Meng, *Journal of Materials Science and Technology*, 26 (2010) 487-522.
- [129] L. Fu, T. Tamanna, W.-J. Hu and A. Yu, *Chemical Papers*, 68 (2014) 1283-1297.
- [130] T. A. Witten and L. M. Sander, *Physical Review Letters*, 47 (1981) 1400-1403.
- [131] J.X. Fang, H.J. You, P. Kong, Y. Yi, X.P. Song, B.J. Ding, *Crystal Growth & Design*, 7 (2007) 864.
- [132] G. Zhang, S. Sun, M. N. Banis, R. Li, M. Cai and X. Sun, *Crystal Growth & Design*, 11 (2011) 2493–2499.
- [133] W. W. Mullins and R. F. Sekerka, *Journal of Applied Physics*, 35 (1964) 444-451;
W. W. Mullins and R. F. Sekerka *Journal of Applied Physics*, 34 (1963) 323 - 329.
- [134] J. L. Barton, J. O. M. Bockris, *Proceedings of the Royal Society of London A*, 268 (1962) 485-505.
- [135] R. S. Wagner, *Acta Metallica*, 8 (1960) 57-60.
- [136] D. R. Hamilton, R. G. Seidensticker, *Journal of Applied Physics*, 31 (1960) 1165-1168.
- [137] C. Lofton and W. Sigmund, *Advanced Functional Materials*, 15 (2005) 1197-1208.
- [138] V. V. Radmilovic, J. Kacher, E. R. Ivanovic, A. M. Minor, and V. R. Radmilovic, *Crystal Growth & Design*, 16 (2016) 467-474.
- [139] S. Xie, X. Zhang, D. Xiao, M. C. Paa, J. Huang and M. M. F. Choi, *The Journal of Physical Chemistry C*, 115 (2011) 9943-9951.
- [140] Z. Zheng, S. C. Tang, S. Vongehr, and X. K. Meng, *Materials Chemistry and Physics*, 129 (2011) 594-598.
- [141] W. P. McConell, J. P. Novak, L. C. Brousseau, R. R. Fuierer, R.C. Tenent and D. L. Feldheim, *The Journal of Physical Chemistry B*, 104 (2000) 8925-8930.
- [142] M. H. Rashid, T. K. Mandal, *The Journal of Physical Chemistry C*, 111 (2007) 16750-16760.
- [143] S. Lal, S. Link, N. J. Halas, *Nature Photonics*, 1 (2007) 641-648.
- [144] X. Wen, Y. Xie, M. W. C. Mak, K. Y. Cheung, X. Li, R. Renneberg and S. Yang, *Langmuir*, 22 (2006) 4836-4842.
- [145] S. S. Hegedus and A. Luque, In *Handbook of Photovoltaic science and Engineering*, A. Luque, S. Hegedus, John Wiley & Sons Ltd, Chichester, UK, 2003, p. 4.
- [146] K. Masuko, M. Shigematsu, T. Hashiguchi, D. Fujishima, M. Kai, N. Yoshimura, T. Yamaguchi, Y. Ichihashi, T. Mishima, N. Matsubara, T. Yamanishi, T. Takahama, M. Taguchi, E. Maruyama, and S. Okamoto, *IEEE Journal of Photovoltaics*, 4 (2014) 1433–1435.
- [147] Photovoltaics report, Fraunhofer Institute for Solar Energy Systems, ISE with support of PSE AG, Freiburg, 2016.

-
- [148] <http://www.solar-frontier.com/>
- [149] A. Chirilă, P. Reinhard, F. Pianezzi, P. Bloesch, A. R. Uhl, C. Fella, L. Kranz, D. Keller, C. Gretener, H. Hagendorfer, D. Jaeger, R. Erni, S. Nishiwaki, S. Buecheler and A. N. Tiwari, *Nature Materials* 12 (2013) 1107–1111.
- [150] M. Saliba, T. Matsui, J.-Y. Seo, K. Domanski, J.-P. Correa-Baena, M. K. Nazeeruddin, S. M. Zakeeruddin, W. Tress, A. Abate, A. Hagfeldt and M. Grätzel, *Energy and Environmental Science*, 9 (2016) 1989-1997.
- [151] C. K. Chiang, C. R. Fincher, Y. W. Park, A. J. Heeger, H. Shirakawa, E. J. Louis, S. C. Gau, and A. G. MacDiarmid, *Physical Review Letters*, 39 (1977) 1098-1101.
- [152] C. J. Brabec, *Solar Energy Materials and Solar Cells* 83 (2004) 273–292.
- [153] M. Corazza, F. C. Krebs and S. A. Gevorgyan, *Solar Energy Materials and Solar Cells* 143 (2015) 467–472.
- [154] S. A. Gevorgyan, M.V. Madsen, B. Roth, M. Corazza, M. Hosel, R. R. Sondergaard, M. Jorgensen, F. C. Krebs, *Advanced Energy Materials*, 6 (2016), In press.
- [155] E. Yousif and R. Haddad, *SpringerPlus*, 2 (2013) 398.
- [156] <http://www.heliatek.com>
- [157] H. Hoppe and N. S. Sariciftci, *Journal of Materials Research*, 19 (2004) 1924–1945.
- [158] C. J. Brabec, N. S. Sariciftci, and J. C. Hummelen, *Advanced Functional Materials* 11 (2001) 15-26.
- [159] J. P. J. Markham, S. C. Lo, S. W. Magennis, P. L. Burn, and I. D. W. Samuel, *Applied Physics Letters* 80 (2002) 2645-2647.
- [160] P. Peumans, A. Yakimov, and S. R. Forrest, *Journal of Applied Physics*, 93 (2003) 3693-3722.
- [161] F. Yang and S. R. Forrest, *ACS Nano* 2 (2008) 1022-1032.
- [162] P. W. M. Blom, V. D. Mihailetchi, L. J. A. Koster, and D. E. Markov, *Advanced Materials*, 19 (2007) 1551-1566.
- [163] S. E. Gledhill, B. Scott, and B. A. Gregg, *Journal of Materials Research*, 20 (2005) 3167-3179.
- [164] M. C. Scharber, D. Wuhlbacher, M. Koppe, P. Denk, C. Waldauf, A. J. Heeger, and C. L. Brabec, *Advanced Materials*, 18(2006) 789–794.
- [165] J. T. McLeskey and Q. Qiao, In *Nanotechnology for Photovoltaics*, L. Tsakalacos Ed., CRC Press Taylor Francis Group, Boca Raton, USA, 2010, p.170.
- [166] A. Haugeneder, M. Neges, C. Kallinger, W. Spirkl, U. Lemmer, J. Feldmann, U. Scherf, E. Harth, A. Güel and K. Mülen, *Physical Review B*, 59 (1999) 15346-15351.
- [167] M. Theander, A. Yartsev, D. Zigmantas, V. Sundstr, W. Mammo, M. R. Andersson and O. Ingan, *Physical Review B*, 61 (2000) 12957-12963.
- [168] S. Thomas and B. Wolfgang, *Journal of Applied Physics*, 90 (2001) p.3632- 3641.
- [169] W. Ma, C. Yang and A. J. Heeger, *Advanced Materials*, 19 (2007) 1387-1390.
- [170] V. D. Mihailetchi, L. J. A. Koster and P. W. M. Blom, *Applied Physics Letters*, 85 (2004) 970-972.
- [171] V. D. Mihailetchi, P. W. M. Blom, J. C. Hummelen and M. T. Rispens, *Journal of Applied Physics*, 94 (2003) 6849-6854.
- [172] A. Gopal, PhD Thesis, *Effects of thickness, morphology and molecular structure of donor and acceptor layers in thermally interdiffused polymer photovoltaics*, Virginia State University, St. Petersburg, USA, 2007, p. 34.

-
- [173] R. Po, C. Carbonera, A. Bernardi, and N. Camaioni, In *Organic Solar Cells: Fundamentals, Devices, and Upscaling*, B.P. Rand and H. Richter Eds., CRC Press Taylor & Francis Group, Boca Raton, USA, 2014, pp. 181-195.
- [174] D. Chen, C. Zhang, Z. Wang, J. Zhang, Q. Feng, S. Xu, X. Zhou, and Y. Hao, *IEEE Transactions On Electron Devices*, 60 (2013) 451 – 457.
- [175] H. Kim, C. M. Gilmore, A. Pique, J. S. Horwitz, H. Mattoussi, H. Murata, Z. H. Kafafi and D. B. Chrisey, *Journal of Applied Physics*, 86 (1999) 6451-6461.
- [176] D. Angmo and F. C. Krebs, *Journal of Applied Polymer Science*, 129 (2013) 1–14.
- [177] R. Steim, F. R. Kogler and C. J. Brabec, *Journal of Materials Chemistry*, 20 (2010) 2499–2512.
- [178] S. Lattante, *Electronics*, 3 (2014) 132-164.
- [179] H. Siringhaus, P. J. Brown, R. H. Friend, M. M. Nielsen, K. Bechaard, B. M. W. Langeveld-Voss, A. J. H. Spiering, R. A. J. Janssen, E. W. Meijer, P. Herwig, and D. M. de Leeuw, *Nature*, 401 (1999) 685-688.
- [180] A. Ullmann, J. Ficker, W. Fix, H. Rost, I. McCulloch, M. Giles, G. E. Jabbour, and N. S. Sariciftci. *Materials Research Society Symposium Proceedings*, 665 (2002).
- [181] J. Hou and X. Guo, In *Organic Solar Cells: Materials and Device Physics*, W. C. H. Choy Ed., Springer-Verlag, London, UK, 2013, pp. 24-33.
- [182] F. Zhang, Z. Zhuo, J. Zhnag, X. Wang, X. Xu and W. Tang *Solar Energy Materials and Solar Cells*, 97 (2012) 71-77.
- [183] J. M. J. Frechet and B. C. Thompson, *Angewandte Chemie International Edition*, 47 (2008) 58 – 77.
- [184] B. Ratier, J. M. Nunzi, M. Aldissi, T. M. Kraft and E. Buncel, *Polymer International*, 61 (2012) 342–354.
- [185] R. L. Patyk, B. S. Lomba, A. F. Nogueira, C. A. Furtado, A. P. Santos, R. M. Q. Mello, L. Micaroni and I. A. Hümmelgen, *Physica Status Solidi*, 1 (2007) R43–R45.
- [186] H. Wang, D. He, Y. Wang, Z. Liu, H. Wu and J. Wang, *Physica Status Solidi*, 208 (2011) 2339-2343.
- [187] M. Helgesen, R. Sondergaard, F. C. Krebs, *Journal of Materials Chemistry*, 20 (2010) 36-60.
- [188] J. Weickert, R. B. Dunbar, H. C. Hesse, W. Wiedemann and L. Schmidt-Mende, *Advanced Materials*, 23 (2011) 1810–1828.
- [189] Q. Zheng, G. Fang, F. Cheng, H. Lei, W. Wang, P. Qin and H. Zhou, *Journal of Physics D: Applied Physics*, 45 (2012) No. 455103.
- [190] V. R. Koppolu, M. C. Gupta, W. Bagienski, Y. Shen, C. Shu, H. W. Gibson and H. C. Dorn, *Proceedings of the 34 IEEE Photovoltaic Specialist Conference*, Philadelphia, USA, 2009, pp. 001252-001257.
- [191] S. Kouijzer, W. Li, M. M. Wienk and R. A. J. Janssen, *Journal of Photonics for Energy*, 5 (2014) 057203–057203.
- [192] A. R. bin Mohd Yussof, H. P. Kim and J. Jang, *Solar Energy Materials and Solar Cells*, 109 (2013) 63-69.
- [193] T. Ameri, N. Li and C. J. Brabec, *Energy and Environmental Science*, 6 (2013) 2390–2413.
- [194] N. Li, D. Baran, K. Forberich, F. Machui, T. Ameri, M. Turbiez, M. Carrasco-Orozco, M. Drees, A. Facchetti, F. C. Krebs and C. J. Brabec, *Energy and Environmental Science*, 6 (2013) 3407–3413.

-
- [195] F. Guo, P. Kubis, N. Li, T. Przybilla, G. Matt, T. Stubhan, T. Ameri, B. Butz, E. Spiecker, K. Forberich and C. J. Brabec, *ACS Nano*, 8 (2014) 12632–12640.
- [196] N. Li, T. Stubhan, D. Baran, J. Min, H. Wang, T. Ameri and C. J. Brabec, *Advanced Energy Materials*, 3 (2013) 301–307.
- [197] R. Meerheim, C. Korner, B. Oesen and K. Leo, *Applied Physics Letters*, 108 (2016) 103302.
- [198] L. C. Hirst and N. J. Ekins-Daukes, *Progress in Photovoltaics*, 19 (2011) 286–293.
- [199] W. Shockley and H. J. Queisser, *Journal of Applied Physics*, 32 (1961) 510-519.
- [200] F. Monestiera, J.-J. Simona, P. Torchioa, L. Escoubasa, F. Flory, S. Bailly, R. de Bettignies, S. Guillerez and C. Defranoux, *Solar Energy Materials and Solar Cells*, 91 (2007) 405–410.
- [201] C. J. Brabec, A. Cravino, D. Meissner, N. S. Sariciftci, M. T. Rispens, L. Sanchez, J. C. Hummelen, and T. Fromherz, *Thin Solid Films*, 368 (2002) 403-404.
- [202] C. J. Brabec, A. Cravino, D. Meissner, N. S. Sariciftci, T. Fromherz, M. T. Rispens, L. Sanchez, and J. C. Hummelen, *Advanced Functional Materials*, 11 (2001) 374-380.
- [203] B. Qi and J. Wang, *Physical Chemistry Chemical Physics*, 15 (2013) 8972-8982.
- [204] C. J. Brabec, *Solar Energy Materials and Solar Cells*, 83 (2004) 273–292.
- [205] P. M. Sommeling, H. C. Rieffe, J. A. M. van Roosmalen, A. Schonecker, J. M. Kroon, J. A. Wienke, A. Hinsch, *Solar Energy Materials and Solar Cells*, 62 (2000) 399–410.
- [206] M. Paradise, T. Goswami, *Materials and Design*, 28 (2007) 1477-1489.
- [207] H.W. Kroto, J.R. Heath, S.C. O'Brien, R.F. Curl, and R.E. Smalley, *Nature*, 318 (1985) 162-163.
- [208] P. Scharff, *Carbon*, 36 (1998) 481–486.
- [209] S. Iijima, *Nature*, 354 (1991) 56-58.
- [210] K. S. Novoselov, A. K. Geim, S. V. Morozov, D. Jiang, Y. Zhang, S. V. Dubonos, I. V. Grigorieva, A. A. Firsov, *Science*, 306 (2004) 666-669.
- [211] K. Awasthi, A. Srivastava, O. N. Srivastava, *Journal of Nanoscience and Nanotechnology*, 5 (2005) 1616-1636.
- [212] E. T. Thostenson, R. Zhifeng, T.-W. Chou, *Composites Science and Technology*, 61 (2001) 1899-1912.
- [213] P. J. F. Harris, *Carbon Nanotubes and Related Structures: New Materials for the Twenty-first Century*, Cambridge University Press, Cambridge, UK, 1999, p. 4.
- [214] C. A. Cooper, R. J. Young, M. Halsall, *Composites: Part A*, 32 (2001) 401-411.
- [215] G. Gao, T. Cagin, W. A. Goddard, *Nanotechnology*, 9 (1998) 184-191.
- [216] T. Uchida, S. J. Kumar, *Journal of Applied Polymer Science*, 98 (2005) 985-989.
- [217] A. De Heer Walt, *MRS Bulletin*, 29 (2004) 281-285.
- [218] S. Berber, Y-K. Kwon, D. Tomanek, *Physical Review Letters*, 84 (2000) 4613-4616.
- [219] Y. T. Ong, A. L. Ahmad, S. H. S. Zein, and S. H. Tan, *Brazilian Journal of Chemical Engineering*, 27 (2010) 227-242.
- [220] X-L. Xie, Y-W. Mai, and X-P. Zhou, *Materials Science and Engineering R*, 49 (2005) 89-112.
- [221] P-C. Ma, N. A. Siddiqui, G. Maron, J-K. Kim, *Composites: Part A*, 41 (2010) 1345-1367.

-
- [222] A. K. Geim and K. S. Novoselov, *Nature Materials*, 6 (2007) 183–191.
- [223] A. Dato et al., (2009), *Chemical Communication*, (2009) 6095–6097.
- [224] A.K. Geim and P. Kim, *Scientific American*, 298 (2008) 90-97.
- [225] M. Segal, *Nature Nanotechnology* 4 (2009) 612–614.
- [226] P. Sutter, *Nature Materials*, 8 (2009) 171-172.
- [227] M. Choucair, P. Thordarson, J.A. Stride, *Nature Nanotechnology*, 4 (2008) 30–33.
- [228] G. Brumfiel, *Nature* 458 (2009) 390-391.
- [229] D. V. Kosynkin, A. L. Higginbotham, A. Sinitskii, J. R. Lomeda, A. Dimiev, B. K. Price and J. M. Tour, *Nature*, 458 (2009) 872-876.
- [230] L. Jiao, L. Zhang, X. Wang, G. Diankov and H. Dai, *Nature*, 458 (2009) 877-880.
- [231] A. Dato, V. Radmilovic, Z. Lee, J. Phillips and M. Frenklach, *Nano Letters*, 8 (2008) 2012-2016.
- [232] Z. Lee, K. J. Jeon, A. Dato, R. Erni, T. J. Richardson, M. Frenklach and V. V. Radmilovic, *Nano Letters*, 9 (2009) 3365-3369.
- [233] D. Kasuya, M. Yudasaka, K. Takahashi, F. Kokai and S. Iijima, *The Journal of Physical Chemistry B*, 106 (2002) 4947-4951.
- [234] A. Eftekhari, and B. Yazdani, *Journal of Polymer Science Part A: Polymer Chemistry*, 48 (2010) 2204-2213.
- [235] K. Saito, J. Nakamura and A. Natori, *Physical Review B*, 76 (2007) 115409.
- [236] *Graphite and Precursors*, P. Delhaes Ed., CRC Press, Amsterdam, Netherlands, 2001.
- [237] S. Goenka, V. Sant, S. Sant, *Journal of Controlled Release*, 173 (2014) 75-88.
- [238] W. E. Gacitua, A. A. Ballerini and J. Zhang, *Cincia y tecnologia*, 7 (2005) 159-178.
- [239] R. A. Vaia and H. D. Wagner, *Materials Today*, 7 (2004) 32-37.
- [240] T. Ramanathan et al., *Nature Nanotechnology*, 3 (2008) 327-331.
- [241] M. Moniruzzaman and K. I. Winey, *Macromolecules*, 39(2006) 5194-5205
- [242] N. G. Sahoo, S. Rana, J. W. Cho, L. Li, S. H. Chan, *Progress in Polymer Science* 35 (2010) 837–867.
- [243] D. Qian, E.C. Dickey, R. Andrews, T. Rantell, *Applied Physics Letters*, 76 (2000) 2868.
- [244] M. J. Biercuk, M. C. Llaguno, M. Radosavljevic, J.K. Hyun, A.T. Johnson, *Applied Physics Letters*, 80 (2002) 2767.
- [245] B. Safadi, R. Andrews, E. A. Grulke, *Journal of Applied Polymer Science*, 84 (2002) 2660–2669.
- [246] M. Cadek, J.N. Coleman, V. Barron, *Applied Physics Letters*, 81 (2002) 5123-5125.
- [247] M. Cadek, J. N. Coleman, K. P. Ryan, V. Nicolosi, G. Bister, A. Fonseca, J. B. Nagy, K. Szostak, F. Beguin and W. J. Blau, *Nano Letters*, 4 (2004) 353–356.
- [248] J. N. Coleman, M. Cadek , R. Blake, K. P. Ryan, C. Belton, A. Fonseca, J. B. Nagy, Y. K. Gunko and W. J. Blau, *Advanced Functional Materials*, 8 (2004) 791–798.
- [249] C. A. Martin, J. K. W. Sandler, M. S. P. Shaffe, M. K. Schwarz, W. Bauhofer, K. Schulte and A. H. Windle, *Composites Science and Technology*, 64 (2004) 2309–2316.
- [250] M. B. Bryning, M. F. Islam, J. M. Kikkawa and A. G. Yodh, *Advanced Materials*, 17 (2005) 1186–1191.
- [251] S. T. Kim, H. J. Choi and S. M. Hong, *Colloid and Polymer Science*, 285 (2007) 593–598.

-
- [252] O. Regev, P. N. B. ElKati, J. Loos and C. E. Koning, *Advanced Materials*, 16 (2004) 248–251.
- [253] G. Wang, Z. K. Tan, X. Q. Liu, S. Chawda, J. S. Ko, V. Samuilov, M. Dudley, *Nanotechnology*, 17 (2006) 5829–5835.
- [254] J. C. Grunlan, A. R. Mehrabi, M. V. Bannion and J. L. Bahr, *Advanced Materials*, 16 (2004) 150–153.
- [255] B. P. Grady, *Polymer Composites: Manufacture, Properties and Applications*, John Wiley & Sons, Inc., Hoboken, USA, 2011, pp. 305-322.
- [256] N. C. Das, Y. Y. Liu, K. K. Yang, W. Q. Peng, S. Maiti and H. Wang, *Polymer Engineering and Science*, 49 (2009) 1627–1634.
- [257] I. Mazov, V. Kuznetsov, S. Moseenkov, A. Usoltseva, A. Romanenko, O. Anikeeva, T. Buryakov, P. Kuzhir, S. Maksimenko, D. Bychanok, J. Macutkevic, D. Seliuta, G. Valusis, J. Banys and P. Lambin, *Physica Status Solidi B*, 246 (2009) 2662–2666.
- [258] S. H. Park, P. Thielemann, P. Asbeck and P. R. Bandaru, *Applied Physics Letters*, 94 (2009) 243111.
- [259] S. M. Yuen, C. C. M. Ma, C. Y. Chuang, K. C. Yu S. Y. Wu, C. C. Yang and M. H. Wei, *Composites Science and Technology*, 68 (2008) 963–968.
- [260] L. L. Wang, B. K. Tay, K. Y. See, Z. Sun, L. K. Tan and D. Lua, *Carbon*, 47 (2009) 1905–1910.
- [261] S. Mall, B. L. Ouper, and J. C. Fielding, *Journal of Composite Materials*, 43 (2009) 2987–3001.
- [262] E. C. W. Ou L. B. Hu, G. C. R. Raymond, O. K. Soo, J. S. Pan, Z. Zheng, Y. Park, D. Hecht, G. Irvin, P. Drzaic and G. Gruner, *ACS Nano*, 3 (2009) 2258–2264.
- [263] G. F. Wang, X. M. Tao and R. X. Wang, *Composites Science and Technology*, 68 (2008) 2837–2841.
- [264] S. Ren, M. Bernardi, R. R. Lunt, V. Bulovic, J. C. Grossman and S. Gradecak, *Nano Letters*, 11 (2011) 5316–5321.
- [265] A. T. Mallajosyula, S. Kumar, S. Iyer and B. Mazhari, *Journal of Applied Physics*, 109 (2011) 124908–124910.
- [266] M. M. Stylianakis, J. A. Mikroyannidis and F. Kymakis, *Solar Energy Materials and Solar Cells*, 94 (2010) 267–274.
- [267] J. M. Lee, J. S. Park, S. H. Lee, H. Kim, S. Yoo and S. O. Kim, *Advanced Materials*, 23 (2011) 629–633.
- [268] S. N. Habisreutinger, T. Leijtens, G. E. Eperon, S. D. Stranks, R. J. Nicholas and H. J. Snaith, *Nano Letters*, 14 (2014) 5561–5568.
- [269] V. Khomenko, E. Frackowiak and F. Beguin, *Electrochimica Acta*, 50 (2005) 2499–506.
- [270] E. Frackowiak, K. Jurewicz, S. Delpeux and F. Beguin, *Journal of Power Sources*, 97-98 (2001) 822–825.
- [271] J. Chen, Y. Liu, A. I. Minett, C. Lynam, J. Wang and G. G. Wallace, *Chemistry of Materials*, 19 (2007) 3595-3597.
- [272] M. L. Auad, M. A. Mosiewicki, C. Uzunpinar, R. J. J. Williams, *Composites Science and Technology*, 69 (2009) 1088–1092.
- [273] P. M. Ajayan, J. Suhr and N. Koratkar, *Journal of Materials Science*, 41 (2006) 7824–7829.
- [274] I. Dinca, C. Ban, A. Stefan, G. Pelin, *INCAS Bulletin*, 4 (2012) 73-83.

-
- [275] P-C. Ma and Y. Zhang, *Renewable and Sustainable Energy Reviews*, 30 (2014) 651–660.
- [276] S. Cosnier, R. E. Ionescu and M. Holzinger, *Journal of Materials Chemistry*, 18 (2008) 5129–5133.
- [277] G. Cheng, J. Zhao, Y. Tu, P. He and Y. Fang, *Analytica Chimica Acta*, 533 (2005) 11–16.
- [278] K. Rege, N. R. Raravikar, D. Y. Kim, L. S. Schadler, P. M. Ajayan and J. S. Dordick, *Nano Letters*, 3(2003) 829–832.
- [279] R. Singh, D. Pantarotto, D. McCarthy, O. Chaloin, J. Hoebeke, C. D. Partidos, J. P. Briand, M. Prato, A. Bianco and K. Kostarelos, *Journal of Americal Chemical Society*, 127 (2005) 4388–4396.
- [280] D. A. X. Nayagam, R. A. Williams, J. Chen, K. A. Magee, J. Irwin, J. Tan, P. Innis, R. T. Leung, S. Finch, C. E. Williams, G. M. Clark and G. G. Wallace, *Small*, 7 (2011) 1035-1042.
- [281] M.O. Ansari, S.P. Ansari, S.K. Yadav, T. Anwer, M.H. Cho, F. Mohammad, *Journal of Industrial and Engineering Chemistry*, 20 (2013) 2010–2017.
- [282] N. Van Hieu, N. Q. Dung, P. D. Tam, T. Trung and N. D. Chien, *Sensors and Actuators B: Chemical*, 140 (2009) 500–507.
- [283] L. F. He, Y. Jia, F. L. Meng, M. Q. Li and J. H. Liu, *Materials Science and Engineering: B*, 163 (2009) 76–81.
- [284] S. Sattari, A. Reyhani, M. R. Khanlari, M. Khabazian, H. J. Heydari, *Journal of Industrial and Engineering Chemistry*, 20 (2013) 1761–1764.
- [285] Y. Wanna, N. Srisukhumbowornchai, A. Tuantranont, A. Wisitsoraat, N. Thavarungkul and P. Singjai, *Journal of Nanoscience and Nanotechnology*, 6 (2008) 3893–3896.
- [286] P. G. Su, C. T. Lee, C. Y. Chou, K. H. Cheng and Y. S. Chuang, *Sensors and Actuators B: Chemical*, 139 (2009) 488–493.
- [287] K. Hu, D. D. Kulkarni, I. Choi and V. V. Tsukruk, *Progress in Polymer Science*, 39 (2014) 1934–1972
- [288] B. Kim, J. Kim, S. Jeong, J. Hwang, D. Lee, D. Shin, S. Choi and S. Kim, *ACS Nano*, 4 (2010) 5464–5470.
- [289] S. Niyogi, E. Bekyarova, M. E. Itkis, J. L. McWilliams, M. A. Hamon and R. C. Haddon, *Journal of Americal Chemical Society*, 128 (2006) 7720-7721.
- [290] V. Singh, D. Joung, L. Zhai, S. Das, S. I. Khondaker and S. Seal, *Progress in Materials Science*, 56 (2011) 1178–1271.
- [291] A. Yasmin, J. J. Luo and I. M. Daniel, *Composites Science and Technology*, 66 (2006) 1182–1189.
- [292] Y. Li, R. Umer, Y. A. Samad, L. Zheng and K. Liao, *Carbon*, 55 (2013) 321–327.
- [293] V. Mittal, *Macromol. Materials Science and Engineering*, 299 (2014) 906–931.
- [294] J. Liang, Y. Huang, L. Zhang, Y. Wang, Y. Ma, T. Guo, Y. Chen, *Advanced Functional Materials*, 19 (2009) 2297-2302.
- [295] G. Broza, K. Piszczek, K. Schulte, T. Sterzynski, *Composites Science and Technology*, 67 (2007) 890-894.
- [296] M. C. Wang, C. Yan and L. Ma, In *Composites and their properties*, H. Ning Ed., InTech, Rijeka, Croatia, 2012, p. 502.
- [297] J. Li, S. Guo, Y. Zhai and E. Wang, *Analytica Chimica Acta*, 649 (2009) 196–201.

-
- [298] H. Bai, K. Sheng, P. Zhang, C. Li and G. Shi, *Journal of Materials Chemistry*, 21 (2011) 18653–18658.
- [299] J. D. Qiu, L. Shi, R. P. Liang, G. C. Wang, X. H. Xia, *Chemistry: A European Journal*, 18 (2012) 7950–7959.
- [300] Y. Zeng, Y. Zhou, L. Kong, T. Zhou and G. Shi, *Biosensors and Bioelectronics*, 45 (2013) 25–33.
- [301] S. Kim, W. K. Oh, Y. S. Jeong and J. Jang, *Advanced Functional Materials*, 23 (2013) 1947–1956.
- [302] L. Wang, K. Y. Pu, J. Li, X. Qi, H. Li, H. Zhang, C. Fan and B. Liu, *Advanced Materials*, 23 (2011) 4386–4391.
- [303] Y. H. Yang, L. Bolling, M. A. Priolo and J. C. Grunlan, *Advanced Materials*, 25 (2013) 503–508.
- [304] I. H. Tseng, Y. F. Liao, J. C. Chiang and M. H. Tsai, *Materials Chemistry and Physics*, 136 (2012) 247–253.
- [305] J. Wang, Z. Ouyang, J. Li, P. Zhang, G. Wei and Z. Su, *Carbon*, 89 (2015) 20–39.
- [306] S. Ahadian, M. Estili, V. Surya, J. Ramón-Azcón, X. Liang, H. Shiku, M. Ramalingam, T. Matsue, Y. Sakka, H. Bae, K. Nakajima, Y. Kawazoe and A. Khademhosseini, *Nanoscale*, 7 (2015) 6436–6443.
- [307] H. Wang, D. Sun, N. Zhao, X. Yang, Y. Shi, J. Li, Z. Su and G. Wei, *Journal of Materials Chemistry B*, 2 (2014) 1362–1370.
- [308] M. Xue, F. Li, J. Zhu, H. Song, M. Zhang and T. Cao, *Advanced Functional Materials*, 22 (2012) 1284–1290.
- [309] S. S. Li, K. H. Tu, C. C. Lin, C. W. Chen and M. Chhowalla, *ACS Nano*, 4 (2010) 3169–3174.
- [310] V. C. Tung, J. Kim and J. Huang, *Advanced Energy Materials*, 2 (2012) 299–303.
- [311] J. Ling, W. Zhai, W. Feng, B. Shen, J. Zhang and W. Zheng, *ACS Applied Materials & Interfaces*, 5 (2013) 2677–2684.
- [312] R. Chen, J. Yan, Y. Liu and J. Li, *Journal of Physical Chemistry C*, 119 (2015) 8032–8037.
- [313] L. M. Hallensleben, In *Ullmann's Encyclopedia of Industrial Chemistry*, Wiley-VCH Verlag, Weinheim, Germany, 2000, pp. 612–614.
- [314] <http://www.kuraray.eu/en/produkte/product-groups/polyvinyl-butyrals/>
- [315] J. Yin, H. Zhu, Y. Wang, Z. Wang, J. Gao, Y. Mai, Y. Ma, M. Wan and Y. Huang, *Applied Surface Science*, 259 (2012) 758–763.
- [316] <http://www.trosifol.de/en/produkte/photovoltaics/>
- [317] A. Bonucci, S. Rondena, A. Gallitognotta, P. Gallina, O. Salomon, W. Wischmann and S. Hiss, *Solar Energy Materials and Solar Cells*, 98 (2012) 398–403.
- [318] J. Ahmad, K. Bazaka, L. J. Anderson, R. D. White, M. V. Jacob, *Renewable and Sustainable Energy Reviews*, 27 (2013) 104–117.
- [319] N. J. Joshi, P. B. Rakshit, G. S. Grewal, V. Shrinet, A. Pratap, *AIP Conference Proceedings*, 1536 (2013) 691–692.
- [320] K. I. Arshak, L. M. Cavanagh, C. Cunniffe, *Thin Solid Films*, 495 (2006) 97–103.
- [321] C. H. Cho, M. S. Cho, J. H. Sung, H. J. Choi, *Journal of Material Science*, 39 (2004) 3151–3153.
- [322] D. Pistek, D. Merinska, Z. Dujkova and M. Tupy, *3rd WSEAS Conference Proceedings*, 3 (2010) 26–29.
- [323] S. A. Ben Hassan, D. B. Stojanovic, A. Kojovic, I. Jankovic-Castvan, D.

-
- Janackovic, P. S. Uskokovic, R. Aleksic, *Ceramics International* 40 (2014) 1139–1146.
- [324] I. Maksimenko and P. J. Wellmann, *Thin Solid Films*, 520 (2011) 1341–1347.
- [325] K. Nakane, T. Kurita, T. Ogihara and N. Ogata, *Composites: Part B*, 35 (2004) 219–222.
- [326] M. Torki, I. Zivkovic, V. R. Radmilovic, D. B. Stojanovic, V. J. Radojevic, P. S. Uskokovic, R. R. Aleksic, *International Journal of Modern Physics B*, 24 (2010) 805–812.
- [327] A. S. Roy, S. Gupta, S. Seethamraju, G. Madras and P. C Ramamurthy, *Composites: Part B*, 58 (2014) 134–139.
- [328] S. Saravanan, S. Gupta, P. C. Ramamurthy and G. Madras, *Polymer Composites*, 35 (2014) 1426–1435.
- [329] J- X. Wang, Q. Sun, B. Chen, X. Wu, X-F. Zeng, C. Zhang, H. – K. Zou and J-F. Chen, *Nanotechnology*, 26 (2015) 195602.
- [330] X-F. ZZeng, X. Li, X. Tao, Z-G. Shen and J-F. Chen, *INEC Conference Proceedings* (2010) 777-778.

3. Experimental

3.1. Synthesis and Processing Methods

Spin Coating

Spin coating is a method of film deposition in which a liquid (solution or suspension) is applied to a substrate, usually by drop casting, which is then subjected to rotation of a certain speed. Alternatively, the substrate can already be in motion while the liquid is being drop cast. With centripetal acceleration, most of the liquid is ejected off the substrate, but the remaining liquid, once the solvent has evaporated, forms a thin film. During film rotation simultaneous processes are occurring: evaporation of solvent, changes in viscosity, radial flow of the solution, shear thinning, molecular organization at different interfaces, diffusion of molecules and changes in molecular orientation as a result of the shear field, formation of aggregates, etc. Although parameters directly set by the experimentalist like amount of deposited liquid (ink), rate of deposition and spinning time seem efficacious, they have very little impact on the thickness, morphology and surface topography of processed film. The parameters that are influential include rotational speed, viscosity, volatility, diffusivity, molecular weight and concentration of the liquid deposited. Acquired film thickness, d , is dependent on the angular velocity ω during rotation and empirical constants related to properties of the liquid k , α :

$$d = k\omega^\alpha$$

This method is frequently used in polymer film processing, because of its ability to achieve uniform layers on planar substrates in a very reproducible way, although subtle variations of defining parameters can result in drastic variations of film morphology. The main drawback of this method is its difficulty in scaling to large area samples.

Working procedure is shown schematically in Figure 3.1. The substrate is mounted onto a chuck where vacuum is formed, keeping the substrate stable. The liquid

is drop cast onto the substrate which can be still, or spinning at small RPM (rounds per minute). With spin acceleration the liquid is uniformly dispersed on the substrate while the excess liquid is ejected off. With time, the solvent evaporates forming the desired film [1,2].

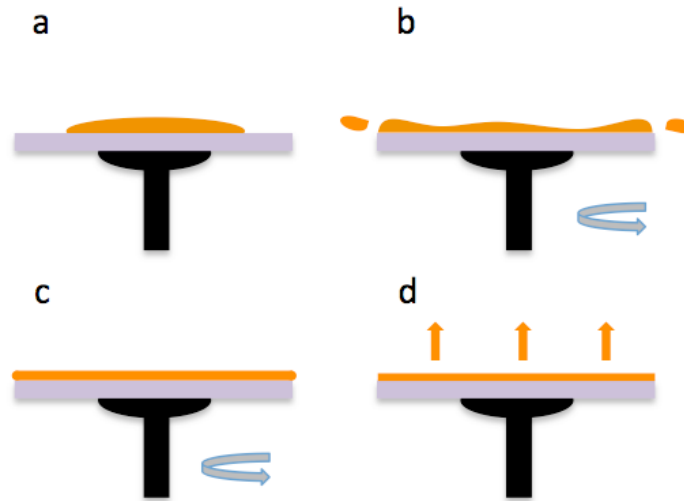


Figure 3.1. Working procedure of spin coating films: a) The ink is drop cast onto substrate, b) elimination of excess material during rotation, c) even ink distribution during rotation, d) solvent evaporation; Grey arrows represent motion of spinning while orange arrows represent evaporation of solvent; After [3].

Doctor Blading

Doctor blading, also called knife or blade coating, is a technique for processing films with a large-scale area on substrates, flexible or non-flexible. It is a very practical method since only ~5% of coating ink (solution or suspension) is lost (as excess). The process consists of positioning a sharp blade at a known and fixed distance from the substrate (Figure 3.2). The ink is placed in front of the blade, which is linearly moved across the substrate. As the blade is moved, a thin wet film is left behind. Adjusting gap width between blade and substrate allows for a variety of film thicknesses to be achieved. In theory, wet layer thickness corresponds to half the height of blade edge (mentioned width gap). However, practically, because of factors like surface energy of the substrate, surface tension and viscosity of ink, as well as shear stress (proportional to speed of deposition, related to meniscus between blade and ink) experimental wet layer thickness does not match theoretical assumption. From the following formula it

can be seen that final thickness of film, d , is proportional to height of blade edge g , concentration of coating liquid (ink) c and density of final deposited film, ρ [1,2].

$$d = \frac{1}{2} g \frac{c}{\rho}$$

The advantage of this method is its ability to rapidly produce multi-layered structures at elevated temperatures. Compared to photovoltaic cells processed by doctor blading, spin coated cells possibly have greater control of layer thickness optimization which yields higher current, although, since only room temperature processing is attainable, poorer fill factors are observed [4].

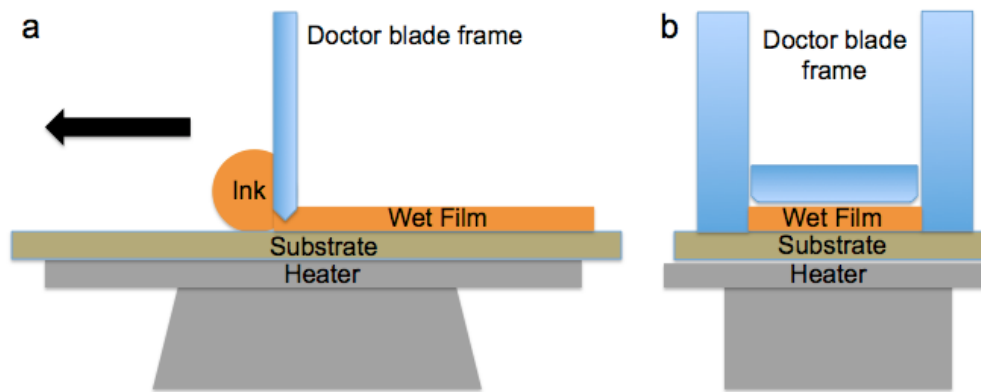


Figure 3.2. Doctor blading setup, a) Side view, b) Frontal view; The arrow indicates direction of blade movement; Width of film is dependent on the width of blade frame.

Electrodeposition

Electrodeposition (electroplating) is a process in which a material, through electrolysis, is deposited on a conducting surface (electrode) from an electrolyte, an ionic conductor containing species of interest of being deposited. This electrolyte can be a molten salt, an aqueous or non-aqueous solution. Typical set-up for this process, shown in Figure 3.3, is comprised of three electrodes: working electrode (where the material is deposited, the cathode), reference electrode and counter electrode (completes the electronic circuit, the anode) all located within the solution containing ions. These electrodes are connected to a potentiostat, which controls the process by keeping the potential of the working electrode constant with respect to the reference electrode.

When an electric field is applied to the working electrode, electrons in the counter electrode are given away to the ions in the electrolyte. This leads to the formation of neutral species that adhere to the working electrode:



Flow of the current occurs between the working and counter electrodes but the potential (electric field strength) is measured versus the reference electrode [5,6,7,8,9].

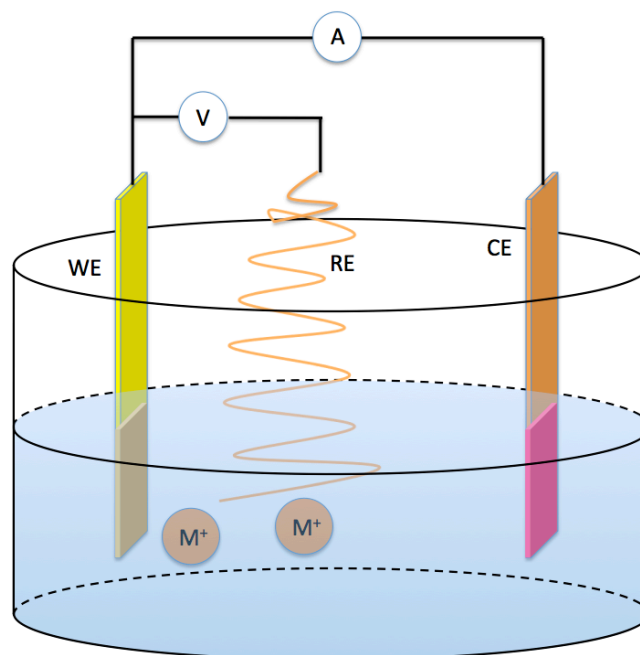


Figure 3.3. Schematic of electrodeposition set-up consisting of three electrodes: working electrode (WE), reference electrode (RE) and counter electrode (CE) immersed in metal ion (M^+) containing electrolyte; Flow of current (A) and potential (V) are marked in the schematic.

Atomic Layer Deposition

Atomic layer deposition (ALD) is a vapor-based method of processing but exhibits major differences compared to well known methods like the chemical vapor deposition (CVD). Unlike CVD, where chemical reactants or “precursors” (at least two) react simultaneously on the surface or gas phase and can decompose, in ALD precursors

react separately without decomposition i.e. react only with the surface and not with each other. This is why this process is called “self-limiting”. The precursors adsorb and desorb from the surface where the reaction occurs and subsequently react with other unreacted surfaces to produce uniform films. Temperature (if within the “temperature window”) and flow uniformity do not greatly influence the quality of deposited film and the thickness is controlled by the number of deposition cycles, not by the exposure time [10]. The deposition cycle consists of 4 steps, presented by a schematic in Figure 3.4:

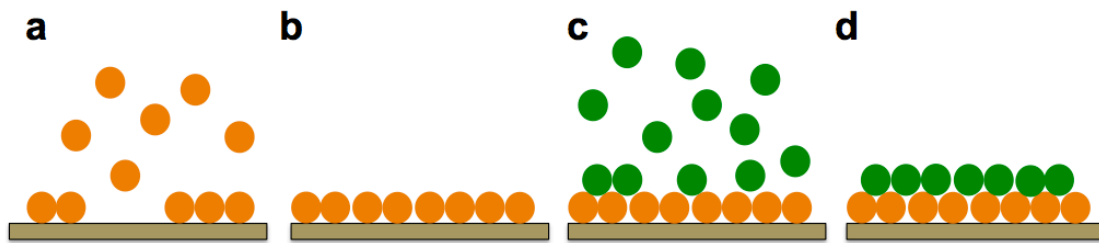


Figure 3.4. Atomic layer deposition cycle consisting of 4 steps: a) pulse of organometallic precursor, b) chamber purging, c) pulse of second precursor, d) chamber purging.

- 1) Exposure of substrate surface to the pulse of organometallic precursor in vapor phase in chamber; Precursor molecules react and are adsorbed as a monolayer onto the exposed surface (surface sites are occupied and the surface is fully saturated);
- 2) Purging of chamber with inert gas for removal of remaining gas-phase precursor (preventing gas-phase reactions with next precursor);
- 3) Exposure to the pulse of second precursor (in case of oxides – the oxide source) being pulsed in vapor phase, reacting with the surface, creating desired material;
- 4) Purging step, which removes any by-products of gaseous reaction.

These growth steps, as part of one cycle, are repeated until film of desired thickness is achieved [11,12,13,14].

Advantages of this technique include: high surface conformality and uniformity of deposited films, reproducibility and production ultra-thin films due to the self-limiting nature of method, production of ultra-thin films due to precise control at the angstrom/monolayer level achieved through self-limiting growth.

Thermal Vacuum Evaporation

Thermal evaporation is a physical vapor deposition (PVD) method used for fabricating thin metallic films. Unlike sputtering (also a PVD technique), which uses plasma for vaporizing the source material, thermal evaporation uses high temperature heat. This method consists of a collective group of following processes [15]:

- Evaporation of material from a solid source (material subjected to high temperature vacuum);
- Transportation of the vapor in (partial) vacuum to the substrate surface;
- Condensation of material onto the substrate (and walls of chamber) forming a thin film; Nominal thickness of film can be determined by knowing specific parameters of the evaporated material (density and Z-ratio) and by in situ measurement using a deposition monitor, placed next to the substrate.

Thermal evaporation, and PVD in general, is used in a variety of optoelectronic applications, mostly for electrode fabrication where conductivity and uniformity of film are of greater importance than optical transmission.

3.2. Characterization Methods

3.2.1. UV-VIS Spectroscopy

Ultraviolet – visible spectrophotometry, or UV-Vis spectroscopy for short, is a spectrophotometric method for measuring absorption/reflection in the ultraviolet and visible wavelength range of electromagnetic spectrum of light. Simply put, using this technique, one can measure the amount of light (usually a generated beam of radiation) a material can absorb/reflect with respect to the amount of incident light reaching that material i.e. with interaction of molecules from the material with solar radiation, absorption is given as intensity as function of wavelength [16,17,18]. The Beer-Lambert law gives the dependence of light absorption on the properties of material interacting with the radiation:

$$A = \log_{10} \left(\frac{I_0}{I} \right) = \epsilon c L$$

where I_0 is the incident intensity of light, I the transmitted intensity of light, ϵ the molar absorptivity of the species (extinction coefficient), c is the concentration of the species while L is the path length. With the formula:

$$T(\%) = 100 * 10^{-A}$$

absorbance (A) can be converted to transmittance (T), preferred property of evaluation in optoelectronics characterization.

3.2.2. Raman Spectroscopy

Raman spectroscopy can be a useful technique in acquiring structural, vibrational and electronic information about a material. It is based on the Raman effect - as the light passes through a molecule, most of it is scattered at the same frequency as the incident light (elastic Rayleigh scattering) but some of it can interact with the molecule, thereby gaining or emitting energy (inelastic Raman scattering). If photons from light excite the molecule to a higher state (scattered with a longer wavelength) this is called the Stokes shift or Stokes Raman scattering. If it is to a lower state (scattered with a shorter wavelength) it is called the anti-Stokes shift or anti-Stokes Raman scattering. The Raman spectrum of a molecule (sample) is the record of wavelength shifts [19,20,21].

Raman Spectrum of Carbon Nanotubes and Graphene

A typical Raman spectrum of carbonaceous materials like carbon nanotubes (CNTs) and graphene consists of 4 characteristic bands: radial breathing modes (RBM), G-band, D-band and the G'-band (or the 2D band), which reveal most of the information about the sample although several other, weaker, bands have also been observed in these structures [21].

Radial breathing modes (RBM) are lower energy modes occurring only in SWCNT and DWCNT Raman spectra. They originate from coherent vibration where atoms move radially in phase, perpendicular to the CNT axis, as if the tube is breathing, which is why these modes are not found in MWCNTs, as the inner tubes are constricted by outer tubes, especially at larger diameters.

The D band is the defect band as it is a disorder-induced part of the spectrum. It originates from the double resonance Raman scattering process. The D-band scattering consists of two processes, one-elastic and one-inelastic where the elastic scattering arises from crystal defects (such as vacancies, impurities and hetero-atoms). This is an energy dispersive band meaning that the frequency peak depends on the energy of laser excitation, as well as on the CNT diameter and chiral angle.

The G' (or 2D) band is a second order overtone of the D band. It originates from a two-phonon process (unlike one phonon emission for D band) - elastic scattering from the D band is changed to an inelastic phonon emission process. This is also an energy dispersive band.

The G band, a first-order Raman band, originates from the vibrations of neighboring carbon atoms in opposite directions along axis and circumference of the CNT, with features around 1580 cm^{-1} in the Raman spectrum, for sp^2 carbonaceous materials. It is comprised of two components (peaks), originating from carbon displacements parallel and perpendicular to the tube axis, a higher energy component (G^+) and a lower energy component (G^-), respectively [22].

3.2.3. Mechanical Characterization by Nanoindentation

Thin film mechanical characterization using nanoindentation usually has the goal of collecting data of material properties like elastic modulus and hardness. Mechanical parameters such as scratch, creep and residual stress can also be elucidated by this method. This technique is based on puncturing or indenting the film with an indenter tip. Analyzing applied load of indenter versus depth of indentation (displacement), gives insight into response of the sample to mechanical stress i.e. its mechanical properties. More specifically, displacement for a given load depends on the magnitude of the load as well as on the nature of the material.

The term nanoindentation simply refers that the scale of penetration depth is measured in nanometers and has proven to be the most accurate method for evaluation the effects of nanofillers on the mechanical properties and deformation behavior of nanocomposites [23].

The Berkovich indenter tip, used in this thesis, has a three-sided pyramid geometry, ensuring relative control over the process. Projected area of indentation for this indenter can be derived using simple schematics of the Berkovich indenter tip shown in Figure 3.5 and the accompanying formulas [24]:

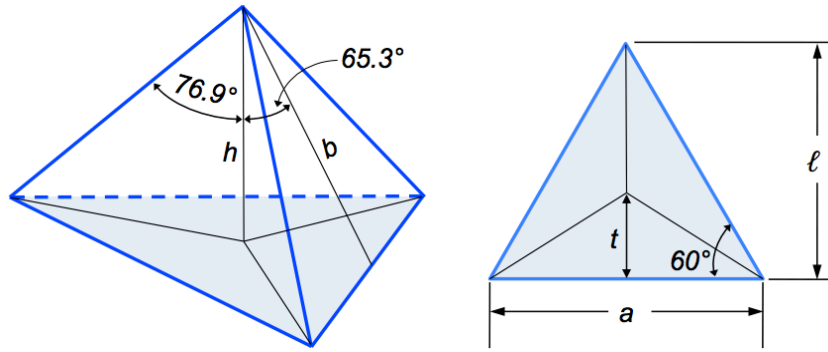


Figure 3.5. Schematic presentation of the Berkovich indenter tip.

$$\tan 60^\circ = \frac{\ell}{a/2}$$

$$\ell = \frac{\sqrt{3}}{2}a$$

$$A = \frac{a\ell}{2} = \frac{\sqrt{3}}{4}a^2$$

$$\cos 65.27^\circ = \frac{h_c}{b}$$

$$h_c = \frac{a \cdot \cos 65.3^\circ}{2\sqrt{3} \cdot \sin 65.3^\circ} = \frac{a}{2\sqrt{3} \cdot \tan 65.3^\circ}$$

$$A = 3\sqrt{3}h_c^2 \tan^2 65.3^\circ$$

where h_c is the depth of penetration and $\theta = 65.3^\circ$ is the semi-angle, which is roughly evaluated for the contact area to:

$$A = 24.5h_c^2$$

Oliver and Pharr [25,26] devised a method, based on the extrapolation of tangents on the unload curves, for calculating indentation depth, at maximum load. This is based on elastic and plastic deformation. Contact stiffness is also acquired giving the Young's elastic modulus of the material, which is actually reduced, as a function of properties of the indenter as well as the sample material.

$$\frac{1}{E_r} = \frac{1 - \nu_{sample}^2}{E_{sample}} + \frac{1 - \nu_i^2}{E_i}$$

or simplified:

$$E_{sample} = \frac{E_r}{0.91}$$

$$E_r = \frac{\sqrt{\pi}}{2C\sqrt{A}} = \frac{\sqrt{\pi} S}{2C\sqrt{A}}$$

where E_r is the reduced modulus, E_{sample} elastic modulus of sample, ν Poisson's coefficient of sample, ν_i and E_i are Poisson's coefficient ($\nu_i = 0.07$), and elastic modulus of indenter ($E_i = 1140$ GPa), respectively, while C is the compliance of the contact, and is equal to dh/dP , and S is the contact stiffness, measured from the slope of the upper part of unload curve at maximum load [27]. For indentation with Berkovich tip, Hardness (mean contact pressure) is:

$$H = \frac{P_{max}}{A} = \frac{P_{max}}{24.5h_c^2}$$

Typical nanoindentation curve is shown in Figure 3.6. Depending on the nature of the material, the loading scheme can be adjusted. For example, some materials exhibit elasto-plastic behavior, and loading/unloading cycle is sufficient to evaluate their mechanical response. However, for materials exhibiting viscous flow during deformation, it is important to introduce an additional experimental parameter - holding time, to evaluate possible creep behavior, as a time-dependent variable. Other

geometrical parameters shown in Figures 3.6 and 3.7 are: h_r final indentation depth, which represents plastic deformation after indenter withdrawal, h_{max} maximum displacement, h_e elastic indentation depth and dP/dh slope which corresponds to the contact stiffness.

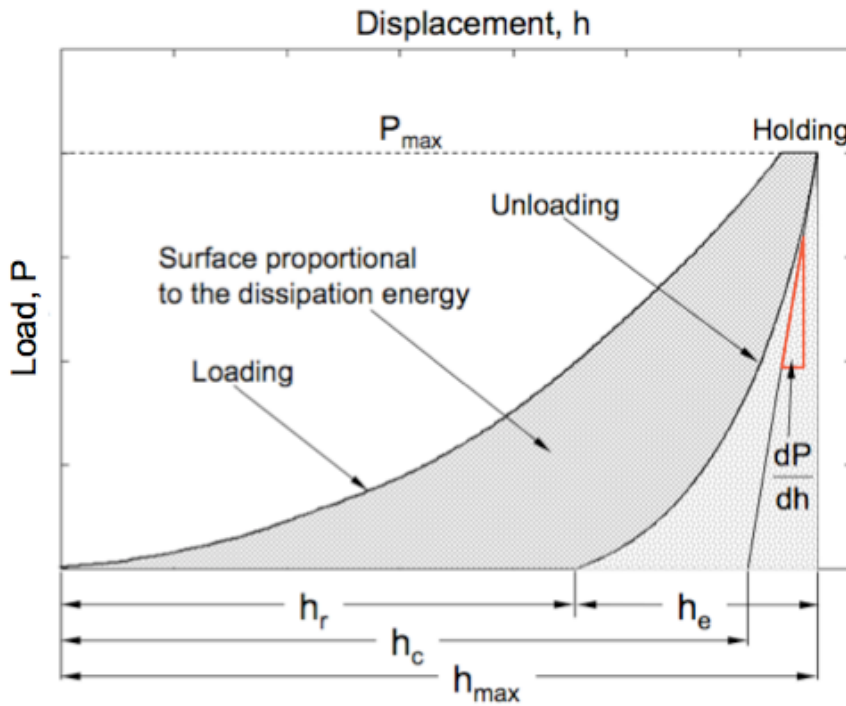


Figure 3.6. Typical loading-unloading curve, shown as load versus displacement (depth).

Schematic showing indenter-sample contact geometry during loading - unloading cycle is given in Figure 3.7.

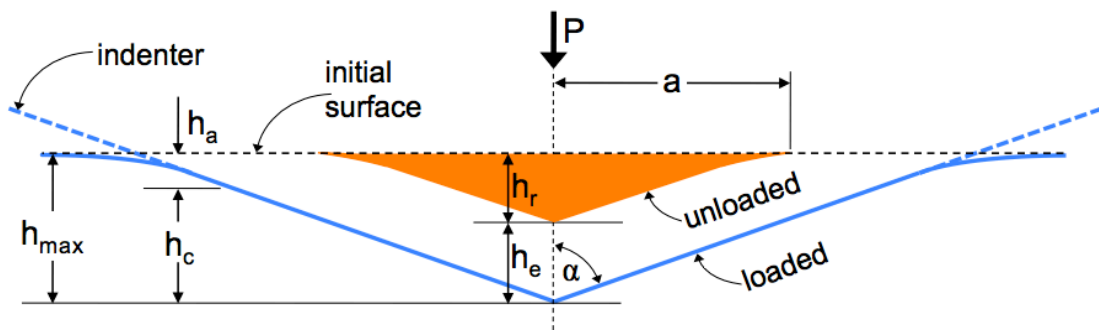


Figure 3.7. Schematic presentation of the loading - unloading cycle geometric parameters characterizing the indenter - sample contact; After [25].

3.2.4. Structural Characterization

Electron microscopy is a very important experimental technique in materials engineering for fine scale microstructural characterization. While scanning electron microscopy (SEM) is based on scattered electrons and it focuses on the surface morphology of sample providing a three-dimensional micrograph (image), transmission electron microscopy (TEM) is based on transmitted electrons and gives insight on the internal composition of the sample providing a two-dimensional micrograph (image) with a much higher resolution than SEM.

3.2.4.1. Scanning Electron Microscopy

Scanning electron microscope is a microscope which can produce an electron beam which scans the surface of interest of the sample. Besides the vacuum system, basic components of the SEM, located in the electron column are: the electron gun (source of electrons), electromagnetic lenses, scanning coils, apertures which control beam width, detectors and a control console comprised of a monitor and control electronics [28,29,30]. Electrons, which are created in the electron gun and continue down the microscope column towards the sample, make up the electron beam. The current of the beam (flux of electrons) can be manipulated with electrostatic lenses and apertures, by changing size, current, convergence, etc. Since electrons are charge carriers, their path can be altered with an electromagnetic field. The purpose of the condenser lens is to control the size of the electron beam i.e. the spot size, which is one of the most important functions in the SEM. Their function resembles the one of glass lenses in the microscope with visible light, since their working principles are similar: condenser lens (CL) condenses electrons, objective lens (OL) focuses the electrons on the sample and the projector lens (PL) projects the image onto the screen. One of the basic characteristics of images produced by SEM is three-dimensionality, which is the result of large depth of the field of vision. Understanding the physics of processes inside the SEM allows for optimal use of this method on a given sample.

Image Forming in the SEM

When the electron beam collides with the sample, scattering of electrons occurs in the bulk, which is called the interaction volume or excitation volume. As a result of this interaction, besides X-rays, heat and visible light, two types of electrons are created, shown in Figure 3.8:

- *Inelastically scattered secondary electrons (SE)*, which derive from inelastic collisions of high energy electrons from the incident beam and conductive electrons from metals or valence electrons in dielectrics or semiconductors. They possess the energy of 50 eV because only a small part of the kinetic energy of primary electrons can be transferred to secondary electrons.
- *Elastically backscattered electrons (BSE)*, formed by elastic interaction of electrons of the primary beam with the nuclei of atoms of investigated sample where their energy remains intact (or changes by < 1 eV). Since their mass remains intact, their direction or speed vector has to change. The angle of scattering can be between 0 and 180° , but is usually $\sim 5^\circ$. This scattering is basically Rutherford scattering. If these electrons leave the sample with scattering, they are known as BSE.

Formation of images of sample surface mostly depends on creating inelastically scattered secondary electrons which have low energy and, if created deeper inside the interaction volume, are absorbed. Only SE from the surface layer (few nanometers thick) can leave the sample [28]. Because BSE (at an angle less than 90° with respect to the incident beam whose energy is usually < 30 kV) have much higher energy, they can leave the sample from a greater depth than the SE.

Surface geometry of the investigated sample greatly influences the amount of created SE, hence different parts of the sample will produce different image contrast. Secondary electrons produced in cavities on the sample surface will be tough to detect by the SE detector, which will result in dark areas on the SEM micrographs. The resulting image is a map of intensity distribution of captured signal by the detector, which is emitted from the scanned surface of the sample.

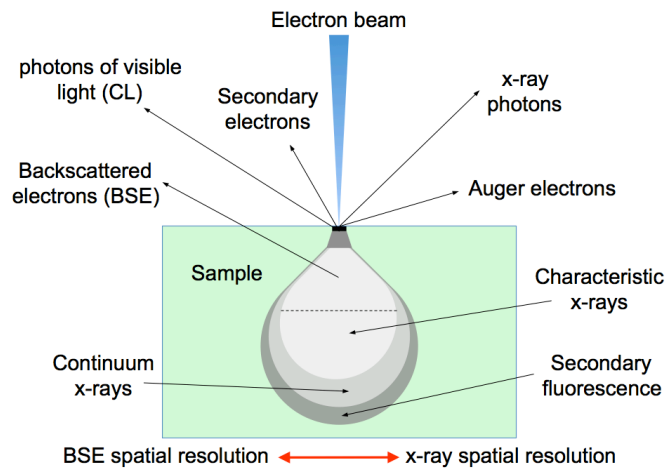


Figure 3.8. Interaction volume between the electron beam and the sample. Note that the BSE can leave the sample from a greater depth than the SE.

Factors which highly influence the resolution i.e. the quality of the SEM image are as follows [28]:

- *Condenser lens current*, which alters the diameter of the electron beam used to scan the sample; Greater current in the condenser lens will produce a smaller beam i.e. a larger resolution of the image.
- *Electron beam current* influences the quantity of SE produced; Greater condenser lens current (larger resolution) is accompanied by the decrease of size (diameter) and with it, the current of the electron beam; Smaller current produces less SE which leads to a higher quality of the image.
- *Astigmatism*, which occurs when the shape of the electron beam is not circular, but elliptical, which is accompanied by resolution decrease and poorer image quality.
- *Working distance of sample*, the distance of last lens from the sample, which influences the spherical aberration because of the electromagnetic lens geometry; With the decrease in working distance, spherical aberration decreases, leading to higher resolution of image.
- *Depth of field*, a parameter which is influenced by the working distance of the sample. As the working distance decreases, scanning of the sample surface will have to be performed at a greater convergence of the electron beam, decreasing

the depth of field. With low roughness (flat) surfaces, the depth of field is less critical, so it is useful to shorten the working distance because it leads to higher resolution.

- *Working voltage*, the voltage applied in the electron gun and in combination with low current allows electrons to leave the filament; In SEM it is usually less than 40 kV, in modern ones (with corrected aberrations) the bottom limit of the working voltage is around 0.5 kV. However, with the reduction of the working voltage, the energy of electrons is reduced i.e. their ability to penetrate the investigated sample. This means that the interaction volume decreases (amount of SE produced) and with it the signal-to-noise ratio i.e. the quality of the image is reduced.
- *Type of sample*. Higher working voltage conditions increase the interaction volume, which is more pronounced in samples with a smaller atomic number (Z). This conditions lower resolution, which depends on the area in which SE are produced and detected and is defined by the size of the electron beam. In that case, SE will be produced outside the area defined by the beam size, which lowers resolution. Higher working voltage also conditions higher SE production from all areas of the sample which lowers the so called *edge effect*, thereby lowering contrast. Lower density of sample, for constant working voltage and atomic number, increases the interaction volume.
- *Conductivity of sample (charge accumulation)*. For SEM investigations, samples should be conductive. If the sample is non-conductive, accumulation of negative charge occurs (from the electron beam) which influences the quality of the image i.e. it distorts it. In the case of biological or ceramic materials, which are non-conductive, a thin layer of metallic material has to be deposited in order for the sample to be conductive. For this application, usually gold, alloys of gold and paladium and osmium are used [31] as well as iridium, tungsten, chromium or graphite (carbon). In modern SEM instruments, which operate at low pressures, negative charge accumulation does not present a problem [32].
- *Depth of field and Focal depth*. Depth of field is a range of distances parallel to the optical axis in which the sample can move without losing the sharpness of the image. It depends on the resolution of the microscope:

$$D = \frac{d}{\beta}$$

where D is the distance between the sample and the top of the objective lens, d is the working distance and β is half angle of the aperture. Focal depth is the distance around the plane of the image in which the image has sharpness. It depends on the second power of magnification (M):

$$D = \frac{d}{\beta} M^2$$

Electron- Backscattered Diffraction (EBSD) based Orientation Imaging Microscopy (OIM)

Orientation imaging microscopy (OIM) technique uses diffraction patterns of electron backscatter diffraction (EBSD), also known as backscatter Kikuchi diffraction (BKD) for measuring crystallographic orientation. As the electron beam scans the crystalline sample, the diffracted electrons form a pattern on a fluorescent screen (grid), characteristic for each crystal structure and orientation of a region in the sample. Thus, produced data represents the scanned area of the sample and in can be used to reconstruct the microstructure of the area by assigning similar colors to points of similar orientation. This method is especially useful for identifying twin domains, achieved by inspection of misorientation between neighboring measurements on the grid. Orientation imaging based on EBSD is a powerful tool for acquiring information about crystal orientation, misorientation, grain size, texture, recrystallized/deformed fraction, strain analysis, phase identification and distribution, etc. [33,34,35].

Focused Ion Beam

Focused ion beam (FIB) system is similar to the SEM, but unlike SEM and electron beam, this technique uses an ion beam for imaging and machining. Most of

modern FIB systems are actually dual-beam meaning that they have two columns, the SEM electron beam and the FIB ion beam, as depicted in Figure 3.9.

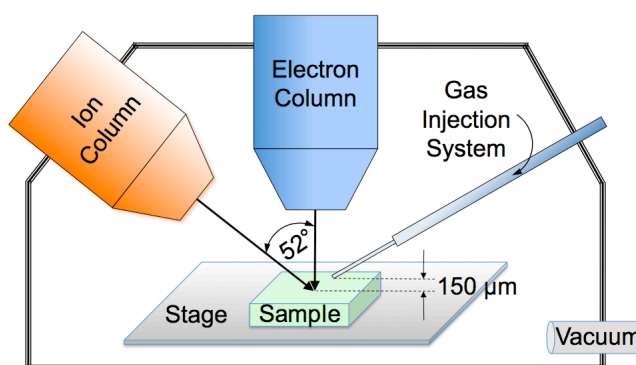


Figure 3.9. Schematic of FIB/SEM dual beam system. Noted are the electron and ion columns, at 52° with respect to each other, as well as the gas injection system (GIS).

In this dual system, the electron and ion columns are at 52° with respect to each other. The ion source in the FIB system is usually gallium because of its excellent thermal and mechanical properties, its energy peaks do not overlap with other materials (for EDS analysis) and it minimizes diffusion reactions between itself and the tungsten needle along which it flows. The current of the electrostatic lenses and the aperture size help adjust the current density and determine the diameter of the ion beam, which can be even lower than 10nm. As the acceleration voltage of ions can be between 1 and 30 keV and the current density between few tens of pA to several hundred nA [36], carbon deposition needs to be introduced in order to prevent gallium ion beam from amorphizing the sample. This is achieved through the gas injection system (GIS). Using the FIB, certain types of micromachining can be performed, such as removing lamellae (membranes) from sample surface and subsequent thinning, as a method of TEM sample preparation [37]. The procedure is as follows: as mentioned, carbon is deposited, first by electron then by ion beam, in order to protect area of interest of the sample. Trenches are then milled by ion beam on each side as well as underneath the lamella. Nanomanipulator is then welded to the lamella by carbon deposition, bridges connecting the lamella to the rest of the sample are milled off and the lamella is lifted out. Finally, the lamella is attached to a TEM grid by carbon deposition after which the nanomanipulator is removed by milling. The final step of TEM sample preparation includes thinning the sample by ion milling. FIB lamella lift-out procedures for certain

samples along with images depicting each step are given in their respective experimental chapters, in the following text.

3.2.4.2. Transmission Electron Microscopy

Transmission electron microscopy is a technique for characterization of materials on a very fine scale, including subatomic levels, in which the electron beam is transmitted through an ultra-thin sample. During beam transmission through the sample there is interaction between electrons and the sample, resulting in processes shown in Figure 3.10:

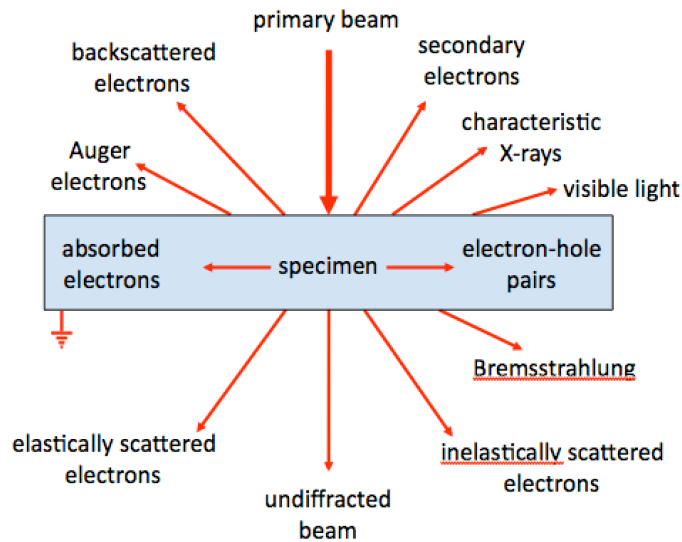


Figure 3.10. Effects occurring during interaction of high energy electron beam with the sample; After [38].

Transmission electron microscopy (TEM) together with scanning transmission electron microscopy (STEM) has three basic modes: imaging, diffraction and spectroscopy, as illustrated by diagram in Figure 3.11, which presents various operation modes in TEM and STEM which include:

- *Imaging*: conventional transmission electron microscopy (CTEM), high resolution transmission electron microscopy (HRTEM) and Z contrast;

- *Diffraction*: selected area diffraction (SAD), conversion beam electron diffraction (CBED) and micro-electron diffraction and nano-electron diffraction (Micro-D and Nano-D);
- *Spectroscopy*: energy dispersive x-ray spectroscopy (EDS), electron energy loss spectroscopy (EELS) and energy filtered transmission electron microscopy spectrum imaging (EFTEM SI).

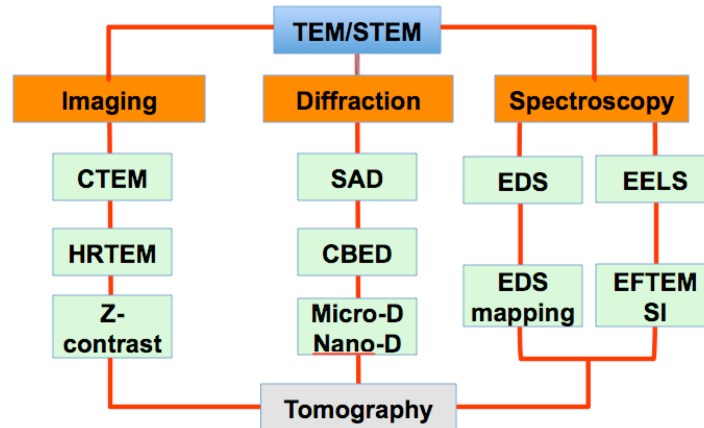


Figure 3.11. Different operation modes in the TEM/STEM.

For conventional TEM the most important types of electrons are elastically scattered electrons because they are used for diffraction contrast and phase contrast imaging in bright field (BF) and dark field (DF) modes as well as HRTEM. For EDS, inelastic scattered electrons are of great importance because, while passing through the specimen, they lose energy and X-rays, which get emitted by ionized atoms, can be detected by the EDS spectrometer.

Basic setup of the transmission electron microscope includes the following main segments:

- *Electron gun*, from where electrons are emitted and accelerated by the electric field (60-300 keV).
- *Condenser system*, comprising of condenser lenses and apertures. Variables controlled by the condenser system include beam size, convergence angle and intensity of brightness. Three variations of electron beam formation are used: almost parallel beam, focused beam (for EDS) and beam translation (for BF and DF imaging as well as STEM).

- *Objective system*, allows two basic types of operations: image forming (BF, DF and HRTEM) and diffraction, which are presented on optical system diagrams in Figure 3.12.

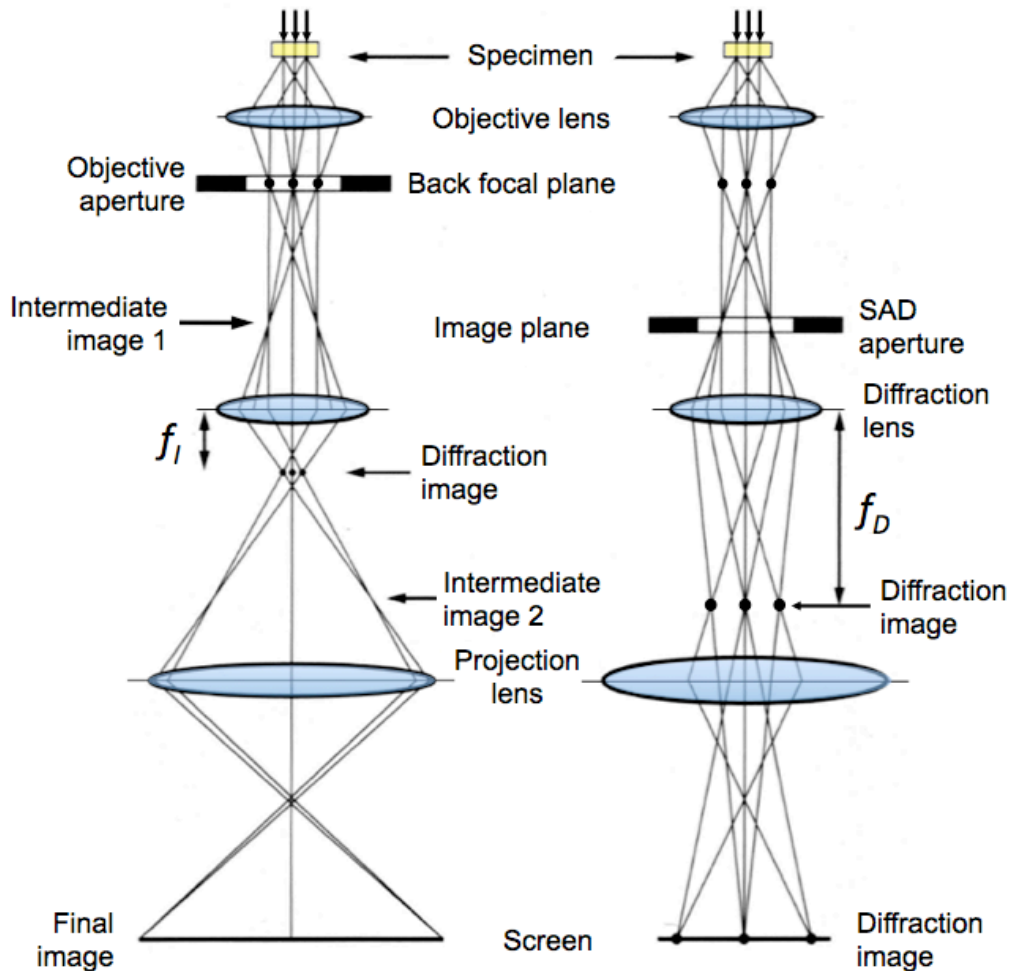


Figure 3.12. Two main modes in TEM: a) forming of BF image and b) forming of diffraction image [39].

By passing the electron wave through the specimen it can change both, its amplitude and phase, which gives rise to contrast. In TEM, by carefully selecting imaging conditions, one imaging contrast can be dominant.

In the formation of diffraction images, SAD aperture plays an important role, because it has a two-fold function: it can reduce the incident electron beam and can limit the area of the sample where the beam passes through and participates in diffraction image formation. The SAD function is presented by a line diagram shown in Figure 3.13.

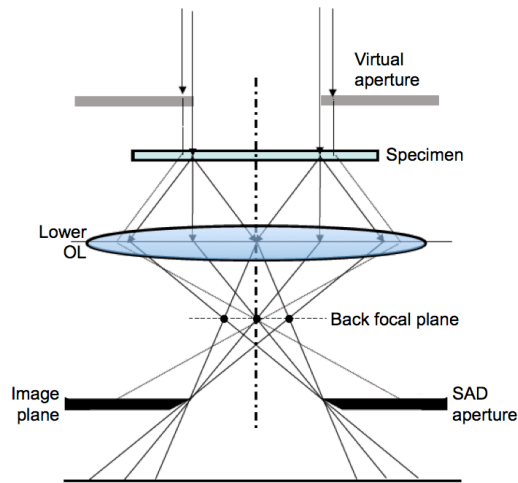


Figure 3.13. Diagram of formation of a SAD image [38].

SAD aperture is placed in the same plane as the image plane. In the case presented in Figure 3.13, only electrons that pass through the virtual aperture will take part in the formation of the diffraction image while all others will be blocked by the SAD aperture.

Forming of BF, DF and high resolution phase contrast images is controlled by the objective aperture (OA) which can be seen from Figures 3.14a,b and c, through the example of an AlScZr (aluminum scandium zirconium) alloy aged 4h at 450°C.

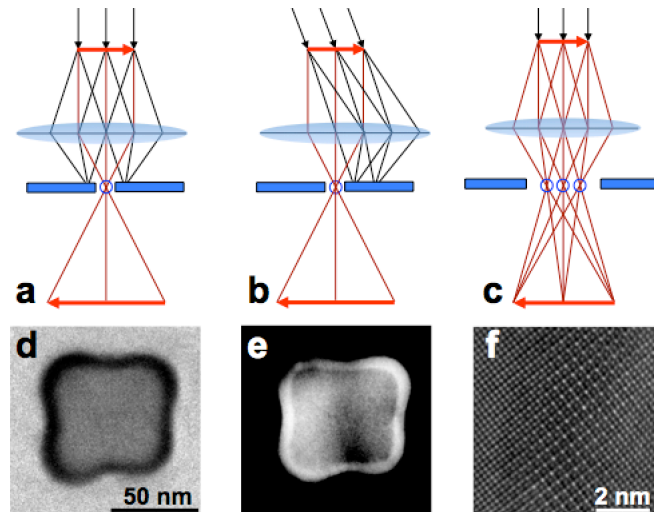


Figure 3.14. Diagram of role of objective aperture and forming of: a) BF image, b) DF image, c) high resolution phase contrast image [38], d) and e) are BF and DF images, respectively, of a $\text{Al}_3\text{Sc-Al}_3\text{Zr}$ core-shell precipitate in aluminum alloy, f) HRTEM image of Al_3Zr shell [40].

Figures 3.14d and e are BF and DF images of a complex core/shell $\text{Al}_3(\text{Sc,Zr})$ precipitate demonstrating clearly size, shape and phase separation. The dark field image was obtained using $g=110$ superlattice reflection, near the 001_{Al} zone axis. Figure 3.14f is an atomic resolution image of Al_3Zr precipitate shell between Al_3Sc core and surrounding aluminum matrix in the AlScZr alloy.

Important mechanisms used for TEM imaging include:

1) *Amplitude contrast*, which has two principal types:

- *Mass contrast*, in combination with contrast derived from sample thickness. The contrast present in the image originates from the difference in processes of scattering inherent to the investigated material. This is the primary contrast in imaging of amorphous materials, and assumes incoherent electron scattering, during which every atom scatters independently. *Z-contrast* is a high resolution version of the same contrast. However, mass contrast is also present in diffraction imaging, where coherent electron scattering is taking place. Typical example is shown in Figure 3.15b, where zirconium, as a heavy element, segregates between scandium-containing core and surrounding aluminum matrix.
- *Diffraction contrast*, characteristic for crystalline materials, which, by using the OA and direct or diffracted electron beam, allows formation of an image which contains crystallographic information if precisely constructed, like with the two beam technique. The basis for this contrast is coherent electron scattering during which atoms do not scatter independently.

Both of these contrasts are seen in BF and DF images. In both types of imaging, the common way to perform imaging with high contrast is the two-beam condition. For DF imaging showing mass/thickness contrast, any scattered electrons can be used. According to kinematic theory, the amplitude contrast can be defined as the difference in intensity of two adjacent areas, which can be written as:

$$C = \frac{I_2 - I_1}{I_1}$$

where C is the amplitude contrast and I_1 and I_2 are intensities of two adjacent areas.

Mass/thickness contrast arises from incoherent elastic scattering, known as the Rutherford scattering, during which incoming electrons interact with atomic nuclei of a target. It is affected by the size of objective aperture (smaller OA yields higher contrast) and the high tension in the electron gun (smaller high tension yields higher contrast).

- 2) *Phase contrast (used in HRTEM)*, where creation of phase shift occurs in the investigated sample. The image is created by recombination of all beams (direct beam and all diffracted beams). The results are appropriate intensities which allow atomic resolution image formation.
- 3) *Atomic (Z) contrast*, in which intensity is proportional to atomic number of elements present. This contrast is created with interaction of electron beam with nuclei of present atoms.

Electron Diffraction

The rule that defines the geometric conditions under which diffraction occurs is called Bragg's law. In the case of parallel planes of atoms, separated by distance d , the condition that has to be satisfied in order for intensity to occur in reflected electron beams is shown by a simple equation:

$$2d \sin \theta = n\lambda$$

where n is the order of reflection which can be 0, 1, 2, 3, etc. and λ is the wavelength of radiation used. This expression is known as Bragg's law. For $n = 1$ the equation is simplified to:

$$2d \sin \theta = n\lambda$$

When Bragg's condition is satisfied, there is constructive interference of transmitted and diffracted electron beams. Basically, there are two types of information which can be acquired from diffraction images [41]:

- *Direction of diffracted beam*, which depends on the lattice geometry and is described by Bragg's law;
- *Intensity of the diffracted beam*, which depends on the lattice motif and is defined by the structural factor.

Calculating the intensity of an *hkl* reflection comes down to the problem of summing up the waves which are characterized by the same wavelength but different amplitudes and phases. In order for diffraction of an atomic plane to occur, besides the Bragg condition, an additional condition that has to be satisfied is that the structural factor has to be greater than zero.

Scanning Transmission Electron Microscopy (STEM)

Unlike CTEM, where imaging occurs by fixed parallel beam and the whole image is produced by illumination of sample, in STEM a focused electron probe is used and scanned over the area of interest on the specimen, hitting one point at a time (probe size determined by lenses). Additionally, TEM magnification depends on lens strength while STEM magnification can be increased by scanning a smaller area of interest. Typical experimental setup for STEM imaging, shown in Figure 3.15, consists of a STEM beam, analyzed sample, annular dark field (ADF) detector, BF detector and convergent beam electron diffraction image. Low angle annular dark field (LAADF) where $\theta < 30$ mrad, high angle annular dark field (HAADF) where $\theta > 30$ mrad and Bragg diffracted discs, $\theta < 10$ mrad, are also presented.

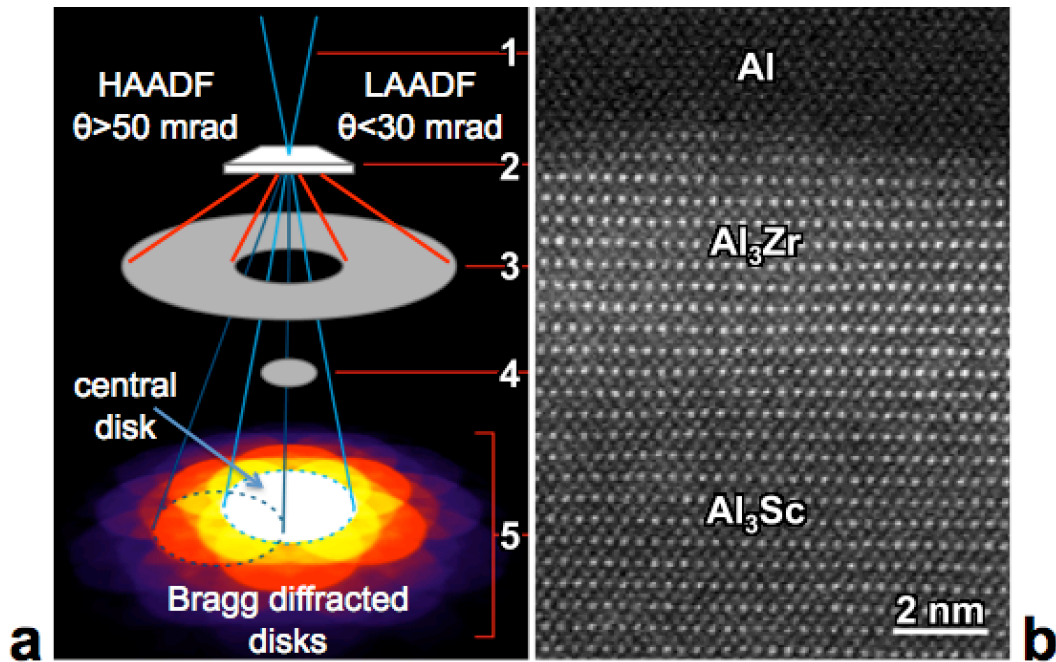


Figure 3.15. a) Typical experimental setup for STEM imaging: STEM beam (1), sample (2), ADF detector (3), BF detector (4) and convergent beam electron diffraction image (5); After [42], b) HAADF image of Al_3Zr shell between Al_3Sc core and aluminum matrix; note the strongest contrast is in the region containing zirconium; After [43].

In HAADF imaging, incoherent high angle scattered electrons are collected by the high angle annular detector with large inner and outer radii. This scattering is based on two processes: Rutherford scattering and thermal diffuse scattering. Scattered electrons strongly depend on the nature of elements present i.e. atomic number, so there is a relation between the intensity I and the atomic number Z , where β is a coefficient which depends on the dominant scattering (thermal or Rutherford) [44,45]:

$$I \sim Z^\beta$$

This dependence is valid for the HAADF imaging conditions when true Z -contrast conditions are approached, i.e. when electrons are scattered at semi-angles greater than 50 milliradians ($\sim 1.43^\circ$).

Energy Dispersive X-ray Spectroscopy (EDS)

Energy dispersive x-ray spectroscopy is a method which allows relatively simple quantification i.e. calculation of the ratio of elements present in the investigated area of the sample. For the process of quantification to be accurate, the part of the spectra originating from the background radiation (Bremsstrahlung) has to be eliminated, which occurs because of deceleration of incident electron beam after penetration into the investigated sample.

This process consists of modeling the line of background radiation, which is achieved by defining areas of spectra from both sides of a peak of a corresponding element. This is a fairly simple process when using modern computer software because it is fully automatized. Quantification is based on a simple model where the elemental compositions are proportional to the number of X-rays under the corresponding peak. This method implies the existence of a standard, which allows determining the constant of proportionality based on the analysis of a material of known composition or a single element material. The sample has to be stable with the minimal number of acquired impulses $>10^5$, for statistical relevance.

Aberration Corrected Transmission Electron Microscopy

All optical systems, based on focusing lenses, due to their poor optical quality, inevitably suffer from axial aberrations, which pose fundamental limitations for achievement of sufficient resolution using specific electromagnetic radiation. However, recent advances in electron optics, electron detectors and computing power, make it possible to overcome these limitations [46]. By correcting axial aberrations such as spherical and chromatic, it is possible to achieve conditions similar to that of an ideal optical system in which an object is almost perfectly reproduced in the final image. As mentioned, the main two axial aberrations are:

- *Spherical*, electromagnetic lens fails to focus electrons passing at different distances from optical axis (due to uneven electrical field); electrons not to reach

the same focal point which creates a disc of least confusion, as indicated by arrows in Figure 3.16a;

- *Chromatic*, electromagnetic lens fails to focus electrons with different energies, focusing them at different distances from the lens, along the optical axis, as indicated by arrows in Figure 3.16b.

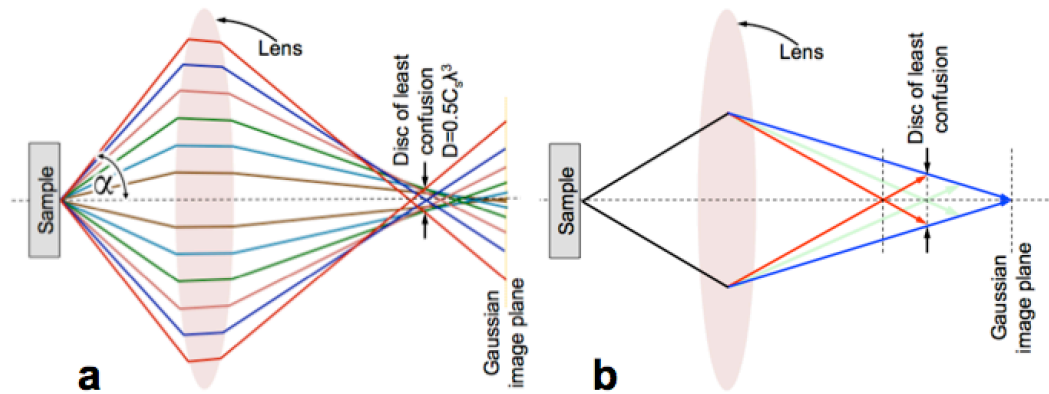


Figure 3.16. Schematic representation of two axial aberrations: a) spherical, b) chromatic; discs of least confusion are indicated by black arrows; blue lines indicate no energy loss; green and red lines indicate energy loss electrons, of energies $E - \Delta E_1$ and $E - \Delta E_2$, respectively [47].

The limits in resolution caused by these two axial aberrations in electromagnetic lenses can be estimated using the following formulas [48]:

- for the spherically limited resolution: $r_s = B \cdot \sqrt[4]{\lambda^3 \cdot C_s}$
- for the chromatically limited resolution: $r_c = A \cdot \sqrt{\lambda \cdot \frac{\Delta E}{E} \cdot C_c}$

where A and B are the numerical values of the order of 1, λ is the electron wavelength, E is the mean energy, ΔE is the energy width of the beam, C_c is the chromatic aberration coefficient and C_s is the spherical aberration coefficient. From these two formulas it is obvious that in order to achieve ultra high resolution (atomic resolution), it is essential to use very high electron beam energies or to decrease aberration coefficients. Until about 10 years ago atomic resolution has been achieved by increasing electron beam

energy (≥ 1000 kV), which causes enormous radiation displacement damage of investigated samples. An alternative is to improve quality of electromagnetic lenses by using aberration correctors achieving atomic resolution at medium (< 300 kV) [46] or even low (30 kV) [49,50] voltages. In order to achieve aberration correction, stability of current (voltage) in the aberration corrector has to be better than 10^{-7} amperes (volts) [51] for the imaging, in theory, not to be affected by axial aberrations in the imaging lenses. Unfortunately, imaging is affected by aberrations of the probe forming lens system itself and, therefore, aberrations have to be improved by the probe aberration corrector [38].

New generations of electron microscopes, with aberration corrections of both, probe and imaging lenses, in tandem with chromatic aberration correctors, are significantly more powerful than older generation instruments. They have achieved significant progress in spatial, temporal and spectral resolution, with higher brightness and sensitivity [46]. These advances provide unprecedented scientific opportunities for atomic level characterization of materials at the ultimate resolution below 50 pm with improved contrast and chemical sensitivity, and energy resolution below 100 meV.

Tomography

Although a very powerful tool, widely used in physical and biological sciences due to its high spatial, temporal and chemical resolution, the main limitation of transmission electron microscopy is the two-dimensional (2D) nature of images used to characterize nanostructures, as they represent projections of three-dimensional (3D) structures. As properties of materials are dependent on their structures, efforts in the 1960s and 1970s in physical and biological sciences have been made in order to understand the third dimension at high resolution, using electron tomography, i.e. performing 3D reconstruction from 2D electron microscopy images [52,53,54,55,56]. In electron tomography, the incident electron beam is transmitted through the sample at an incremental degree of rotation creating a series of 2D electron images.

The first mathematical formulation of 3D reconstruction was given by German mathematician Johan Radon in 1917, where he explained that an object in real space can

be described by the mapping function $f(x,y)$ i.e. by the projections, or line integral, through f along all possible lines L with unit length ds [57]:

$$R_f = \int_L f(x,y) ds$$

This operation, named after Johan Radon the *Radon transform*, converts every point in real space:

$$x = r \cos \phi$$

$$y = r \sin \phi$$

into a line at a constant angle θ in *Radon space* $[l, \theta]$ where l is the line perpendicular to the projection direction, and θ is the angle of projection. These two are related by the equation:

$$l = r \cos(\theta - \phi)$$

For a sufficient number of 2D projections, adequate sampling of Radon space can be provided and, by applying an inverse Radon transform, a real object in space can be reconstructed [58]. More projections in real space means more sampling of Radon space which consequently leads to better reconstruction.

Unlike the *Fourier space reconstruction*, whose implementation is not straightforward, especially in situations when projections are missing, due to self-shadowing or limiting tilt in the microscope, forward and reverse Radon transforms like the *back-projection (BP)*, offer a fast and simple method of describing complex nanosized objects. The most common method of 3D real space reconstruction method is the *weighted back-projection (WBP)*, which convolutes the 3D reconstruction with a simple radial weighting filter thereby increasing linearity to a maximum at a high cut-off value [58,59]. Weighted filtering is applied after the real-space back-projection calculations are completed [59].

The incremental degree of rotation is very often limited in the TEM to $\pm 70^\circ$ and, unless the sample holder is dedicated for $\pm 90^\circ$ rotation, missing wedge information inevitably affects the final tomographic reconstruction. Assuming that the tomography

series is acquired by sample rotation around x axis, resolution along y axis (d_y) for an object of radius R , is defined by the number of 2D projections, N , over a tilt range of $\pm 90^\circ$, derived from geometrical sampling of Fourier space [60,59]:

$$d_y = \frac{2\pi R}{N}$$

Since tilting of sample around y axis is limited to $\alpha < 90^\circ$, thus defining resolution along z axis, as the original projection direction, any feature along z direction will be stretched by a factor e_{xz} given for the maximum tilt angle α [61]:

$$e_{xz} = \sqrt{\frac{\alpha + \sin \alpha \cos \alpha}{\alpha - \sin \alpha \cos \alpha}}$$

In order to avoid the effect of the missing wedge information, a tilted series of images (2D projections) that covers a 360° angular range is required, although with $e_{xz}=1.3$ for equally spaced tilt series limited to $\pm 70^\circ$ for an object with no obvious symmetry, an interpretable reconstructed tomogram can be obtained. The rule of thumb is that with a larger tilt range the effect of the missing wedge information on the final 3D reconstruction is smaller.

Unfortunately, various factors can degrade the final quality of reconstruction and lead to reduced resolution. These include: beam damage, microscope instability during long tilt series recording, sample charging under electron beam, pixel resolution, sample thickness, tilt-series alignment, etc.

Orientation and Strain Mapping

One of the most important properties of nanostructured semiconducting and metallic materials, such as thin films, nano-dots, or nanowires for transparent electronic applications is elastic strain. Typical examples are AgNWs with pentagonal cross-sections, which exhibit significant elastic strain during their growth, as well as during annealing, carried out in order to improve electrical conductivity [62]. One of the

methods widely used to analyze coherent strain distribution in nanostructures is based on geometric phase analysis (GPA), performed on high resolution transmission electron micrographs, which have a limited field of view (FOV), typically less than 100 nm with current detectors. In addition, if used for coherent strain mapping, HRTEM and HRSTEM require all atomic columns to be clearly resolved across the FOV, which requires high quality of very thin samples. However, the thinner the sample the higher the susceptibility to elastic strain relaxations, causing potentially unreliable strain measurements. It has been already demonstrated that STEM imaging combined with nano-beam electron diffraction (NBED) collected at equally spaced positions, can increase resolution [63,64]. Recently, NBED strain mapping in tandem with direct electron detection camera, such as Gatan K2[®] has been used at the National Center for Electron Microscopy (NCEM) at UC Berkeley to measure elastic strain distribution in complex alloy microstructures [65] and semiconductor devices [66].

This method is essentially based on acquisition of nano-beam electron diffraction patterns in each pixel of the camera, and based on the diffracted beam positions across field of view of several hundreds of nanometers, elastic strain distribution can be elucidated.

3.3. Ag NWs and Ag NW Based Nanocomposites – Experimental Procedure

Nanowire synthesis was performed by polyol reduction of silver nitrate (AgNO₃). The amount of 5mL of ethylene glycol – EG (99.9%, VWR[®]), in a glass vial, was suspended in an oil bath at 151°C undergoing magnetic stirring for 1h at 260 RPM. After 1h, 40 μL copper (II) chloride dehydrate (CuCl₂•2H₂O, 99.999+%, Aldrich[®]) solution was introduced to EG and the solution was then heated for another 15min. Finally, 1.5 mL of a 0.147 M polyvinylpyrrolidone - PVP (average M_w ≈ 55 000, Aldrich[®]) solution was injected into EG along with 1.5 mL of a 0.094 M AgNO₃ (99.999+%, Aldrich[®]). When the AgNWs were formed, suspension was cooled to room temperature. After the synthesis, the AgNWs were subjected to centrifugation at acceleration of 7900 m/s² for 5 min with ethanol as the dispersion agent and were stored, dispersed in ethanol.

For further characterization and processing, AgNWs suspension was drop cast

on silicon substrate, previously cleaned by ultrasonication in acetone, isopropanol and deionized (DI) H₂O and subsequently dried with nitrogen and on glass (microscope cover slides, Carl Roth®). Glass substrates were cleaned for 30 min with peroxymonosulfuric acid (H₂SO₅), so called “Piranha solution”, a mixture of sulfuric acid (H₂SO₄, 96%) and hydrogen peroxide (H₂O₂) at a 2:1 ratio. After subsequent rinsing in DI H₂O the substrates were dried using nitrogen.

Annealing of the AgNW networks was carried out at 250 °C for 3 minutes in air on a VWR® hotplate.

Coating of annealed AgNW networks on Si substrate by AZO film was performed by atomic layer deposition (ALD), at 200°C using a BENEQ® TFS200 ALD system. Fundamentals of ALD method are given in Section 3.1.4. Diethyl zinc (DEZ, Zn(C₂H₅)₂) and DI H₂O were used as precursors for the deposition of ZnO cycles while trimethyl aluminum (TMA, Al(CH₃)₃) and DI H₂O were used as precursors for aluminum oxide (Al₂O₃) deposition, with ultra-pure nitrogen (99.9999 %) as the purging gas. A ratio of 15:1 of ZnO to Al₂O₃ cycles was used for the formation of a macrocycle and the amount of macrocycles used was targeted as to acquire an AZO film with ~100 nm thickness. Macrocycle contained 1.5 - 3.37 at. % aluminum, measured by glow discharge mass spectrometry (GDMS). This method consists of collision between plasma (glow discharge) and sample atoms, which at first are excited but then lose energy through atomic emission. Observing this emission gives insight on the atom's identity (through wavelength) and concentration (through intensity) [62,67].

Surface roughness of AgNW and AgNW/AZO networks was measured on a Dektak®-150 profilometer with diamond tip of 12.5µm radius, low-force mode up to 1 mg tracking force and vertical resolution between 0.1 and 1 nm, depending on the thickness range used for scanning.

Pristine AgNWs were characterized by X-ray diffraction analysis using Panalytical® X'Pert³ MRD at 45 kV and 40mA using Cu Kα X-ray source.

Optical transmittance was measured by a Cary 5000 UV/Vis/NIR spectrophotometer (Varian Inc.®) consisting of an integrating sphere and a UV-Vis detector. The wavelength range in which the measurements were taken was 300 - 1100 nm and since no background subtraction of glass substrate was made, all results show

optical properties of films on glass.

Electrical measurements via the 4-point probe test were carried out for the all electrodes on glass substrates at room temperature using a 4200-SCS parameter analyzer (Keithley Instruments[®]).

Scanning electron microscopy (SEM) of pristine and heated AgNWs as well as AgNW/AZO nanocomposite was performed on FEI[®] Helios Nanolab 660 DualBeam Focused Ion Beam (2 kV and 0.1 nA operating voltage and current respectively, unless otherwise noted). In order for samples to be protected from gallium ion beam, which is powerful enough to completely destroy the sample, electron and ion beam carbon deposition was performed. An area of interest, cross-section of welded AgNWs encapsulated by AZO, was chosen and a focused ion beam (FIB) lamella lift-out from the sample was performed (FIB lift-out procedure given in Section 3.2.4.1, images shown in Figure 3.17). Finally, the lamella, attached to a TEM half-grid was thinned (ion beam at 30 kV) to under 100nm in thickness for the enabling of high quality TEM and STEM investigations.

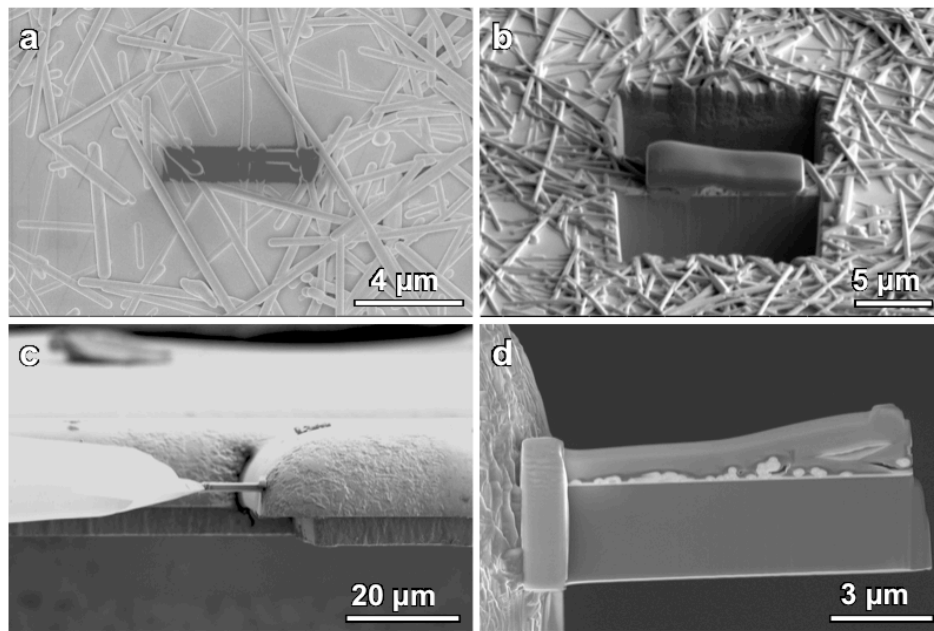


Figure 3.17. Sequence of the FIB sample preparation procedure of Ag NWs encapsulated with AZO, a) carbon deposition, b) trench milling, c) Lamella lift-out and attachment to half-grid by carbon deposition, with nanomanipulator, d) high magnification image of lamella attached to half grid for final thinning. Note the nanowire cross-section is perpendicular to the electron beam.

Transmission electron microscopy and scanning transmission electron microscopy investigations were performed on the FEI[®] TITAN³ Themis 60-300 double aberration corrected microscope at 200kV operating voltage, equipped with the Super-X Energy Dispersive Spectrometry (SuperX EDS) system controlled with Bruker Esprit software. CTEM was also performed on the Philips CM30 transmission electron microscope at 300 kV. For this investigation, the sample was prepared by dimpling and argon ion milling of the sample from the silicon substrate side.

For tomography characterization, AgNWs in water (Cambrios[®], ClearOhm ink) with an average diameter of ~30nm were drop cast onto lacey carbon 300 mesh copper TEM grid and dried. Subsequently, the grid was held for 30 seconds at 210°C on a hot plate (AgNW side up) and then immediately inserted into transmission electron microscope. Tilt series of STEM HAADF 512x512 pixel images for tomographic reconstructions were acquired automatically on the FEI[®] Titan-X operated at 200kV, using camera length of 160 mm and an inner collection angle of 60 mrad. Images were recorded using FEI[®] tomography software, with a dwell time of 6 μ s from -70 to +70° in 1° intervals, without fiducial markers, with a pixel size of 0.57 nm. The dose rate was $\sim 10^5$ e⁻/nm²s. Although the Titan-X exhibited exceptional stability, compensations for sample drift, as well as image focus were used between successive image acquisitions. Three-dimensional reconstructions were performed from the tilt series with 141 images by applying an algorithm for weighted back-projection (WBP) described in important papers on STEM and EFTEM tomography of nanostructures by several authors [58,59,60,61]. The data was aligned manually in the Tomviz[®] software suite and reconstructed using the simultaneous iterative reconstruction technique (SIRT) algorithm in TomoPy[®] 1.0.0 and Python[®] 2.7 softwares. Post-processing and visualization was accomplished using Tomviz[®] and quantitative analysis was accomplished using custom scripts in Python[®].

Samples investigated for orientation and strain distribution were AgNW nanowelds, created by thermally induced solid-state and surface diffusion processes. Series of images were taken on the FEI[®] TEAM_1 aberration corrected microscope, equipped with a high-brightness field emission gun, operated in STEM mode using a sub-nanometer electron probe with a 10 μ m condenser aperture at 300 kV. NBED

patterns were recorded using the Gatan[®] K2 camera at a frame rate 400 per second and HAADF image size 128x128 pixels, with pixel size between 5 and 7 nm. During single image acquisition, the electron beam is scanned over selected area in a raster and a NBED pattern is recorded at each position. The orientation and strain maps were calculated from the diffraction maps by detecting the diffracted beam positions using pattern recognition algorithm written for MatLab[®] software. The standard deviation of calculated coherent strain was $\pm 0.1\%$.

In order to facilitate the AgNWs/AZO layer as a transparent electrode, silicon wafer-based solar cells with a diffused p–n junction were produced. A 15x15 mm² boron doped silicon wafer (p-type semiconductor) was cleaned by ultrasonication using ethyl acetate, isopropanol and DI H₂O. This was followed by dipping of the wafer into 5% hydrofluoric acid (HF) in order to remove native oxide in the silicon wafer. The next step included spin coating, at 2000 RPM, spin-on glass (Filmtronics[®]) containing phosphorous (n-type semiconductor), an agent which promotes dopant diffusion. This was followed by annealing at 900° C for 15 min. Couple of more HF steps were introduced for removal of spin-on glass and thermal oxide in between which annealing was performed at 500° C for 5 min. The sample was then rinsed with DI H₂O rinse and dried with nitrogen. Finally, AgNWs were deposited, annealed, after which AZO layer was introduced by ALD (production of AgNWs/AZO already described in this chapter).

3.4. Tandem Organic Solar Cells – Experimental Procedure

AgNWs Used as Electrodes in Tandem Organic Solar Cells

AgNWs in water (Cambrios[®], ClearOhm ink) with an average diameter of ~30nm were deposited on glass substrates by Zehntner[®] ZAA 2300 Automatic Film Applicator by doctor blading at 50° C and afterwards dried at 120 °C for 3 min for solvent evaporation. Processing parameters for all samples are shown in Table 3.1.

Thickness of films was measured on a Tencor[®] Alpha Step D 100 profilometer. Resistivity measurements were performed with R-Check[®] Surface Resistivity Meter using 4-point technique. The optical transmittance was measured by a UV-Vis-NIR spectrometer (Lambda 950, from Perkin Elmer[®]) in the wavelength range of 300-700

nm with 2nm step. Surface roughness was obtained by Dektak[®]-150 profilometer with diamond tip of 12.5 μ m radius, low-force mode up to 1 mg tracking force and vertical resolution between 0.1 and 1 nm, depending on the thickness range used for scanning.

Table 3.1. Processing parameters of doctor bladed Ag NWs.

Sample	Height of blade [μ m]	Volume of deposited ink [μ L]	Speed of blade [mm/s]
1	500	80	1
2	300	60	1
3	300	80	1
4	400	120	1
5	500	120	2

Morphological line segmentation method for series of datasets of SEM images in order to analyze area coverage of AgNWs was performed using MatLab[®] software.

Double Junction Tandem OSC

The device were fabricated on glass (2.5x2.5 cm) subsequent to the ultrasonication in acetone and isopropanol for 10 minutes each. All layers were deposited by doctor blading technique, on Zehntner[®] ZAA 2300 Automatic Film Applicator. First layer deposited was PEDOT:PSS (Heraeus - Clevios[™], P VP AI 4083). The second layer was an Ag ink (InkTec[®], TEC-PR-010) deposited at 50 °C and baked at 130 °C for 5 min. This produced a reflective Ag bottom electrode. The third layer deposited was PEDOT:PSS after which it was dried at 130 °C for 5 min (in nitrogen atmosphere to limit charge recombination). The fourth layer deposited was a polymer nanocomposite comprising of matrix GEN-2 (Merck[®]) and nanofiller PC₆₁BM (Solenne[®] BV, 99.5%) previously mixed at a ratio of 1:2 wt.% and dissolved in dichlorobenzene at a total concentration of 30 mg mL⁻¹. The fifth layer deposited was a layer consisting of ZnO nanoparticles dispersed in isopropanol (Nanograde[®] AG, Product N-10) after which it was dried at 80 °C for 3 min. The sixth layer deposited was neutral PEDOT:PSS (Agfa[®], NT5-3417286/2) or N-PEDOT for short, after which it was dried at 80 °C for 3

min. The seventh layer deposited was a polymer nanocomposite comprising of matrix pDPP5T-2 alternating copolymer (BASF[®], GKS1-001, $M_w = 47000 \text{ g mol}^{-1}$) and nanofiller PC₆₁BM previously mixed at a ratio of 1:2 wt.% and dissolved in a solvent mixture of dichlorobenzene and chloroform (ratio of 1:9 vol.%) at a total concentration of 24 mg mL^{-1} . The eighth layer deposited was again ZnO after which it was dried at 80 °C for 5 min. The final, top layer deposited was AgNWs (Cambrios[®], ClearOhm ink).

Photoelectric characterization was performed using a source measurement unit from BoTest. Illumination obtained was from a solar simulator (Oriel Sol 1A, from Newport[®]) with AM1.5G spectra at 100 mWcm^{-2} , calibrated with a standard single-crystal Si photovoltaic cell. The active area of the cell was defined by the overlap of the bottom and top electrode.

The optical transmittance was measured by a UV-Vis-NIR spectrometer (Lambda 950, from Perkin Elmer[®]).

The thicknesses of the films were measured with a profilometer Tencor[®] Alpha Step D 100.

Structural characterizations of solar cell on glass substrate were performed by SEM and TEM. Scanning electron microscopy investigations as well as FIB sample preparation i.e. lamella lift-out were performed on the FEI[®] Helios Nanolab 660 DualBeam FIB system. Solar cell was cleaved (broken) along the vertical axis and mounted on 45° pre-tilt holder for cross-section imaging, at 2 kV and 0.1nA, and on a regular holder for lamella lift-out (FIB lift-out procedure given in Section 3.2.4.1). After lift-out, lamella was attached to a TEM half-grid was thinned (ion beam at 30 kV) to under 100nm for TEM investigations. TEM and STEM investigations were performed on the FEI[®] TITAN³ Themis 60–300 double aberration corrected microscope at 200 kV operating voltage.

Triple Junction Tandem OSC

Devices were fabricated on ITO coated glass (Weidner Glas[®], 2.5 X 2.5 cm, $15 \text{ } \Omega\text{sq}^{-1}$) at ambient conditions, after it was laser-patterned and cleaned by ultra-sonication acetone and isopropanol for 10 minutes each. All layers were deposited by doctor blading technique except MoOx/Ag electrode. First layer deposited on ITO coated glass

substrate was PEDOT:PSS (Heraeus - CleviosTM, P VP AI 4083) diluted in isopropanol at 1:3 vol.% ratio and annealed at 140 °C for 5 min (in nitrogen atmosphere to limit charge recombination). The second layer deposited at 45 °C was a polymer nanocomposite comprising of matrix DPP (BASF[®]) and nanofiller PC₆₁BM (Solenne BV[®], 99.5%) previously mixed at a ratio of 1:2 wt.% and dissolved in a solvent mixture of dichlorobenzene and o-chloroform (ratio of 1:9 vol.%). The third layer deposited at 50 °C was a layer consisting of ZnO nanoparticles dispersed in isopropanol (Nanograde[®] AG, Product N-10) after which it was dried at 80 °C for 5 min. The fourth layer deposited at 50 °C was N-PEDOT (Agfa[®], NT5-3417286/2), after which it was dried at 80 °C for 5 min. The fifth layer deposited at 55 °C was a polymer nanocomposite comprising of matrix DPP (BASF[®]) and nanofiller PC₆₁BM (Solenne BV[®], 99.5%) previously mixed at a ratio of 1:2 wt.% and dissolved in a solvent mixture of dichlorobenzene and o-chloroform (ratio of 1:9 vol.%). The sixth layer deposited was again ZnO under same conditions. The seventh layer deposited at 50 °C was N-PEDOT (Agfa[®], NT5-3417286/2), after which it was dried at 80 °C for 5 min. The eighth layer deposited 45 °C was AgNWs (Cambrios[®], ClearOhm ink). The ninth layer deposited was again ZnO under same conditions. The tenth layer deposited at 60 °C was a polymer nanocomposite comprising of matrix PCDTBT (1-MaterialsTM) and nanofiller PC₇₁BM (Solenne BV[®], 99.5%). Subsequently, Q-tips drenched in toluene were used to clean edges of the substrate exposing the middle AgNW and bottom ITO electrodes. Finally, the last two layers – MoO_x and Ag were deposited by thermal evaporation through a shadow mask with an opening of 10.4 mm². MoO_x powder and Ag pellets were introduced into the Leybold[®] Univex 350G vacuum thermal evaporation coating machine under parameters: 2.6-4.9 bar of pressure, 5ppm of oxygen, 0.1ppm of H₂O and a starting deposition rate of 0.5 Å/s while the total deposition time was 20min.

Optical transmittance and photoelectric measurements were performed on same instruments and with same parameters as for the double junction cell.

Structural characterizations of the triple junction cell were performed on same instruments and with same parameters as for the double junction cell.

3.5. Ag Dendrites – Experimental Procedure

Ag dendrites were synthesized by the electrodeposition method which was performed in a set-up consisting of a platinum cathode (geometric surface area 0.53 cm^2) and reference (wire) and counter (foil, surface area $\sim 0.80 \text{ dm}^2$) electrodes, both of pure silver (same material used in order to maintain the concentration of the metal ions in the solution constant). The working electrode was placed in the center of the cell, the counter electrode was placed close to the cell walls while tip of the reference electrode was $\sim 0.2 \text{ cm}$ from the working electrode surface. The electrolyte solution was a mixture of 0.06 M AgNO_3 , $1.2 \text{ M sodium nitrate (NaNO}_3)$ and $0.05 \text{ M nitric acid (HNO}_3)$ with a volume of 100 mL where double distilled water was the solvent. Working voltage was 100 mV at a time (t) of 72 s at room temperature. Figure 3.18 explains the relationship of working parameters with potentiostatic polarization measurements. Polarization curve in Figure 3.18a shows how a plateau of the limiting diffusion current density (j) corresponds to a range of overpotentials (η) between 75 and 175 mV . The $j - t$ dependence of electrodeposition (at $\eta = 100 \text{ mV}$) is presented Figure 3.18b showing an exponential increase of j with the passage of time. The overpotential of 100 mV was chosen because it belongs to the plateau of limiting diffusion current density and dendrites are formed in a diffusion-controlled process.

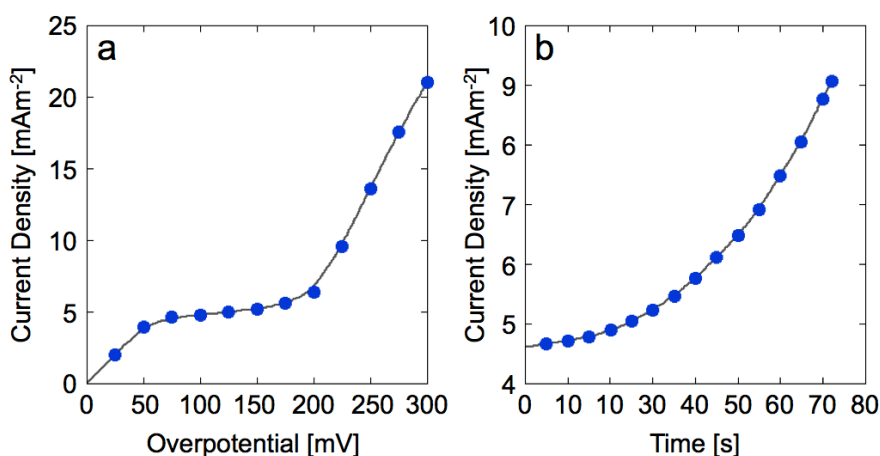


Figure 3.18. a) Polarization curve of Ag electrodeposition, b) Current density as a function of time, at an overpotential of 100 mV [8].

After synthesis, the dendrites were subsequently rinsed in distilled water and ethanol, and kept in ethanol for further characterization.

Annealing of the Ag dendrite network, with 250 μL drop cast on a substrate, was carried out at 250 $^{\circ}\text{C}$ for 3 minutes in air on a VWR[®] hotplate.

Optical transmittance was measured by a Cary 5000 UV/Vis/NIR spectrophotometer (Varian Inc. [®]) The wavelength range in which the measurements were taken was 300 - 800 nm and since no background subtraction of glass substrate was made, all results show optical properties of films on glass.

Electrical measurements via the 4 point probe test were carried out at room temperature using a 4200-SCS parameter analyzer (Keithley Instruments[®]).

Morphology, topography, microstructure and crystallography of Ag dendrites were evaluated using FEI[®] Strata 235 dual beam FIB, equipped with an EBSD allowing OIM analysis without breaking vacuum. Imaging was performed at 2kV and 0.1nA current. For OIM analysis, the surface silver oxide (Ag_2O) layer was removed by FIB milling at 30kV in order to increase the signal to noise ratio. For FIB-machining and OIM analysis, drop cast Ag dendrites on silicon substrate were mounted onto a 45 $^{\circ}$ pre-tilted specimen holder. The 45 $^{\circ}$ holder was used because it allowed optimal Ag dendrite orientation for oxide layer removal (parallel to the ion beam after tilting of stage by 7 $^{\circ}$), shown in Figure 3.19a. The sample stage was then tilted, for 45 $^{\circ}$ for electron beam imaging (sample perpendicular to electron beam), shown in Figure 3.19b. Finally, the stage was rotated for 180 $^{\circ}$ and tilted 25 $^{\circ}$ as to have the sample at 70 $^{\circ}$ with respect to incident electron beam for EBSD analysis (Figure 3.19c). OIM analysis was performed using a TSL-EDAX OIM system at 20 kV, with a spot size of 5, step size of 100 nm, and working distance of \sim 10 mm. No data cleaning (interpolation) was performed on the datasets, but low-confidence points were filtered out from the data. Because of the fact that Ag dendrites did not lie flat on the substrate, the collected orientation data was rotated to align $\langle 111 \rangle$ orientation normal to broad dendrite surface. Pole figures of the orientation data were constructed using a harmonic series expansion with a resolution of 5 $^{\circ}$.

For TEM characterization, Ag dendrites were rinsed in ethanol and drop-cast on copper lacey carbon grids. Phase contrast HRTEM and HAADF imaging was performed in the FEI[®] Titan-X and the aberration corrected FEI[®] TEAM 0.5 transmission electron microscopes operated at 200 kV and 300 kV, respectively.

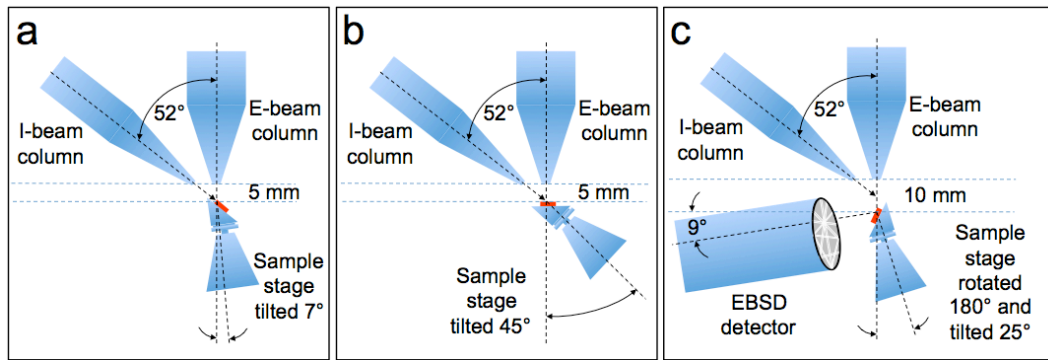


Figure 3.19. Schematic representation of the Ag dendrite sample preparation and EBSD based OIM analysis: a) Sample surface is parallel to the ion beam after tilting of stage by 7° ; b) Sample surface is perpendicular to electron beam; c) Sample surface is 70° with respect to incident electron beam for EBSD analysis [9].

For cross-sectional structural characterization, an area of interest was chosen and a FIB lamella lift-out from the sample was performed (FIB lift-out procedure given in Section 3.2.4.1, images shown in Figure 3.20). Finally, the lamella, attached to a Cu grid pole was thinned to under 100nm in thickness for the enabling of high quality TEM and STEM investigations.

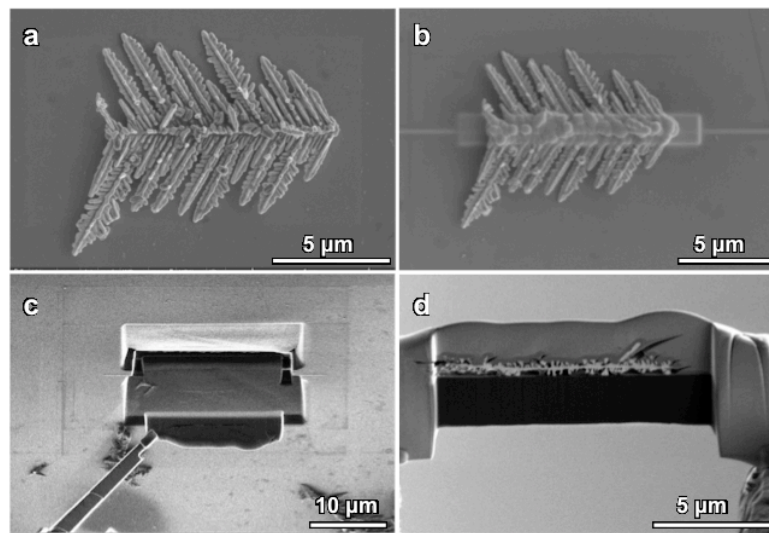


Figure 3.20. Sequence of the FIB sample preparation procedure of Ag dendrites, a) Selection of a typical Ag nanodendrite, b) carbon and platinum protection layer deposition, c) lamella lift-out by nanomanipulator, after trench milling after initial thinning, d) lamella attachment on Cu grid poles, followed by final thinning.

3.6. Polymer Nanocomposites – Experimental Procedure

Polymer nanocomposites were processed with the solution blending method. Polyvinyl butyral - PVB (Mowital[®], B60H, mol. weight 50-60.000 g/mol) was purchased from Kuraray[®]. The polymer was mixed with ethanol with the total polymer concentration fixed at 10 wt.%. PVB/ethanol solution was prepared by magnetic stirring at room temperature overnight at 200 rpm. MWCNTs, SWCNTs, and graphene were used as received from Cheaptubes Inc.[®], where they were synthesized using combustion chemical vapor deposition (CCVD) and purified using concentrated acid chemistry. The specifications, stated by Cheaptubes Inc.[®] were as follows: MWCNTs have an outer diameter of 13-18nm and length of 3-30 μm (with >99wt% purity), SWCNTs have an outer diameter of 1-2 nm and length of 3-30 μm (with >99wt% purity), and graphene, grade 4, has a diameter of 1-2 μm and surface area of >700 m^2/g (with >99wt% purity).

Ultrasonication was performed with Vibra-Cell Ultrasonic Processor VCX 750, 19 mm Ti horn, 20 kHz, 750 W/cm^2 , Newtown[®]. PVB/ethanol solutions were mixed at 50% amplitude and in pulse mode (1 s off, 1 s on function) with either (dependent on the sample), 1wt % of MWCNTs, 1wt % SWCNTs or 1wt % graphene for 1h (effectively for 30min) and kept constantly at a temperature of 20° C with ice.

Spin-coating system (Model WS-400BX-6NPP-LITE, Laurell Technologies Corporation[®]) was set up with a vacuum pump and a nitrogen tank. Substrates used were laboratory glass 20mm X 20mm with thicknesses 0.13mm-0.17mm and Si wafer parts, type n-semiconductor, orientation {110}, flat <111> with thickness of 500-550 μm and resistance of 1-10 Ω/cm . Prior to suspension deposition, ultrasonication in acetone, isopropanol and DI H₂O was performed. Suspensions were deposited in the middle of substrates with a BD 5ml syringe with a 1.9mm inner diameter (2.1mm outer diameter) metallic needle before they were spun. Conditions under which the samples were spin-coated were as follows: 60 PSI (40.1 bar) of nitrogen pressure, V=22-24" Hg and T=20°C. Spin-coating speed was 4000 RPM, amount of deposited material arbitrary, as to cover the substrate, while the time of spin-coating was kept constant at 30s. After spin-coating, samples were dried in an oven for 2h at 50°C for removal of residual solvent and kept in an exicator.

Film thicknesses were obtained by APLHA-STEP 500 Surface Profiler, Tencor[®], with resolution 1 to 2.5 nm, depending of height scanning range.

Gold contact pads utilized as electrodes, were deposited directly onto the film using thermal vacuum evaporation process. The square contact pads were 187 μm in size with a separation distance of 45 μm , seen in Figure 3.21.

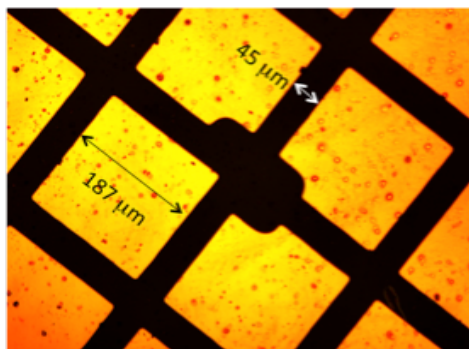


Figure 3.21. Gold contact pads as electrodes on the nanocomposite film; noted are size of pads and spacing in between them.

A 100 mesh PELCO TEM grids from Ted Pella Inc.[®] was used as a mask for this purpose. A ~ 50 nm thick layer of high purity gold was deposited onto the polymer film with mask at a chamber pressure of $\sim 10^{-6}$ torr. Electrical characterization was performed by Keithley[®] 236 source measure unit and Keithley 2636A Sourcemeter, in four point probe (Figure 3.22) mode with voltages ranging from 24 V to 14 V, in steps of 0.1 V.

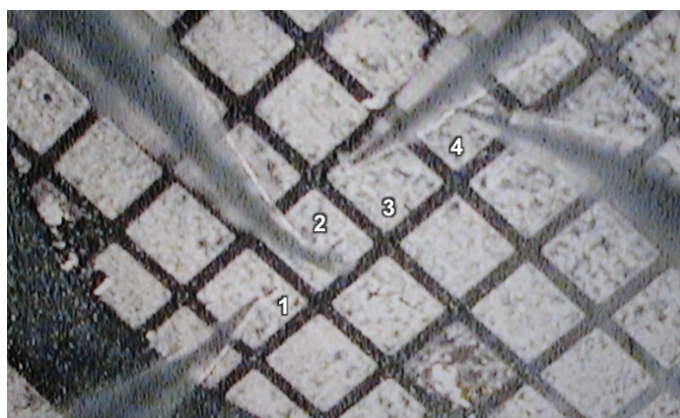


Figure 3.22. Four point probe electrical measurements on PVB nanocomposite films with gold contact pads as electrodes. Numbers 1 - 4 represent electrodes on which conductivity was measured.

Optical absorbance was measured by BioTek[®] Synergy 4 Plate, using resolution of 2 nm in the range from 300 to 700 nm, to cover transmittance in UV region (~360 nm) and visible light region (~550 nm). Set-up of optical measurement system shown in Figure 3.23.

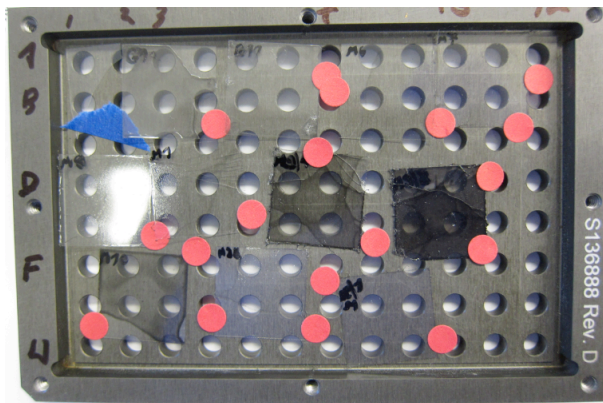


Figure 3.23. Image of BioTek Synergy 4 Plate with numerous samples characterized simultaneously.

Raman spectroscopy was performed on a Horiba Jobin Yvon[®] LabRAM HR800 confocal micro-Raman spectrometer using a MPC 6000 laser of 633 nm wavelength with a diffraction limited spot size of 1 μm .

Mechanical properties of the films were measured using a commercially available nanoindentation load-depth sensing instrument (Hysitron[®] TriboIndenter), equipped with an AFM. All tests were performed under identical conditions, using a standard diamond Berkovich indenter tip and an applied load of 2000 μN . In order to avoid the effects of the substrate, nanoindentation depth was kept from 1/5 to 1/3 of the film thickness. Loading – unloading (strain) protocol in the nanoindentation experiment is graphically demonstrated in Figure 3.24. Approach rate, starting at $P=0 \mu\text{N}$ (initial load) was of 200 μNs^{-1} until maximum load, $P_{\text{max}}=2000 \mu\text{N}$ was achieved. At maximum load, hold (dwelling) time was 2s after which the withdraw rate was 200 μNs^{-1} until load again reached value $P=0 \mu\text{N}$. Five nanoindents were performed for each investigated sample. Total testing time of whole procedure was 24 seconds.

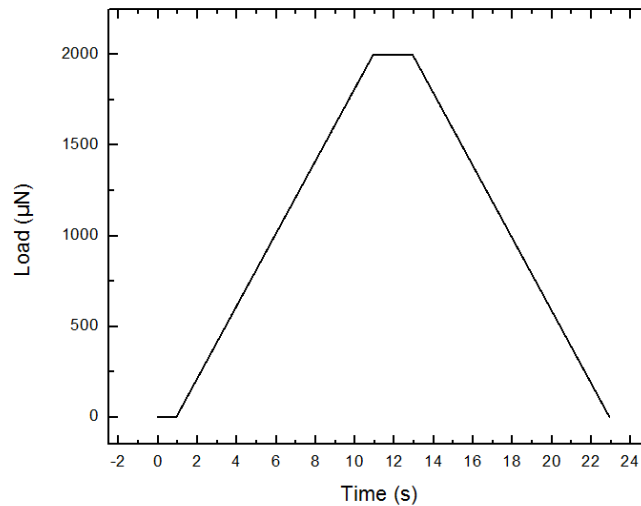


Figure 3.24. Graph depicting load as a function of time. Experimental indentation parameters for all sample measurements are: Initial load 0 μN , loading/unloading rate 200 μNs^{-1} , maximum load 2000 μN , and hold time, at maximum load, 2 s.

Structural characterization was performed by Olympus[®] CX41 optical light microscope and FEI[®] TEAM 0.5, 80-300 kV double-aberration-corrected (scanning) transmission electron microscope at 80.0 kV in imaging mode. Sample preparation for structural characterization of pristine nanofillers was as follows: as received graphene flakes, MWCNTs and SWCNTs were dispersed in isopropanol (Emsure, 99.8% purity) and sonicated for 1 min, after which they were deposited by micropipette on lacey carbon grids (Ted Pella Inc., S 166 – 3 i.e. 300 mesh). TEM sample preparation for nanocomposite thin films was as follows: the film was scraped from the wafer with a razor blade and the ball of film was positioned on a small triangular piece of a new small silicon wafer pieces. The film was encapsulated and attached to the wafer with M-Bond 610 and was set on a low temperature hot plate for 1.5 – 2h. The wafer along with the specimen was secured onto the microtome, and sections of the ball sitting at the top of the silicon piece were cut. PVB-nanofiller film sections with nominal thickness in the range of 50 – 80 nm were microtomed at room temperature using RMC Boeckeler[®] PT XL Ultramicrotome.

REFERENCES

- [1] F. C. Krebs, *Solar Energy Materials and Solar Cells*, 93 (2009) 394–412.
- [2] D. P. Birnie, In *Sol - Gel Technologies for Glass Producers and Users*, M. A. Aegerter and M. Mennig eds., Springer Science, New York, USA, 2004, p. 49-53.
- [3] <http://plasticphotovoltaics.org>
- [4] Z. Tang, Master Thesis, *Studies of Inverted Organic Solar Cells Fabricated by Doctor Blading Technique*, Linkoping University, Sweden, 2010, p. 40.
- [5] K. I. Popov, S. S. Djokic, B. N. Grgur, *Fundamental Aspects of Electrometallurgy*, Kluwer Academic Publishers, New York, USA, 2002, p. 225.
- [6] Y. D. Gamburg, G. Zangari, *Theory and Practice of Metal Electrodeposition*, New York, USA, 2011, p. 56.
- [7] S. Djokic, N. Nikolic, P. Zivkovic, K. Popov, N. Djokic, *ECS Transactions*, 33 (2011) 7-31.
- [8] E. R. Ivanovic, N. D. Nikolic, V. R. Radmilovic, *Journal of Serbian Chemical Society*, 80 (2015) 107–113.
- [9] V. V. Radmilovic, J. Kacher, E. R. Ivanovic, A. M. Minor, V. R. Radmilovic, *Crystal Growth & Design*, 16 (2016) 467–474.
- [10] T. Kaariainen, D. Cameron, M. - L. Kaariainen, A. Sherman, *Atomic Layer Deposition: Principles, Characteristics, and Nanotechnology Applications*, Second Edition, Scrivener Publishing LLC, Salem, USA, 2013, pp.14-15.
- [11] M. Leskela, M. Ritala, *Angewandte Chemie International Edition*, 42 (2003) 5548–5554.
- [12] BENEQ.COM
- [13] J. Niinisto and L. Niinisto In *Atomic Layer Deposition of Nanostructured Materials*, N. Pinna and M. Knez Eds., Wiley-VCH, Weinheim, Germany, 2012, pp. 16-18.
- [14] M. Lubitz, P. A. Medinal, A. Antic, J. T. Rosin, B. D. Fahlman, *Journal of Chemical Education*, 91 (2014) 1022–1027.
- [15] D. M. Mattox, *Handbook of Physical Vapor Deposition (PVD) Processing*, Second Edition, Elsevier, Oxford, UK, 2010, pp. 195-232.
- [16] H-H. Perkampus, *UV-VIS Spectroscopy and Its Applications*, Springer-Verlag, Berlin, Germany, 1992, p. 3.
- [17] T. Owen, *Fundamentals of UV-visible spectroscopy: A Primer*, Agilent Technologies, Germany, 1996.
- [18] L. B. Scaffardi, D. C. Schinca, M. Lester, F. A. Videla, J. M. J. Santillan, and R. M. A. Ekeroth, *UV-VIS and Photoluminescence Spectroscopy for Nanomaterials Characterization*, C. S.S.R. Kumar Ed., Springer-Verlag, Berlin, Germany, 2013.
- [19] P. E. J Flewitt and R. K. Wild, *Physical Methods for Materials characterization*, B. Cantor and M. J. Goringe Eds, Institute of Physics Publishing Bristol, UK, 2003, p. 210.
- [20] B. Chen, In *Dekker Encyclopedia of Nanoscience and Nanotechnology*, Vol. 1-6, Second Edition, C. I. Contescu and K. Putyera Eds., CRC Press Taylor & Francis Group, Boca Raton, USA, 2009, p. 3682-3683.
- [21] E. Smith and G. Dent, *Modern Raman spectroscopy-A practical approach*, John Wiley & Sons Ltd, Chichester, UK, 2005, pp. 4-5.
- [22] M. S. Dresselhaus, G. Dresselhaus, A. Jorio, A. G. Souza, and R. Saito, *Carbon*, 40 (2002) 2043-2061.
- [23] A. K. Dutta, D. Penumadu and B. Files, *Journal of Materials Research*, 19 (2004)

158–164.

- [24] A. C. Fischer-Cripps, In *Nanoindentation*, W. O. Winer, A. E. Bergles, G. A. Klutke, K. K. Wang, I. Finnie, J. R. Welty, M. D. Bryant, H. T. Yang, V. C. Mow, F. A. Leckie, D. Gross Eds., Third Edition, New York, Springer Science, New York, USA, 2011, p. 27.
- [25] W. C. Oliver, G. M. Pharr, *Journal of Materials Research*, 7 (1992) 1564–83.
- [26] W. C. Oliver, G. M. Pharr, *Journal of Materials Research*, 19 (2004) 3–20.
- [27] M. Lei, B. Xu, Y. Pei, H. Lu and Y. Q. Fu, *Soft Matter*, 12 (2016) 106–114.
- [28] L. Reimer, *Scanning Electron Microscopy: Physics of Image Formation and Microanalysis*, Second edition, Springer-Verlag, Berlin, Germany, 1998, pp. 1–3.
- [29] G. I. Goldstein, D. E. Newbury, P. Echlin, D. C. Joy, C. Fiori, E. Lifshin, *Scanning electron microscopy and x-ray microanalysis*, Plenum Press, New York, USA, 1981, p. 17.
- [30] P. Finkel, *Electron Microscopy*, Lecture notes, Drexler University, USA, 2011.
- [31] E. Suzuki, *Journal of Microscopy*, 208 (2002) 153–157.
- [32] G. D. Danilatos, *Advances in Electronics and Electron Physics*, 71 (1988) 109–250.
- [33] S. I. Wright, R. J. Larsen, *Journal of Microscopy*, 205 (2002) 245–252.
- [34] M. Bieda, K. Sztwiertnia, A. Korneva and J. Kawalko, In *The Transmission Electron Microscope*, K. Maaz Ed, InTech, Rijeka, Croatia, 2012, pp. 51–66.
- [35] B. L. Adams, *Ultramicroscopy* 67 (1997) p. 11–17.
- [36] J. Ayache, L. Beaunier, J. Boumendil, G. Ehret, D. Laub, *Sample Preparation Handbook for Transmission Electron Microscopy: Methodology*, Springer Science, New York, USA, 2010, pp. 96–98.
- [37] C. R. Perrey, C. B. Carter, J. R. Michael, P. G. Kotula, E. A. Stach and V. R. Radmilovic, *Journal of Microscopy*, 214 (2004) 222–236.
- [38] D. B. Williams, C. B. Carter, *Transmission Electron Microscopy: A Textbook for Materials Science*, Second Edition, Springer Science Business Media LLC, New York, USA, 2009, p. 7.
- [39] P. E. Champness, *Electron Diffraction in the Transmission Electron Microscope*, Taylor & Francis, New York, USA, 2001, p. 5.
- [40] A. Tolley, V. R. Radmilovic, U. Dahmen, *Scripta Materialia*, 52 (2005) 621–625.
- [41] C. Hammon, *The Basics of Crystallography and Diffraction*, Oxford University Press, New York, USA, 1997, p. 166.
- [42] C. Ophus, Molecular Foundry, National Center for Electron Microscopy, LBNL, Berkeley; private communication.
- [43] V. R. Radmilovic, private communication.
- [44] P. A. Midgley and M. Weyland, In *Scanning Transmission Electron Microscopy: Imaging and Analysis*, S. J. Pennycook and P. D. Nellist Eds., Springer Science+Business Media, LLC, New York, USA, 2011, p. 370.
- [45] S. Wenner, PhD Thesis, *Transmission electron microscopy and Muon Spin Relaxation studies of Precipitation in Al-Mg-Si Alloys*, Norwegian University of Science and Technology, Trondheim, Norway, 2014, p. 30.
- [46] TEAM Project (Transmission Aberration-Corrected Electron Microscope), National Center for Electron Microscopy, Lawrence Berkeley National Laboratory, Berkeley, USA.

-
- [47] E. Spiecker, Friedrich Alexander University of Erlangen-Nuremberg, Germany, private communication.
- [48] J. Zach, *Philosophical Transactions of the Royal Society A*, 367 (2009) 3699–3707.
- [49] <http://www.ceos-gmbh.de/English/research/revolution.html>
- [50] SALVE Project, University of Ulm, Germany.
- [51] M. Haider, P. Hartel, H. Müller, S. Uhlemann, J. Zach, *Philosophical Transactions of the Royal Society A*, 367 (2009) 3665–3682.
- [52] A. M. Cormack, *Journal of Applied Physics*, 34 (1963) 2722-2727.
- [53] D. J. de Rosier, A. Klug, *Nature*, 217 (1968) 130-134.
- [54] W. Hoppe, R. Hegerl, In *Computer Processing of Electron Microscope Images*, P. W. Hawkes (Ed.), Springer, Berlin, Germany, 1980, pp. 127-128.
- [55] W. Hoppe, R. Langer, G. Knesch, C. Poppe, *Naturwissenschaften*, 55 (1968) 333-336.
- [56] G. N. Hounsfield, *A Method and Apparatus for Examination of a Body by Radiation such as X or Gamma Radiation*, Patent No. 1283915-A, The Patent Office, London, UK, 1972.
- [57] J. Radon, *IEEE Transactions on Medical Imaging*, 5 (1986) 170–176; *J. Radon Math.- Phys. KI.* 69 (1917) 262-277.
- [58] P. A. Midgley and M. Weyland, *Ultramicroscopy*, 96 (2003) 413-431.
- [59] P. Ercius, O. Alaidi, M. J. Rames, and G. Ren, *Advanced Materials*, 27 (2015) 5638–5663.
- [60] R. A. Crowther, D. J. DeRosier, A. Klug, *Proceedings of the Royal Society of London A*, 317 (1970) 319-340.
- [61] M. Radermacher, *Journal of Electron Microscopy Technique*, 9 (1988) 359-394.
- [62] M. Gobelt, R. Keding, S. W. Schmitt, B. Hoffmann, S. Jackle, M. Latzel, V. V. Radmilovic, V. R. Radmilovic, E. Spiecker and S. Christiansen, *Nano Energy*, 16 (2015) 196-206.
- [63] J. Rodenburg, B. McCallum, P. Nellist, *Ultramicroscopy*, 48 (1993) 304-314.
- [64] J. Cowley, *Ultramicroscopy*, 87 (2001) 1–4.
- [65] C. Gammer, V. B. Ozdol, C. H. Liebscher, A. M. Minor, *Ultramicroscopy*, 155 (2015) 1–10.
- [66] V. B. Ozdol, C. Gammer, X. G. Jin, P. Ercius, C. Ophus, J. Ciston, and A. M. Minor, *Applied Physics Letters*, 106 (2015) 253107.
- [67] S. W. Schmitt, C. Venzago, B. Hoffmann, V. Sivakov, T. Hofmann, J. Michler, S. Christiansen, G. Gamez, *Progress in Photovoltaics: Research and Applications*, 22 (2014) 371-382.

4. Results

4.1. AgNWs and AgNWs/AZO Nanocomposite

Figure 4.1a shows AgNWs as synthesized by polyol reduction method and deposited on silicon substrate via drop casting method, imaged at 5kV voltage and 0.1 nA current. Figure 4.1b represents a histogram of diameter distribution of AgNWs. From this data, the average diameter of AgNWs is calculated to be 132.3 ± 32.2 nm with the majority of the NWs being in the 100 - 150 nm range.

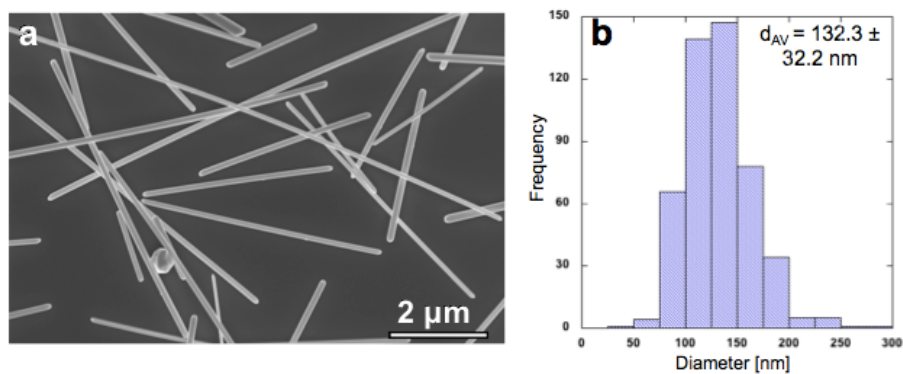


Figure 4.1. a) Scanning electron micrograph of as synthesized AgNWs, b) Histogram of diameter distribution.

Figure 4.2 shows scanning electron micrographs, imaged at 5kV voltage and 0.1 nA current, using through lens detector (TLD), of AgNWs annealed at nominal temperature of 250 °C for 3 minutes.

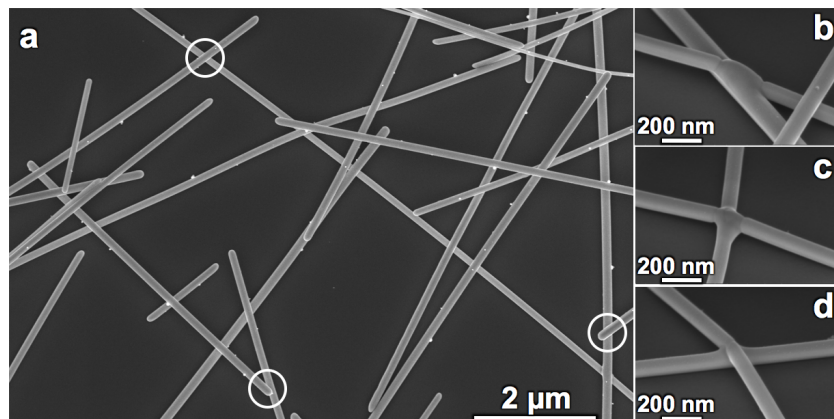


Figure 4.2. a) Scanning electron micrograph AgNWs after annealing, b-d) High magnification scanning electron micrographs of random welded junctions; After [1]; Circles denote welded junctions.

Figures 4.2b-d are high magnification SEM micrographs showing random welded junctions in more detail. It can be seen that after annealing AgNWs are welded. These welded junctions are not the ones noted by white circles in Figure 4.2a.

Figure 4.3. is X-ray diffraction (XRD) graph showing intensity as a function of 2θ angle, of AgNWs drop cast on 100 silicon (Si) wafer substrate. Present peaks correspond to Ag 111 and 200 lines as well as Si 400 line. This XRD was recorded in the 2θ angle range of 25-80°.

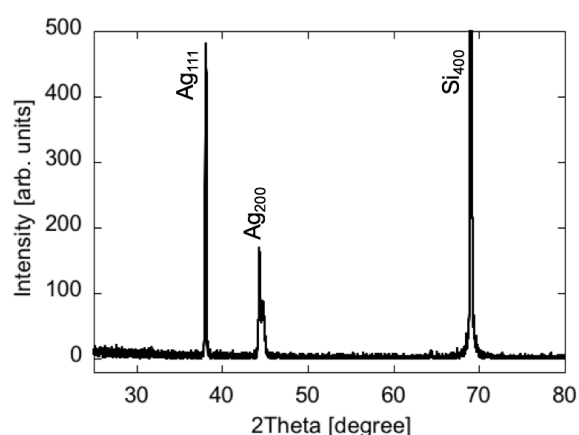


Figure 4.3. X-ray diffraction analysis of investigated AgNWs.

Figure 4.4a shows AgNWs on Si wafer substrate after annealing and the atomic layer deposition of AZO. Figure 4.4b represents a histogram of AgNWs diameter distribution. From this data, the average diameter of AgNWs is calculated to be 310.4 ± 38.2 nm.

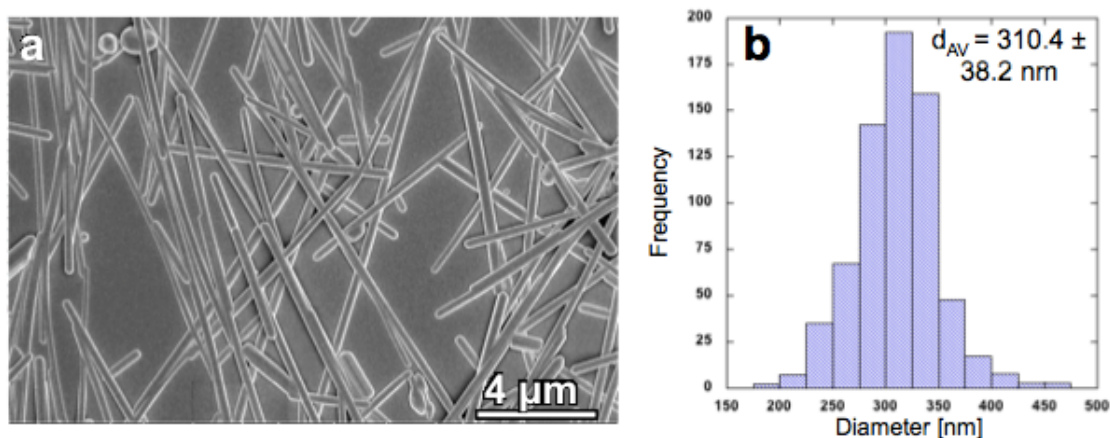


Figure 4.4. a) Scanning electron micrograph of AgNWs after annealing and AZO deposition, b) Histogram of diameter distribution.

Figure 4.5 shows scanning electron micrographs of AgNWs, annealed at nominal temperature of 250 °C for 3 minutes and then encapsulated with aluminum doped zink oxide (AZO) by atomic layer deposition. Figures 4.5b-d are high magnification micrographs showing random welded junctions in more detail. These welded junctions are not the ones noted by white circles in Figure 4.5a.

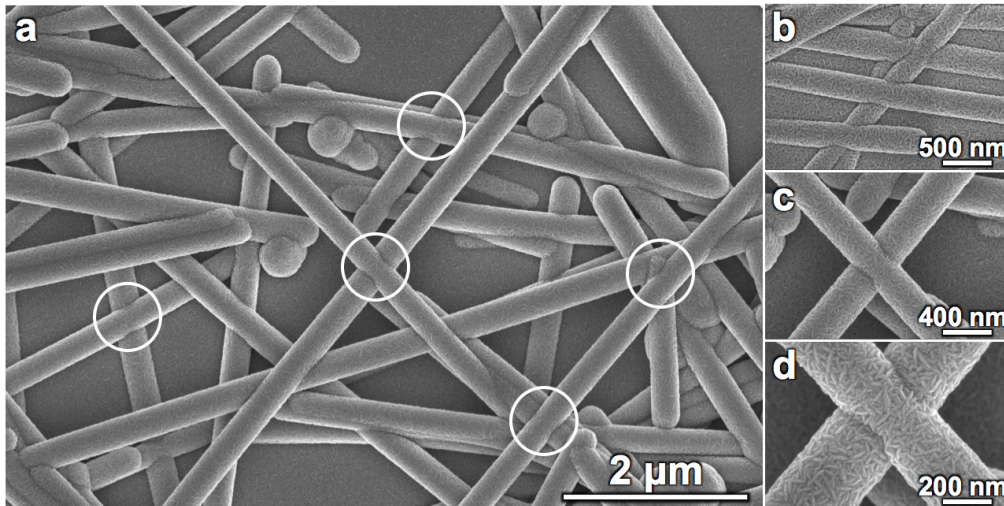


Figure 4.5. a) Scanning electron micrograph AgNWs with AZO encapsulation, b-d) High magnification scanning electron micrographs of random welded junctions. Circles denote welded junctions.

Figure 4.6a is a scanning transmission electron microscopy (STEM) high angle annular dark field (HAADF) image of AgNWs encapsulated with AZO.

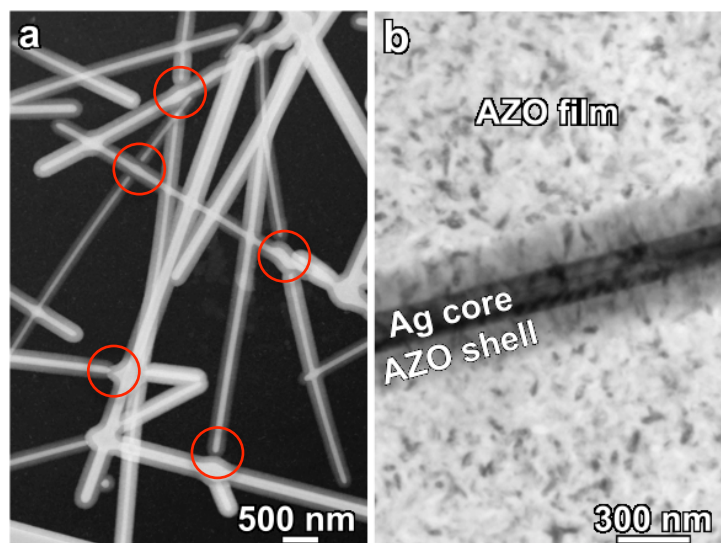


Figure 4.6. a) HAADF STEM image of AgNWs encapsulated with AZO, b) CTEM image of an AgNW encapsulated with AZO in plain view.

Numerous welded junctions can be seen from the image as well as discontinued welded junctions where integrity is not preserved, noted by red circles. Figure 4.6b is a conventional transmission electron microscopy (CTEM) image of a plain view AgNW encapsulated with aluminum doped zinc oxide (AZO) showing the uniform thickness of AZO shell encapsulating the AgNW core. This image shows also that the AZO nano-grains exhibit columnar growth on Ag.

Figure 4.7a is a CTEM image of AZO film. Homogenous crystalline film can be observed exhibiting a nano-grain structure. Figure 4.7b represents SAD pattern of the area shown in Figure 4.7a while Figure 4.7c represents a simulated ring diffraction pattern of ZnO wurzite structure where the first ten rings are of the following indices: 010, 002, 011, 012, 110, 013, 020, 112, 021, and 004. In Figure 4.7d rotational average line profile is given as intensity as a function of spacing, of experimental SAD pattern, showing Miller indices for the first ten rings.

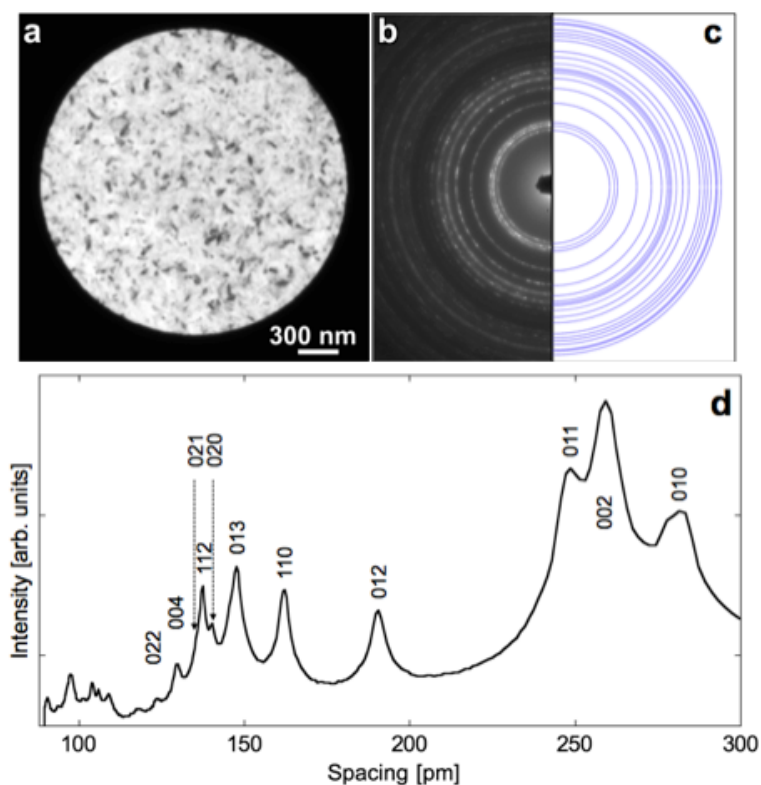


Figure 4.7. a) Conventional transmission electron micrograph of AZO, taken with inserted selected area diffraction pattern; b) Selected area diffraction (SAD) pattern of area shown in a); c) simulated ring diffraction pattern for ZnO wurzite structure, d) rotational average line profile of experimental SADP shown in b).

Figure 4.8a is a high resolution phase contrast image of AZO layer. Three grains of AZO (1, 2 and 3) are marked and their respective FFTs are shown as insets.

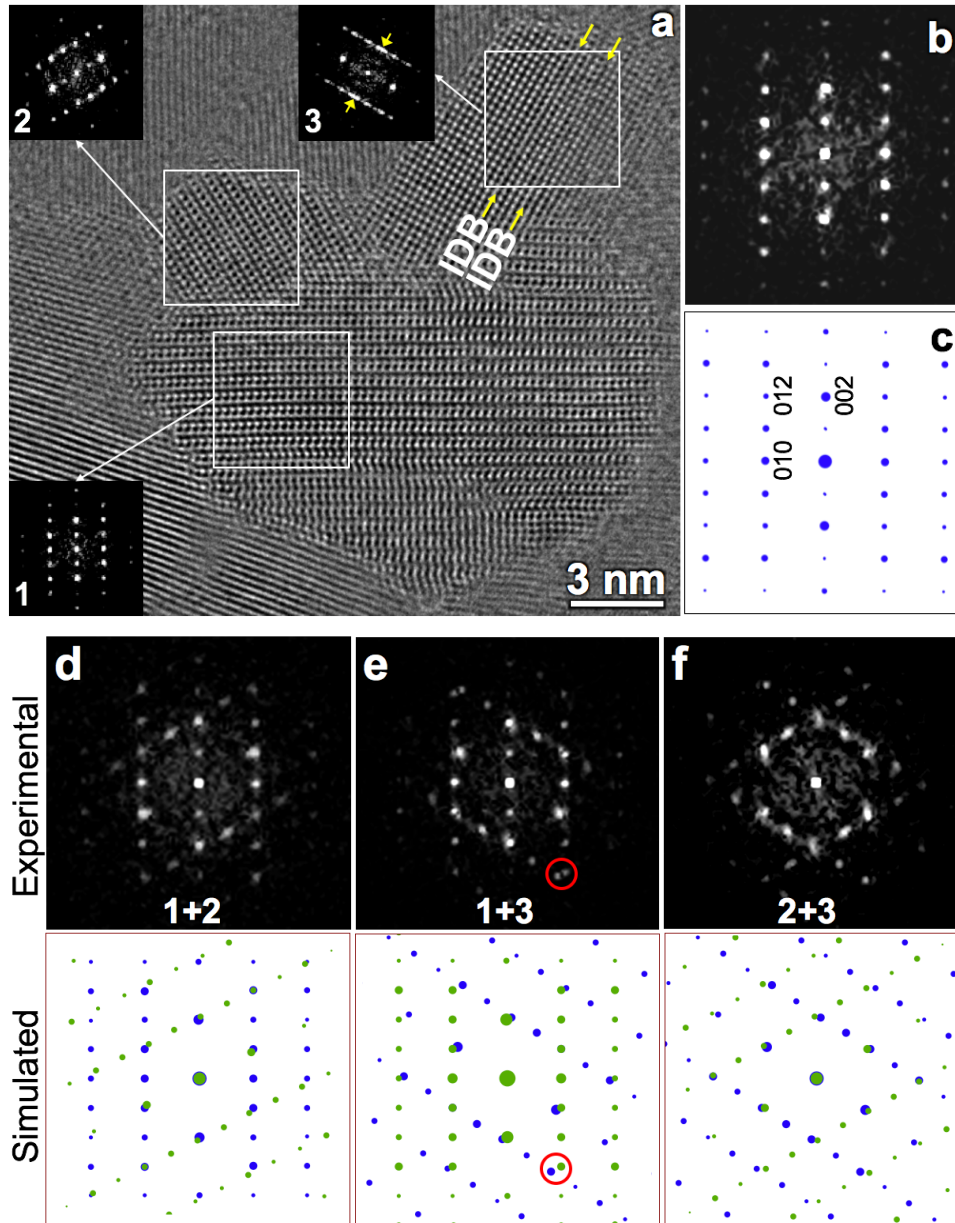


Figure 4.8. a) High resolution phase contrast image of AZO taken close to $[100]$ zone axis; insets present Fast Fourier Transform (FFT) of grains shown in white squares; Inversion domain boundary (IDB) noted by white arrows; b) Enlarged FFT taken from AZO grain 1; c) Simulated ZnO wurtzite structure in $[100]$ zone axis with noted reflections; d-f) Composite FFTs of grains 1 + 2, 1 + 3 and 2 + 3, respectively; Simulated structures are presented below each FFT composite; Red circles represent $\sim 5^\circ$ difference in rotation between grains 1 and 3.

The presence of inversion domain boundary (IDB) can be seen in grain 3. Enlarged FFT of grain 1 is shown in Figure 4.8b while the simulated AZO wurtzite structure in [100] zone axis is shown in Figure 4.8c, where 010, 002 and 012 reflections are noted. Figure 4.8d is an composite FFT of grains 1 and 2, showing their crystallographic relationship as $(100)_1 // (100)_2$ $[010]_1 // [013]_2$, verified by the simulated structure in image below. Figure 4.8e is a composite FFT of grains 1 and 3, showing their crystallographic relationship as $(100)_1 // (100)_3$ $[010]_1 // [013]_3$, verified by the simulated structure in image below, where the red circles show that grain 3 is rotated $\sim 5^\circ$ counter clockwise around [100] direction with respect to grain 1. Figure 4.8f is a composite FFT of grains 2 and 3, showing their crystallographic relationship as $(100)_2 // (100)_3$ $[011]_2 // [002]_3$, verified by the simulated structure in image below.

Figure 4.9a represents an HAADF image of AgNWs encapsulated with AZO and EDS maps corresponding to the HAADF image. The maps displays individual elemental

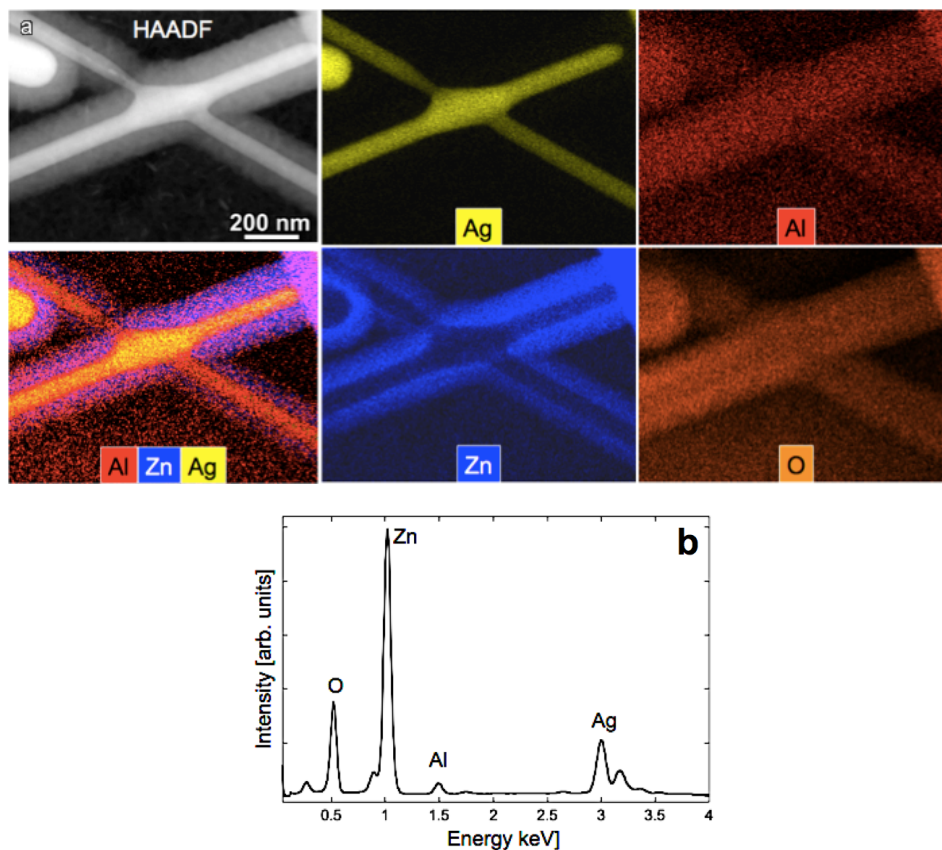


Figure 4.9. a) HAADF image of AgNWs encapsulated with AZO and energy dispersive spectroscopy (EDS) maps of silver (yellow), aluminum (red), zinc (blue) and oxygen (orange) [1], b) EDS spectrum taken from the area shown in the HAADF in a).

distribution of silver, aluminum, zinc, oxygen as well as an Al/Zn/Ag composite of elemental distribution. It can be seen that silver distribution (yellow) corresponds to the location of AgNWs cores in the HAADF image, while zinc (blue), aluminum (red) and oxygen (orange) are present in the AZO shell. Figure 4.9b is a cumulative EDS spectrum of the region showing the lines of all elements present in this nanocomposite structure.

Figure 4.10 is a low magnification STEM annular dark field (ADF) image of AgNW cores encapsulated with AZO columnar nano-grain shells, displayed as white and grey regions, respectively. It is clear that the AZO film is very homogenous in thickness distribution and structure, and it seems to grow radially from the AgNWs and substrate outward. AgNWs are confirmed to have a mostly pentagonal twinned structure with fairly uniform diameter distribution. Some AgNWs present in Figure 4.10, appear to be blurry, the result of their axes being tilted with respect to electron beam. Also shown are the electron and ion beam protective carbon deposited layers.

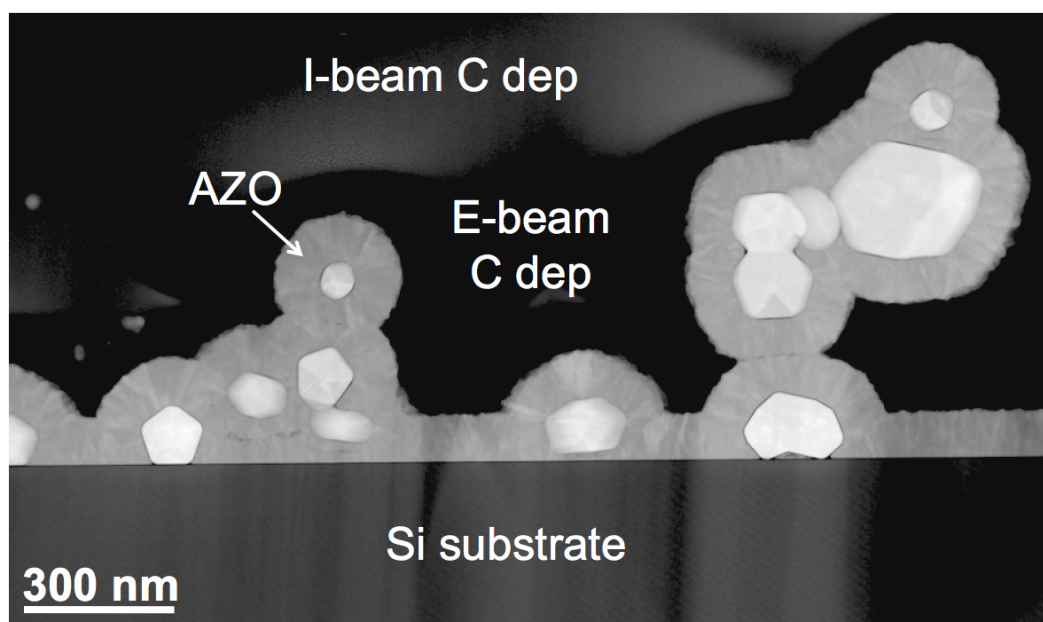


Figure 4.10. Low magnification ADF scanning transmission electron micrograph of a cross-section of AgNWs/AZO nanocomposite; note the pentagonal cross-section of AgNWs and columnar growth of AZO nano-grains.

Figure 4.11a is an ADF STEM image of a single AgNW encapsulated with AZO, slightly above the silicon substrate, tilted close to $\langle 110 \rangle$ zone axis. It can be seen

here in more detail, with heterogeneous intensity distribution, the columnar grain structure of AZO and the pentagonal twin structure of the AgNW. Interfacial region between the AgNW and AZO is distinctly seen as a black rim.

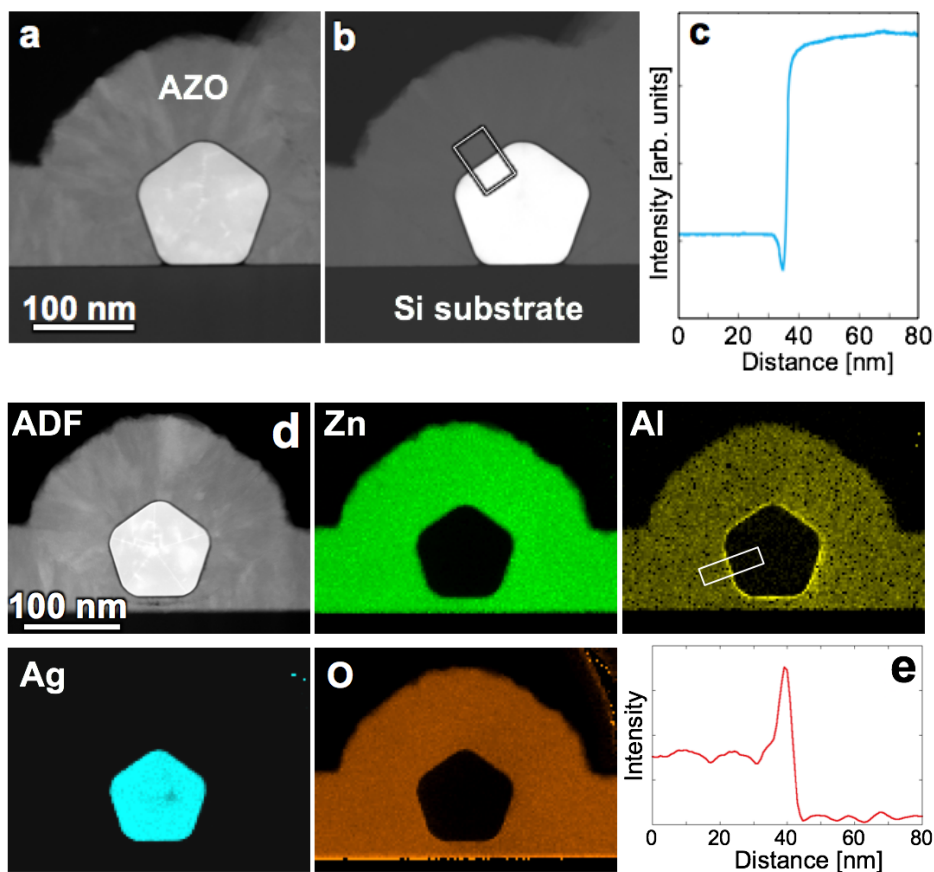


Figure 4.11. a) ADF micrograph of single AgNW encapsulated with AZO; b) HAADF micrograph of same NW; c) integrated line profile across AgNW/AZO interface within white rectangle in b); d) ADF image of a different AgNW with appropriate EDS maps for silver, zinc, oxygen, and aluminum [2]; e) integrated line profile across AZO/black pentagonal region interface within white rectangle in aluminum map.

Figure 4.11b is a HAADF (pure Z-contrast) STEM image of same structure where no strain can be seen in the AgNW core as well as no structural details in the AZO shell. Figure 4.11c represents a graph depicting an integrated line profile across the AgNW/AZO interface (black rim) within the white rectangle noted in Figure 4.11b. The thickness of the interfacial region was calculated to be $\sim 3\text{-}5\text{nm}$. The corners in this pentagonal AgNW seem to be rounded as opposed to sharp. Figure 4.11d is an ADF STEM image of a different AgNW encapsulated with AZO from which EDS maps

showing elemental distribution of zinc (green), aluminum (yellow), silver (turquoise) and oxygen (dark orange) were acquired. In the EDS map of aluminum, a thin layer of increased concentration of aluminum species is segregated on the AgNW (black pentagonal region)/AZO interface. Figure 4.11e represents a graph depicting an integrated line profile (as intensity as a function of distance) across the AgNW (black pentagonal region)/AZO interface within the white rectangle noted in map corresponding to aluminum distribution. From this graph, the thickness of the thin layer of increased concentration of aluminum was calculated to be ~3-5nm. In the EDS map of oxygen, a thin layer of increased concentration of oxygen species is present at the bottom of the sample, indicating the presence of native SiO₂ layer on silicon substrate surface.

Figure 4.12a is a low magnification ADF STEM image of a cross-section of welded AgNWs encapsulated with AZO before tilting of the sample. The AgNWs appear blurry. Tilting of the left AgNW close to <110> zone axis, different welded regions between 3 AgNWs can be observed and are indicated by white arrows shown in Figure 4.12b. From this image, five twin segments of the AgNW tilted to <110> zone axis, as well as the present strain within each twin segment, manifested by bright areas, can clearly be observed.

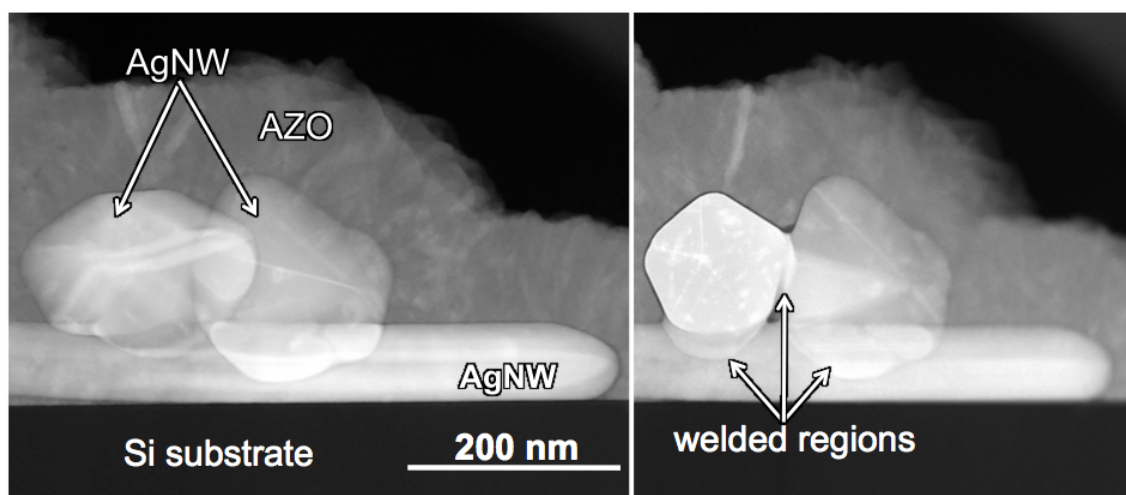


Figure 4.12. Low magnification ADF scanning transmission electron microscopy cross-sectional image of welded Ag NWs a) before tilting; b) after tilting, where welded regions are indicated by white arrows; note rounded interface between welded zone and bottom NW; After [1].

Figure 4.13a is a high resolution ADF STEM image of a welded region between two AgNWs. Red dotted line represents twin plane between neighboring twin segments.

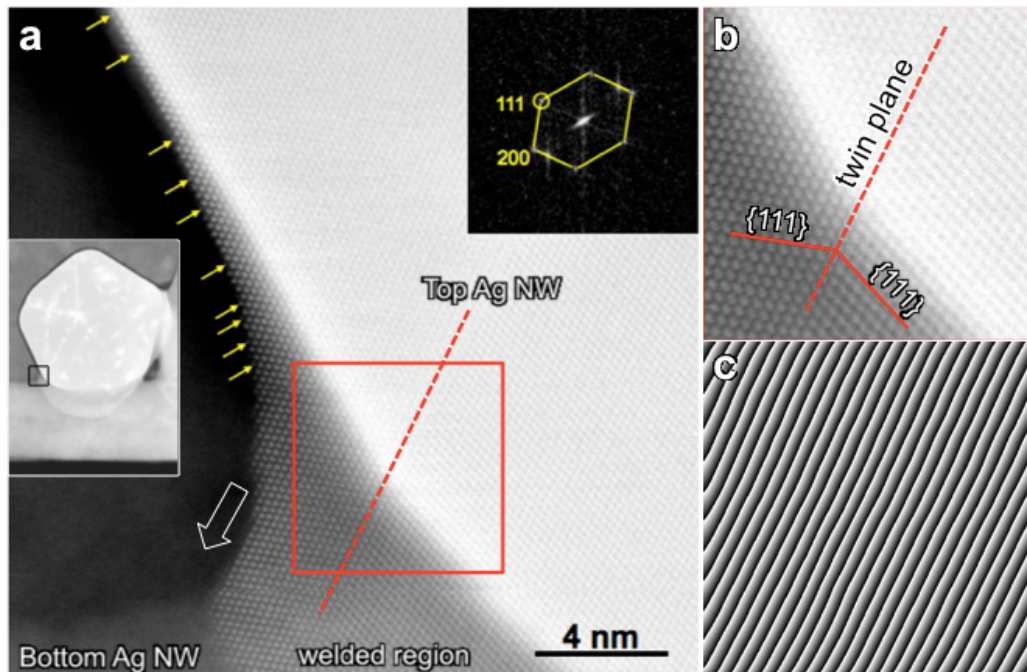


Figure 4.13. a) High resolution ADF STEM cross-sectional image of welded region between two Ag NWs; left inset: low magnification image with black square showing analyzed region; right inset: FFT from the red square region; b) enlarged region indicated by red square in a); c) moiré pattern obtained using 111 reflection indicated by yellow circle in FFT inset in a); Dotted red lines represent twin plane, extending from the top NW into the welded region; After [1].

The left inset is a low magnification image of two AgNWs with a black square denoting the analyzed region. Right inset is an FFT from the region denoted by the red square where the yellow hexagon indicates $\langle 110 \rangle$ zone axis. Wetting angle between top NW and welded region was measured to be $\sim 4.8^\circ$. Yellow arrows indicate 200 terraces in the welded zone, formed during attachment of Ag atoms, while the white arrow denotes welded zone growth direction. Figure 4.13b is an enlarged image of region denoted by the red square in 4.13a. Red dotted line represent twin plane while red solid lines represent orientation of $\{111\}$ planes symmetrical to each other with respect to $\{111\}$ twin plane. It is evident that there is a continuation and no visible distortion of $\{111\}$ planes, parallel to the twin plane, going from the top NW into the welded region. This is confirmed by the moiré pattern (Figure 4.13c) obtained using 111 reflection, indicated

by a yellow circle in FFT inset in Figure 4.13a, which clearly shows continuation i.e. no change of orientation.

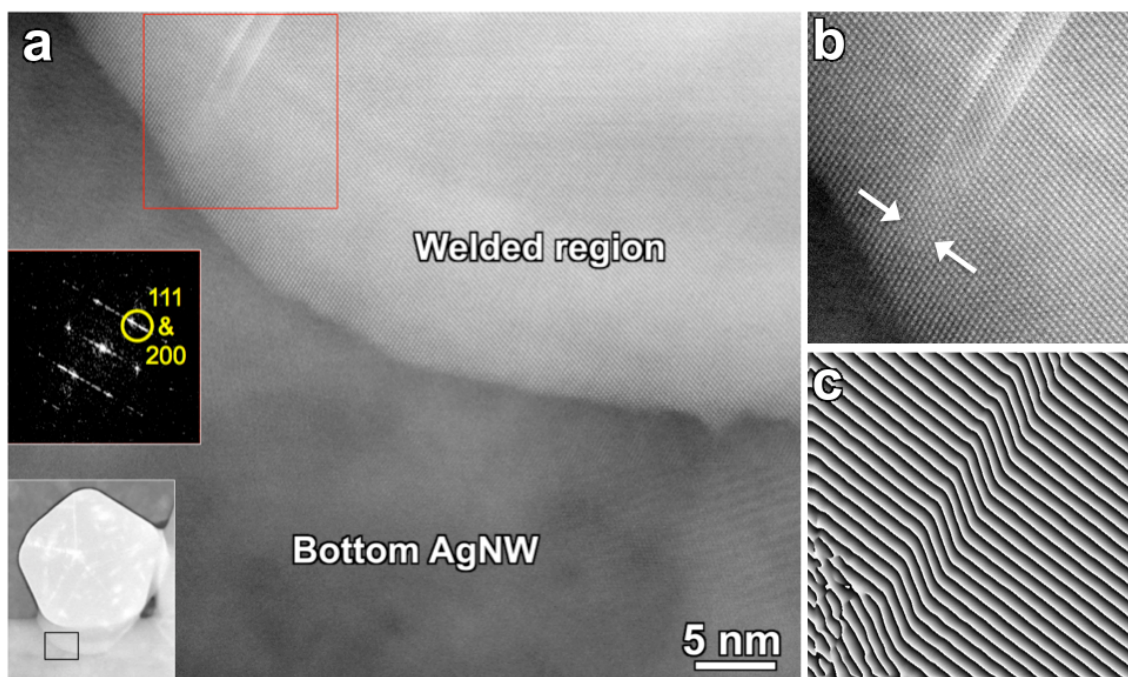


Figure 4.14. a) High resolution ADF STEM cross-sectional image of welded region between two Ag NWs; bottom left inset: low magnification image with black square showing analyzed region; upper left inset: FFT from the red square region; b) image of enlarged region indicated by red square in a) with noted twin planes by white arrows, c) moiré pattern obtain using 111 & 200 reflections indicated by yellow circle in FFT.

Figure 4.14a is a high resolution ADF STEM image of a welded region between two AgNWs. The bottom left inset is a lower magnification image of two AgNWs with a black square denoting the analyzed region. Upper left inset is an FFT from the region denoted by the red square where, which indicates $\langle 110 \rangle$ zone axis and the presence of a twin. From Figure 4.14a a rough interface between welded region and bottom AgNW, with protrusions into the bottom NW can be seen. Figure 4.14b is an enlarged region indicated by red square in Figure 4.14a, where a twin is clearly present with white arrows indicating twin planes. Figure 4.14c is a moiré pattern obtained using 111 and 200 reflections, indicated by a yellow circle in left FFT in Figure 4.14a.

Figure 4.15a is a high resolution ADF STEM image of the right-hand side welded region between two AgNWs. The left inset is a lower magnification image of two AgNWs with a black square denoting the analyzed region.

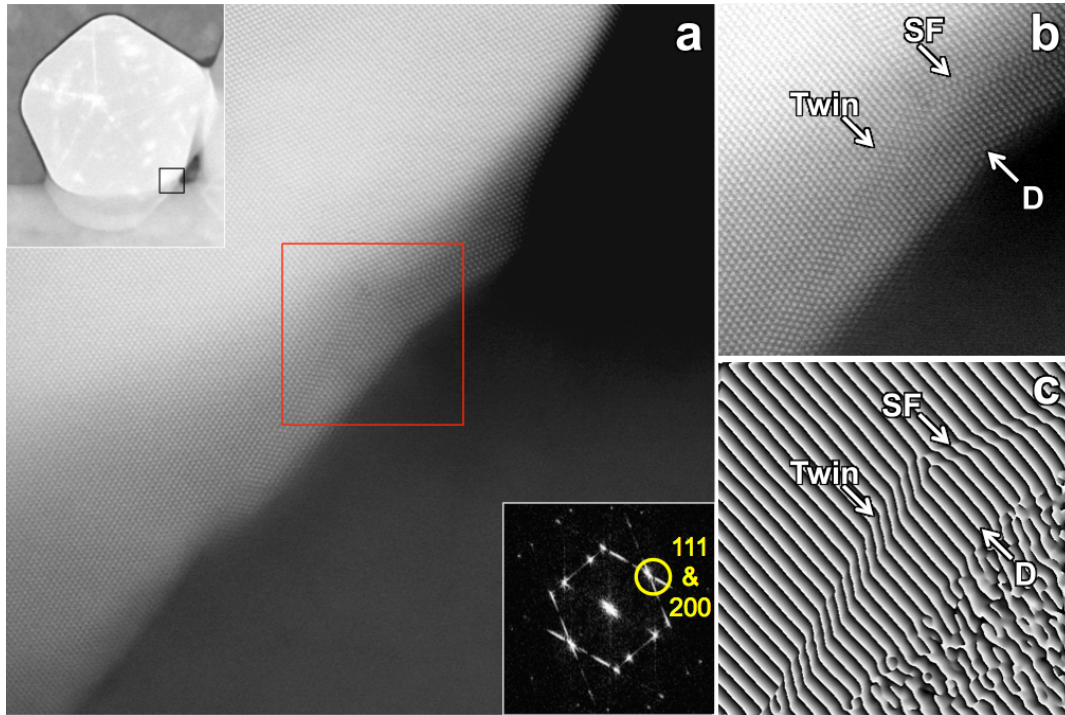


Figure 4.15. a) High resolution ADF STEM cross-sectional image of the right-hand side welded region between two Ag NWs; left inset: low magnification image with black square showing analyzed region; right inset: FFT from the red square region, b) enlarged region indicated by red square in a); c) moiré pattern obtain using 111 and 200 reflections indicated by yellow circle in FFT inset in a).

Right inset is an FFT from the region denoted by the red square, displaying $\langle 110 \rangle$ zone axis. Figure 4.15b presents an enlarged region indicated by red square in 4.15a. The presence of a twin, stacking fault (SF) and dislocation (D), inside the welded zone can be observed, denoted in both, Figs. 4.15b and c. Figure 4.15c is a moiré pattern obtained using 111 and 200 reflections, indicated by a yellow circle in FFT inset in Figure 4.15a.

Figure 4.16 represents a high resolution scanning transmission electron microscopy (HRSTEM) image of the center of an AgNW taken close to $\langle 110 \rangle$ crystallographic direction with appropriate displacement and strain maps. Inset is an showing the decahedral symmetry of the pentagonal structure. Direct atomic column measurements of crystal lattice distortion are represented as maps in Figures 4.16b-e as horizontal, vertical, radial and annular displacements, respectively. The first derivatives of displacement maps are strain maps shown in Figures 4.16f-i. Displacement and strain are mostly localized in twin segments in 1 and 2, partially in twin segment 3 while twin segments 4 and 5 exhibit minor, mostly horizontal displacement and strain.

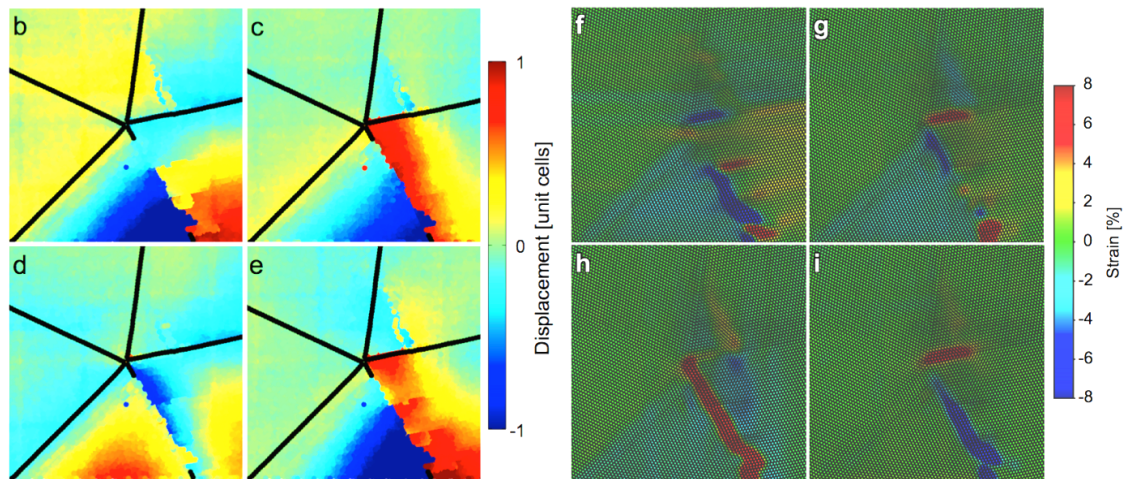
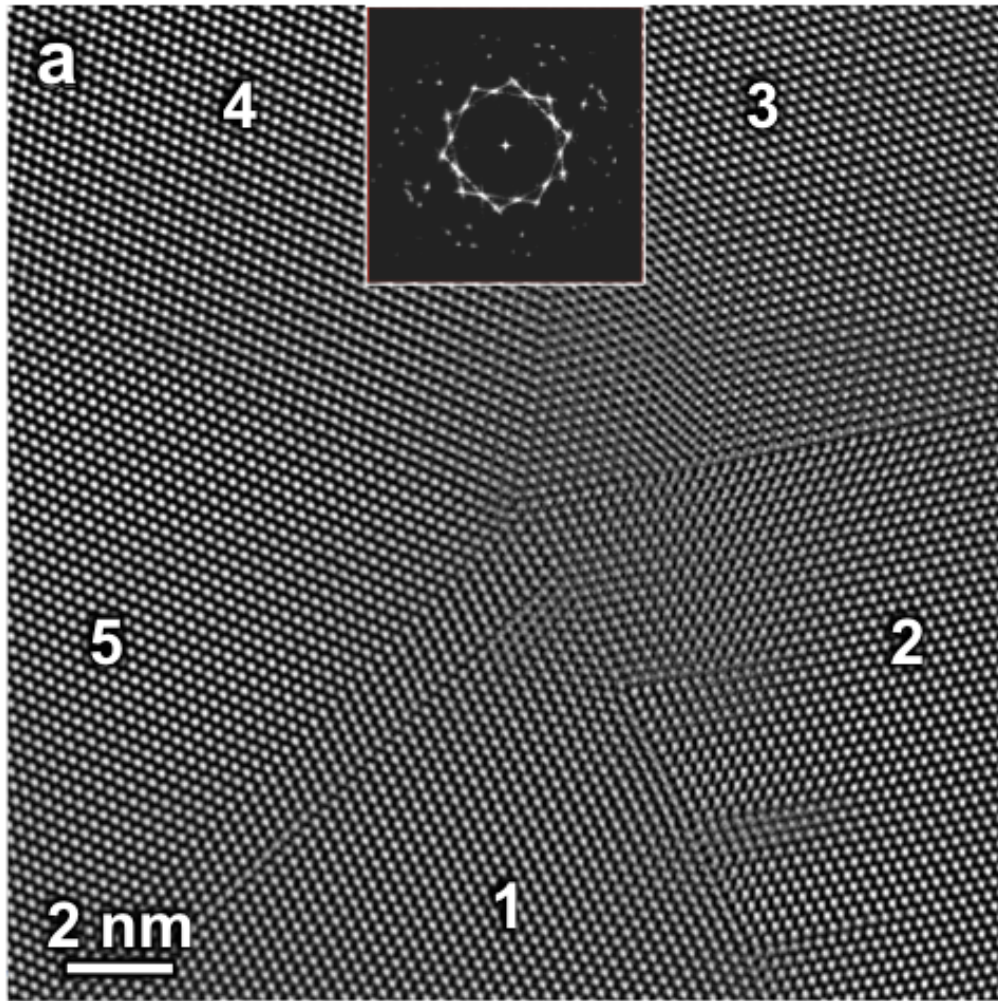


Figure 4.16. a) HRSTEM HAADF image of AgNW with twin segments indicated by numbers 1-5; inset is an FFT from twin segment 1; Displacement maps: b) Horizontal; c) Vertical; d) Radial; e) Annular; Strain maps: f) Horizontal (ϵ_{xx}), g) Shear (ϵ_{xy}), h) Vertical (ϵ_{yy}), i) rotational (θ).

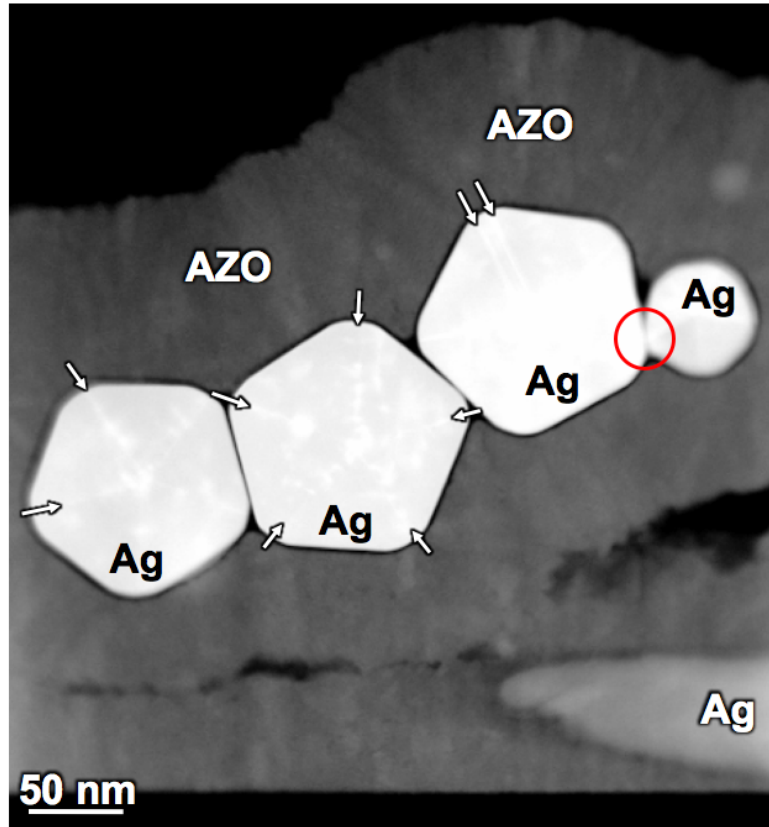


Figure 4.17. ADF scanning transmission electron micrograph of AgNWs encapsulated in AZO; White arrows indicate twin planes and red circle indicates formation of neck region [1].

Figure 4.17 is a low magnification STEM ADF image of AgNWs encapsulated in AZO. Three larger AgNWs are in contact with each other via 100 flat surfaces where no welded regions are present. In the area indicated by the red circle, corner of the small NW is in contact with the flat area (100 facet) of the neighboring larger AgNW and a welded region is present. AgNW twin segments, orientated close to $\langle 110 \rangle$ zone axis, are symmetrical with respect to the twin planes, noted by white arrows.

Figure 4.18a represents a HRSTEM image of a corner of an AgNW. Figure 4.18b presents enlarged image indicated by red square in Figure 4.18a showing that the reentrant angle is $\sim 141^\circ$, at the corners of pentagonal cross-section where two twin segments meet. Red dots illustrate FCC unit cells in neighboring AgNW twin segments, orientated close to 110 zone axis, symmetrical with respect to the $\{111\}$ twin plane, denoted by white dotted line.

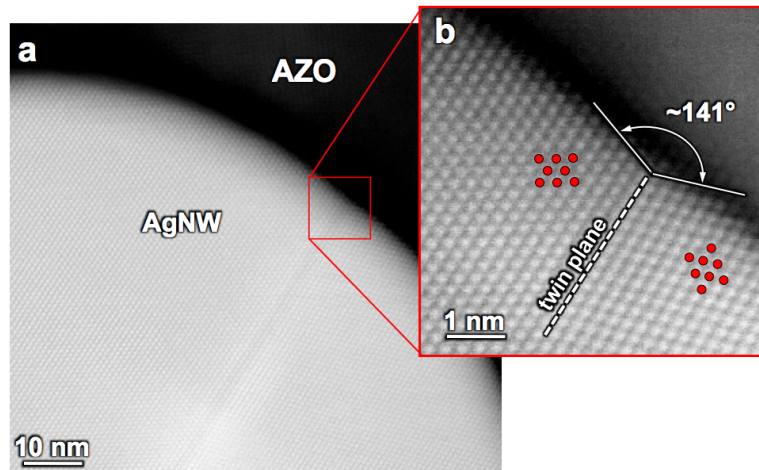


Figure 4.18. a) HRSTEM image of AgNW corner and b) enlarged region indicated by red square in a) showing a reentrant angle of $\sim 141^\circ$ at the corners of pentagonal cross-section where two twin segments meet; red dots illustrate FCC unit cells in neighboring AgNW twin segments.

Figure 4.19 presents a graph depicting surface roughness (height) of the AgNWs/AZO nanocomposite as a function of distance.

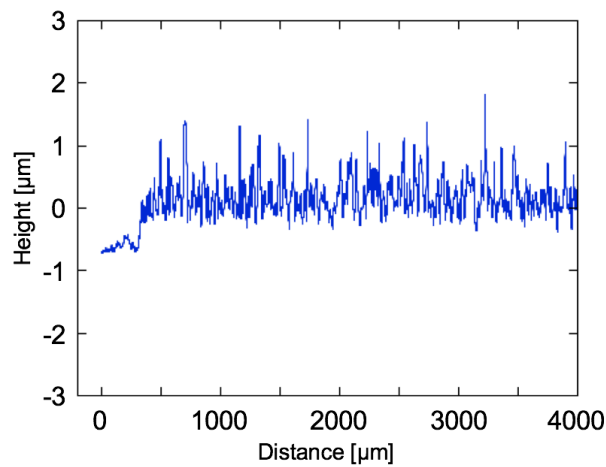


Figure 4.19. Roughness measurement for AgNWs/AZO nanocomposite presented as height as a function of distance.

Using the formula:

$$R_a = \frac{1}{l} \int_0^l f(x) dx$$

where l is the evaluation length and $f(x)$ is the profile height function, the average surface roughness can be calculated, which is the arithmetic average of the surface

profile (peaks and valleys). The value calculated was 236.19 nm. Using the formula:

$$R_q = \left[\frac{1}{l} \int_0^l f(x)^2 dx \right]^{1/2}$$

root mean square (RMS) surface roughness can be calculated, which is the root mean square average of the profile height deviations from the mean line recorded within the evaluation length. The value calculated was 309.52 nm.

Figure 4.20 shows optical transmittance for various electrodes. It can be seen that transmittance of AgNWs and AZO is above 80% at 550nm. Sheet resistance for AZO is 368 Ω /sq while sheet resistance for AgNWs was too high to be measured by the experimental setup. The AZO encapsulated AgNW composite, where AgNWs have not been annealed, has the sheet resistance of 343 Ω /sq with a transmittance of ~55% at 550nm. Annealed AgNWs exhibit a resistance drop down to 18 Ω /sq without affecting the transmittance. Annealed AgNWs that are subsequently encapsulated with AZO show the lowest resistance of 12 Ω /sq, but also with the lowest transmittance of ~55% at 550nm.

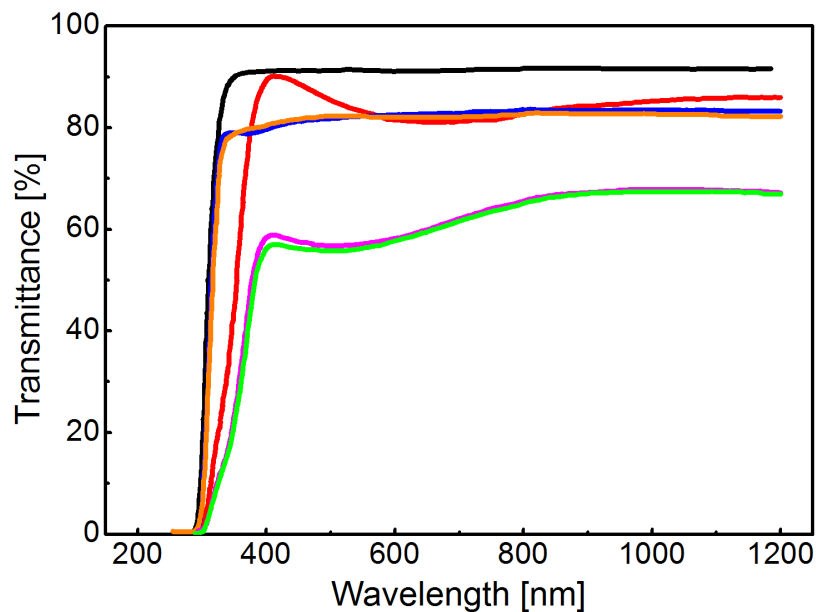


Figure 4.20. Optical transmittance of various electrodes in the UV-VIS/NIR spectra: 100 nm thick AZO film (red line), AgNWs (orange line), heated AgNWs (blue line), AgNWs encapsulated by 100 nm thick AZO film (green line), heated AgNWs and subsequently encapsulated by 100 nm thick AZO film (pink line). Bare glass substrate is represented by a black line; After [2].

Figure 4.21 represents a graph of current density as a function of voltage for silicon based solar cells with various top electrodes, measured under AM1.5 illumination conditions (standard solar spectra at Earth's surface). From this graph various solar cells parameters can be obtained: open circuit voltage (V_{OC}), short circuit current density (J_{SC}), fill factor (FF) and power conversion efficiency (PCE), which are presented in Table 4.1. Also present in Table 4.1. is the series resistance (R_S) of the solar cells.

From Table 4.1 it can be seen that V_{OC} , J_{SC} , FF are higher while R_S is lower for the solar cell with AgNWs/AZO as the electrode than for just the AZO, resulting in a higher PCE.

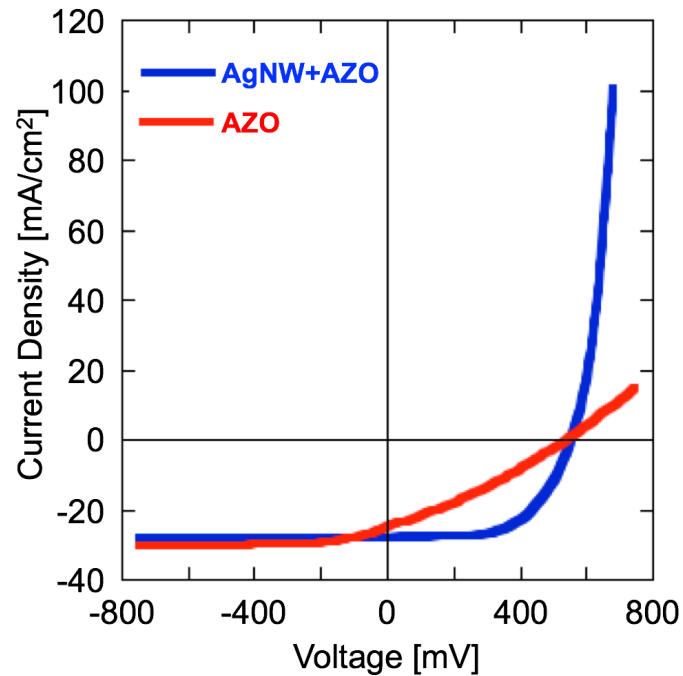


Figure 4.21. Current density as a function of voltage for silicon based solar cells with various top electrodes; After [2].

Table 4.1. Various solar cell working parameters with respect to type of top electrode used; After [2].

Type of electrode in solar cell	V_{OC} (V)	J_{SC} (mA/cm^2)	FF (%)	PCE (%)	R_S ($\Omega \text{ cm}^2$)
AZO	0.547	25.1	30.1	4.1	17.9
AgNWs/AZO	0.559	28.0	60.1	9.4	4.4

4.1.1. Electron Tomography of Thin AgNWs

Figure 4.22. is a STEM image showing AgNWs of average thickness ~ 30 nm, after annealing for 30 seconds at 210°C . It can be observed that the process yielded welded junctions with preserved integrity (blue circles) as well as junctions where annealing led to a discontinuation of welded junctions (red circles).

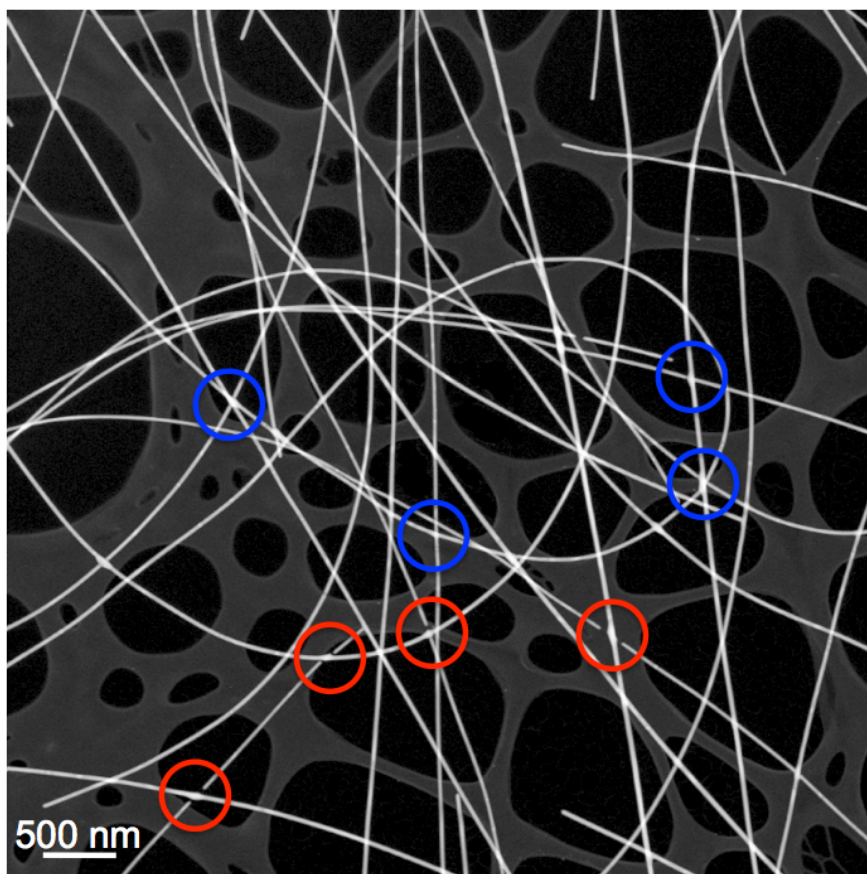


Figure 4.22. STEM image of welded AgNWs. Disconnected welded junctions are indicated by red circles while welded junctions with preserved integrity are indicated by blue circles. Background corresponds to lacey carbon grid.

Figure 4.23 is a HAADF STEM image of a welded junction between two AgNWs, recorded at 0° tilt angle. White arrows indicate diameters of 35.4 nm and 40.7 nm for the two AgNWs. Acquisition of the 2D projection series was performed from the area noted in this image.

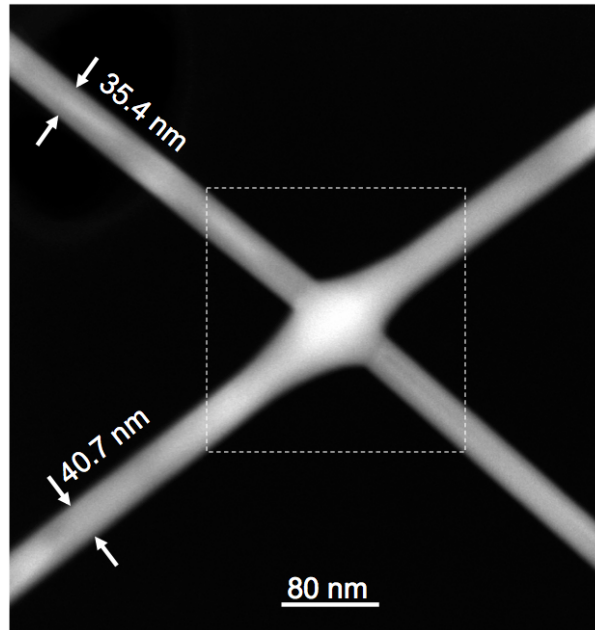


Figure 4.23. HAADF STEM image of welded junction between two AgNWs. White arrows indicate NW diameters.

Figure 4.24 represents a 3D reconstructed image of the section noted by white dotted square in Figure 4.23.

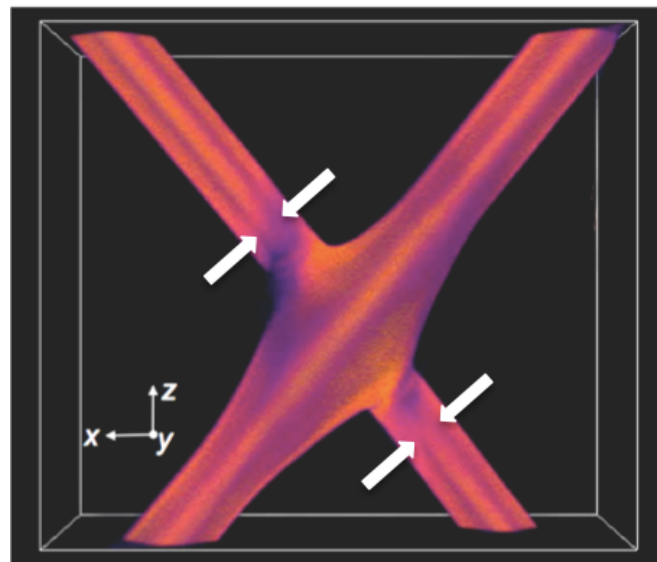


Figure 4.24. 3D structure of the reconstructed welded junction between two AgNWs. White arrows indicate central ridge of thinner NW terminated close to the nanoweld.

Unlike that HAADF STEM image, this reconstructed image exhibits some features that indicate faceted morphology and five-fold symmetry of two AgNWs creating a

nanoweld after annealing for 30 seconds at 210°C. It can clearly be seen that the central ridge in thicker AgNW remains uninterrupted along entire length, while the central ridge in the thin AgNW stops at the nanoweld, indicated by white arrows.

Figures 4.25a and b represent two projections of the 3D surface of welded AgNWs rotated 180° with respect to each other. It is a rendering of the simultaneous iterative reconstruction algorithm of consecutive 2D slices obtained from 140 2D STEM images, acquired between -70° and +70° in an equally spaced tilt series, with 1° steps apart. From these two images it is clear that both AgNWs are characterized by the presence of five surface facets and a pentagonal cross-section. It is also evident that the top corner of the thinner NW was in contact with the bottom flat facet of the thicker NW before heating was performed.

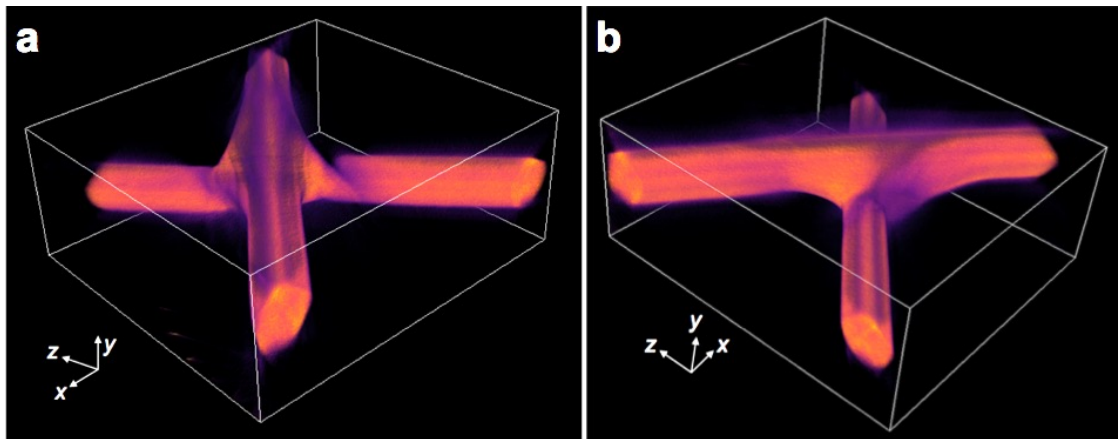


Figure 4.25. 3D volume renderings of welded AgNWs, shown from different viewpoints; a) is rotated 180° with respect to b); Cartesian coordinates are indicated.

4.1.2. Diffraction Orientation and Strain Mapping of AgNWs

HAADF STEM image of the welded region between two AgNWs is shown in Figure 4.26a, while the nano-beam electron diffraction (NBED) pattern, taken from the welded zone indicated by the red circle is shown in Figure 4.26b. The NBED pattern, taken close to $[\bar{1}12]$ zone axis, confirms $\langle 110 \rangle$ growth direction of the thinner AgNW.

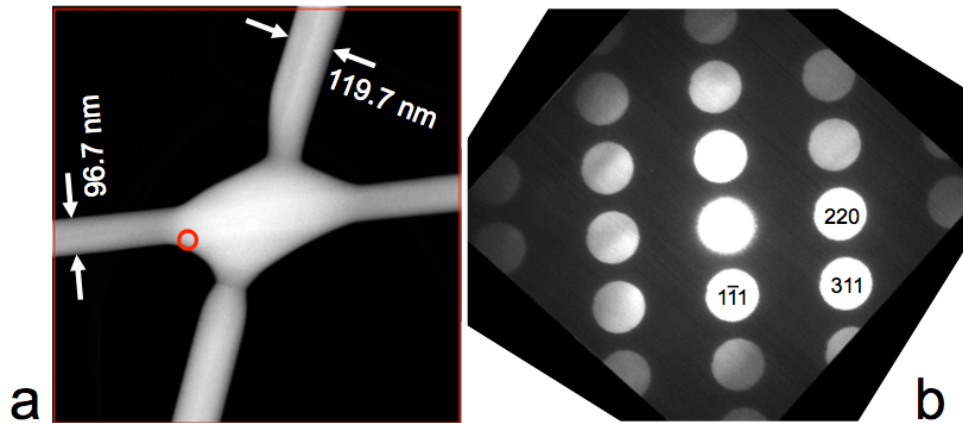


Figure 4.26. a) HAADF STEM image of welded AgNWs with indicated thicknesses, b) NBED pattern taken close to $[\bar{1}12]$ zone axis from the region indicated by red circle in a).

Figure 4.27 shows orientation maps, demonstrating specific alignment of twin segments within both AgNWs, as well as the welded zone. Each map shows strength

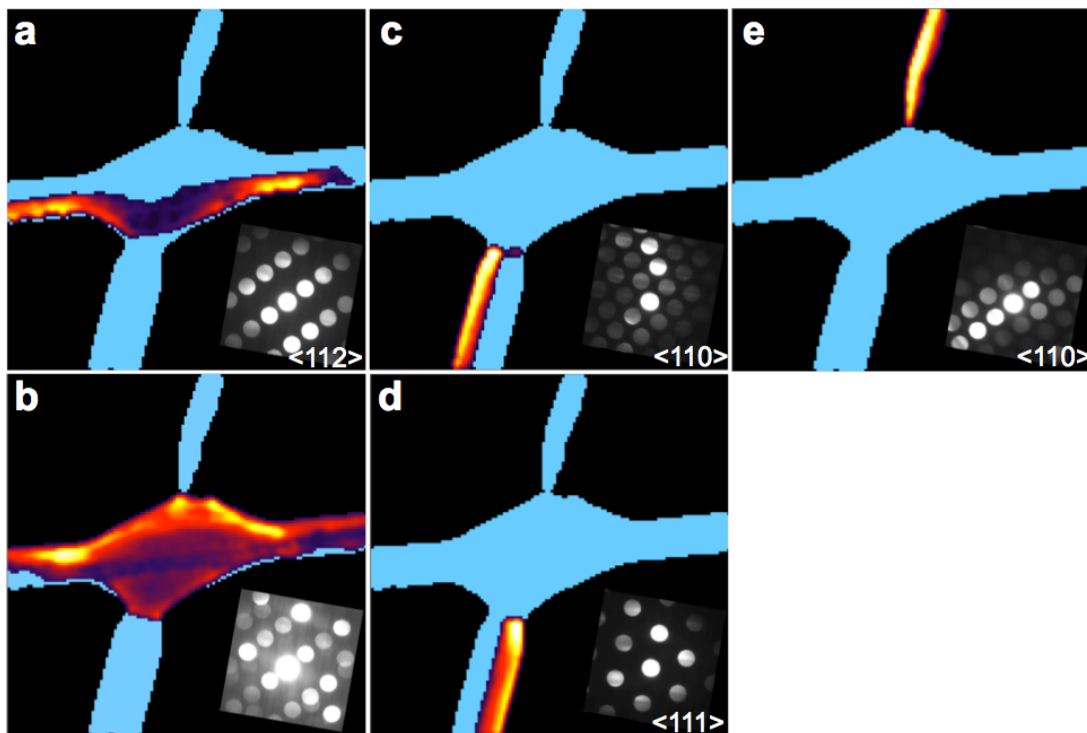


Figure 4.27. Orientation maps for various sections of both AgNWs and the welded zone; a) and b) are maps of thinner NW and the welded zone; c) and d) are maps of left and right sections of the thicker NW, below the welded zone; e) Map of left section of thicker NW above the welded zone; light blue color indicates area where diffraction signal > 0 , black color depicts area with no diffraction signal, white color represents area with highest signal; Insets represent NBED patterns with noted orientations.

of the diffraction signal, using the color-map: black, purple, red, orange, yellow and white, where white represents areas with the highest signal and black represents areas with no diffraction signal, or too low to classify. The light blue regions represent areas where the diffraction signal is greater than 0 value, from any of the spots. These relative values are arbitrary, changing from pattern to pattern and are just a representation of how much signal is in a given area. Orientations of NBED patterns for corresponding AgNW segments and the welded zone are as follows: $\langle 112 \rangle$ in Figure 4.27a, $\langle 110 \rangle$ in Figures 4.27c and e, $\langle 111 \rangle$ in Figure 4.27d and $\langle 110 \rangle$ in Figure 4.27e while for Figure 4.27b the NBED pattern displays $\langle 112 \rangle$ as well as several other orientations with very weak signals. The criterion of 10% deviation from crystal structure orientation of the neighboring pixels is used to consider them to be of the same orientation. These orientation maps show that the welded zone has the same crystallographic orientation as the NW to which it is attached. Figure 4.28 represents color-coded maps of coherent strain and lattice distortion (rotation) distribution within AgNWs and nanoweld region.

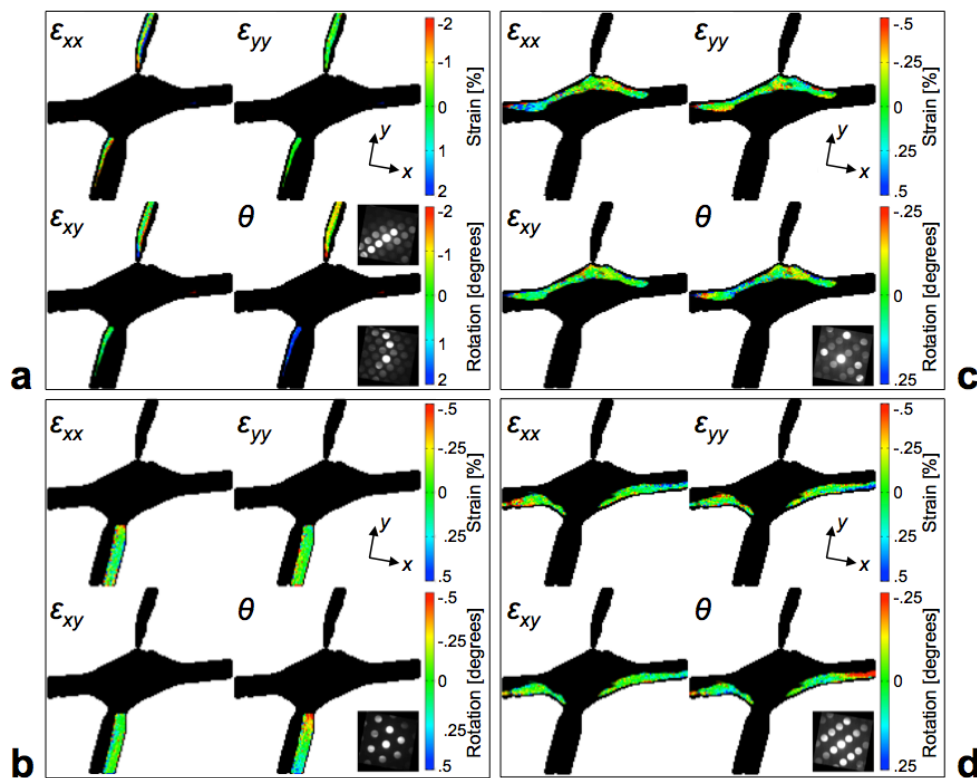


Figure 4.28. Color-coded maps of coherent strain (ϵ_{xx} , ϵ_{yy} , ϵ_{xy}) and lattice rotation angle (θ) distribution within AgNWs and the welded zone; black color indicates contour of investigated sample; Insets represent NBED patterns corresponding to indicated color-coded areas. Also noted are Cartesian coordinates.

For each area of investigated sample, both for AgNWs and the welded zone, 2D maps of ε_{xx} (horizontal strain), ε_{yy} (vertical strain) and ε_{xy} (shear strain) are shown as well as maps of rotational angle (θ) distribution. Unfortunately, due to large diameters of AgNWs, only a limited area of investigated sample was evaluated for coherent strain distribution. From Figure 4.28a it can be observed that, above the welded zone, ε_{xx} ranges from -2% to 2%, ε_{yy} ranges from -0.25% to 0.25%, ε_{xy} ranges from -2% to 2% and θ ranges from -2° to 0.25° while below the welded zone ε_{xx} ranges from -2% to 0.25%, ε_{yy} ranges from -0.25% to 0.25%, ε_{xy} ranges from -0.25% to 0.25% and θ is mostly $\sim 2^\circ$. From Figure 4.28b it can be observed that ε_{xx} , ε_{xy} and ε_{yy} all range from -0.5% to 0.5%, with the majority of strain in the region -0.1% to 0.1% while θ ranges from -0.25° to 0.25° with the majority of strain rotation in the region -0.1° to 0.1° . From Figure 4.28c it can be observed that ε_{xx} , ε_{xy} and ε_{yy} all range from -0.5% to 0.5%, with the majority of strain in the region -0.1% to 0.1% while θ ranges from -0.25° to 0.25° with the majority of strain rotation in the region -0.1° to 0.1° . From Figure 4.28d it can be observed that ε_{xx} , ε_{xy} and ε_{yy} all range from -0.5% to 0.5%, with the majority of strain in the region -0.1% to 0.1% while θ ranges from -0.25° to 0.25° with the majority of strain rotation in the region -0.1° to 0.1° . Insets in Figures 4.28a-d represent NBED patterns of corresponding AgNW segments and welded zone with orientations noted in Figure 4.27. In Figure 4.28a, two NBED patterns are present, one corresponding to part of thicker NW above the welded zone while the other corresponding to part of thicker NW below the welded zone.

4.2. Tandem Organic Solar Cells

4.2.1. AgNWs Used as Electrodes in Tandem Organic Solar Cells

Table 4.2 presents information about various AgNW networks including thickness and sheet resistance with respect to the parameters used during processing, which can be found in Table 3.1 in Section 3.4.1.

Table 4.2. Various AgNW networks with differing processing parameters.

Sample	Thickness [nm]	Sheet Resistance [Ω /sq]
1	53 \pm 2	19
2	80	17
3	95 \pm 5	9
4	150 \pm 20	6
5	160	6

Figure 4.29 is a graph depicting optical transmittance of AgNW samples 1-5. Sample 1 (blue line), 50nm in thickness with a sheet resistance of 19 Ω /sq has a transmittance of 93% at 550nm and 74% at 360nm. Sample 2 (blue line), 80nm in thickness with a sheet resistance of 17 Ω /sq has a transmittance of 90% at 550nm and 63% at 360nm.

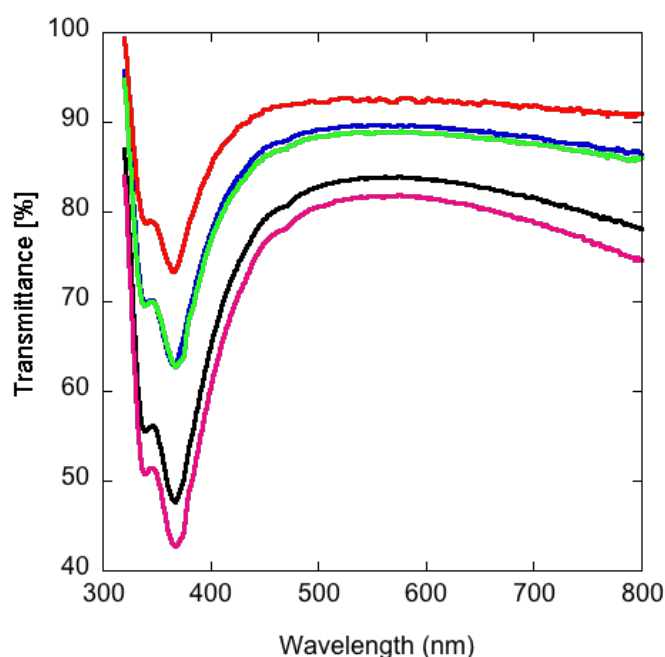


Figure 4.29. Optical transmittance of AgNW samples: 1 (red line), 2 (blue line), 3 (green line), 4 (black line) and 5 (pink line).

Sample 3 (green line), 95 \pm 5nm in thickness with a sheet resistance of 9 Ω /sq has a transmittance of 89% at 550nm and 63% at 360nm. Sample 4 (black line), 150 \pm 20nm in thickness with a sheet resistance of 6 Ω /sq has a transmittance of 84% at 550nm and 49% at 360nm. Sample 5 (pink line), 160nm in thickness with a sheet resistance of 6 Ω /sq has a transmittance of 82% at 550nm and 45% at 360nm.

Figure 4.30 represents surface roughness of AgNW samples 1-5. Using the formulas for calculating average surface roughness (R_a) and root mean square (RMS) surface roughness (R_q), the following values were acquired: $R_a=19.17$ nm and $R_q=29.74$ nm for Sample 1, $R_a=19.36$ nm and $R_q=26.52$ nm for Sample 2, $R_a=12.95$ nm and $R_q=25.41$ nm for Sample 3, $R_a=10.69$ nm and $R_q=18.19$ nm for Sample 4 and $R_a=10.24$ nm and $R_q=26.31$ nm for Sample 5.

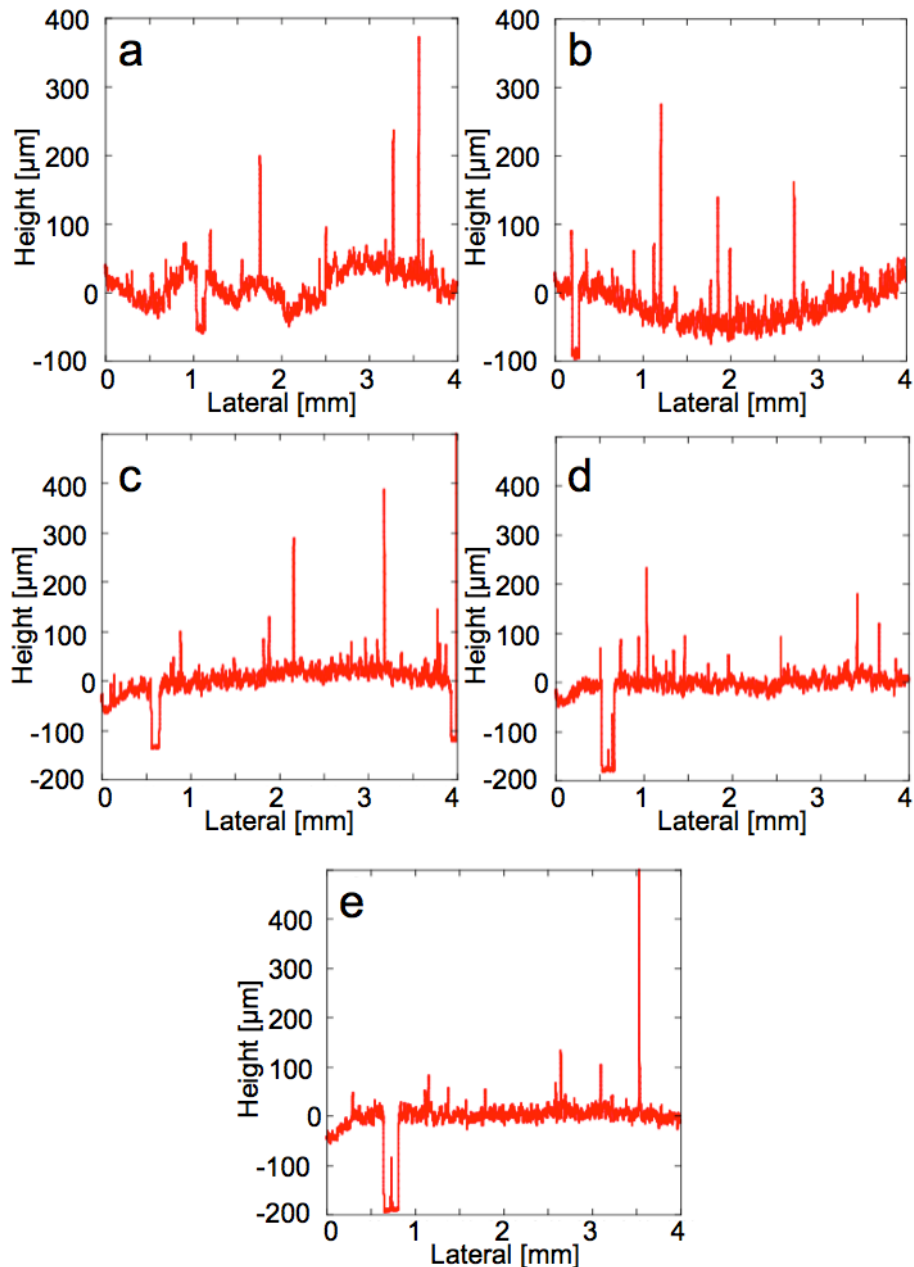


Figure 4.30. Surface roughness (height as a function of distance) of AgNWs: a) Sample 1, b) Sample 2, c) Sample 3, d) Sample 4 and e) Sample 5.

AgNW Area Coverage Determination

A typical SEM image of AgNWs, in Figure 4.31a, shows white contrast against a dark background, where these NWs form a continuous network. To measure the NW density, a custom image processing routine written in Matlab was utilized. Two possible artifacts are present in some of the images: firstly, some of the NWs are slightly degraded by oxidization and produce less contrast and secondly, substrate regions with no NWs will show a very strong false signal due to charging from the electron beam. Therefore, a filtering procedure was developed to prevent either of these artifacts from affecting the NW density estimates. For each sample type, NW densities were measured from multiple micrographs (at least 16 images), and the densities were averaged, in order to produce accurate estimates.

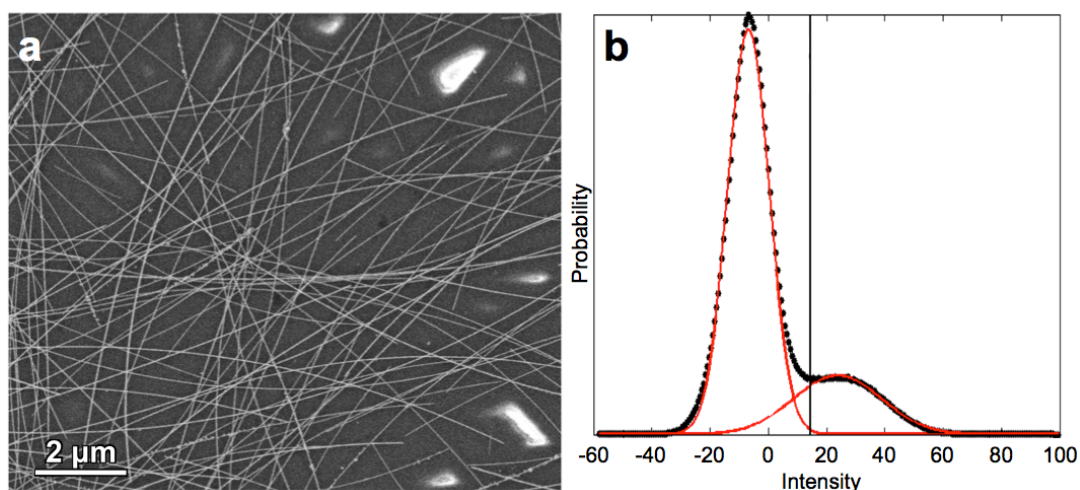


Figure 4.31. a) SEM image of an undesirable structure which includes oxide particles and charged patches, b) Histogram of intensities with fit double Gaussian function showing a peak corresponding to the background (left) and a peak corresponding to the AgNWs (right).

The first step was to up-sample the original images which improved accuracy when binary thresholding was used. Next, a small smoothing kernel was applied to the up-sampled images to mitigate the effect of digital noise. From this image, a histogram of the pixel intensities was acquired (Figure 4.31b). Subsequently, two Gaussian distributions were fitted to this histogram, to determine an initial threshold for the substrate intensity. The Gaussian function to the left fits the pixel intensities of the

substrate, and the threshold is set to the substrate mean plus three times the Gaussian function standard deviation. The second Gaussian is included only to improve the accuracy of the fit to the substrate intensities.

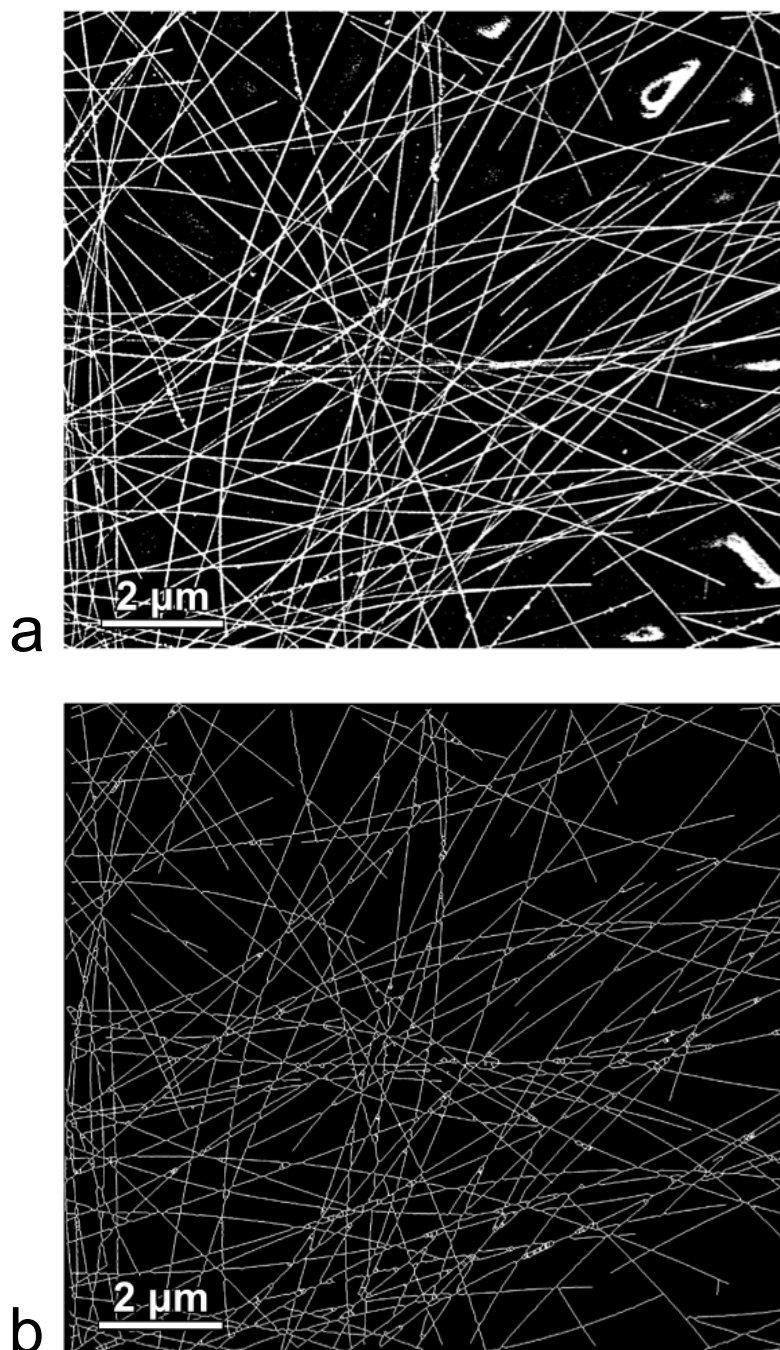


Figure 4.32. a) Up-sampled SEM image using a factor of 2, smoothed slightly, after applying threshold value, indicated in histogram in Figure 4.31b, b) Skeleton SEM image with all non-NW features removed.

A binary image was computed using the substrate threshold, shown in Figure 4.32a, after which a skeleton image of the NW network was produced by applying the morphological dilate operation to the binary image twice, followed by the morphological shrink operation twelve times (Figure 4.32b). These operations bridge small erroneous gaps (perhaps due to oxidization of the NWs) and reduce the width of all wires to a single pixel (a skeleton image of the network). All binary objects present in this skeleton image were subsequently detected and classified. The NWs form a network over the whole field of view, while any false positives generated by charged regions form compact thick objects.

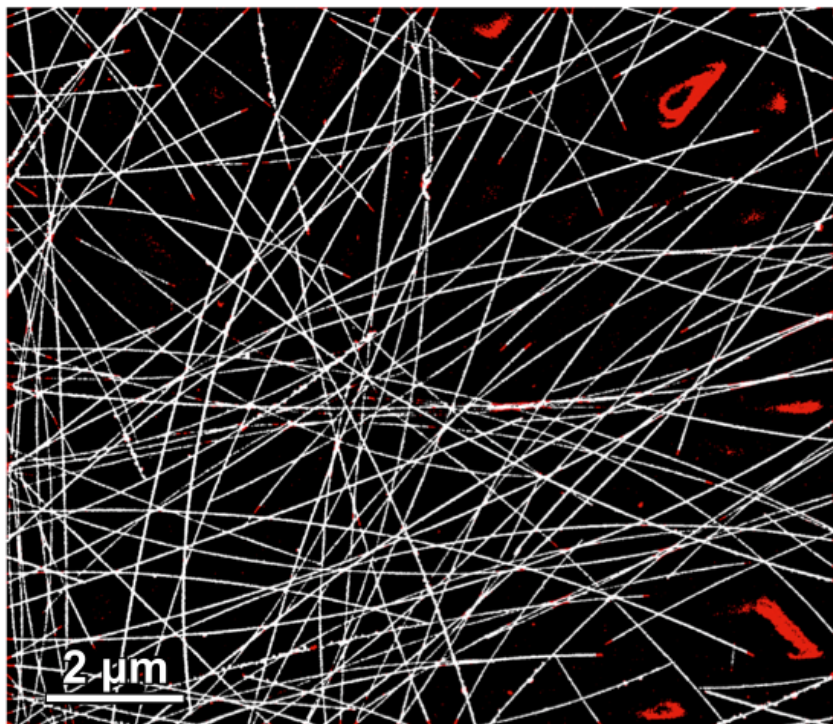


Figure 4.33. Correction of skeleton image from Figure 4.32b.

All clusters of binary pixels (objects), except for the cluster corresponding to the NW network, were removed after which the binary morphological dilate operation was applied to the filtered skeleton image four times and used as a mask for the original threshold image (Figure 4.33). This step removes both, false positive and false negative digital noise generated by the charged substrate regions, presented in Figure 4.34.

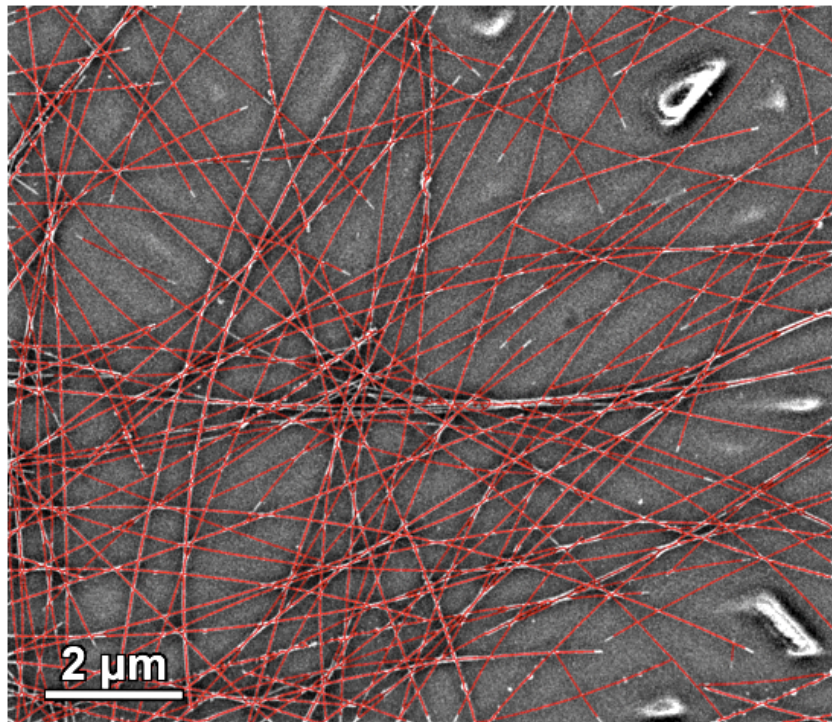


Figure 4.34. Correction of image in Figure 4.33. Note that all non-NW features are successfully removed from the final image used for statistical analysis.

Finally, the NW density is measured from the masked threshold image. We can also estimate the total length of wires present in the image from the skeletonized image. The width of NWs in the corrected image is defined by the average diameter calculated by method shown in Figure 4.35, with the histogram of diameter size distribution shown in Figure 4.36b.

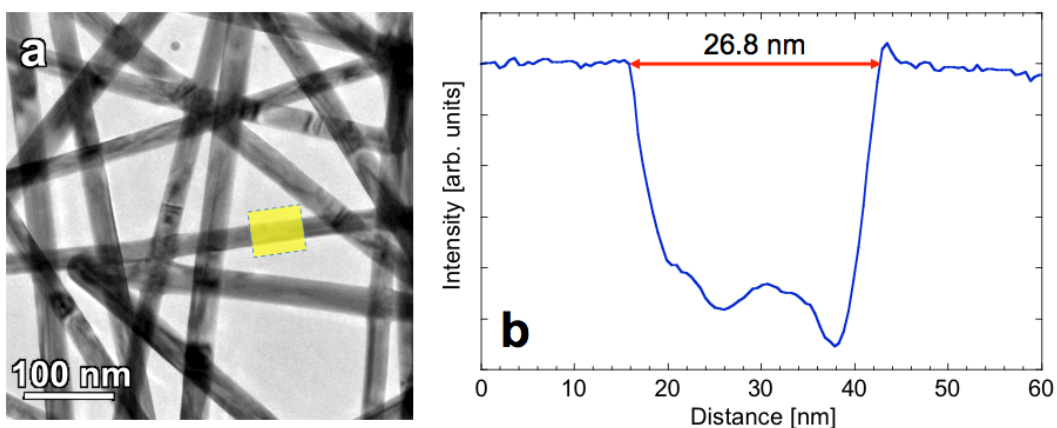


Figure 4.35. a) BF image of AgNWs, b) Intensity line profile averaged along yellow rectangle in shown in a).

Figure 4.35a is a BF TEM image of AgNWs from which the intensity line profile was acquired, noted by yellow rectangle. The NW diameter was defined as the distance at the level of the background noise, in this case 26.8 nm, shown in Figure 4.35b.

Figure 4.36a is a BF TEM image of a typical AgNW network used as a transparent electrode in tandem organic solar cells presented in this thesis.

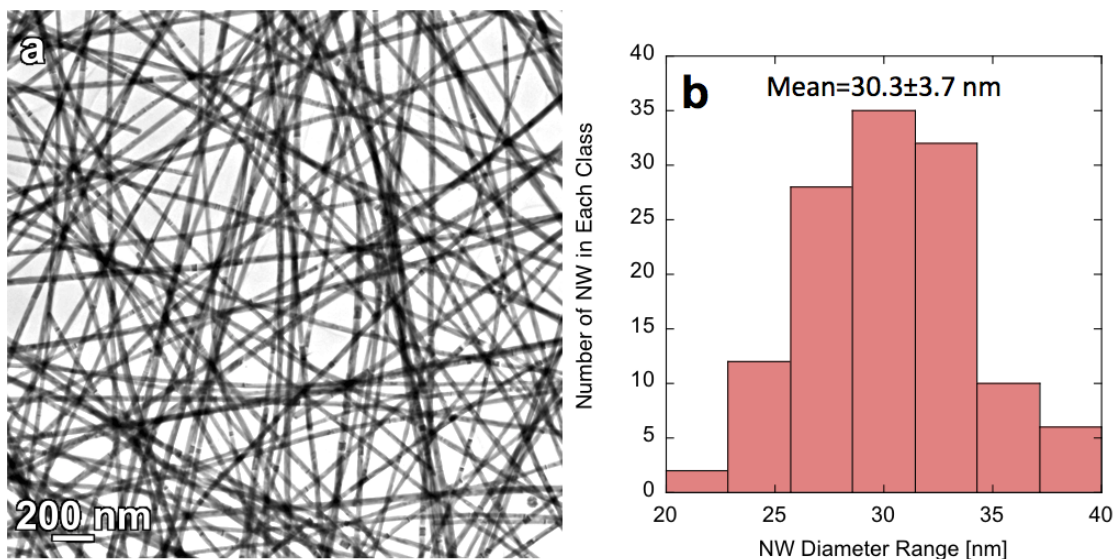


Figure 4.36. a) BF image of an AgNW network, b) Histogram of diameter size distribution of AgNWs; Analysis of AgNW network was performed based on the average diameter of AgNWs (Figure 4.36b), calculated by measuring NW diameters by intensity line profile averaging, as shown in Figure 4.35a and b.

Table 4.3. Statistical analysis of AgNW surface coverage.

Sample	Thickness (nm)	Median Area Coverage (%)	Number of Images Analyzed	Area Error Bar (%)
1	53±2	18.2	64	0.36
2	80	18.7	24	0.49
3	95 ± 5	18.7	24	0.49
4	150 ± 20	19.3	16	0.63
5	160	19.7	16	0.34

Statistical analysis of surface coverage is shown in Table 4.3 which presents values for median area coverage of samples with various thicknesses, including the number of images analyzed and the area error bar.

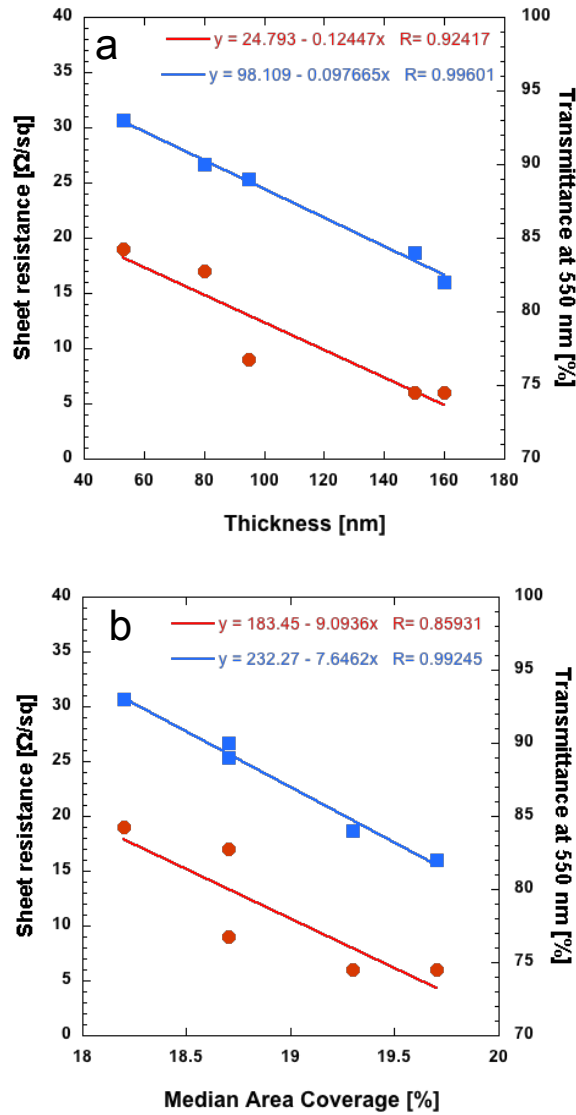


Figure 4.37. Effects of a) AgNW network thickness and b) area coverage on optical transmittance (blue squares) and sheet resistance (red circles) of AgNWs.

Figures 4.37a and b represent graphs showing effects of AgNW network thickness and area coverage on optical transmittance (red squares) and sheet resistance (blue circles) of AgNWs. These graphs demonstrate that resistance and transmittance decrease linearly with the increase in network thickness and area coverage. The goodness of fit for transmittance and sheet resistance as a function of network thickness is $R=0.996$ and 0.924 , and as a function of area coverage $R=0.992$ and 0.859 , respectively.

Figure 4.38 shows a graph noting the linear relationship between thickness of AgNWs network and the total area coverage, with goodness of fit of $R=0.963$. The total area coverage increases linearly with the increase of AgNW network thickness.

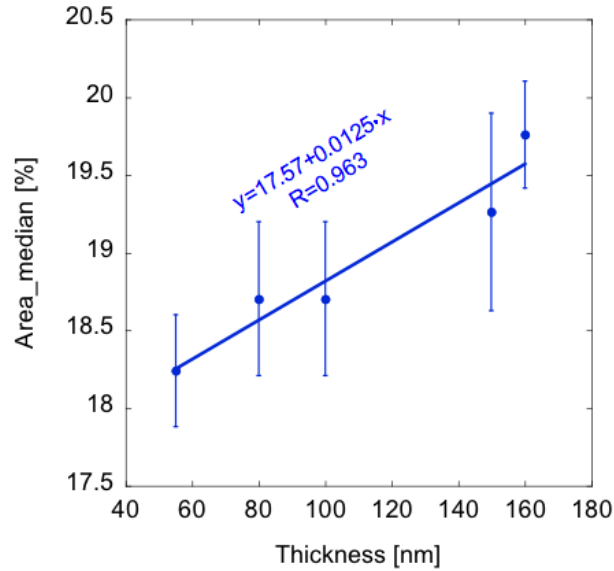


Figure 4.38. Relationship between AgNW network thickness and the total area coverage.

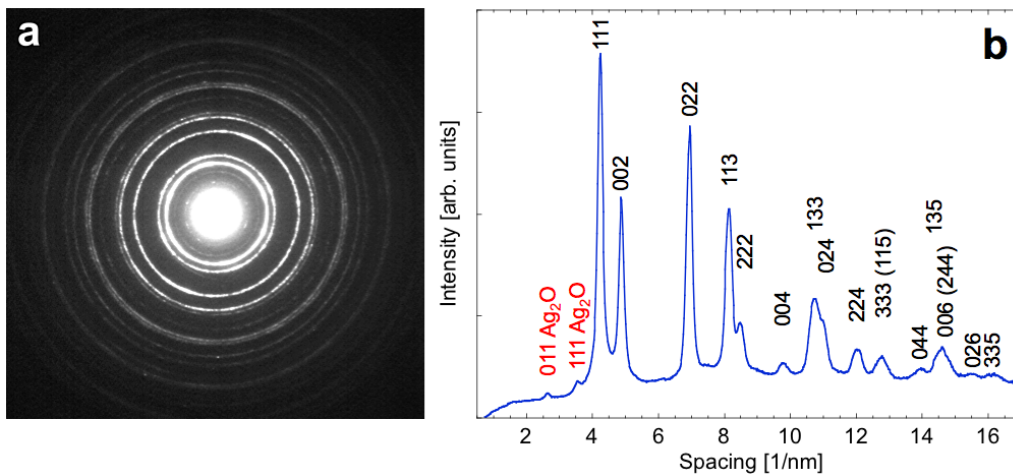


Figure 4.39. a) Selected area ring diffraction pattern; b) Intensity line profile showing, besides FCC Ag rings, the presence of Ag₂O surface oxide film on AgNWs, given in red.

Selected area ring diffraction pattern (Figure 4.39a) taken from the area shown in Figure 4.36a reveals the presence of an Ag₂O surface oxide, clearly visible in radial integration of ring pattern shown in Figure 4.39b.

4.2.2. Double Junction Tandem OSC

Figure 4.40 represents a schematic of all layers that comprise the tandem double junction organic solar cell. Layers from bottom to top: Glass, PEDOT:PSS, Printed Ag, PEDOT:PSS, GEN-2:PC₆₁BM, ZnO, N-PEDOT, pDPP5T-2:PC₆₁BM, ZnO and Ag NWs.

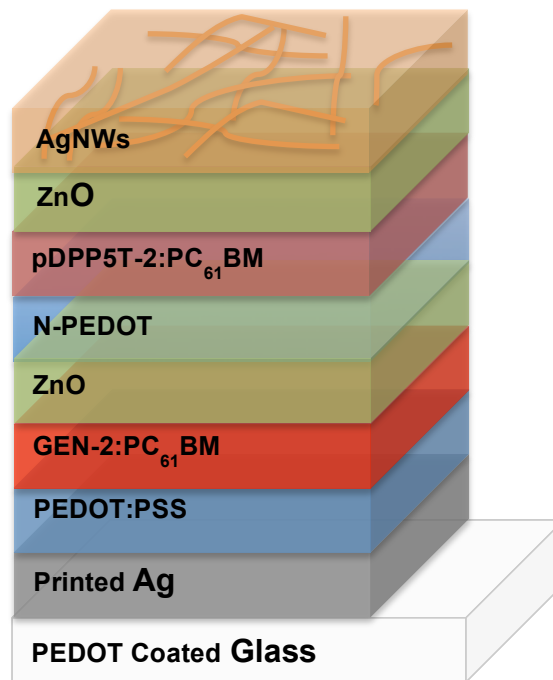


Figure 4.40. Schematic of layout of tandem double-junction BHJ organic solar cell [3].

Figures 4.41a-c represent SEM images of the double junction tandem OSC after cleaving. No FIB milling of cells has been performed at this point so damage of structure of cross-section surface due to cell cleaving can be observed. From Figure 4.41b, the structure of printed Ag and ZnO layers can be observed as well as structure of the polymer nanocomposite layers. Polymer PEDOT layers can barely be observed because of their small thickness. AgNW network exhibits high density, also observed from Figure 4.41c, which represents a top view of the solar cell. It can be seen from this image that the AgNWs are uniformly distributed along the surface of the ZnO.

Figure 4.42 is a SEM image of the double junction tandem OSC cross-section after FIB milling. Unlike Figure 4.41, all layers of the solar cell can be seen as well as nanostructural details like porosity of the printed Ag (P_Ag) bottom electrode.

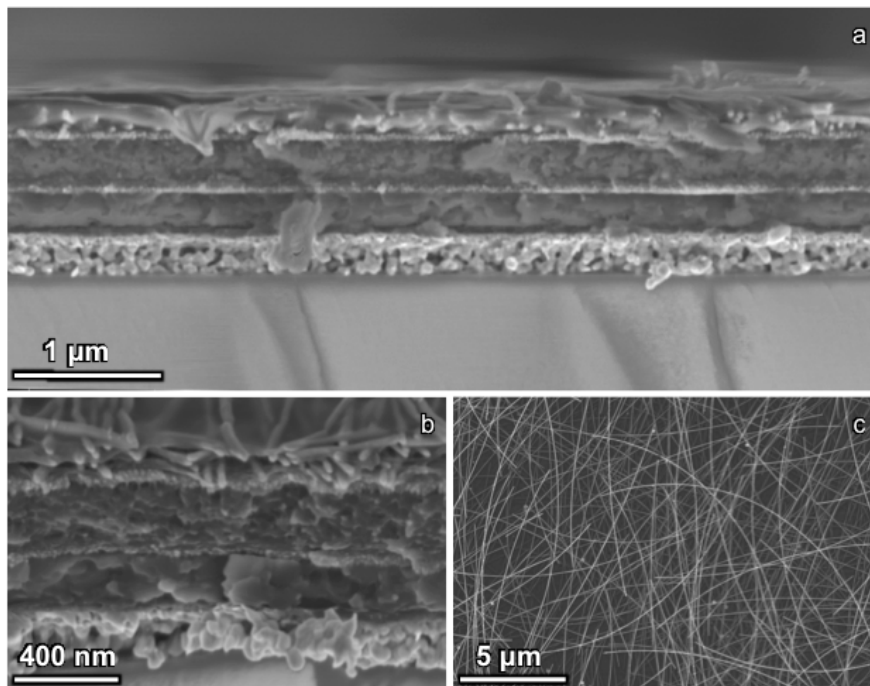


Figure 4.41. a) Low magnification scanning electron micrograph of tandem double-junction organic solar cell cross-section after cleaving; b) higher magnification of image in a), c) top view of solar cell.

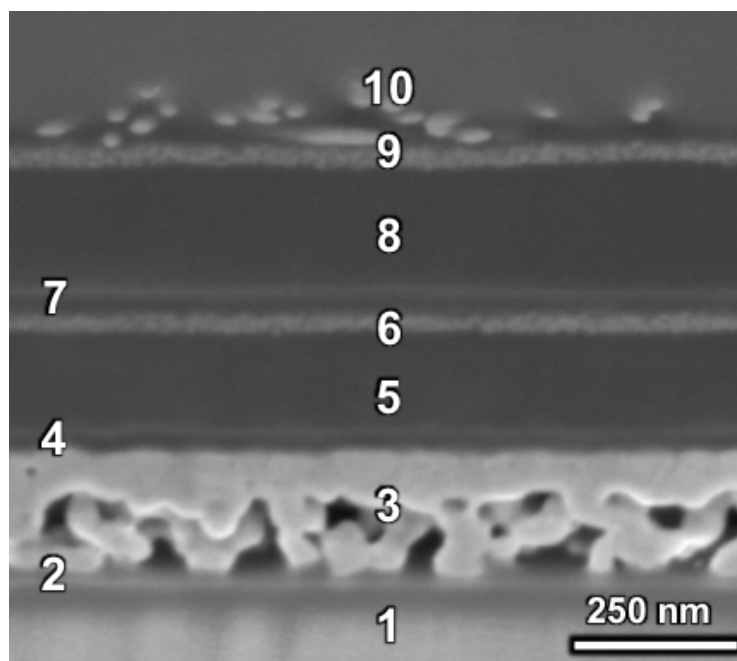


Figure 4.42. Scanning transmission electron micrograph of tandem double-junction organic solar cell cross-section after FIB milling. The layers 1-10 are as follows: glass (1), PEDOT:PSS (2), printed Ag (3), PEDOT:PSS (4), GEN-2:PC₆₁BM (5), ZnO (6), N-PEDOT (7), pDPP5T-2:PC₆₁BM (8), ZnO (9), AgNWs (10).

Figure 4.43a is a bright field (BF) CTEM image of tandem double-junction organic solar cell cross-section acquired from FIB lamella prepared by lift-out cross-sectional method. Structural details like pentagonal AgNWs, very uniform thickness of ZnO and relatively uniform thickness of PEDOT layers can be observed as well as the porous P_Ag electrode. Average diameter of pores was calculated to be 21.6 ± 7.5 nm. Non-uniform distribution of pores is present in the P_Ag as no pores appear at the top of the layer, near the interface with PEDOT:PSS which is characterized by low surface roughness.

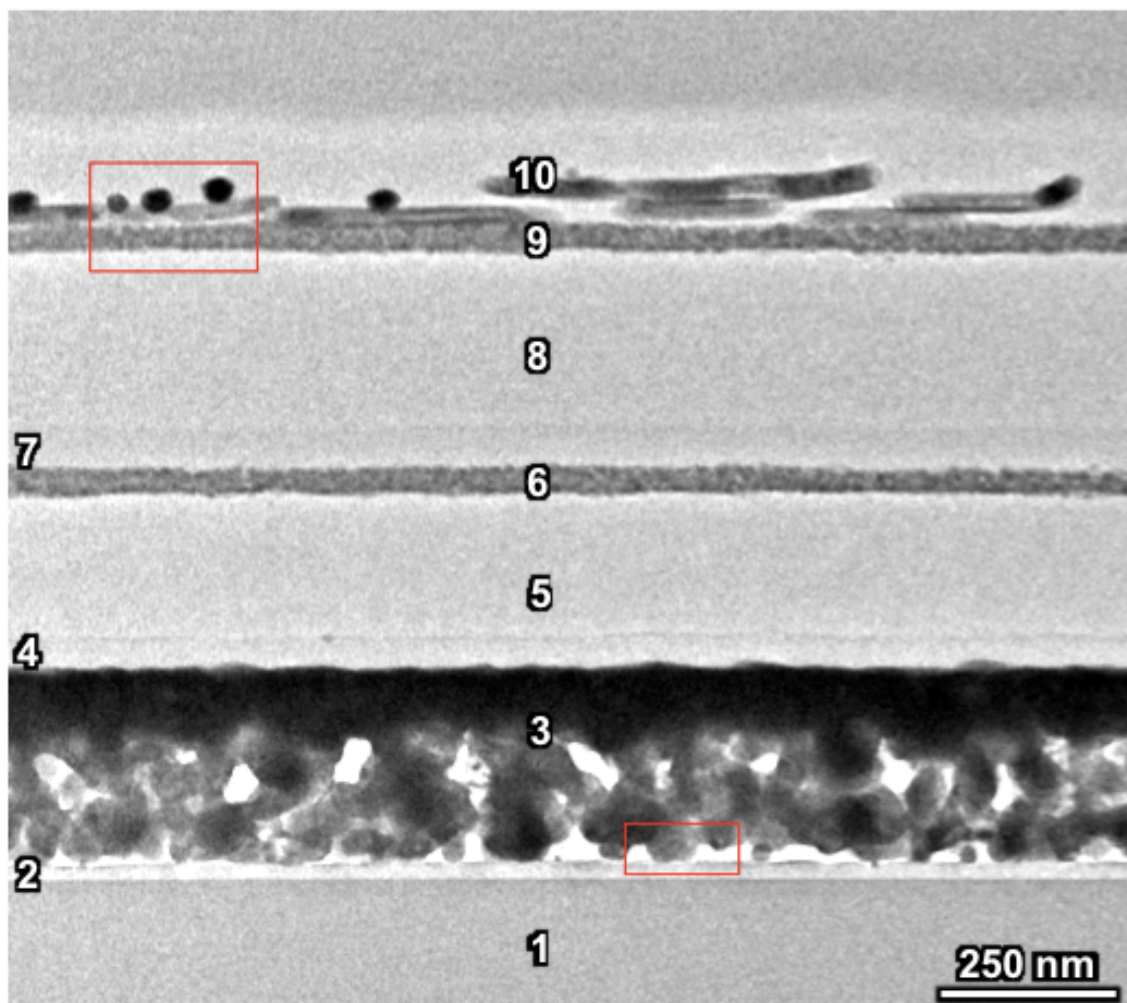


Figure 4.43. a) BF CTEM micrograph of tandem double-junction organic solar cell cross-section acquired using FIB lamella prepared by lift-out method; Layers 1-10 correspond to the ones in Figure 4.42; After [3].

The transparent electrode consisting of an AgNW network appears to possess non-uniform thickness, i.e. lowest thickness of AgNW network corresponds to thickness of single NW. Thickness values for all layers of the double junction cell are given in Table 4.4.

Figure 4.44a represents a low magnification BF TEM image of area in P_Ag, represented by bottom red rectangle in Figure 4.43a.

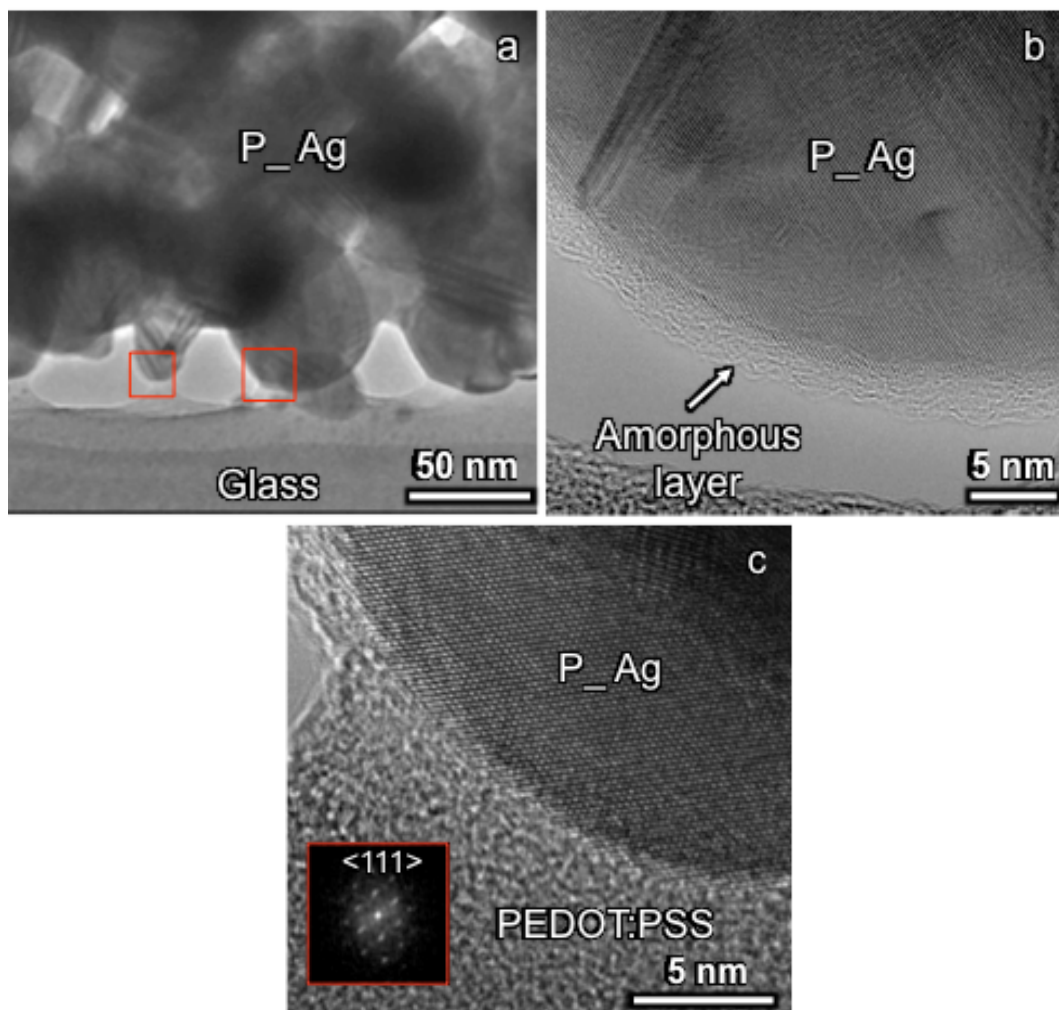


Figure 4.44. a) Low magnification BF image of glass/P_Ag interface structure; b) and c) HRTEM images of Ag nanoparticles in P_Ag electrode; inset is FFT of Ag particle.

Figure 4.44b is a detailed high resolution image of left red square denoted in Figure 4.44a revealing the presence of twins inside the P_Ag structure as well as an amorphous layer ~2nm in thickness, on P_Ag surface. Figure 4.44c is a high resolution detailed image of right red square denoted in Figure 4.44a showing the interface between crystal

P_Ag and amorphous PEDOT:PSS. Inset is an FFT of the P_Ag showing crystallographic orientation close to $\langle 111 \rangle$ zone axis.

Figure 4.45a represents a high magnification BF TEM image of area in AgNWs, represented by top red rectangle in Figure 4.43a.

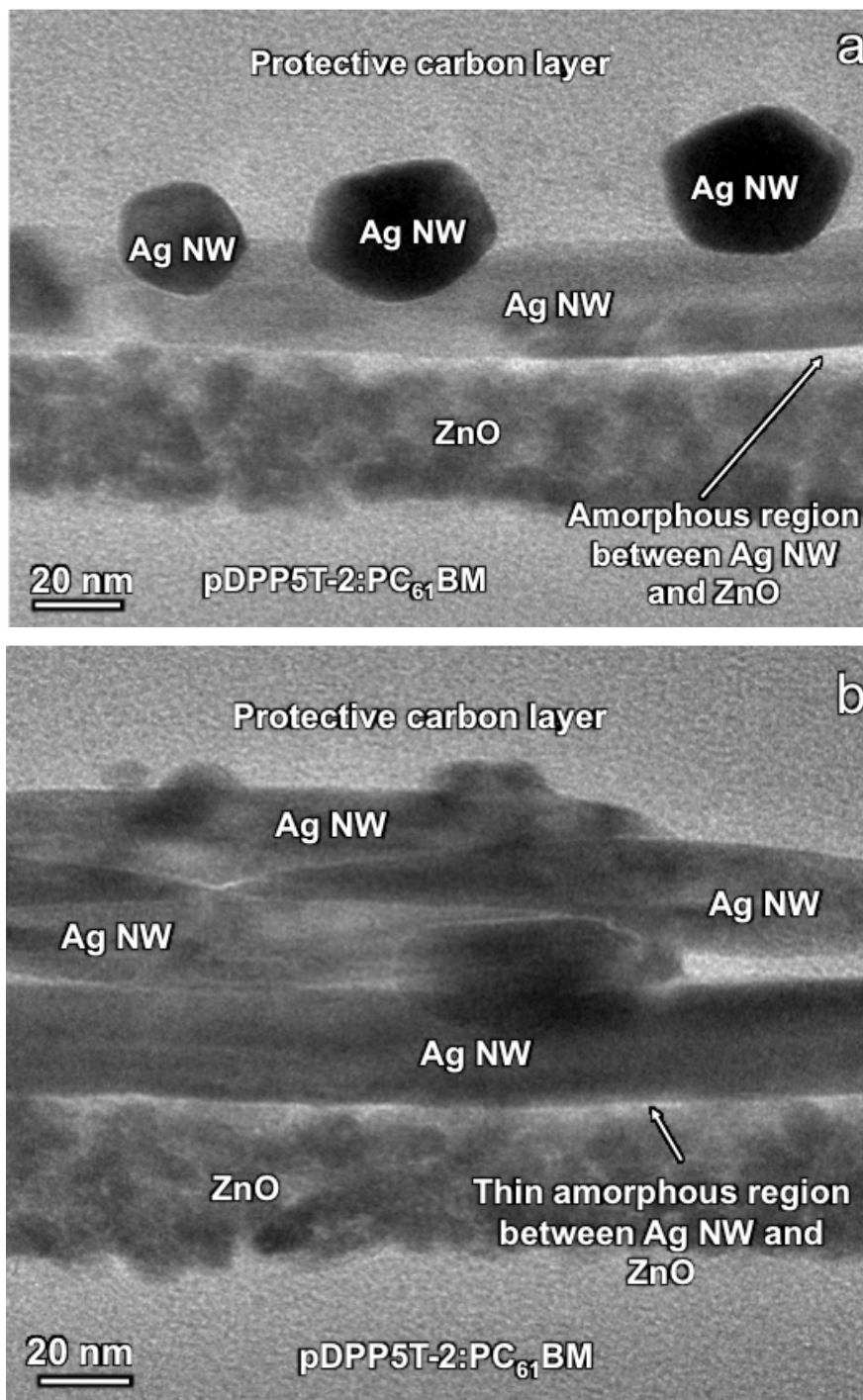


Figure 4.45. High magnification transmission electron micrograph of AgNW electrode in a) low thickness area, b) area of high thickness.

Besides the protective carbon layer and the top active polymer nanocomposite layer, another amorphous region is present, between the AgNWs and the crystalline ZnO. This amorphous region corresponds to the polymer capping agent PVP introduced during AgNW synthesis. Note the clear pentagonal structure of the AgNWs as well as the uniform thickness of the ZnO layer. Figure 4.45b shows an AgNW bundle in the transparent electrode, a thicker region of the layer. In this image the amorphous layer between AgNWs and ZnO can be observed as well.

Figure 4.46 is an HAADF STEM image of the tandem double-junction organic solar cell cross-section with identical layer sequence described in Figure 4.42.

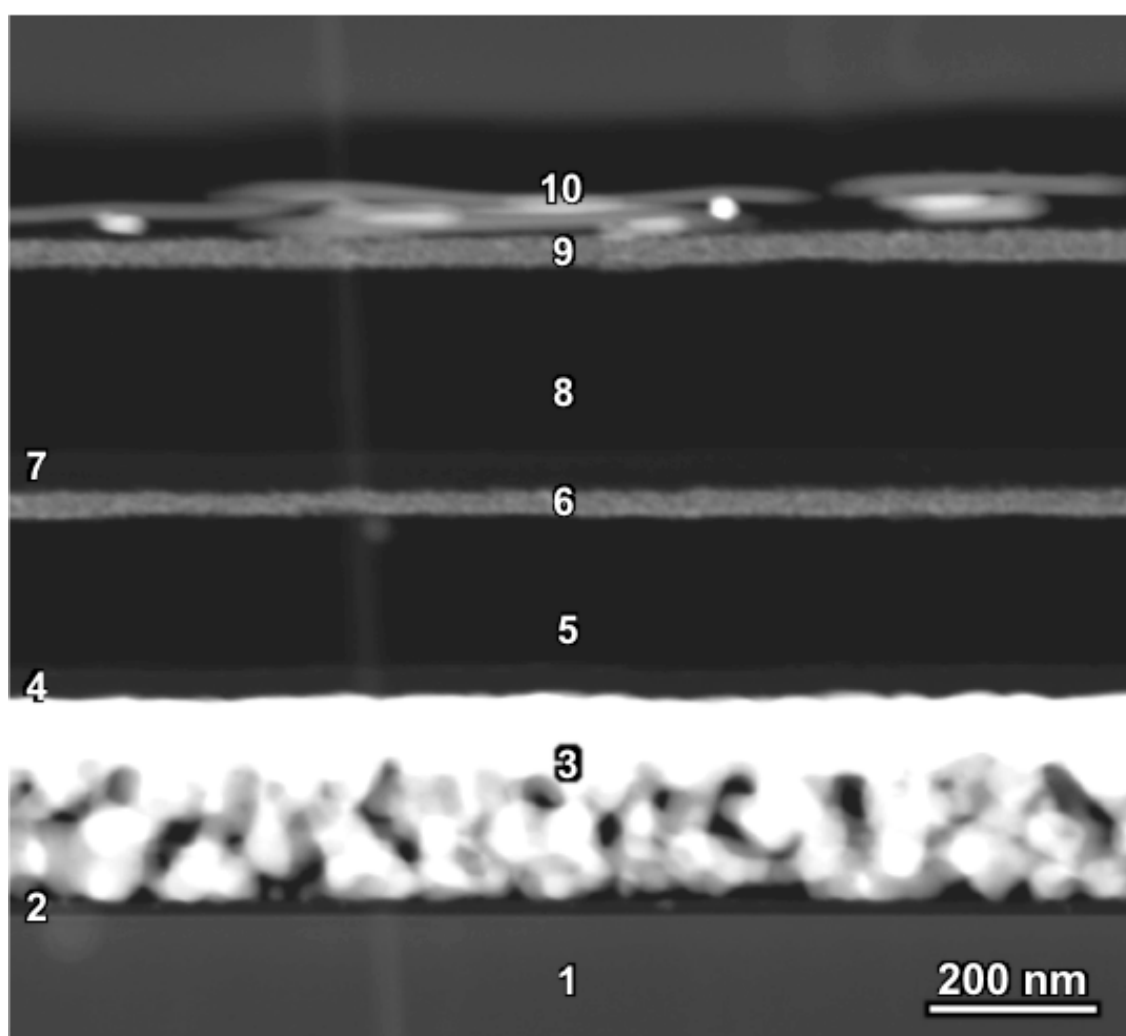


Figure 4.46. HAADF STEM micrograph of tandem double-junction organic solar cell cross-section acquired by FIB lift-out lamella [3]; Layers 1-10 correspond to the ones in Figure 4.42.

Table 4.4. includes thicknesses of all layers in the tandem double-junction organic solar cell acquired by measuring with profilometer and with a line profile across the TEM and STEM cross-sectional images of the cell. It can be observed that most of the experimentally measured values exhibit discrepancy in regards to the method of measurement.

Table 4.4. Thicknesses measured by profilometer [3] and by line profile from TEM and STEM images of layers in the tandem double-junction organic solar cell.

Layer	Thickness by profilometer [nm]	Thickness by TEM [nm]
PEDOT:PSS	20	26±1
Printed Ag	200	266±5
PEDOT:PSS	40	33.5± 8.5
GEN-2:PC ₆₁ BM	200	177.5± 5.5
ZnO	35	46.5± 0.5
N-PEDOT	35	40.5±1.5
pDPP5T-2:PC ₆₁ BM	200	226.5±2.5
ZnO	35	45±2
Ag NWs	100	Up to 73.5±6.5***

*** As previously mentioned, AgNW network cannot be a continuous film, hence thickness results considerably vary and the given result is the maximum thickness measured.

Figure 4.47 shows a STEM image from which EDS maps of elemental distribution of silver, zinc, oxygen, sulfur and nitrogen were acquired. Uniform distribution of zinc and oxygen can be observed, originating from ZnO and native oxide on the silicon substrate. High resolution of EDS is observed as porosity of printed Ag can clearly be seen as well as the non-uniform distribution of AgNWs along with their pentagonal cross-sections. Nitrogen can be seen present mostly in the P_Ag area. Sulfur is present in almost every part of the cell, with increased signal at locations of the PEDOT layers.

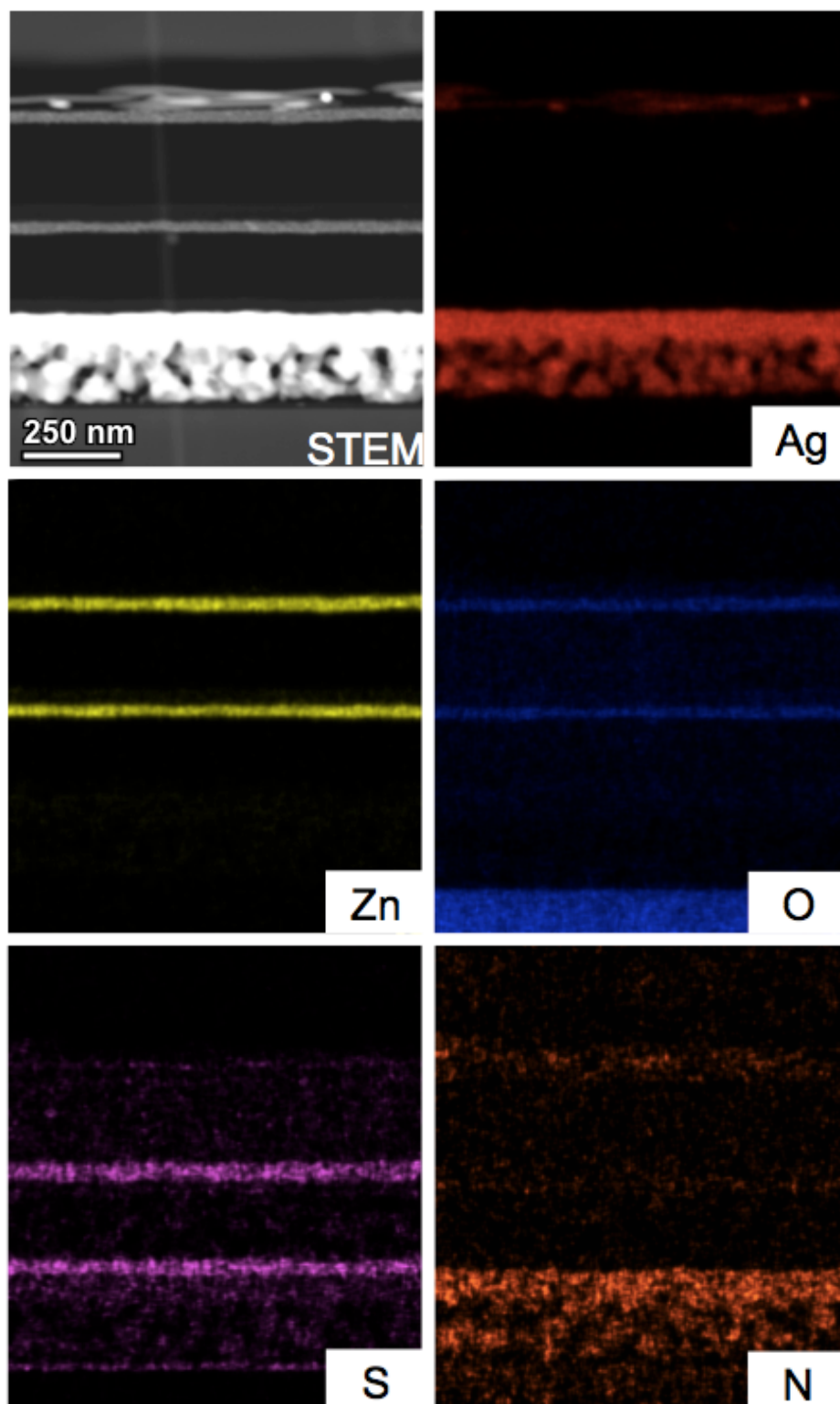


Figure 4.47. HAADF scanning transmission electron micrograph of tandem double-junction organic solar cell and EDS maps of silver (red), zinc (yellow), oxygen (blue), sulfur (pink) and nitrogen (orange) taken from the HAADF STEM image [3].

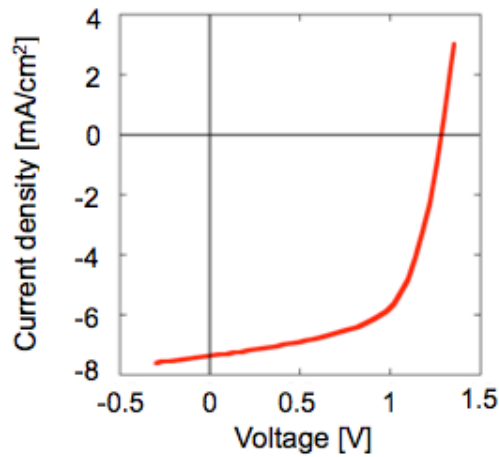


Figure 4.48. Current density as a function of voltage for the tandem double-junction organic solar cell processed on glass; After [3].

Figure 4.48 represents a graph of current density as a function of voltage for tandem double-junction organic solar cell. Calculated values are as follows: $V_{OC} = 1.29$ V, $FF=61\%$, $J_{SC} = 7.38$ mA/cm², $PCE=5.81\%$. Parallel resistance (R_p) calculated at ~ 0 V was $R_p=26.3$ k Ω cm², while series resistance (R_s) calculated at ~ 2 V was $R_s=17$ Ω cm² [3].

4.2.3. Triple Junction Tandem OSC

Figure 4.49 represents a schematic of all layers that comprise the tandem triple junction organic solar cell. Layers from bottom to top include: glass substrate,

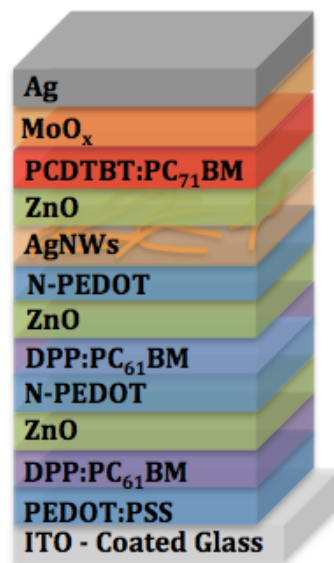


Figure 4.49. Schematic of layout of tandem triple-junction BHJ organic solar cell [4].

PEDOT:PSS, DPP:PC₆₁BM, ZnO, DPP:PC₆₁BM, ZnO, N-PEDOT, AgNWs, ZnO, PCDTBT: PC₇₁BM, MoO_x and Ag.

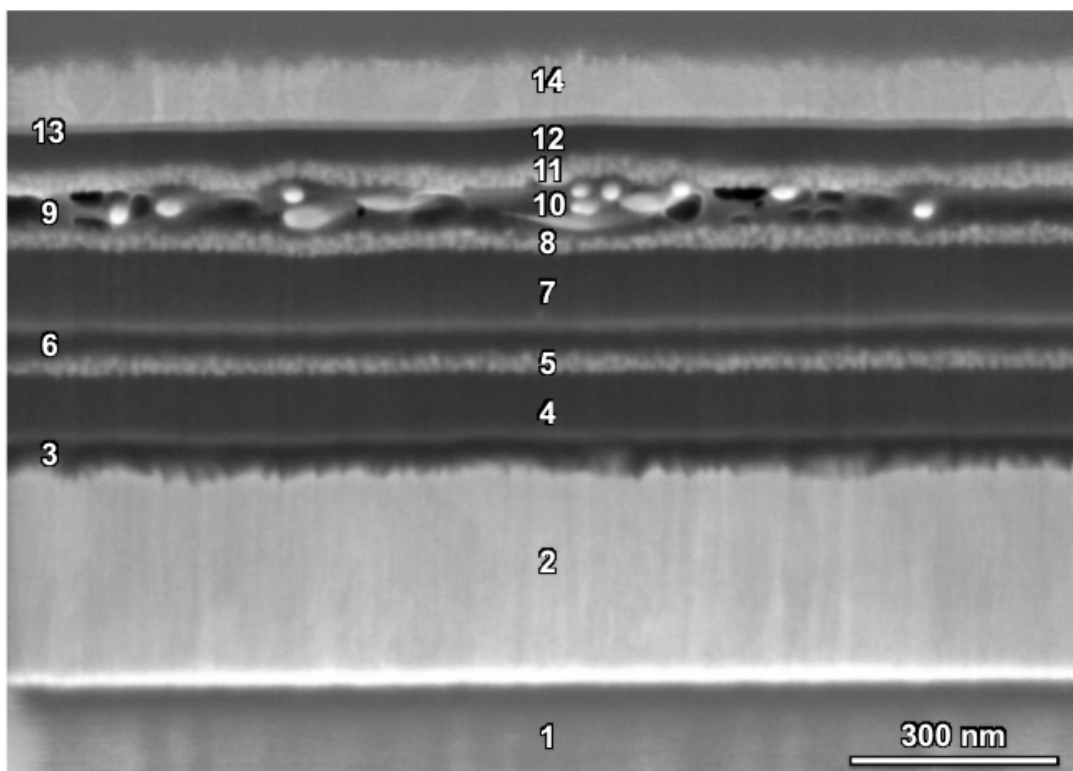


Figure 4.50. Scanning transmission electron micrograph of tandem triple junction organic solar cell cross-section after FIB milling. Numbers 1-14 correspond to the following layers: glass (1), ITO (2), PEDOT:PSS (3), DPP:PC₆₁BM (4), ZnO (5), N-PEDOT (6), DPP:PC₆₁BM (7), ZnO (8), N-PEDOT (9), AgNWs (10), ZnO (11), PCDTBT:PC₇₁BM (12), MoO_x (13) and Ag (14).

Figure 4.50 is a SEM image of the tandem triple junction organic solar cell cross-section after FIB milling. High surface roughness of top Ag electrode can be observed, as well as of ITO, at the interface with PEDOT:PSS.

Figure 4.51 is a BF TEM image of tandem triple junction organic solar cell cross-section acquired by lifting out a lamella from the cross-section by FIB machining. Structural details like very uniform thickness of ZnO and relatively uniform thickness of PEDOT layers can be observed as well as the surface roughness of ITO and top Ag electrode.

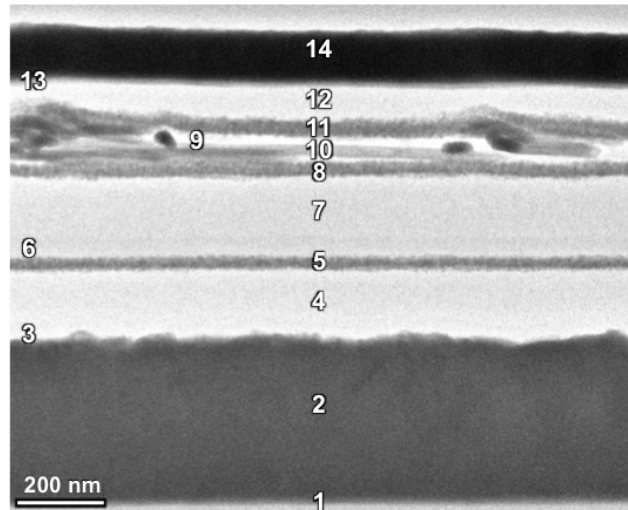


Figure 4.51. a) BF transmission electron micrograph of tandem triple junction organic solar cell cross-section acquired by FIB lamella lift-out; After [4]; Layers 1-14 correspond to the ones in image 4.50.

It is observed as if the AgNWs are embedded in the PEDOT layer i.e. even though the AgNWs were deposited on top of the N-PEDOT layer, they seem to have sunk, even coming in contact with the middle ZnO layer. Top ZnO layer exhibits high surface roughness.

Figure 4.52 is a HAADF STEM image of tandem triple junction organic solar cell cross-section acquired lifting out a lamella from the cross-section by FIB machining.

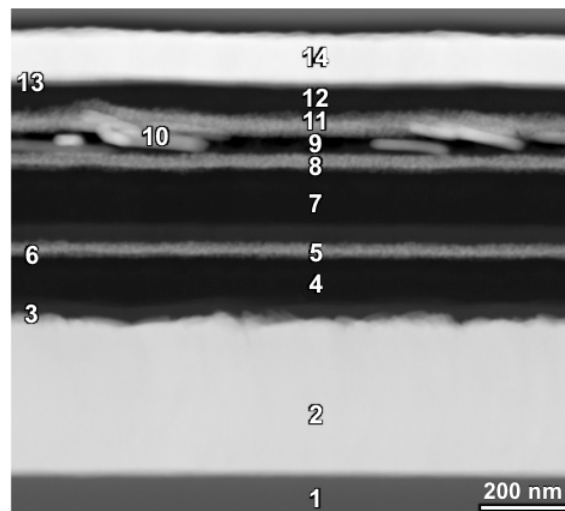


Figure 4.52. a) HAADF STEM image of tandem triple junction organic solar cell cross-section acquired by FIB lamella lift-out; After [4]; Layers 1-14 correspond to the ones in image 4.50.

From Figures 4.43, 4.46, 4.51 and 4.52 it can be seen that, since the AgNW network cannot be a continuous film, the thickness results considerably vary and the given result is the maximum thickness measured. Thickness values for all layers of the triple junction cell are given in in Table 4.5.

Table 4.5. Thicknesses measured by profilometer [4] and by line profile from TEM and STEM images of layers in the tandem triple junction organic solar cell.

Layer	Thickness by profilometer [nm]	Thickness by TEM/STEM [nm]
ITO	400	374-384
PEDOT:PSS	40	29-38
DPP:PC ₆₁ BM	50	105-118
ZnO	35	33-45
N-PEDOT	35	31-47
DPP:PC ₆₁ BM	80	125-139
ZnO	35	40-49
N-PEDOT	35	39-41
Ag NWs	80	***
ZnO	35	41-55
PCDTBT:PC ₇₁ BM	80	60-68
MoO _x	15	12-17
Ag	100	115-121

*** As previously mentioned, Ag NW cannot be a continuous film, hence thickness results considerably vary.

Table 4.5. includes thicknesses of all layers in the tandem triple junction organic solar cell acquired by measuring with profilometer and with a line profile across the TEM and STEM cross-sectional images of the cell. It can be observed that most of the experimentally measured values exhibit discrepancy in regards to the method of measurement.

Figure 4.53 shows a STEM image from which EDS maps of elemental distribution of silver, zinc, oxygen, indium, tin, sulfur and molybdenum were acquired.

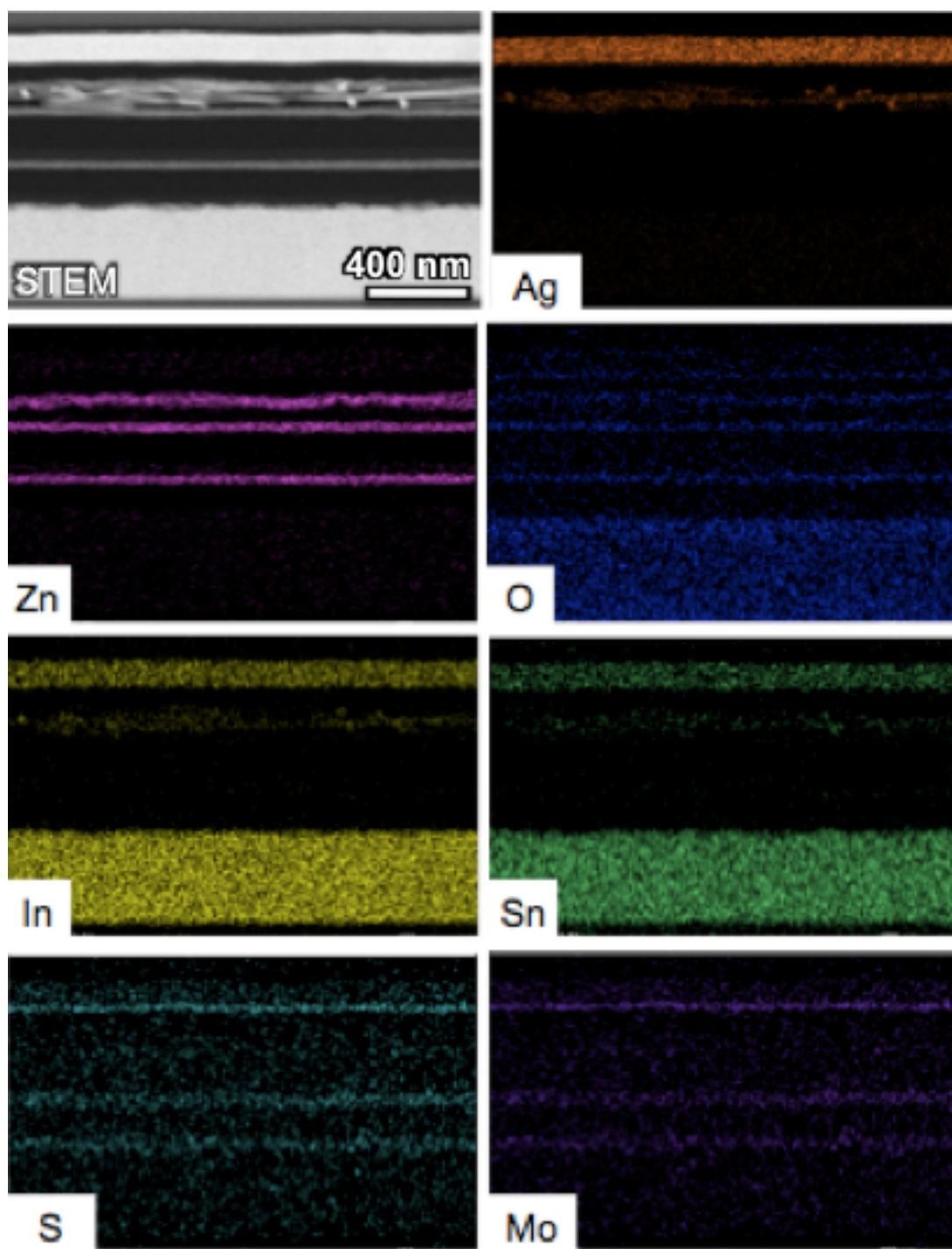


Figure 4.53. HAADF scanning transmission electron micrograph of tandem triple junction organic solar cell and EDS maps of silver (orange), zinc (pink), oxygen (blue), indium (yellow), tin (green), sulfur (turquoise) and molybdenum (purple) taken from HAADF STEM image; After [4].

Very high resolution of Ag map can be observed as the pentagonal cross-sections of AgNWs can be seen. Uniform distribution of zinc and oxygen can be observed, originating from ZnO. High surface roughness of top ZnO can be observed. Besides the ITO, indium and tin are also observed in the area corresponding to the top Ag electrode and the AgNWs. Sulfur is present in almost every part of the cell, with increased signal at locations of the PEDOT layers as well as the MoO_x layer, where the strongest molybdenum signal is located.

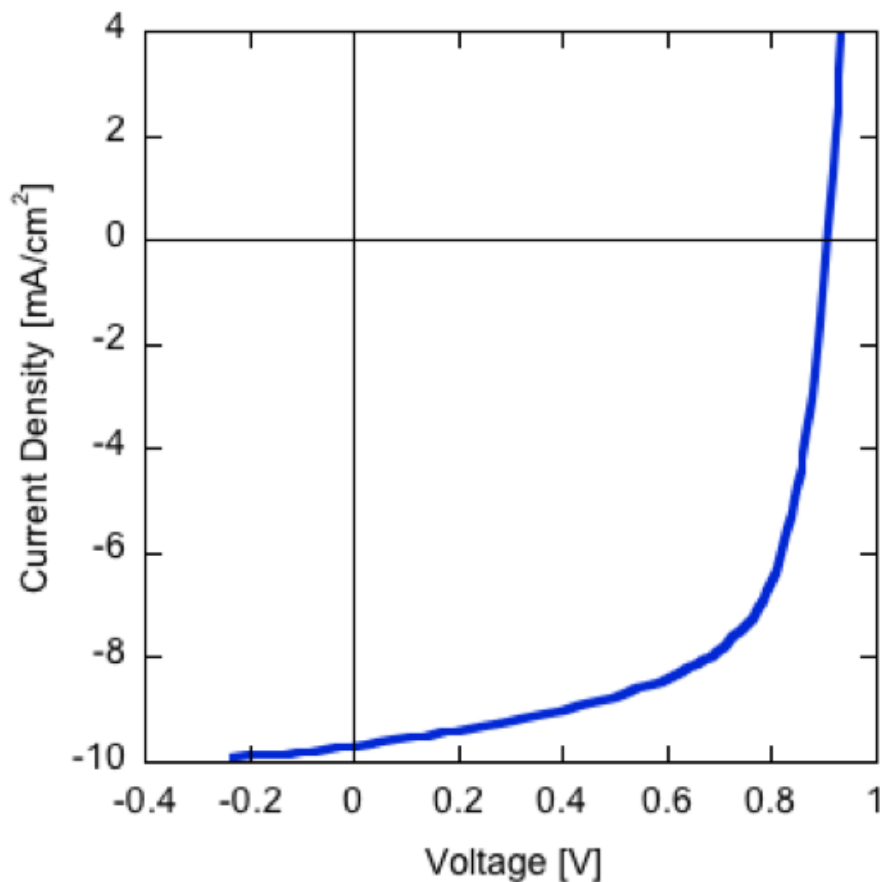


Figure 4.54. Current density as a function of voltage for the tandem triple junction organic solar cell; After [4].

Figure 4.54 is a graph depicting current density as a function of voltage for the tandem triple junction organic solar cell from where the following parameters can be obtained: $V_{OC}=0.89$ V, $FF=63.1$ %, $J_{SC}=9.67$ mA/cm², $PCE=5.43$ %. Series resistance (R_s) calculated at ~ 2 V was 1.04 Ωcm^2 [4].

4.3. Ag dendrites

Figure 4.55 is a SEM image of Ag dendrites deposited on a silicon substrate.

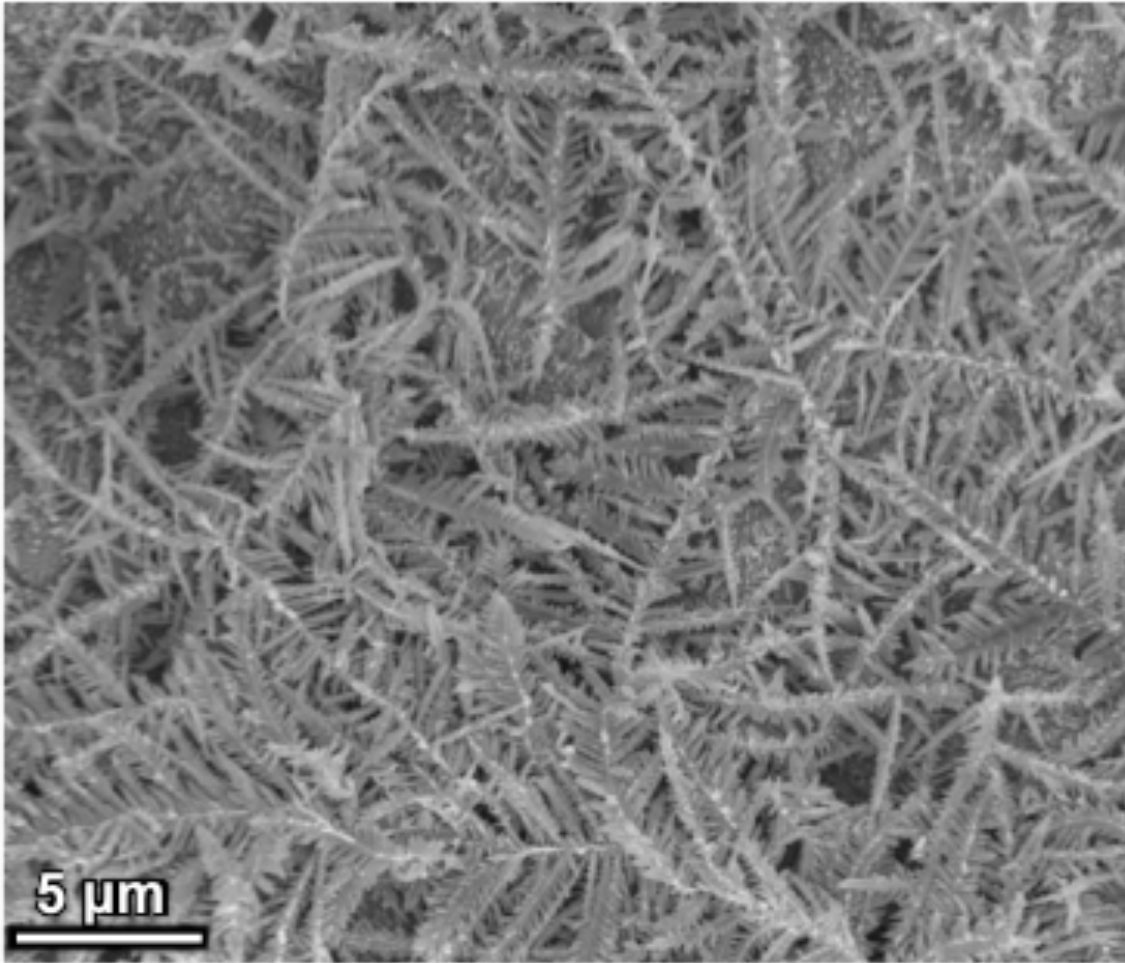


Figure 4.55. Scanning electron micrograph of Ag dendrites on silicon substrate.

This image reveals a high degree of branching of the dendrites as well as their random orientation. High density of Ag dendrites is also observed.

Figure 4.56 shows the topography and morphology typical for an Ag dendrite. Images were taken at 3 different tilts: 0° (perpendicular to the broad dendrite surface), 75° and 90° (parallel to the broad dendrite surface). It is clear that these structures are highly anisotropic and consist of a trunk, primary, secondary, and, occasionally, ternary arms (branches). Primary branches perpendicular to trunk are significantly smaller than the primary side branches.

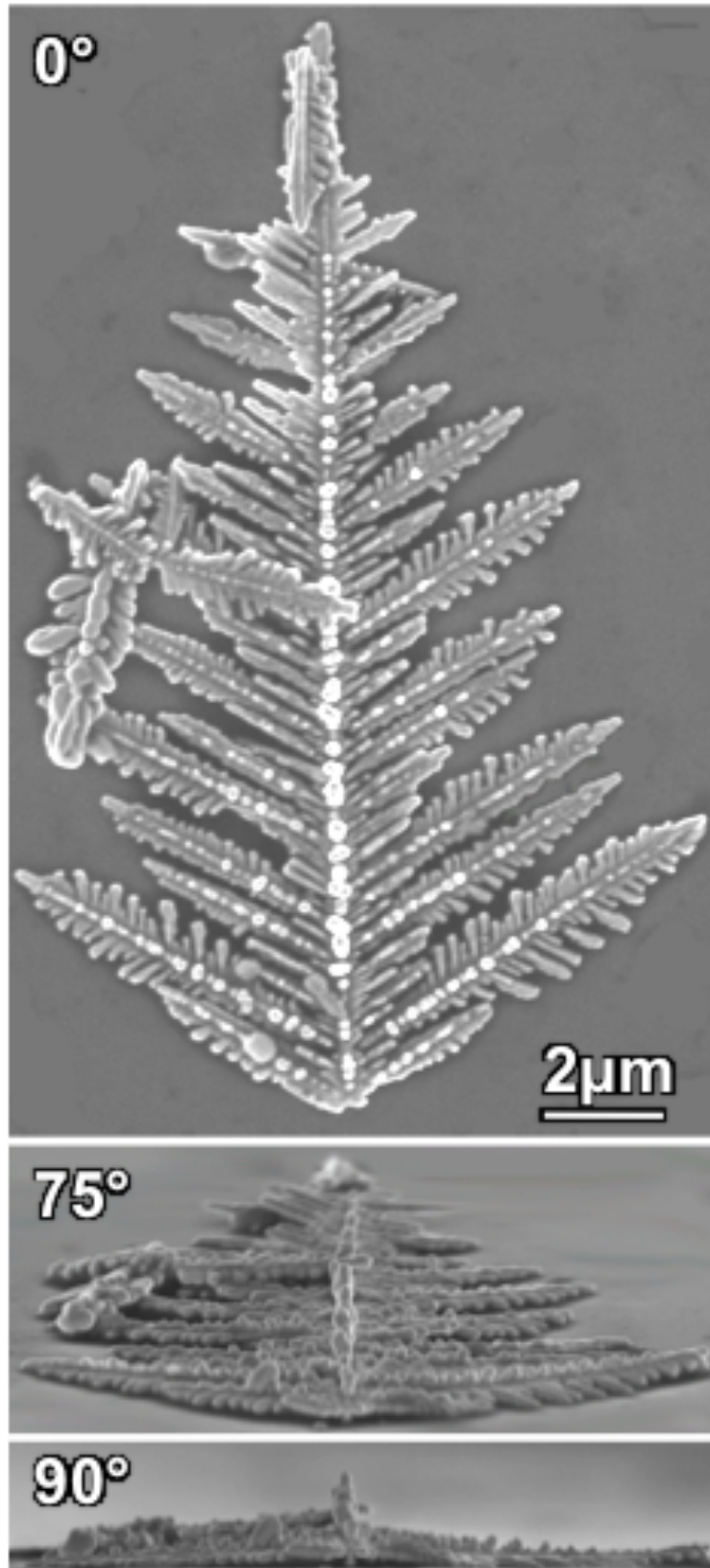


Figure 4.56. Scanning electron micrographs of Ag nanodendrites on silicon substrate taken at different tilt angles [5].

Images taken at 0° and 90° tilts, shown in Figure 4.56, demonstrate the two-dimensional nature of Ag dendrites with thickness-to-length aspect ratio greater than 10.

Figures 4.57a and b represent SEM images of an Ag dendrite taken at 0° and 52° tilts, respectively. After protective carbon layer deposition and FIB cutting along the main trunk, a cross-section image taken at 52° tilt can be seen in Figure 4.57c. Detailed analysis of the main trunk in Figure 4.57d (enlarged area indicated by white rectangle in Figure 4.57c) reveals the presence of twins of different thicknesses (light regions). A high density of twins is present. White arrows indicate 60° rotational twin boundaries.

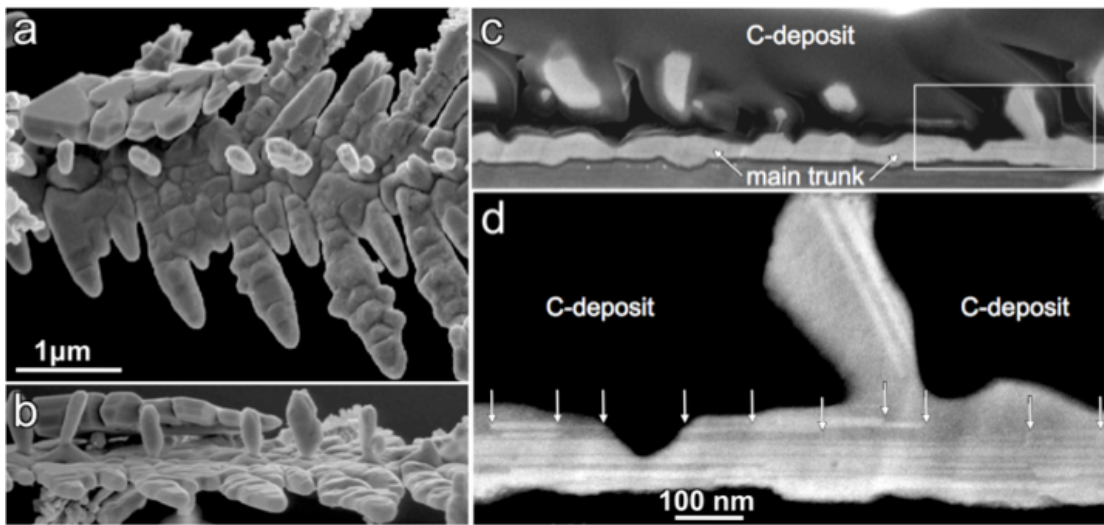


Figure 4.57. a) and b) Scanning electron micrographs of an Ag dendrite taken at different tilts, c) cross-section of an Ag dendrite, d) enlarged area indicated by white rectangle in c) [5].

Figure 4.58a is a HAADF transmission electron micrograph of an Ag dendrite where most features (trunk and branches) exhibit similar contrast. The exceptions are bright white dots lined up along the trunk of the dendrite. Figure 4.58b is an enlarged segment showing roots of a couple of branches i.e. areas between the trunk and the branches. This image shows the presence of a large number of white lines, indicated by white arrows. These lines are located 30° with respect to the trunk axis $[\bar{1}1\bar{2}]$ and are perpendicular to the branch axis $[12\bar{1}]$.

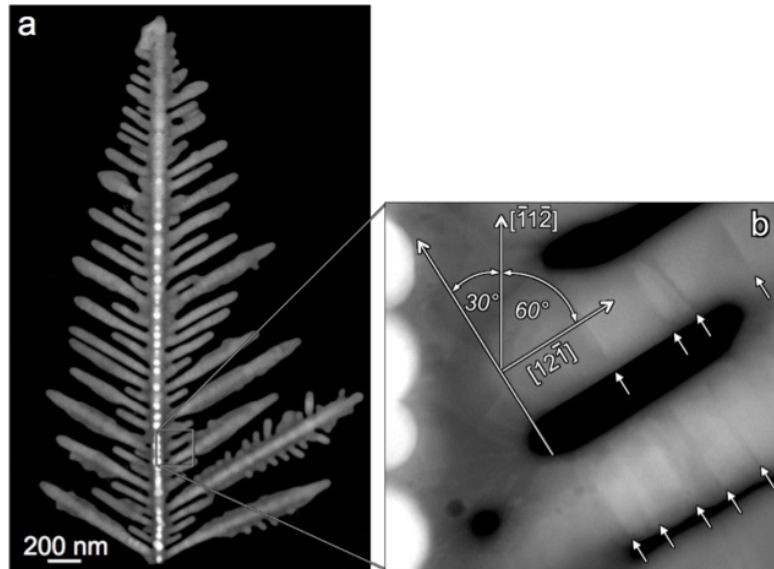


Figure 4.58. a) HAADF transmission electron micrographs of an Ag dendrite showing white spherical islands along the trunk, b) enlarged area indicated by white rectangle in a); white arrows indicate numerous white lines perpendicular to branch axis [5].

Bright field TEM image of an Ag dendrite taken close to $[\bar{1}11]$ zone axis, is shown in Figure 4.59, indicating the broad surface plane to be of $\{111\}$ type.

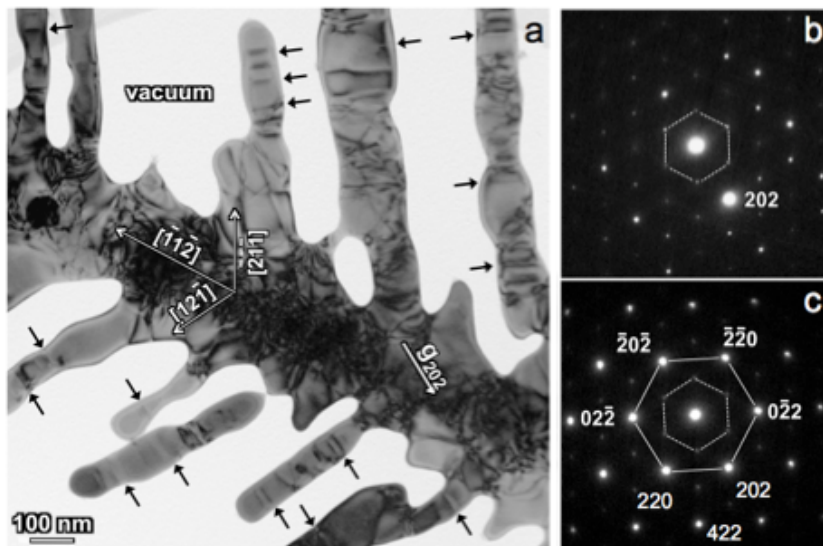


Figure 4.59. a) BF transmission electron micrograph of an Ag dendrite, b) SAD pattern of dendrite shown in a) after tilting into two-beam condition; c) SAD pattern of dendrite taken close to $[\bar{1}11]$ zone axis; black arrows indicate numerous black lines/strips perpendicular to branch axis; Growth directions of type $\langle 112 \rangle$ of trunk and branches are given in square brackets.

Figures 4.59b and c represent selected area diffraction (SAD) patterns of the Ag dendrite from Figure 4.59a, taken using g_{202} two-beam condition and close to $[\bar{1}11]$ zone axis, respectively. Strong 220 reflections are connected with solid lines forming a larger hexagon, while weaker $\frac{1}{3}422$ reflections are connected with dotted white lines, forming a smaller hexagon.

Figure 4.60a presents a TEM image of the tip of an Ag dendrite branch with detailed defect structure analysis presented in Figure 4.60b, a HRTEM phase contrast image taken close to $\langle 110 \rangle$ Ag zone axis. In this image, brighter region on the left represents silver oxide, Ag_2O , while the dark region on the right is the Ag dendrite branch. Left inset is an FFT of Ag_2O showing 200, 220 and 020 reflections. Right inset is an FFT of twins present in the Ag dendrite showing 200 and 111 reflections. Besides Ag_2O and twins, stacking faults are also present in the structure and are noted by white arrows, just like the twins.

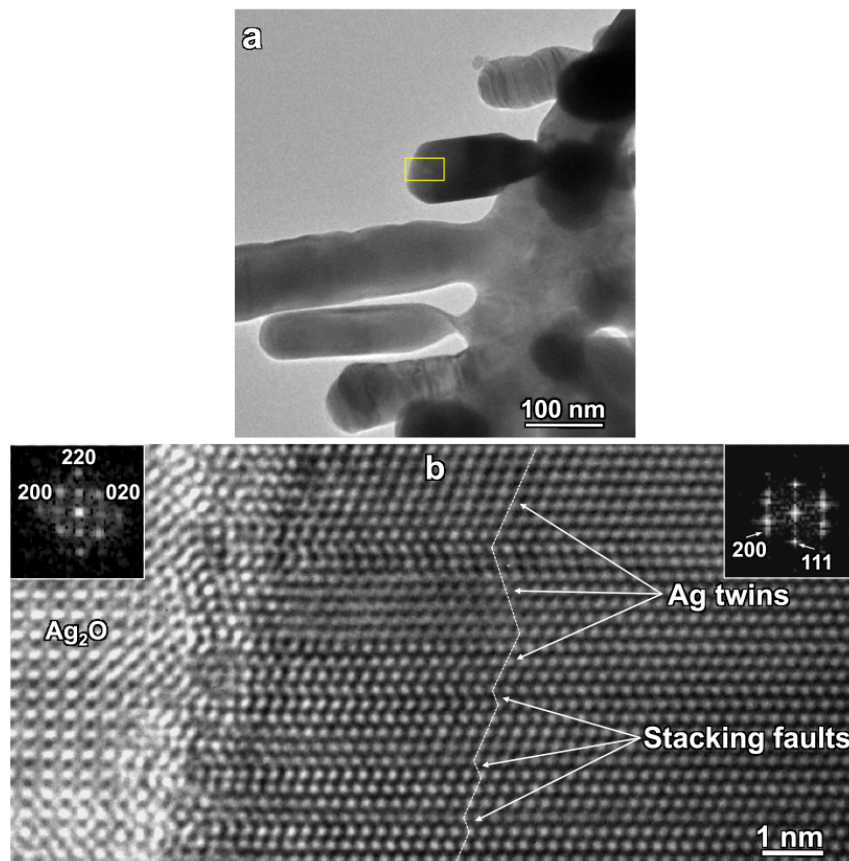


Figure 4.60. a) Transmission electron micrograph of an Ag dendrite, b) High resolution phase contrast image of enlarged area indicated by yellow rectangle in a); left inset: FFT of Ag_2O ; right inset: FFT of Ag twins.

Figure 4.61a is a HRTEM image of an Ag dendrite arm, taken close to $\langle 110 \rangle$ zone axis. The white dotted line indicates traces of $\{111\}$ planes. Moiré pattern obtained using 200 and 111 reflections is shown in Figure 4.61b, demonstrating locations of defects in the FCC lattice of Ag. Figure 4.61c represents a lattice rotation angle map obtained by geometric phase analysis (GPA) with the look up color table with values ranging from -0.2 to 0.2 radians.

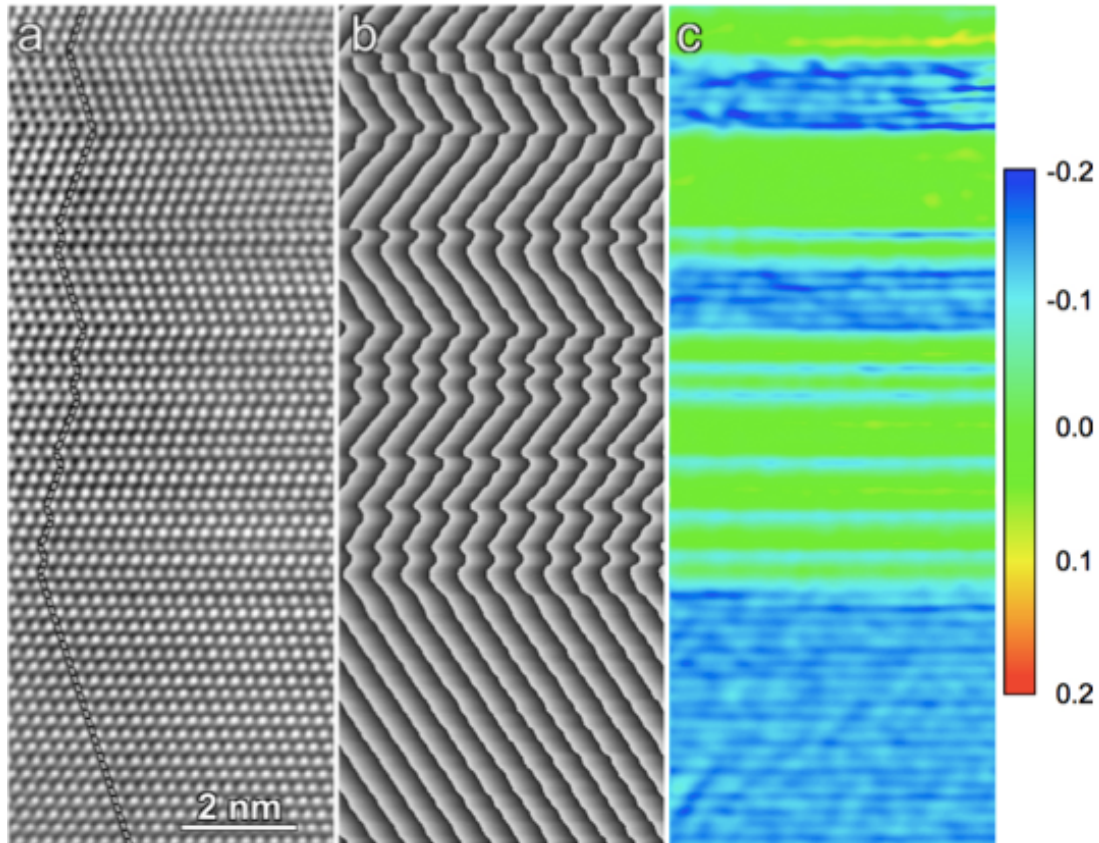


Figure 4.61. a) HRTEM image of an Ag dendrite arm; the dotted white line indicates traces of $\{111\}$ planes, b) moiré pattern obtain using 200 and 111 reflections, c) lattice rigid rotation angle map with the look up color table given in radians [5].

Figure 4.62a represents a SEM image of an Ag dendrite after FIB polishing. Figure 4.62b represents an orientation map of the dendrite in Figure 4.62a, where white lines indicate twin boundaries. Also present is the look up stereographic triangle which shows crystallographic orientation in the dendrite. Figure 4.62c represents an orientation imaging color map showing two twin variants. Figures 4.62d and e represent 100 and 111 pole figures, respectively, reconstructed from orientation data. The look up color table is a logarithm scale of units of random times. Present black and white

squares and triangles represent 100 and 111 poles, respectively, in the 111 standard stereographic projection.

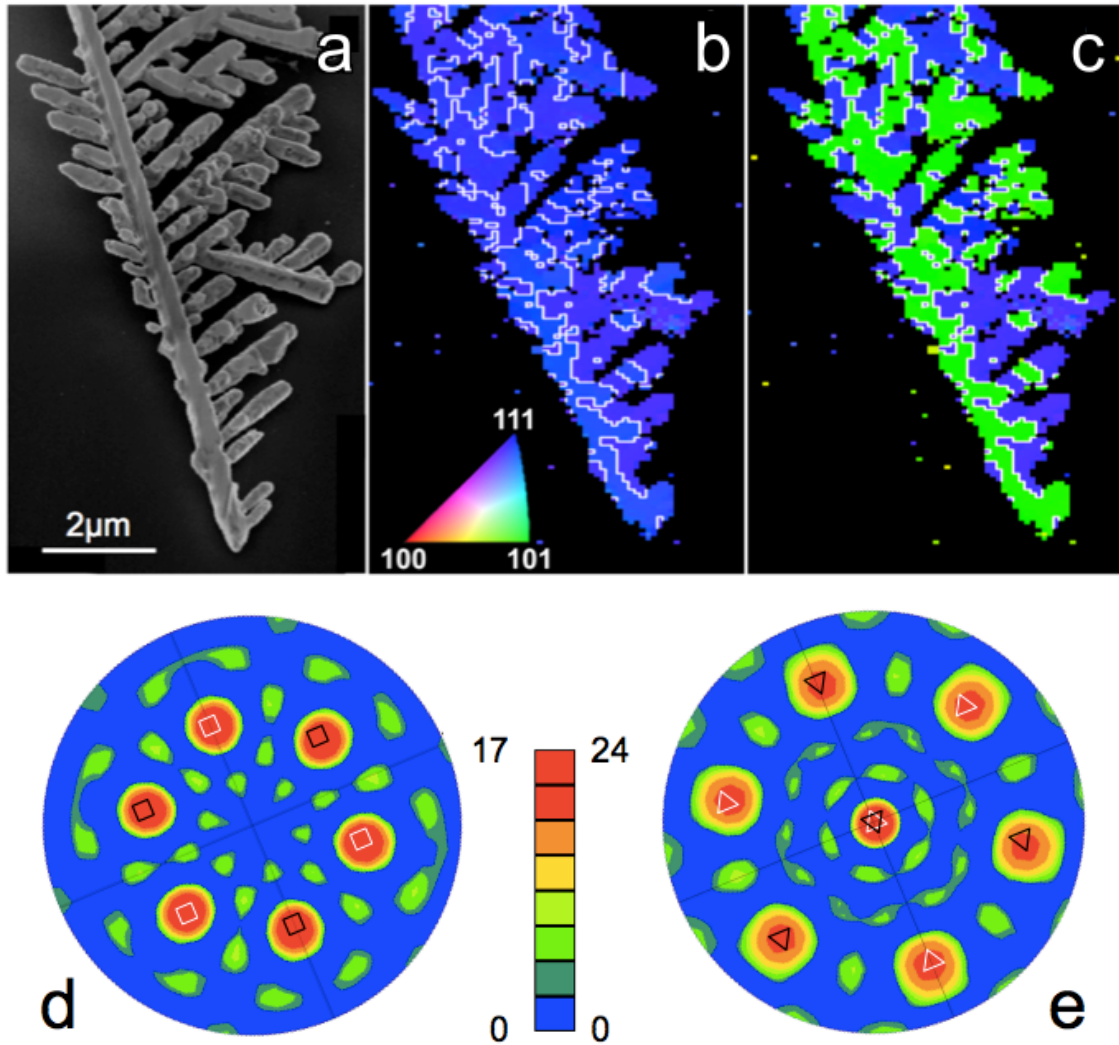


Figure 4.62. a) Scanning electron micrograph of an Ag dendrite, b) orientation map of dendrite with the lookup stereographic triangle and white lines which indicate twin boundaries, c) the orientation imaging color coded map showing two twin variants; d-e) The 100 and 111 pole figures constructed from the orientation data [5].

Figure 4.63a represents a HRTEM image of area between the dendrite trunk and branch taken close to $\langle 110 \rangle$ zone axis, near the root of the dendrite branch. Narrow twin bands can be observed from the image.

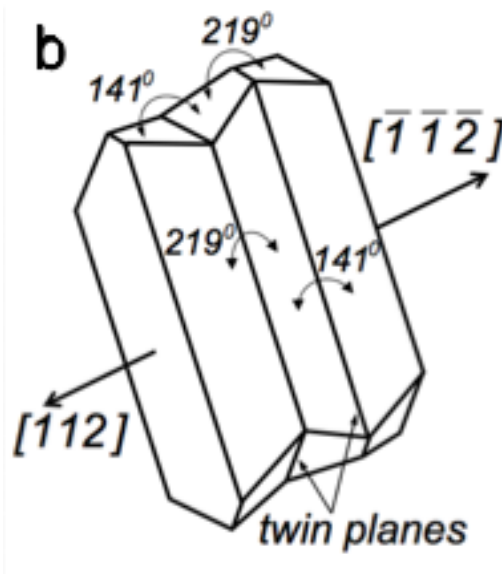
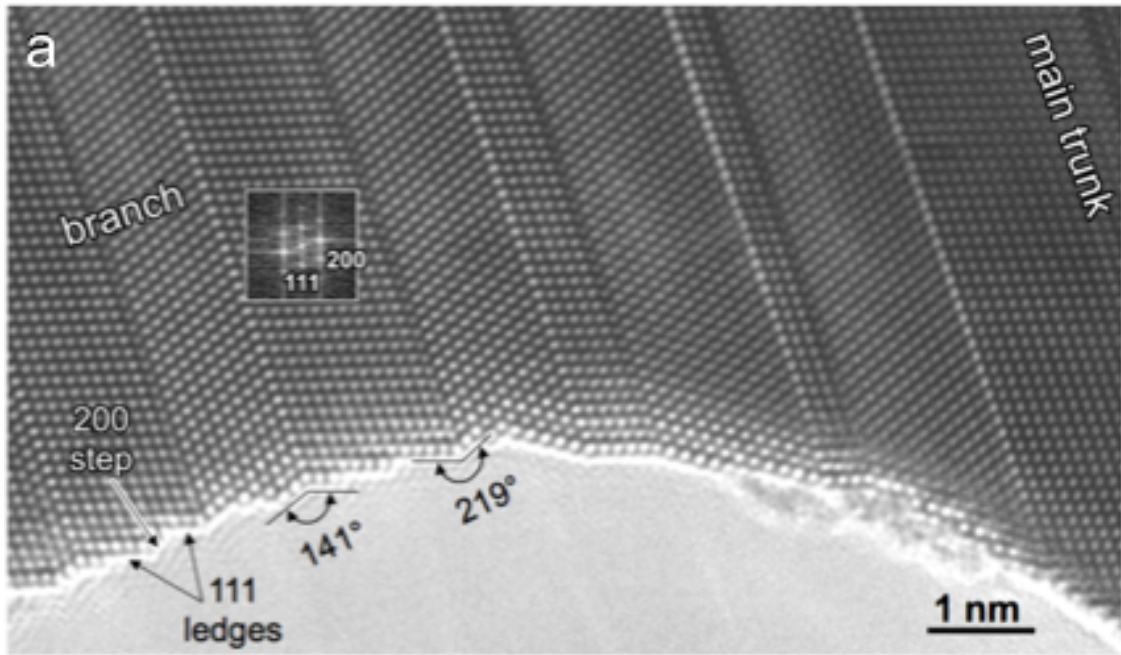


Figure 4.63. a) High resolution transmission electron micrograph of twins in the zone between the dendrite trunk and arm; inset is an FFT taken from the area indicated by the white square, b) schematic illustration of twin planes with respect to growth directions and distinctive angles [5].

These twins are perpendicular to the $\langle 112 \rangle$ dendrite branch growth direction. Reentrant corners and twin junctions (ridges) present exhibit angles of 141° and 219° , respectively. Various twins can be observed from this image. The inset is an FFT taken from the area indicated by white square, showing 111 and 200 orientations. Figure

4.63b is a schematic illustrating the presence of a two-twin configuration with 141° and 219° angles and $[112]$ and $[\bar{1}\bar{1}\bar{2}]$ growth directions noted.

Figure 4.64 represents a SEM image of an Ag dendrite with a high aspect ratio. These images were taken at two different tilt angles: -15° and $+20^\circ$.

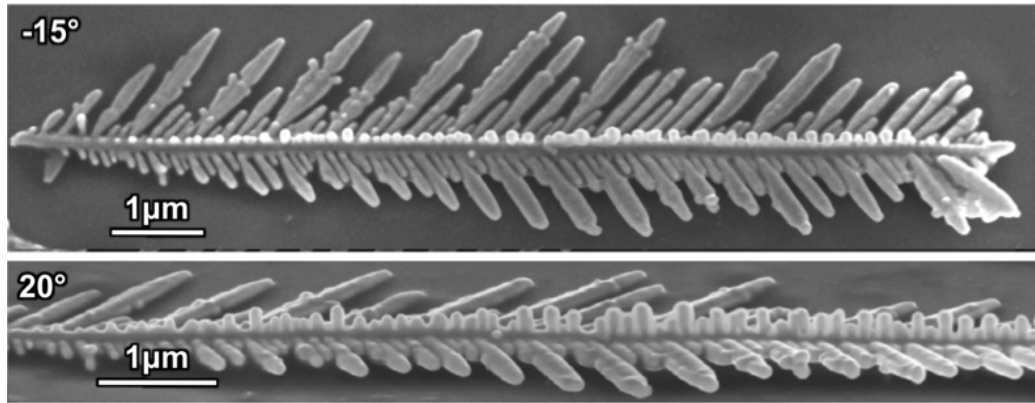


Figure 4.64. Scanning electron micrograph of an Ag dendrite taken at two different tilt angles.

Figure 4.65 represents an optical microscopy image of Ag dendrites deposited by drop casting on a glass substrate. From this image a uniform distribution of dendrites is apparent as well as evident percolation.

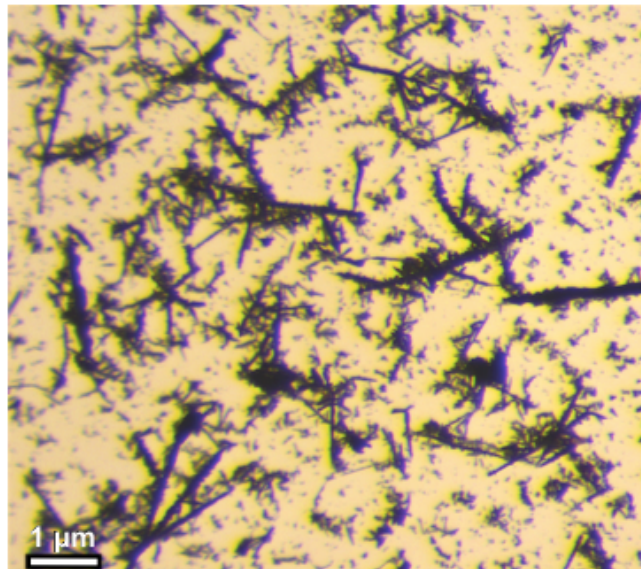


Figure 4.65. Optical micrograph of a drop cast Ag dendrite on glass; note uniform distribution of dendrites.

Figure 4.66 is a graph depicting resistance of Ag dendrites before and after annealing for 3 minutes at nominal temperature of 250°C. Resistance is calculated from the graph as the slope. Dendrites experienced significant drop in resistance, from 37.3 ± 4.6 to $16.9 \pm 2.1 \Omega \text{sq}^{-1}$, after annealing.

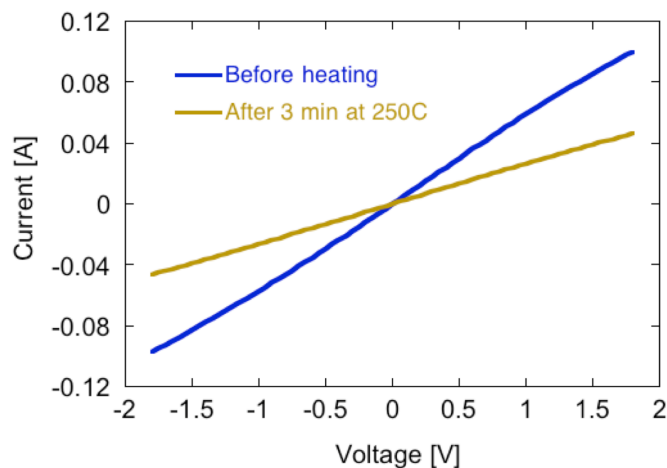


Figure 4.66. Current as a function of voltage of 250 μL drop cast Ag dendrites before (blue) and after heating 3 minutes at 250°C (beige).

Figure 4.67 depicts optical transmittance at 300-800nm wavelength range of light for different volumes of Ag dendrites deposited on a glass substrate. Deposited 50 μL of Ag dendrite solution yielded a transmittance of 88.3% at 360 nm and 89.3% at 550 nm.

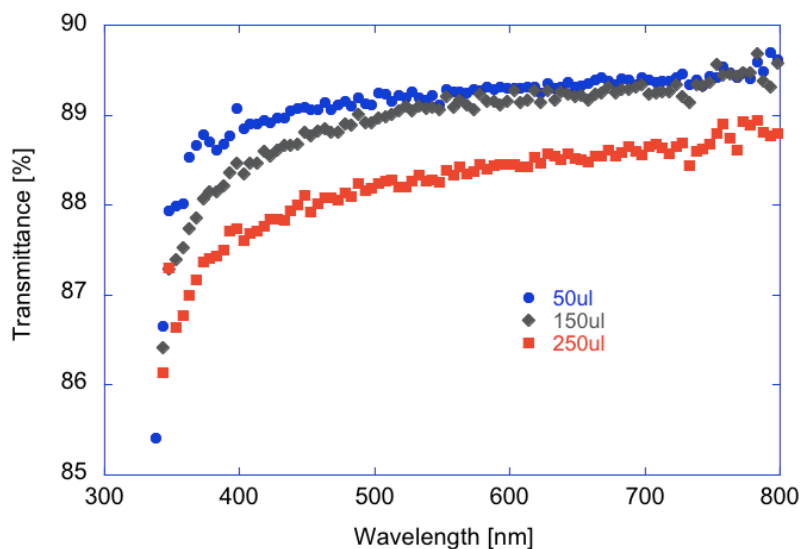


Figure 4.67. Transmittance as a function of wavelength for various volumes of Ag dendrites deposited on glass: 50 μL (blue), 150 μL (dark grey) and 250 μL (red).

Deposited 150 μL of Ag dendrite solution yielded a transmittance of 87.5% at 360 nm and 89% at 550 nm. Deposited 250 μL of Ag dendrite solution yielded a transmittance of 86.8% at 360 nm and 88.3% at 550 nm.

4.4. Polymer Nanocomposites

Figures 4.68a, b and c represent optical microscopy images of PVB nanocomposites with multi-walled carbon nanotubes, single-walled carbon nanotubes and graphene as the nanofiller, respectively. It can be noticed that, unlike CNTs, which have a tendency to form agglomerates, graphene is relatively finely dispersed in the polymer matrix.

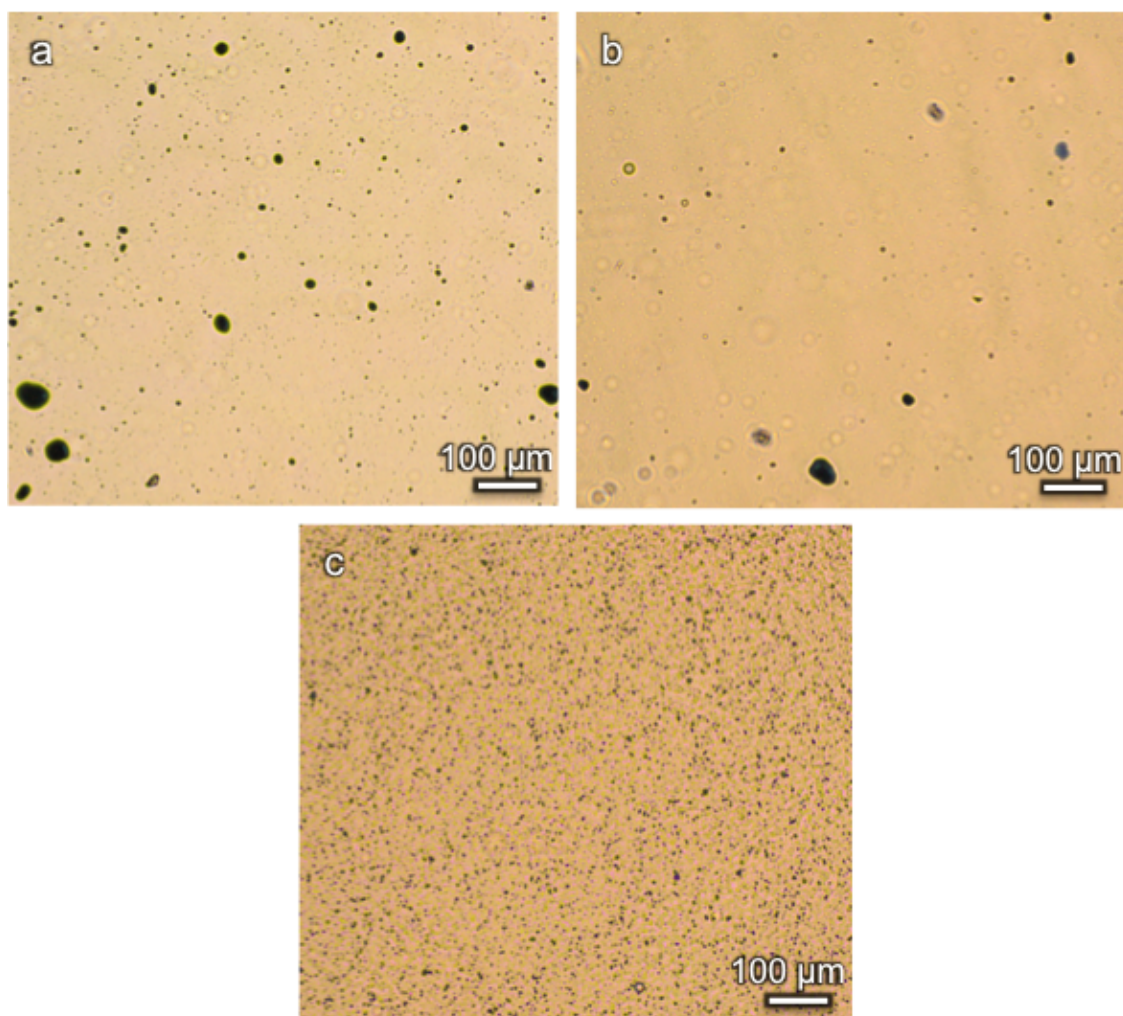


Figure 4.68. Optical micrographs of a) PVB nanocomposite with MWCNTs, b) PVB nanocomposite with SWCNTs, c) PVB nanocomposite with graphene.

Figure 4.69a represents a HRTEM image of a single MWCNT. Figure 4.69b represents a HRTEM image of a bundle of SWCNTs were double-walled carbon nanotubes (DWCNTs) can also be noticed. Figure 4.69c represents a HRTEM image of a few layer graphene sheet.

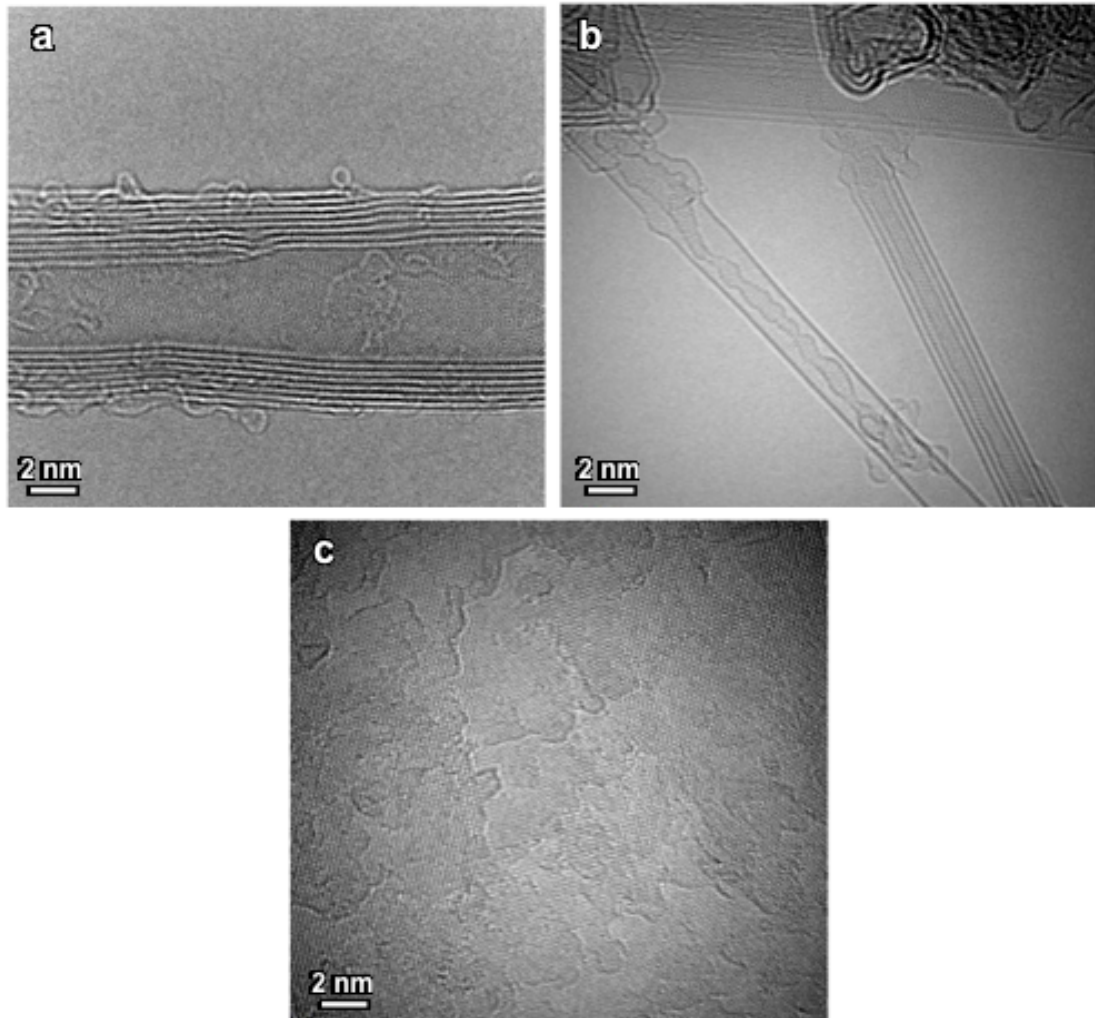


Figure 4.69. High resolution transmission electron micrographs of as received a) MWCNTs, b) SWCNT, and c) graphene [6].

Figure 4.70a represents a low magnification TEM image of the nanocomposite PVB with MWCNTs and it is clearly seen that this sample is characterized by non-uniform distribution of CNTs in the polymer matrix. Figure 4.70b is a HRTEM image showing intimate attachment between the PVB polymer and an individual MWCNT.

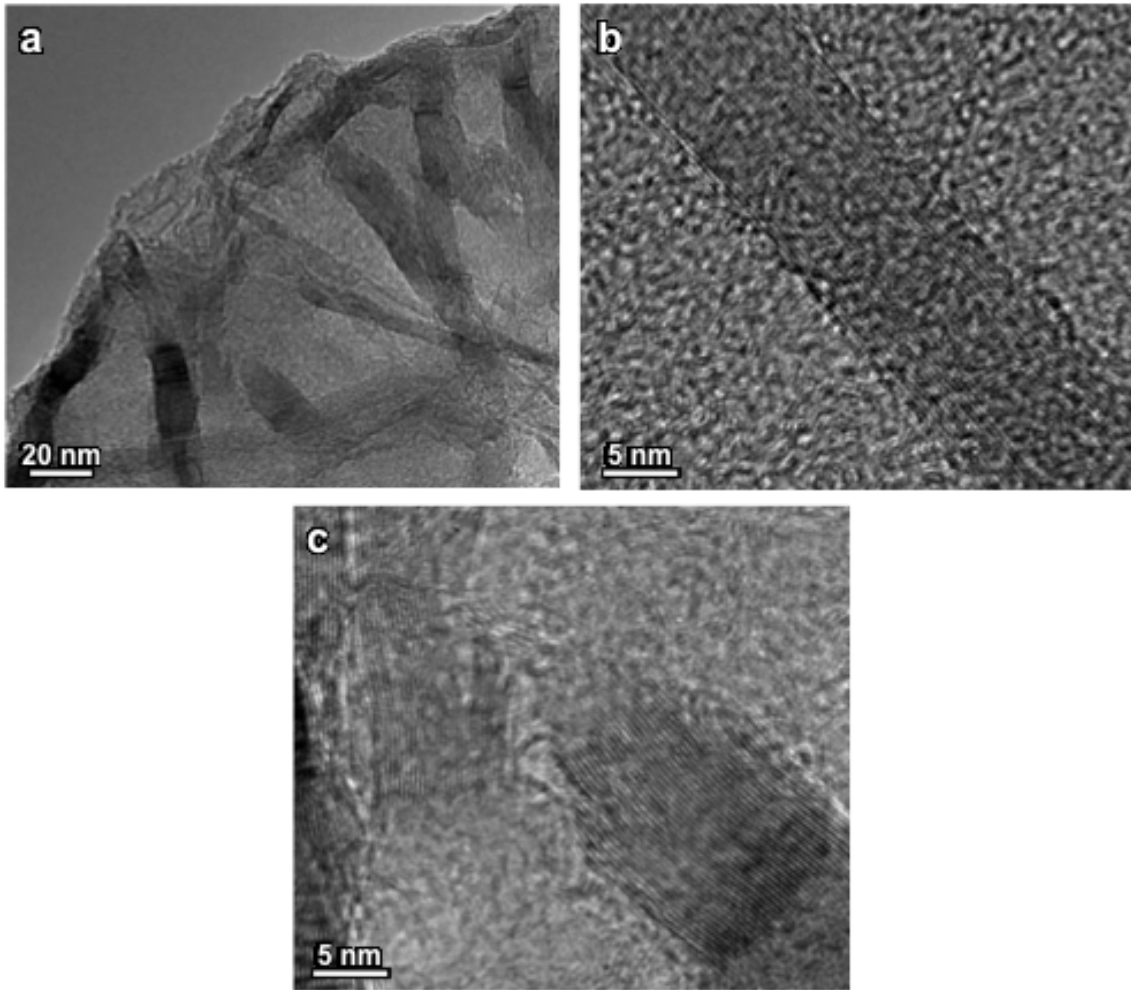


Figure 4.70. a) Low magnification transmission electron micrograph of nanocomposite PVB with MWCNTs, b) High resolution transmission electron micrograph of individual MWCNT embedded in PVB matrix [6], c) MWCNT exhibiting tearing inside the PVB matrix.

Using profile imaging, the number of walls in this MWCNT was calculated to be 12, with the outer diameter of 10nm and the inner diameter ~2nm. Analysis by FFT expectedly confirmed the amorphous nature of the polymer matrix, even though some short-range order can be detected. Figure 4.70c is a HRTEM image of PVB nanocomposite with MWCNTs showing tearing of tubes taking place during vigorous mixing with the ultrasonic processor.

Figure 4.71 represents a partial Raman spectra of pristine MWCNTs (pink), PVB (blue) and nanocomposite PVB with MWCNTs where Figure 4.71a is a part of the spectrum in the range of 1200-1700 cm^{-1} and Figure 4.71b is a part of the spectrum in

the range of 2500-3000 cm^{-1} . It can be observed that the peak corresponding to the D band of MWCNTs shifts from 1326 cm^{-1} in pristine form to 1331 cm^{-1} as the filler in the nanocomposite, while the peaks corresponding to G and D' bands shift from ~ 1580 cm^{-1} to ~ 1590 cm^{-1} and ~ 1605 cm^{-1} to ~ 1615 cm^{-1} , respectively.

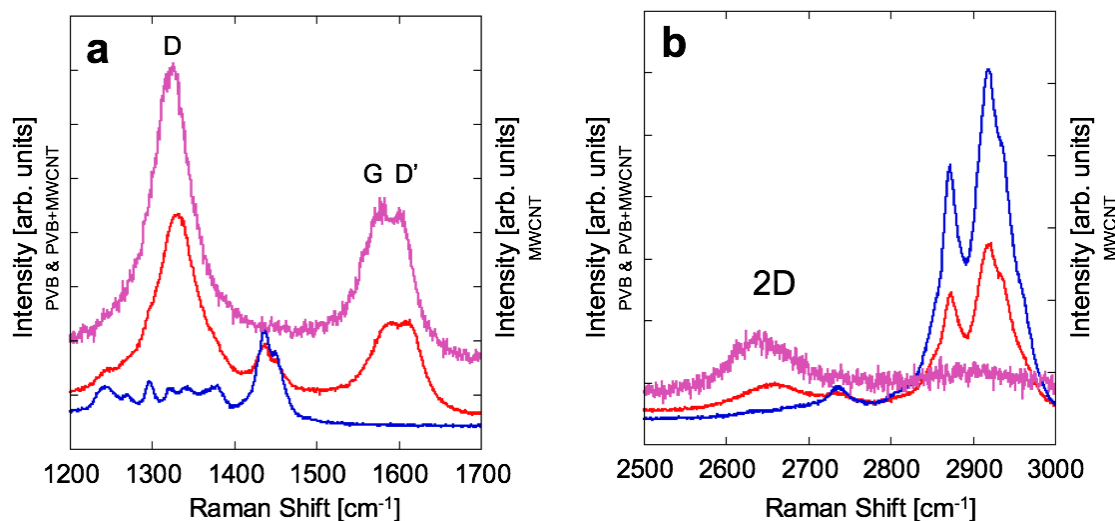


Figure 4.71. Raman shift (as a function of intensity) of pristine MWCNTs (pink), PVB polymer (blue) and nanocomposite PVB with MWCNTs (red) in the range of 1200-1700 cm^{-1} (a), and 2500-3000 cm^{-1} (b); Characteristic D, G, D' and 2D peaks are noted [6].

It is clear from Figure 4.71b that the peak corresponding to the 2D band of MWCNT shifts from ~ 2638 cm^{-1} to ~ 2657 cm^{-1} .

Figure 4.72 represents a partial Raman spectra of pristine SWCNTs (pink), PVB (blue) and nanocomposite PVB with SWCNTs. Figure 4.72a is a part of the spectrum in the range of 100-400 cm^{-1} . It can be observed that the peaks corresponding to the RBM band of SWCNTs have frequencies of 155 cm^{-1} , 188 cm^{-1} , 210 cm^{-1} , 245 cm^{-1} , 306 cm^{-1} , 333 cm^{-1} . For the nanocomposite, peaks originating from SWCNTs are found at 156 cm^{-1} and 171 cm^{-1} as well as in the interval 185-200 cm^{-1} . Figure 4.72b is a part of the spectrum in the range of 1200-1700 cm^{-1} . It can be observed that the peak corresponding to the D band of SWCNTs shifts from 1309 cm^{-1} to 1319 cm^{-1} , while the peak corresponding to G band shifts from ~ 1569 cm^{-1} to ~ 1588 cm^{-1} . Figure 4.72c is a part of the spectrum in the range 2500-3000 cm^{-1} where the peak corresponding to the 2D band of SWCNTs is shifts from ~ 2602 cm^{-1} to ~ 2633 cm^{-1} .

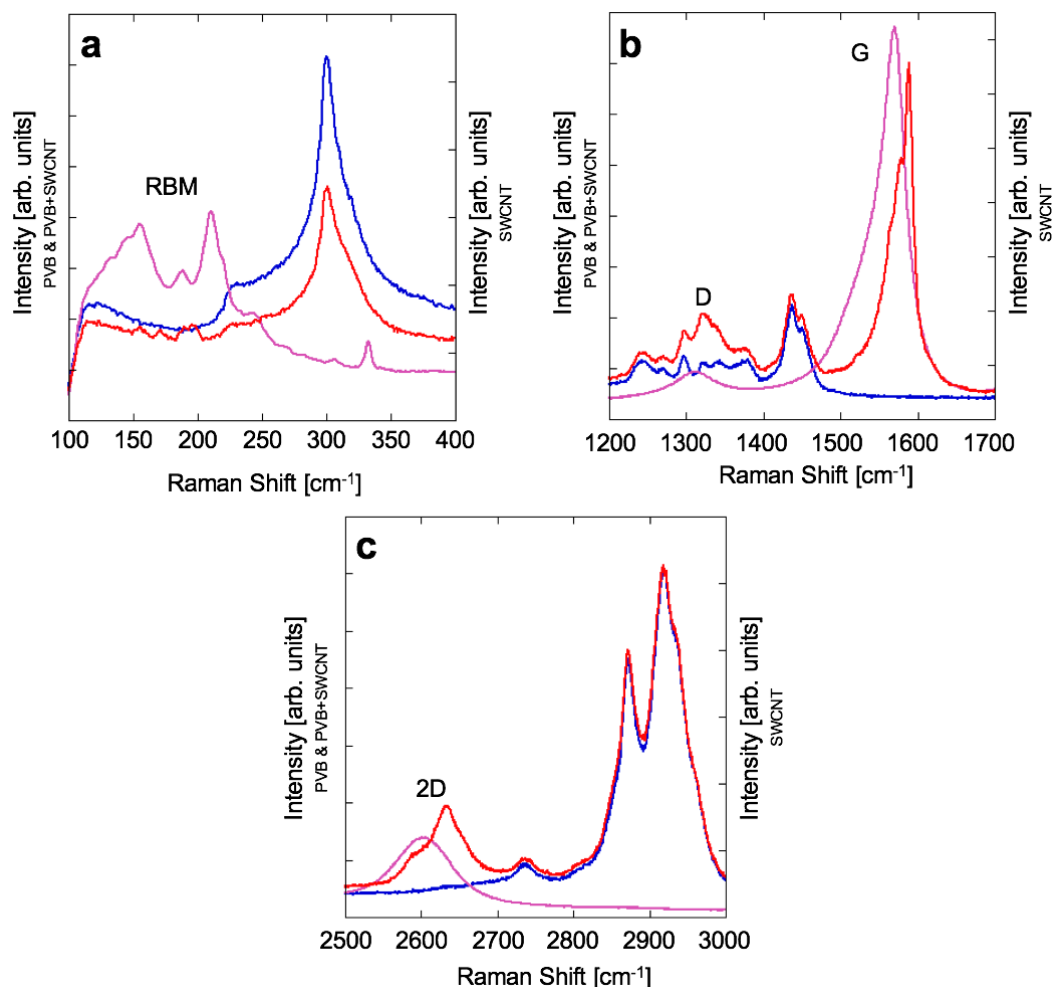


Figure 4.72. Raman shift (as a function of intensity) of pristine SWCNTs (pink), PVB polymer (blue) and nanocomposite PVB with SWCNTs (red) in the range of 100-400 cm⁻¹ (a), and 1200-1700 cm⁻¹ (b) and 1200-1700 cm⁻¹ (c); Characteristic RBM, D, G and 2D peaks are noted [6].

Figure 4.73 represents a partial Raman spectra of pristine graphene (pink), PVB (blue) and nanocomposite PVB with graphene. Figure 4.73a is a part of the spectrum in the range of 1200-1700 cm⁻¹. It can be observed that the peak corresponding to the D band of graphene shifts from 1330 cm⁻¹ in pristine form to 1333 cm⁻¹ as the filler in the nanocomposite, while the peaks corresponding to G band shifts from ~1570 cm⁻¹ to ~1579 cm⁻¹. Figure 4.73b is a part of the spectrum in the range of 2500-3000 cm⁻¹ where the peak corresponding to the 2D band of graphene is shifts from ~2670 cm⁻¹ to ~2675 cm⁻¹.

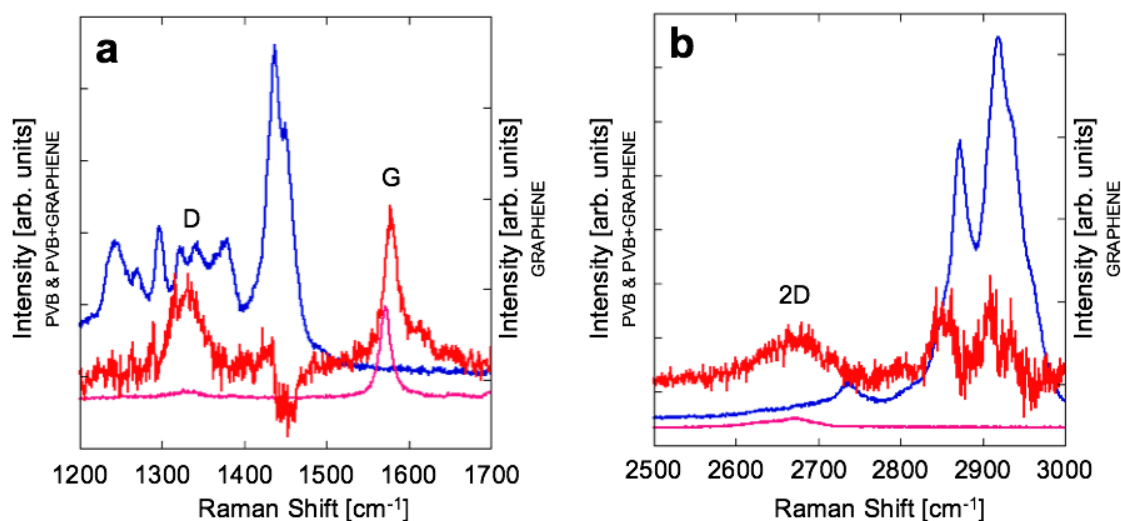


Figure 4.73. Raman shift (as a function of intensity) of pristine graphene (pink), PVB polymer (blue) and nanocomposite PVB with graphene (red) in the range of 1200-1700 cm^{-1} (a), and 2500-3000 cm^{-1} (b); Characteristic D, G and 2D peaks are noted [6].

Figure 4.74a represents a graph of transmittance as a function of wavelength for pure PVB (blue) and nanocomposites PVB with MWCNT (black), PVB with SWCNT (pink) and PVB with graphene (red). All samples were processed under identical conditions (spin speed, time and amount deposited). At 360nm wavelength, in the UV region, transmittance appears to be ~84, 85, 89, and 91% while at 550nm, the Vis region, it is ~84, 88, 90, and 92%, for nanocomposites with graphene, MWCNTs, SWCNTs, as well as pure PVB, respectively.

Figure 4.74b represents a graph of transmittance as a function of wavelength for three nanocomposite samples of PVB with MWCNTs which differ in thickness. The M9/2 is a two-layer sample with 4.77 μm thickness, exhibiting transmittance of 76% at 360nm and 82% at 550nm. M9/4 is a four-layer sample with 10.52 μm thickness, exhibiting transmittance of 44% at 360nm and 55% at 550nm. M9/8 is an eight-layer sample with 46.49 μm thickness, exhibiting transmittance of 23% at 360nm and 34% at 550nm. Figure 4.74c represents a graph of transmittance, at 360nm and 550nm, as a function of thickness for PNC samples presented in Figure 4.74b.

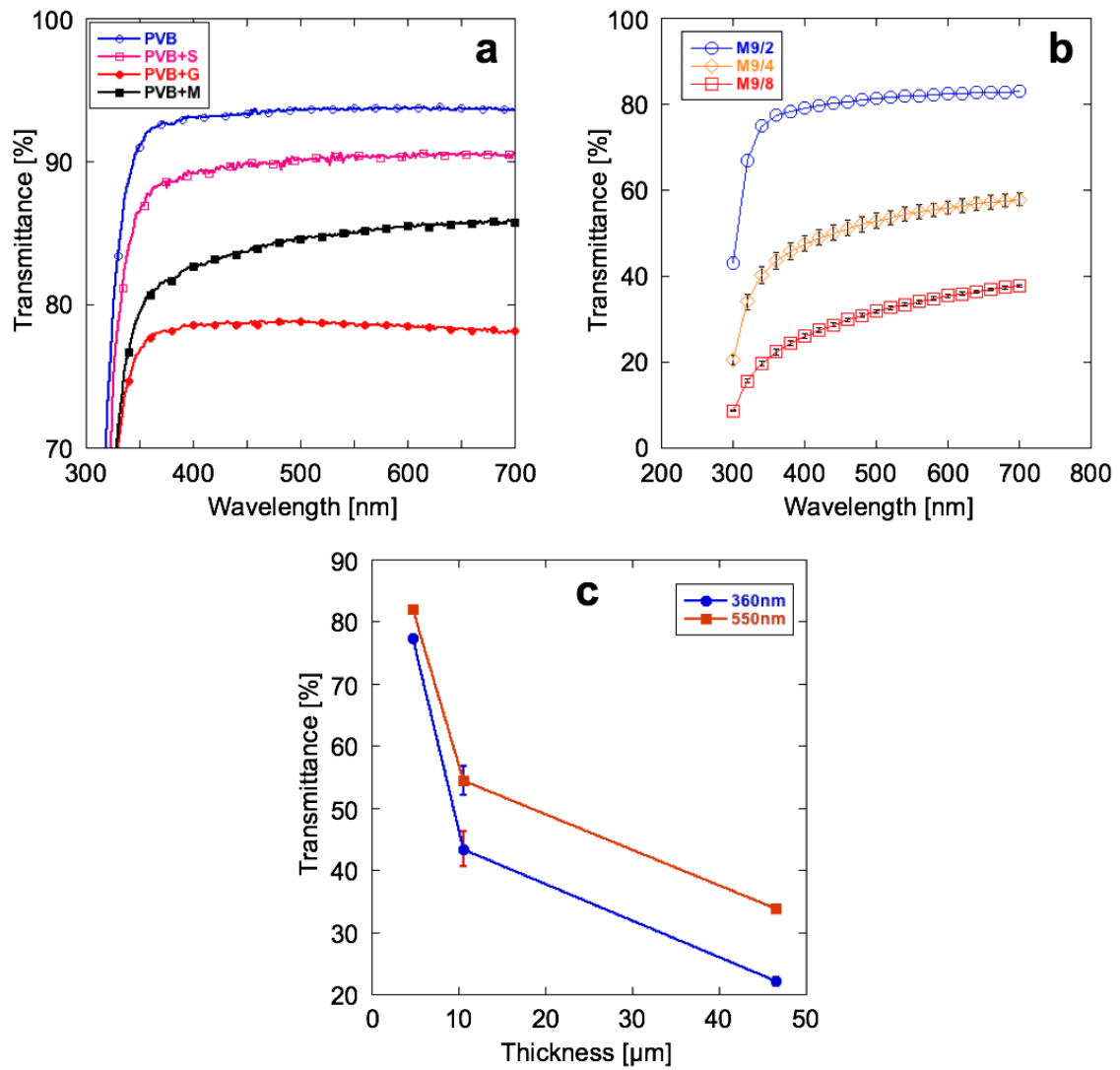


Figure 4.74. a) Transmittance as a function of wavelength for samples processed under identical conditions, b) transmittance as a function of wavelength for nanocomposite samples PVB with MWCNTs for different sample thicknesses, c) transmittance as a function of thickness at two different wavelengths, 360 nm (circles) and 550 nm (squares), for nanocomposite samples PVB with MWCNTs [6].

Figure 4.75 is a graph of applied load as a function of displacement i.e. penetration depth of indenter for pure PVB (black line), PVB with MWCNTs (blue line), PVB with SWCNTs (red line), and PVB with graphene (green line).

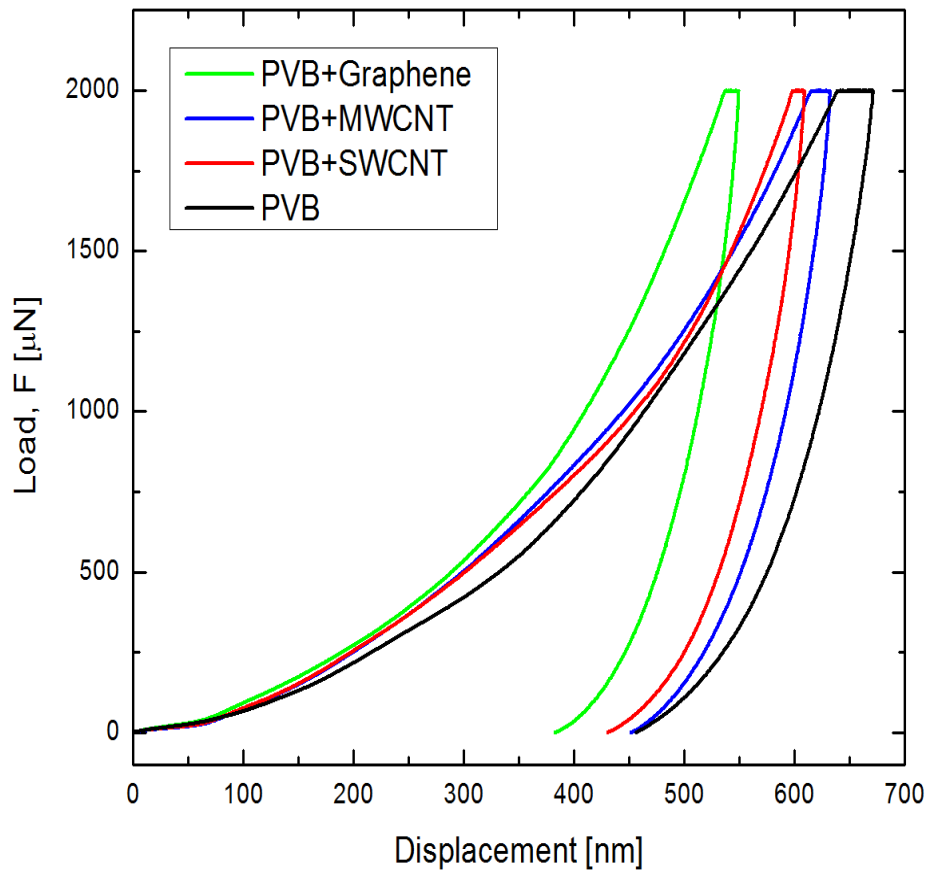


Figure 4.75. Typical load – displacement curves for pure PVB (black line), PVB with MWCNTs (blue line), PVB with SWCNTs (red line), and PVB with graphene (green line).

Table 4.6. Displacement before and after hold at maximum load P_{\max} as well as final displacement of pure PVB, PVB with MWCNTs, PVB with SWCNTs and PVB with graphene. Values obtained from Figure 4.75.

Displacement	h at P_{\max} before hold [nm]	h at P_{\max} after hold [nm]	h_r, final depth after unload [nm]
PVB	638.9	671	456.8
PVB with MWCNTs	614.8	632.4	451.3
PVB with SWCNTs	597.3	608.3	430.8
PVB with graphene	536.6	549.1	382.6

Using the equations given in Section 3.2.3. of this thesis, which apply to hardness and reduced modulus calculations from the slope of curve, the hardness and modulus values were calculated and are given in Figure 4.76 and Table 4.7. Both, hardness and reduced modulus increase in the following order: PVB, PVB+MWCNTs, PVB+SWCNTs and PVB+Graphene.

Figure 4.76 represents graph of hardness (blue) and reduced modulus (orange) values of pure PVB as well as PVB nanocomposites, presented in Table 4.7.

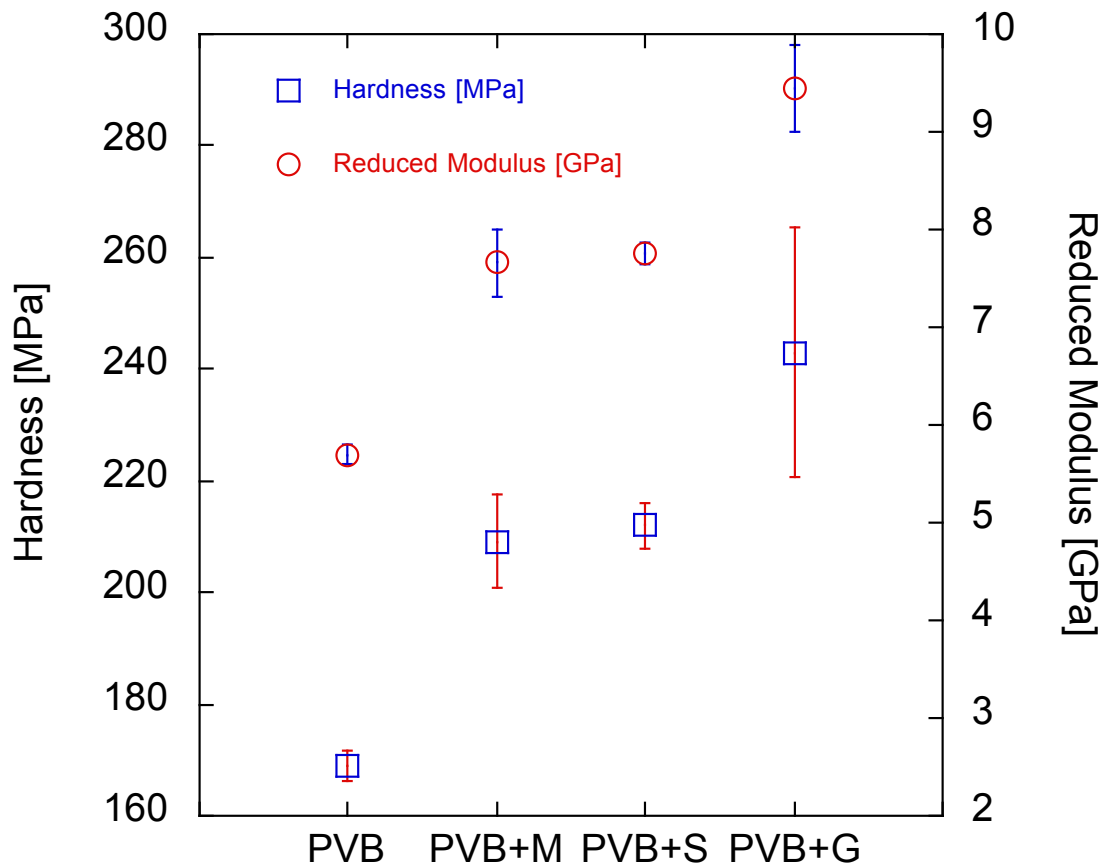


Figure 4.76. Reduced modulus (red circles) and hardness values (blue squares) for pure PVB film, PVB with SWCNTs (PVB+S), PVB with MWCNTs (PVB+M), and PVB with graphene (PVB+G) nanocomposites; Also displayed are the standard deviations; After [6].

It is clear that hardness and reduced modulus increase in the following sequence: pure PVB, PVB with MWCNTs, PVB with SWCNTs and PVB with graphene with values given in Table 4.7.

Table 4.7. Hardness and reduced modulus values of pristine PVB, PVB with MWCNTs, PVB with SWCNTs and PVB with graphene; After [6].

Sample	Reduced Modulus [GPa]	Hardness [MPa]
PVB	5.7 ± 0.1	169 ± 3
PVB with MWCNTs	7.75 ± 0.09	210 ± 2
PVB with SWCNTs	8.05 ± 1.09	212.08 ± 22.90
PVB with Graphene	9.44 ± 0.44	242.98 ± 22.35

Figure 4.77 is a graph of electrical resistivity of pure PVB and nanocomposites PVB with MWCNT, PVB with SWCNT and PVB with graphene.

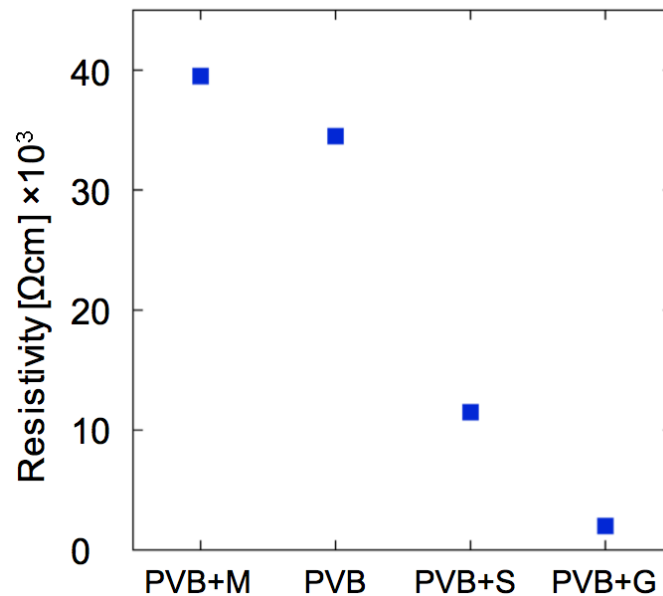


Figure 4.77. Electrical resistivity of pure PVB, PVB with SWCNTs (PVB+S), PVB with MWCNTs (PVB+M), and PVB with graphene (PVB+G) nanocomposites [6].

The values are as follows: 39.75 kΩcm for PVB with MWCNTs, 34.5 kΩcm for pure PVB, 11.5 kΩcm for PVB with SWCNTs and 2 kΩcm for PVB with graphene. Note that resistivity for all investigated samples was in the kΩcm range.

REFERENCES

- [1] V. V. Radmilovic, M. Goebelt, S. Christiansen, E. Spiecker, V. R. Radmilovic, *Advanced Functional Materials*, 2016, Submitted.
- [2] M. Goebelt, R. Keding, S. W. Schmitt, B. Hoffmann, S. Jaeckle, M. Latzel, V. V. Radmilovic, V. R. Radmilovic, E. Spiecker, S. Christiansen, *Nano Energy*, Volume 16, 2015, Pages 196-206.
- [3] F. Guo, N. Li, V. V. Radmilovic, V. R. Radmilovic, M. Turbiez, E. Spiecker, K. Forberich and C. Brabec, *Energy and Environmental Science*, 8 (2015) 1690-1697.
- [4] F. Guo, N. Li, F. Fecher, N. Gasparini, C. O. Ramírez Quiroz, C. Bronnbauer, Y. Hou, V. V. Radmilovic, V. R. Radmilovic, E. Spiecker, K. Forberich, C. Brabec, *Nature Communications*, 6 (2015) 7730.
- [5] V. V. Radmilovic, J. Kacher, E. R. Ivanovic, A. M. Minor, V. R. Radmilovic, *Crystal Growth & Design*, 16 (2016) 467-474.
- [6] V. V. Radmilovic, C. Carraro, P. S. Uskokovic, V. R. Radmilovic, *Polymer Composites*, 2016, DOI: 10.1002/pc.24079.

5. Discussion

5.1. AgNWs and AgNWs/AZO Nanocomposite

From Figures 4.1 and 4.2 it is clear that the polyol reduction method of synthesizing AgNWs and ALD deposition of AZO (Figure 4.4) provide a high level of monodispersity. This implies that, as most of the AgNWs have very similar diameter sizes, and AZO exhibits homogenous thickness throughout the sample, a random junction taken for detailed analysis provides a very relevant picture of what occurs in the entire structure.

Figure 4.6a represents HAADF STEM imaging of AgNWs encapsulated with AZO, a very useful technique to identify different chemical species, elemental distribution, etc., but not microstructural features such as grain size and their orientation. These can be acquired from CTEM images like the one shown in Figure 4.6b.

By comparing Figure 4.7b, a SAD pattern of area shown in Figure 4.7a with a simulated ring diffraction pattern of the wurtzite structure in Figure 4.7c it is clear that they correspond to each other by matching of the ring indices, corroborated with rotational average line profile from Figure 4.7d. It is clear from that aluminum, as a dopant, has no effect on the AZO structure which is identical to the wurtzite structure of ZnO.

High resolution phase contrast image of AZO, shown in Figure 4.8a, gives evidence of sympathetic nucleation [1], which relates to nucleation of grains of a phase on the already formed grains of the same phase. In this case, nano-grains exhibit crystallographic co-dependence, shown by the crystallographic relationships in Figure 4.8. In Figure 4.8b, a FFT of grain 3, present 010 spot splitting is a consequence of the presence of an inversion domain boundary (IDB). These IDBs in the ZnO wurtzite structure were found to be associated with indium [2,3], or in this case, can be the result of doping with aluminum. Formation of IDBs is also facilitated by low stacking fault energy of 43 mJ/m^2 [4] on the basal ZnO wurtzite plane. EDS spectra in Figure 4.9, shows that aluminum ions are successfully incorporated in the ZnO crystal lattice, acting as a dopant. Figure 4.9 also demonstrates the presence of silver (yellow) which is limited to the cores of the analyzed structure while zinc (blue), oxygen (orange), and

aluminum (red) distributions are shown present in the AZO shells. However, due to overlapping of cores and shells during mapping of the sample in plan view, zinc, oxygen and aluminum signals are found to be present in both, cores and shells.

Partitioning of the elements present in the AgNWs/AZO composite structure was performed in a more accurate manner using a cross-section of the sample shown in Figure 4.11. A single AgNW encapsulated with AZO, seen in Figure 4.11a, exhibits heterogeneous intensity distribution i.e. contrast, which is the result of strain and diffraction contributions. Inside the AgNW, white lines represent twin planes while white irregular shaped regions represent strain, whose origin is explained in Section 2.1.2 of this thesis. Radial growth of AZO is observed from the AgNW as well as the Si substrate, as they both act as the substrate for AZO growth during ALD deposition. For HAADF STEM imaging, the formula $I \sim Z^\beta$ is applicable, as explained in the Experimental section 3.2.4.2. As the β coefficient has values between 1.5-1.9, depending of various factors, and the value of I is based on intensity corresponding to Ag in the white region, Z value of the ~ 3 -5nm black rim around the AgNW observed in Figure 4.11b, is calculated by line profiling to be ~ 30 , very close to the Z value of $\text{AlO}_{1.5}$, possibly indicating non-stoichiometric nature of Al_2O_3 at interface. This is in good agreement with the increased concentration of aluminum rich species around the black pentagonal area (AgNW) presented in EDS map of aluminum in Figure 4.11. There are two possible explanations for the origin of this layer, one being that Ag acts as a catalyst for Al_2O_3 growth via phenomenon noted by John et al. [5] while the other states that ALD process utilized in this experiment starts with an Al_2O_3 cycle and the catalytic decomposition of the trimethylaluminum (TMA) precursor at the Ag surface is likely [6]. Higher concentration of oxygen species, observed in the EDS map of oxygen, is due to the native SiO_2 present at the surface of Si substrate.

Some AgNW cross-sections encapsulated by AZO, as seen in Figure 4.10, appear to be blurry. The reason for this is because they are inclined with respect to the electron beam, i.e. their $\langle 110 \rangle$ growth direction is not parallel to incident electron beam. The observed radial distribution of AZO nano-grains in Figure 4.10 indicates that they exhibit columnar growth, typical for highly textured films [7], consistent with van der Drift 2D [8], and Smereka et al. 3D [9] competitive grain growth models.

The ADF STEM image presented in Figure 4.12 demonstrates how specimen tilting may affect the microstructure characterization of a sample, as in this case tilting close to $\langle 110 \rangle$ zone axis gave detailed insight on the microstructure of an AgNW and its welded zones. After tilting, shown in Figure 4.12b, the right-hand NW still appears blurry because it is inclined with respect to the electron beam. This image is very important as it shows that multiple welding can occur between NWs which drastically reduces the electrical resistance of the entire NW network.

During solid-state wetting and subsequent welding of two AgNWs, ledges in the welded zone form 100 facets, as shown by yellow arrows in Figure 4.13a. From this HRSTEM image it is clear that the welded zone expands with the incorporation of Ag atoms into close packed $\{111\}$ planes, which results in a growth direction parallel to the noted white arrow in the image. This means that Ag atoms diffuse along the surface of the NW and are epitaxially attached on the 100 facet of the upper NW resulting in $\{111\}$ planes growing in the direction toward the bottom AgNW. In this study, the epitaxial attachment was proposed to be called *homoepitaxial growth* as Ag atoms from one AgNW are attached to the other AgNW. The term *epitaxial recrystallization*, as proposed by Garnett et al. [10] implies a deformed structure being replaced by a non-deformed structure, which is not the case here, as it has been proven that the epitaxially attached structure (welded zone) has inherent defects from the top NW as well as novel defects, which will be addressed later in this chapter. The terms *NW site specific coarsening* or *NW sintering* are also more apt for naming this process instead of *NW welding* as no filler material is used for the joining of the AgNWs. However, the term *NW welding* will be used, since a consensus has been made about the use of the term for this kind of process as literature suggests.

Roughness of interface between bottom AgNW and welded zone, seen in Figure 4.14a, promotes diffusion across the interface, especially if it is incoherent, which is the case here. A grain boundary (GB) can be considered between the epitaxially attached welded zone (a sort of neck) and the twin segment(s) of the bottom NW which supply the welded zone with Ag atoms. Just like for the welded zone shown in Figure 4.13b, in Figure 4.14b it is observed that the welded zone has defects, ruling out the recrystallization concept. Change of orientation of $\{111\}$ planes in the moiré pattern

from Figure 4.14c is an indication of the presence of twins inherent from the top AgNW.

Nano-twins, i.e. few layer thick twins, inside other twins, are observed in the welded zone, shown in Figure 4.15b. The presence of nano-twins can be related to small stacking fault energy for Ag of 16 mJ/m^2 [11], but can be also ascribed to possible relaxation of strain. This includes change of crystallographic orientation with respect to the orientation of bottom NW twins in contact with top NW and confirms that the NW contact formation causes surface-to-volume energy reduction. From Figures 4.15b and c dislocations and stacking faults (SF) can also be observed which again confirm that this region is not defect-free therefore it did not occur as the result of recrystallization. With the analysis of three different parts of the welded region (left, center and right) it can be concluded that it is homoepitaxially attached with an orientation and defects like twins and stacking faults, inherent from the top AgNW.

Observing the cross-section of an AgNW, five twin segments clearly create a decahedron, confirmed by the FFT of the area, in Figure 4.16. Spacings of $\sim 0.236 \text{ nm}$ and $\sim 0.204 \text{ nm}$, between atomic planes, can be assigned to $\{111\}$ and $\{100\}$ FCC Ag planes, respectively. The atomic configuration of $\{111\}$ planes shows the presence of stacking faults and nano-twins, already observed in Ag dendrites [12], creating the appearance of an HCP (hexagonal close packed) local atom arrangement in an FCC AgNW [13]. This is caused by Shockley partial dislocations [14,15,16]. In direct atomic column measurements of crystal lattice distortion, horizontal and vertical displacements are in horizontal and vertical directions, respectively, radial displacement is along the direction pointing away from the origin while annular displacement is along the direction perpendicular to the direction pointing away from the origin i.e. 90° apart from radial displacement.

ADF STEM image in Figure 4.17, clearly shows solid-state wetting and subsequent welding occurring only if two NWs are in contact with each other via points of large difference of radii of curvature. This means one NW has to be in contact through a corner (small radius of curvature) while the other through a facet i.e. flat surface (large radius of curvature). This was the motivation for proposition of the following model of NW solid-state wetting and subsequent welding, illustrated in Figure 5.1, which consists of four stages:

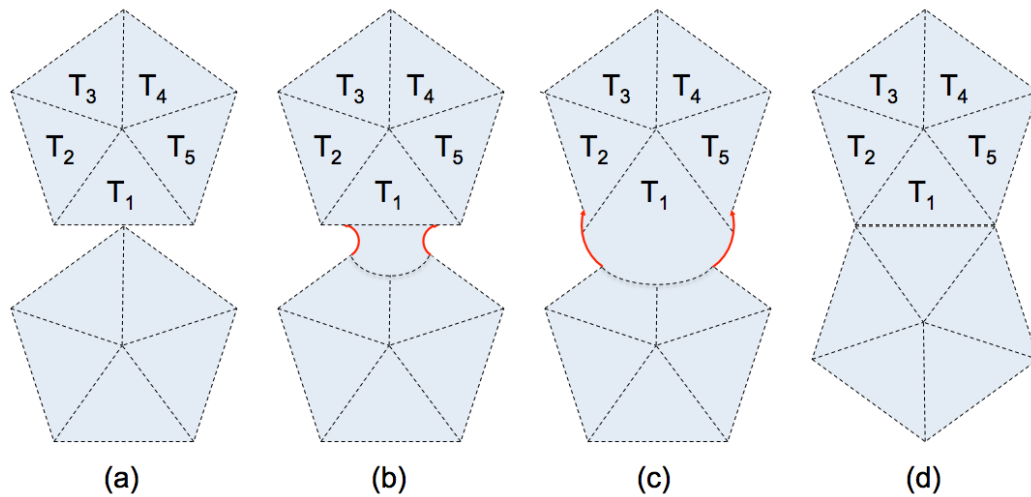


Figure 5.1. Proposed model of solid-state wetting and subsequent welding of two AgNWs during annealing; a) before the formation of a neck region, b) after the formation of a neck region, c) neck expansion; d) two NW in contact along 100 facet, where the formation of a neck region is significantly delayed [13].

- *Dissolution* of the corner of the bottom AgNW;
- *Solid-state diffusion* of Ag atoms from the corner (small radius of curvature) of the bottom NW, toward the 100 facet (large radius of curvature) of the T₁ twin segment of upper NW, creating conditions for solid-state wetting. This is dominated by the surface diffusion path. Modeling and simulation of initial sintering kinetics for copper powder demonstrated that for smaller particle sizes the surface diffusion contribution is greater [17]. Strong experimental evidence has also been presented which states that at the beginning of the sintering process, surface diffusion is the predominant mass transport mechanism [18];
- *Epitaxial attachment* by solid-state wetting of Ag atoms on 100 facets, forming a neck between two AgNWs (welded zone). When the GB between the neck and the twin segments of the bottom NW, which supply Ag atoms, is formed, the GB diffusion mechanism starts contributing to mass transport of Ag atoms during sintering, as activation energy for diffusion is lower along the GB than through nano-grains. Homoepitaxial growth in the welded zone resembles abnormal grain growth, observed in other alloy systems, due to solid-state wetting [19]. In this case, the welded zone and the twin segment on which it is epitaxially attached can be defined as an abnormally grown nano-grain;

- *Growth* (widening) of neck (welded zone) by incorporation of Ag atoms into {111} planes and their lateral growth parallel to the neck wall, toward the bottom AgNW.

Figure 5.1d represents the case where two NWs are touching each other via facets i.e. similar large radii of curvature, therefore significant delay or no wetting and subsequent welding occurs.

The driving force for this process is the decrease of high surface energy of AgNWs in contact. Formation of the welded zone simultaneously, on one side, decreases the total free energy of the system by removing free surface area of 100 facet section (A_{100}), twin interface area of NW (A_{TNW}) and strained volume of NW (V_{NW}) while on the other side, increases the free energy of the system by increasing surface area of welded zone (A_w), area of twin boundary in welded zone (A_{tw}) and strain energy of the welded zone (σ_w). Sintering of the NWs takes place when a certain thermodynamics criterion is met [13]:

$$A_w\gamma_w + A_{tw}\gamma_T + V_w\sigma_w < A_{100}\gamma_{100} + A_{TNW}\gamma_T + V_{NW}\sigma_{NW}$$

where γ_w is the surface energy of the welded zone, V_w is the volume of the welded zone, γ_{100} is the surface energy of 100 facet section, σ_{NW} is the strain energy of NW and γ_T is the surface energy of a twin boundary. This energy reduction is offset by the energy of GB creation and the energy balance dictates the final shape of the welded zone, i.e. transition from kinetics to thermodynamics driven shape. Kinetically driven shape of the AgNW welded zone (shown in Figure 4.12b) is characterized by rounded interface between welded zone and the bottom NW. Initial stage of the neck formation is dominated by the surface diffusion process, because it requires the lowest activation energy and it is the easiest mass transport path, as suggested for Ag nanoparticle sintering [20]. This process can be correlated with the Ostwald ripening phenomenon [21], in which the particle with a smaller diameter, which corresponds to the corner of the NW where two twin segments meet, feeds additional material to the particle with a larger diameter, which corresponds to a 100 facet of one of the twin segments where initial epitaxial layer forms during sintering. In some cases, it is observed (Figure 4.6a

red circles noting discontinued welded junctions) that Ostwald ripening at lower temperatures is accompanied by the Rayleigh effect [22,23], because of fast diffusion of Ag atoms from the regions adjacent to the point of contact [13].

Due to the enormous difference in radii of curvature, the atoms near the corner of pentagonal NW cross-section are driven strongly toward the touching 100 facet, creating conditions for epitaxial attachment. Attachment of Ag atoms to a 100 facet of the top AgNWs is facilitated by small step-ledge barrier [24,25,26], which implies that the next atomic layer may nucleate before the previous layer completes [27], as illustrated by Figure 5.2. This resembles 2D growth of Ag 200 films, where a smooth and flat growth surface is left behind [28]. Contrary to this, very rough growth is observed on Ag 111 surfaces, because of significantly larger step-edge barrier of approximately 0.45 eV [29], which is 0.15 eV larger than on surface. This leaves behind a fractal shaped surface, as it can be seen in the vicinity of the 111 facet shown in Figure 5.2.

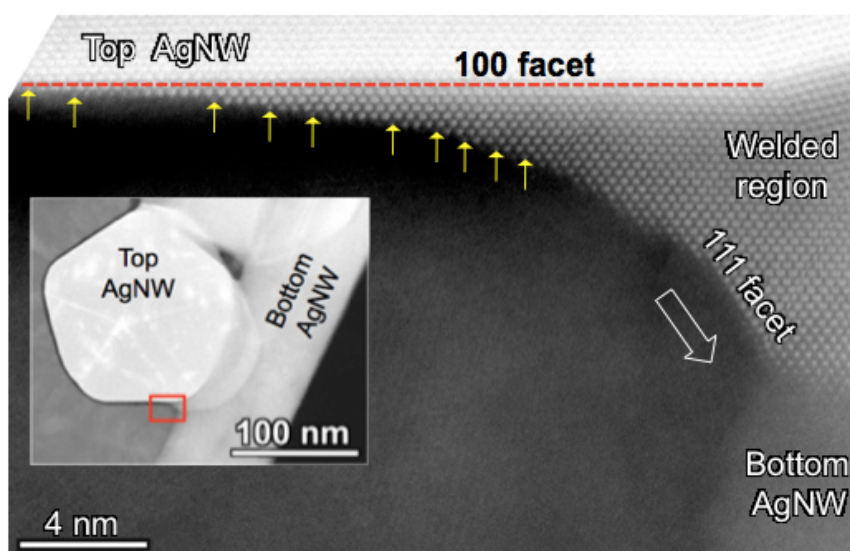


Figure 5.2. HRSTEM ADF image illustrating atomic layer nucleation; yellow arrows indicate 100 facets while white arrow indicates growth direction of 111 planes. This image is modified from Figure 4.13a with inset representing low magnification image with red square showing analyzed region.

Based on this atomic resolution evidence, it seems that kinetics of nanoweld formation are controlled by 111 step motion, i.e. diffusion rate of Ag atoms on 111

planes. However, in order to establish an accurate growth model, a temperature dependent study of AgNW nanoweld formation would be required.

Figures 4.20 and 4.21 were presented just as a way of putting the AgNWs and the AgNW/AZO nanocomposite in context of its application. As optoelectronic characterization of the AgNWs and the AgNW/AZO nanocomposite as well as complete solar cell characterization was not the focus of this thesis, literature review and comparison with similar research was not included.

5.1.1. Electron Tomography of Thin AgNWs

By analyzing HAADF STEM image recorded at 0° tilt angle, of welded junction, shown in Figure 4.23, as well as at different tilt angles, ranging from -70° to $+70^\circ$, it is evident that the weld is of highly anisotropic shape. Inability to draw any conclusion about the geometry of the welded junction and AgNW surface morphology from these images clearly indicated that 3D characterization of the structure was needed. HAADF imaging is very useful for 3D characterization of nanostructure because, as electrons undergo pure Rutherford scattering and the captured signal is proportional to Z^2 (the square of atomic number), contrast sensitivity to compositional and thickness variations is provided [30]. Since the AgNW welded junctions consists of only Ag atoms, variations in contrast are due to differences in thickness and geometry of the junction. From Figures 4.23 and 4.24 it is not possible to elucidate the type of crystallographic facets through which the NWs are in contact, but based on cross-sectional atomic resolution images and tomographic reconstruction, shown in Figures 4.25a and b, it can be concluded that they are of $\{100\}$ type. In addition, Figure 4.25 clearly shows that the corner of the bottom AgNW is in contact with the flat 100 facet of the top AgNW. This tomographic 3D characterization of the AgNW welded junction appears to be crucial for understanding the weld formation mechanism and underlying thermodynamics, explained in the previous section.

5.1.2. Diffraction Orientation and Strain Mapping

It is interesting to note that no remarkable strain fluctuation has been observed across AgNWs and their welded junctions. In order to measure strain at the nanometer

scale, various TEM methods of direct strain measurement have been used [31]:

- Convergent-beam electron diffraction (CBED) [32,33];
- Nano-beam electron diffraction (NBED) [34,35];
- HRTEM/STEM [36];
- Dark-field electron holography (DFEH) [37].

Employing TEM/STEM imaging for this purpose, was avoided because it requires fully resolved atomic columns across the entire welded zone. Additionally, mistilt of crystal structure and overlapping of different pentagonal twin segments through the bulk of welded NWs would render HRSTEM/HRTEM imaging inadequate for strain evaluation of this structure. Instead, because of the relatively large thickness of the welded zone, on average above 200 nm, NBED was utilized in order to acquire spatially resolved maps. The use of NBED mapping, in scanning mode, for evaluating strain in welded AgNWs through automated analysis by dedicated MatLab algorithm [38] of a large data volume set proved to be a very efficient way of acquiring precise information on strain distribution in each pixel of the scanned AgNW junction. This allowed measuring change in the local lattice parameter and orientation of the lattice planes with respect to unaltered sections of the welded AgNWs. Due to a relatively large field of view, $\sim 1 \mu\text{m}^2$, bending and twisting of AgNWs, as a result of drop cast deposition, resulted in a substantial mistilt of the crystal structure orientation. This can be clearly seen in Figure 4.28a, where rotation angle θ can differ for more than 3° for various segments of the same NW. Variation of θ angle value is present even within the same segments of the NW, as shown in Figures 4.28b, c and d, but it is significantly smaller, usually less than 0.5° . Overall, relatively large diameters of these AgNWs make them too thick to be considered completely reliable to draw a final conclusion about coherent strain distribution.

For the orientation maps, a list of peaks (up to 40) was made, followed by the classification of those peaks as belonging to one of five orientations: $\langle 112 \rangle$, $\langle 110 \rangle$, $\langle 110 \rangle$, $\langle 111 \rangle$ and an undefined orientation due to insufficient number of available reflections for identification. Any pixels that had diffraction intensity from one of the five patterns above some threshold (10% of the maximum signal) were classified as "the

same". The intensity of the main plot shows how strongly the given peaks (insets in Figure 4.27) were measured.

It should be noted that the right-hand part of the NW above the weld in Figures 4.27 and 4.28 is missing. This is a consequence of the region being too tilted i.e. if the NW is tilted more than 3°, there is no Bragg diffraction pattern. This does not mean that an AgNW segment is missing, but that Figures 4.27 and 4.28 present maps of areas where diffraction signal is present. The HAADF STEM image in Figure 4.26 clearly shows the preserved the integrity of the whole NW above the weld.

5.2 Tandem Organic Solar Cells

5.2.1 AgNWs Used as Electrodes in Tandem Organic Solar Cells

Optoelectronic characterization results have shown that with increasing film thickness, both, sheet resistance (R_s) and optical transmittance (T) decrease as well as surface roughness. By using the equation for optical transmittance [39,40]:

$$T = \left(1 + \frac{188.5 \sigma_{OP}}{R_s \sigma_{DC}}\right)^{-2} = \left(1 + \frac{188.5}{R_s \text{ FoM}}\right)^{-2}$$

at 550 nm wavelength, where σ_{OP} is optical conductivity, σ_{DC} is direct current conductivity, figures of merit, FoM (ratios between σ_{DC} and σ_{OP}) of AgNWs are as follows: 268 for Sample 1, 205 for Sample 2, 349 for Sample 3, 345 for Sample 4 and 301 for Sample 5. With value of FoM=349 and RMS surface roughness of 25.1 nm, which is in the range of acceptable roughness for AgNWs with average diameters of ~30 nm [41,42], Sample 3 has proven to be the optimal network among the presented samples for the application as a transparent electrode in optoelectronic devices, in this case, tandem organic solar cells.

One of the essential characteristics of transparent electrodes based on NW networks is the area coverage. With large area coverage, sheet resistance is reduced, which is favorable although optical transmittance is also reduced, which is not favorable. This is clearly demonstrated in Figure 4.37b. The use of SEM images is not necessarily the most accurate way of measuring area coverage, due to non-zero probe size, charging due to oxidation of Ag nanowires, variance in local area coverage, etc.

However, as long as all images are analyzed using the same method, the results should be self-consistent. From the results shown in Figures 4.37a and b it can be seen that sheet resistance and optical transmittance linearly decrease with increasing thickness and area coverage, demonstrating a trade-off between optical transmittance and electrical resistance. Variations in goodness of fit for effects of thickness and area coverage on optoelectronic properties can be explained by quite significant error bars for the measurements of the relationship between AgNW network thicknesses and the total surface coverage, shown in Figure 4.38. This is a consequence of solution processed randomness of AgNW distribution during deposition.

5.2.2 Double Junction Tandem OSC

High sheet resistance of electrodes hinders efficient collection of photo-generated charge carriers, resulting in fill factor and current losses. This can be prevented by dividing the entire device into independent sub-cells (single junction cells with one active layer), which are connected in series. This way, charge carrier paths are drastically shortened for their collection, reducing resistance losses. The research in this thesis did not deal with analysis of individual working principles of sub-cells and the series and/or parallel connections of sub-cells as they can be found in the PhD thesis of Guo [43].

The counter electrode in solar cells should be highly refractive in order to allow more than one flow of photons into the active layer. This effect enhances photocurrent generation. For this reason the bottom electrode was chosen to be produced from opaque Ag, solution processed from a precursor ink. This method of processing greatly reduces manufacturing costs [44,45] while keeping optoelectronic properties like reflectance and electrical sheet resistance of the produced Ag film almost identical to the conventional solution which is an evaporated Ag electrode [46]. However, this processing method has some inherent drawbacks which include high porosity of the printed Ag (P_Ag) film due to a high density of bubbles formed during the conversion of the Ag precursor ink to film at 130 °C as well as low adhesion to substrate. This drawback was addressed by depositing a thin film of PEDOT:PSS (noted as layer 2 in various images of this particular tandem OSC) on the glass substrate before Ag ink

deposition, which served as an adhesive between the glass and the P_Ag electrode. Reduced porosity can best be seen in the top part of the electrode, closer to the PEDOT:PSS layer noted as layer 4 in various images of this particular tandem OSC. As the opaque P_Ag has a smaller surface roughness than AgNWs, with RMS (root mean square) roughness of 3.3 nm compared to 13.4 nm [46], the P_Ag is best utilized as a bottom electrode. This arises from the fact that, with low roughness, subsequently deposited layers have lower roughness themselves, which hinders the possibility of shunts [47], unwanted short circuits between two contacts. Moreover, utilizing P_Ag as the top electrode can lead to a short circuit as the Ag precursor ink can permeate polymer layers leading to their corruption and overall hindering of device operation [46]. Roughness of AgNWs networks with respect to their thicknesses was given in the previous section of this thesis.

From both, BF TEM and STEM images of the tandem double junction OSC cross-section, fairly uniform thicknesses can be observed for all layers except the AgNWs, suggesting that charge carrier diffusion to their respective electrodes should be uniform throughout the cell. In the case of AgNWs, non-homogenous thickness as well as high surface roughness is expected since AgNWs are a network, not a continuous film.

Large discrepancy is observed for measured thicknesses of certain layers of the tandem OSC obtained from two methods, by profilometer and by TEM/STEM. This is explained by the large difference in measuring possibilities of the instruments but, since TEM has sub-nanometer resolution, it can be concluded that this method is much more accurate. Discrepancy of thicknesses can have a large effect on simulations regarding power conversion efficiency (PCE) as a function of thicknesses of active layers.

Because of superior possibilities of TEM compared to SEM, especially for acquired sub-nanometer resolution for TEM and ~10nm resolution for SEM, EDS elemental mapping was chosen to be performed in TEM/STEM mode. This is especially evident for the EDS map of Ag distribution, as pentagonal cross-sections of AgNWs can be observed as well as the porous structure of the P_Ag, which would be next to impossible to acquire by using EDS in the SEM. Maps of zinc and oxygen distribution show that locations of zinc and oxygen correspond to the locations of two ZnO layers present in the cell while the map of oxygen also corresponds to the location of the glass

used for the transparent substrate, as it is composed primarily of SiO₂. Map of sulfur distribution shows the location of sulfur, with highest concentration corresponding to the locations of PEDOT:PSS and N-PEDOT layers. Polymer pDPP5T-2 also contains small percentage of sulfur. The weaker signal corresponds to noise, although some contamination originating from cross-sectional FIB machining cannot be excluded. Map of nitrogen distribution shows the location of nitrogen, with highest concentration corresponding to the location of P_Ag, whose origin might be a residual of the drying process in nitrogen atmosphere, as well as of polyvinylpyrrolidone (PVP) polymer encapsulating the AgNWs, which contains small percentages of nitrogen. The weaker signal corresponds to noise, although some contamination originating from cross-sectional FIB machining cannot be excluded.

For this device, normal architecture was employed. The intermediate bi-layer, dividing the two active layers (sub-cells) consists of ZnO and N-PEDOT. The ZnO nanoparticle layer was used as an electron extraction layer because of its high electron mobility and a work function which matches the energy levels of the donor and acceptor in the active layers. This layer is also a good mechanical foundation i.e. stable substrate, for the deposition of AgNWs. As the ZnO is dissolvable in acidic environment, instead of PEDOT:PSS, a neutral alternative N-PEDOT was used. This polymer serves as a protective layer, preventing damage to the active layer when a solvent is introduced during the top active layer deposition. The high fill factor (FF) value is an indication that the intermediate layers have efficiently connected the two sub-cells.

Concerning AgNWs, a polymer capping agent PVP, introduced during synthesis in order to stabilize AgNWs [46,48], prevents direct contact of AgNWs and ZnO nanoparticles, which increases resistance and contributes to lower FF and PCE. This capping agent, noted as an amorphous region in Figure 4.45, although negatively impacting the PCE, is detrimental to the formation and growth of AgNWs during synthesis [49], which is explained in the Theoretical Background chapter of the thesis.

Even with all the hindering effects in mind, the PCE of this cell of 5.81% deposited on a glass substrate is, so far, the highest PCE reported for a fully solution processed double junction tandem OSC [46]. Moreover, to this date, no TEM investigations of double junction tandem OSC cross-section have been reported.

5.2.3 Triple Junction Tandem OSC

The need for developing triple-junction tandem OSCs originates from the idea of further enhancing the overall absorption of incident light. In this research, a novel configuration was developed which combines a series and a parallel interconnection, where the two sub-cells with DPP:PC₆₁BM polymer nanocomposites as the active layers are connected in series and, together, they are connected to the top sub-cell, with PCDTBT:PC₇₁BM as the active layer, via parallel connection. The benefit of this architecture is that it dramatically reduces material requirements for voltage and current matching, and has the possibility of reaching efficiency limits with a wide range of material combinations. Solution processed intermediate layers, with ZnO/N-PEDOT for the series connection and ZnO/N-PEDOT/AgNWs/ZnO for the parallel connection, allows for an efficient coupling of the three sub-cells without resistance losses i.e. high FF value is an indication that the intermediate layers have efficiently connected all three sub-cells [50]. Like for the double-junction tandem OSCs discussed in section 5.2.2, this research dealt with the structural characterization of the AgNWs and the OSC as a whole, while the detailed analysis of individual working principles of sub-cells and the series and/or parallel connections of sub-cells can be found in the PhD thesis of Guo [43]. From both, BF TEM and STEM images of the triple junction tandem OSC cross-section, fairly uniform thicknesses can be observed for all layers, suggesting that charge carrier diffusion to their respective electrodes should be uniform throughout the cell. Exceptions include: 1) ITO/PEDOT:PSS interface, which exhibits high surface roughness possibly due to instability since indium can diffuse into PEDOT:PSS [51] and 2) AgNWs. In the case of AgNWs, non-homogenous thickness is observed. This is due to the fact that the AgNW network is not a continuous film so individual AgNWs sank through the PEDOT:PSS layer beneath them as AgNW suspension contained water while PEDOT:PSS is a water soluble polymer. As the AgNWs sank into the PEDOT:PSS, the PVP capping polymer cannot be distinguished from either TEM or STEM images. Evaporated Ag/MoO_x electrode is in direct contact with the top ZnO nanoparticle layer, which significantly lowers resistance and contributes to higher FF and PCE.

Like for the double junction tandem OSC, large discrepancy is observed for

measured thicknesses of certain layers of the OSC obtained from two methods, by profilometer and by TEM/STEM.

As explained with the double junction tandem OSC, superior possibilities of TEM compared to SEM, influenced the choice of TEM EDS elemental mapping from STEM mode. This is especially evident for the EDS map of Ag distribution, as pentagonal cross-sections of AgNWs can be observed. Map of zinc distribution shows that location of zinc corresponds to the locations of three ZnO layers present in the cell. Map of oxygen distribution shows that location of oxygen corresponds to the locations of three ZnO layers present in the cell as well as ITO coated glass. Map of sulfur distribution shows the location of sulfur, with highest concentration corresponding to the locations of PEDOT:PSS and N-PEDOT layers. Polymers DPP and PCDTBT also contain small percentages of sulfur. The top line representing a high concentration of sulfur actually corresponds to molybdenum but since there is an overlap of energy lines of $K\alpha$ (2.307 keV) for sulfur and $L\alpha$ (2.293 keV) for molybdenum, the signal is mistaken for sulfur element distribution [50]. The weaker signal corresponds to noise, although some contamination originating from cross-sectional FIB machining cannot be excluded. Maps of indium and tin distribution show the locations of indium and tin, with highest concentration corresponding to the location of ITO although some signals are from the locations of evaporated Ag and AgNWs which is the result of overlap of energy lines of $L\alpha$ (2.984 keV) of silver and $L\alpha$ (3.286 keV) of indium and $L\alpha$ (3.443 keV) of tin. Map of molybdenum distribution shows the location of molybdenum, with highest concentration corresponding to the location of MoO_x layer, but also of areas where sulfur is present, which is the result of overlap between energy lines of sulfur and molybdenum, already explained in this paragraph.

Although, this research reports the first series-parallel interconnection in a triple junction tandem OSC, making, by proxy, 5.43% the highest recorded PCE, this efficiency is limited by a relatively low V_{OC} of the triple junction. This can be addressed by employing new combinations of materials for sub-cells which are compatible for series-parallel interconnections. High FF of 63.1% suggests that intermediate layers have efficiently coupled all three sub-cells into a triple junction [50]. Moreover, to this date, no TEM investigations of a triple junction tandem OSC cross-section have been reported.

5.3. Ag Dendrites

Different tilts of Ag dendrites in the SEM were performed and by comparing different images, especially at 0° and 90° tilt, it is clear that the structure is two-dimensional, with a high aspect ratio of width and length of ~10:1, with respect to the protrusion height, clearly visible at 90° tilt. Because of this high aspect ratio, they can be considered 2D crystals [52].

Analysis of various Ag dendrites revealed that they all contain multiple thin micro- and nano-twins and stacking fault lamellae parallel to the broad dendrite surface, visible in the cross-section, in Figure 4.57d, which shows twins of different thicknesses, due to random twinning events. The indication of multiple twin domains in each crystal is given through dark and light grey regions in Figure 4.57d, representing two variants of 60° rotational twins, where light regions represent twins of different thicknesses while dark regions are untwined regions.

Using STEM in HAADF mode, detailed microstructural features were observed, including the trunk, primary and secondary branches. These features exhibit similar contrast, indicating their similar thicknesses (Figure 4.58a). The bright white dots located along the trunk are the exceptions, which indicate that some of the primary branches grow vertical with respect to the trunk and the broad dendrite surface. Since the broad dendrite surface has a {111} orientation, it seems that protrusions from this surface must grow along the <111>, unless the growth direction is altered by the presence of twins and stacking faults. In Figure 4.48b, lines at 30° with respect to the trunk axis represent defects which could be either stacking faults of {111} orientation or {111} <112> growth twins which lie on inclined {111} planes with respect to {111} broad dendrite surface. It was calculated that the angles between the trunk and the primary branches, as well as between primary and secondary branches are all 60°. These relationships indicate that the main axis of the dendrite is parallel to the $[\bar{1}1\bar{2}]$ direction, and two sets of primary branches are parallel to $[12\bar{1}]$ and $[\bar{2}\bar{1}\bar{1}]$ crystallographic directions, confirmed by SAD pattern in Figure 4.59.

The Ag dendrite is a single crystal with an FCC structure, which was confirmed by diffraction patterns taken in several different orientations, which showed bright spots of 220 type, typical for an FCC crystal. Literature on AgNS [53], allows for the claim that SAD patterns shown in Figures 4.59b and c suggest that the Ag dendrite

contains planar defects such as twins and stacking faults. Weaker reflections, faint spots connected with dotted lines forming the inner hexagon are of $\frac{1}{3}\langle 422 \rangle$ orientation, which are formally forbidden reflections in perfect FCC crystals but were observed in trigonal lamellar particles (nanoprisms) of Au and Ag [54,55]. Stacking faults and nano- and micro twins are the origin of these faint spots. They are located on $\{111\}$ planes parallel to the broad surface of the Ag dendrite and extend through the entire dendrite. This is comparable to the diffraction effects observed in similarly synthesized Ag dendrites [56].

Confirmation of the presence of a high density of defects (twins and stacking faults) can be acquired by tilting one of the dendrite arms to $\langle 110 \rangle$ zone axis, shown in Figure 4.60b. This is in agreement with previous observations in electrodeposited Ag dendrites [57,58,59,60,61]. Geometric Phase Analysis (GPA) was used to analyze local lattice rotation/distortion in the Ag FCC lattice created by the presence of a high density of defects, twins and stacking faults (SF) using HRTEM imaging. GPA is based on the calculation of local lattice distortion with respect to the undistorted lattice (referred to as reference lattice), which allows mapping of displacement and strain fields [36]. Positions of SF and twin planes running parallel to the Ag dendrite arm axis can be identified from the moiré pattern and lattice rotation angle map in Figures 4.61b and c, respectively, which show lattice distortion within the same slab of twin segments.

For electron-backscatter diffraction (EBSD) analysis, the surface oxide layer and Ag protrusions perpendicular to the broad dendrite surface had to be removed by FIB machining. From Figure 4.62b it is obvious that the broad dendrite surface is of $\{111\}$ orientation. Besides the white lines, which indicate the positions (distribution) of twin boundaries, two twin variants can be observed in the orientation imaging color coded map in Figure 4.62c. Pole figures, shown in Figures 4.62d and e, constructed from orientation data, also confirm the presence of 60° rotational twins. This is clearly seen from the three-fold symmetry of the 100 (Figure 4.62d) and 111 (Figure 4.62e) poles in the 111 standard stereographic projections, represented by white squares and triangles, respectively. In order to generate the poles of the twinned Ag dendrite, it was necessary to rotate them 60° around the 111 zone axis. In other words, they have to be rotated 60° around the center of the 111 standard stereographic projection. This is represented by black squares and triangles in 100 and 111 pole figures, respectively. It is clear, by

comparing Figures 4.62a, b and c that details like small, closely spaced dendritic branches, are lost in the orientation map. This is the result of limited resolution of orientation imaging microscopy (OIM) analysis. A random distribution of two Ag twin variants rotated 60° around the 111 direction, perpendicular to the dendrite $\{111\}$ broad surface plane is clearly seen in Figures 4.62b and c. Growth directions of the dendrite trunk, close to $[\bar{1}1\bar{2}]$, and branches, close to $[12\bar{1}]$ and $[\bar{2}\bar{1}\bar{1}]$, are confirmed by the previously presented results. This is indicative that twin planes, parallel to the broad dendrite surface plane [62,63], are accompanied by two twin variants related to each other by a 60° rotation around the $\{111\}$ direction (Figure 4.62c). These twins are sometimes called 180° rotational twins [64] and seem to have a random distribution in the Ag dendrite.

High amounts of planar defects are observed in the structure which leads to the conclusion that Ag dendrite growth is promoted through the formation of twins and stacking faults on $\{111\}$ planes, assisted by the low stacking fault energy of Ag, $\sim 16\text{mJ/m}^2$ [65]. From habit planes of these defects it would be expected that growth directions of trunk and branches are close to $\langle 111 \rangle$, but the actuality is that they are close to $\langle 112 \rangle$, confirmed by SAD pattern in Figure 4.59.

Analyzing the HRTEM image taken close to $\langle 110 \rangle$ zone axis (Figure 4.63), with the focus on the root of the dendrite branch, narrow twin bands are observed, which illustrates how the twin plane reentrant edge (TPRE) mechanism takes place and how twins are related to dendrite trunk and branch growth directions. Slow growth of $\{111\}$ planes (facets) limits growth of Ag crystals. Due to the aforementioned low stacking fault energy of Ag, random twinning may occur on the $\{111\}$ oriented trunk planes. This leads to the creation of reentrant corners, of 141° , and protruding twin junctions, of 219° (ridge morphology), which are characterized by rapid nucleation and growth. As multiple twinning occurs, dendrite branches are formed while the area between the trunk and the branch is characterized by a concave surface (Figure 4.63a). Keeping in mind the fact that it was established that crystal growth (of metals) via reentrant edge mechanism requires the presence of multiple twin planes [66,67,68], it can be concluded that the formation of Ag dendrite branches has to be accompanied by multiple twinning. It was observed that a high density of nanotwins is present on $\{111\}$ planes. Besides the twins perpendicular to the $\langle 112 \rangle$ direction of branch growth, twins

parallel to the $\langle 112 \rangle$ direction were also observed, while no visible deviation in orientation between the twinning bands has been observed. It can be concluded that, by fragmenting dendrite facets into thermodynamically stable 111 and 200 steps and structural ledges of appropriate length, $\langle 112 \rangle$ growth directions are maintained. This twin configuration has already been proposed for germanium dendrite formation [67], as seen in Figure 6.43b. From this illustration, the role of twinning in the dendrite arm nucleation and growth with the, previously mentioned, 141° and 219° angles and $\langle 112 \rangle$ growth directions can be understood.

The optoelectronic measurements of Ag dendrites which show small sheet resistance of $16.9 \pm 2.1 \Omega \text{sq}^{-1}$ after annealing and high optical transmittance of 86.8% (at 360 nm) and 88.3% (550 nm), presented in Figures 4.66 and 4.67, respectively, demonstrate their significant potential for applications as transparent electrodes in solar cells.

5.4. Polymer Nanocomposites

Optical microscopy images in Figure 4.68 show the dispersion of various nanofillers inside the PVB polymer matrix. From optical micrographs of polymer nanocomposites (PNCs) with multi-walled carbon nanotubes (MWCNTs) and single-walled carbon nanotubes (SWCNTs) it is evident that agglomerations (bundles of entangled tubes) are present. The cause of this phenomenon are van der Waals forces which attract tubes to each other [69]. This is aided by their large aspect ratio and their size. Optical micrograph of PNC with graphene exhibits superior dispersion of nanofiller compared to other samples. Although graphene is prone to re-stacking, due to van der Waals forces and strong π - π stacking effects [69,70], van der Waals forces between CNTs appear to be much stronger, resulting in greater agglomeration and hence poorer dispersion in the polymer matrix. This is critical in comparing and understanding various properties of these PNCs since good dispersion of nanofillers in the polymer matrix and hence enhanced interfacial region between nanofiller and matrix [71] results in enhanced properties, through synergy of materials, compared to the pristine polymer.

TEM investigation of pristine nanofillers shown in Figure 4.69, was insightful in revealing typical structures for MWCNTs and graphene, as well as the presence of double-walled CNTs (DWCNTS) in the SWCNTs batch.

Transmission electron micrographs of the PNC with MWCNTs as the nanofiller reveal insufficient dispersion of nanofillers, which negatively affects the properties of the PNC although there are some cases where the MWCNTs were not agglomerated, like the one shown in Figure 4.70b. As shown in Figure 4.70c, turbulent solution mixing of MWCNTs and polymer, not only did not lead to optimal dispersion of nanofiller but it led to tearing of tubes as well. From this it can be concluded that the use of ultrasonicators for vigorous mixing can be detrimental for PNC structure and therefore their properties. Hence, it is probably far more likely to obtain optimal dispersion of nanofillers in PNCs with the use of surfactants or by functionalization of nanofiller surface then by optimizing processing methods.

Raman spectrum of pristine MWCNTs, shown in Figure 4.71, revealed that the positions of D and G bands, 1326 cm^{-1} and 1580 cm^{-1} respectively, which is in good agreement with already published data [72,73]. The intensity ratio of D band to G band is fairly large which suggests that numerous defects are present in the structure. Another feature is present, the D' band exhibiting itself as a shoulder of the G band at a frequency of $\sim 1605\text{ cm}^{-1}$. This is typical for graphitic materials with defects [72]. While the G band has a single peak, arising from its graphitic nature, no RBM band is present since the signal from MWCNTs with large diameters i.e. larger number of walls is too weak to be detected [74]. In Figure 4.71b, the Raman spectrum of the nanocomposite, peaks at 1430 cm^{-1} , 1450 cm^{-1} , 2735 cm^{-1} , 2870 cm^{-1} , 2920 cm^{-1} originate from the PVB polymer, and their locations are inherent from the pure PVB Raman spectrum (no shift). These peaks are dominant, which is expected as only 1 wt.% of nanofiller was introduced to form the nanocomposite.

Raman spectrum of SWCNTs, shown in Figure 4.72, revealed that the location of the D band, at 1309 cm^{-1} , is at a lower frequency than for MWCNTs and graphene. The reason lies in the fact that, as the diameter of the CNTs decreases, the downshift increases i.e. follows the $\omega_d = f(d_t)$ dependence, where ω_d is the frequency of the D band and d_t is the tube diameter [72,75,76]. The intensity ratio of D band to G band is very small, unlike for the MWCNTs, which suggests that only few defects are present in

the structure. Putting the G band in focus, it can be observed that it is a single peak band, with the peak located at 1569 cm^{-1} . Splitting of the G band into a G^- peak (linked to in-plane vibrations along the tangential direction) and G^+ peak (linked to in-plane vibrations along the tube axis), characteristic for SWCNTs is absent. This can be explained by large diameter distribution variation in the SWCNTs as well as the presence of a high content of DWCNTs in the sample, since G band splitting is one of the main characteristics of single shell vibrations [77]. Peak shifts of the RBM band of SWCNTs as a nanofiller from the RBM band of pure SWCNTs show that 1wt.% load of nanofillers is easily overshadowed by the polymer matrix i.e. peaks deriving from PVB have far greater intensity than peaks deriving from SWCNTs. This can be seen in Figure 4.72a as peaks of SWCNTs as the nanofiller, with frequencies above 250 cm^{-1} cannot even be seen from the dominating PVB peak at 300 cm^{-1} . In the rest of the nanocomposite Raman spectrum, various peaks at $1242\text{-}1448\text{ cm}^{-1}$, 2735 cm^{-1} , 2870 cm^{-1} , and 2920 cm^{-1} originate from the PVB polymer and their locations are inherent from the pure PVB Raman spectrum (no shift). These peaks are dominant, which is expected as only 1 wt.% of nanofiller was introduced to form the nanocomposite.

Similar to the MWCNTs and SWCNTs, in the Raman spectrum, the signal deriving from the small amount of graphene in the PNC is overwhelmed by the PVB signal. Hence, background subtraction of polymer spectrum was introduced in order to reveal subtle peak shifts in the spectral bands of graphene (Figure 4.73). The intensity ratio of D band to G band is, unlike for the MWCNTs, very small which suggests that only few defects are present in the structure. From the shape of the 2D band it can be concluded that it is a multicomponent peak with an underlying structure constructed from multiple peaks derived from multiple layers of graphene. The position of the 2D peak at 2670 cm^{-1} suggests that this is indeed multi-layer graphene and not graphite [78]. Small shifts of D, G and 2D bands of graphene as the nanofiller compared to bands of pristine graphene are consistent with electrostatic interaction between graphene and PVB matrix, rather than strain effects [79]. As most peaks in PNC Raman spectra, derived from carbonaceous nanofillers, have up-shifted i.e. transferred to higher frequencies, this means that anti-Stokes Raman scattering was present - atoms lost energy since the scattered photon had more energy than the incident photon. From a characterization point of view, this gives insight that the nanofillers were dispersed in

the matrix to a level sufficient enough for the PNC to exhibit superior mechanical properties compared to pristine polymer.

Comparing optical transmittance measurements, shown in Figure 4.74, for all PNC samples as well as the pristine polymer, it can be concluded that the difference in light transmission of only a few percent can be for different reasons: difference in nanofiller nature and their dispersion uniformity, surface roughness, thickness variations, etc., but the deconvolution of the effects of these factors was not the subject of this research. Optical transmittance measurements of nanocomposite samples with different thicknesses, with MWCNTs as the nanofiller (Figure 4.74b), revealed that deviations in results originate from the variation in film thickness throughout the sample, as well as non-homogenous dispersion of MWCNTs. Figure 4.74c shows the non-linear decrease of optical transmittance as the film thickness increases, for both, UV and Vis regions, explaining the non-uniform gap sizes between each curve in Figure 4.74b.

Concerning the properties of PNC, it has already been established that, although the volume fraction of nanofillers was not sufficient to reach a needed level of percolation threshold, it has been demonstrated that these carbonaceous nanostructures have an obvious effect on the properties of PNCs [80]. Although some results regarding hardness and reduced Young's modulus for PNCs with carbonaceous nanofillers can be found in literature, it is a question of how can they be comparable because methods of processing differ as well as the structure and load of nanofillers and type of polymer matrix. Besides, very limited research has been done in the field of PNCs with carbonaceous materials like CNTs and graphene as the nanofiller (especially at load of 1 wt.%) and PVB as the polymer matrix.

Hardness value of 212.08 ± 22.90 MPa for the PNC with MWCNTs slightly exceeds the interval reported in literature (0.14-0.19 GPa) while the reduced modulus of 7.75 ± 0.09 GPa is higher than the value of 4.33-7.66 GPa reported in literature [81]. For the PNC with SWCNTs, the reduced modulus value of 8.05 ± 1.09 GPa is higher than the value of 1.55 ± 0.76 GPa reported in literature [82], although in epoxy-SWCNTs PNCs the reduced modulus value goes up to 4.5 GPa while the hardness reaches 300 MPa [83], a higher value than reported in the research of this thesis. Higher values of reduced modulus and hardness for PNC with SWCNTs than the values for PNC with MWCNTs

are expected because of the nature of SWCNTs, which includes smaller diameter, greater surface area, higher structural perfection and uniformity than the MWCNTs [84]. Value of reduced modulus for the PNC with graphene as the nanofiller is in the same order of magnitude as the value reported by Zhang et al. [85], of 6.69 GPa where epoxy was utilized as the matrix with a slightly lower nanofiller load of 0.7 wt.% although the hardness in that research was stated as 510 MPa, ~2 times the value reported in this research.

Electrical measurements revealed that the lowest resistivity exhibited the PNC with graphene, of $1.9 \times 10^3 \Omega\text{cm}$, which is in good correspondence with the resistivity of $10^3 \Omega\text{cm}$ reported for a polystyrene (PS)/graphene system by Stankovich et al., [86]. The values of $4 \times 10^4 \Omega\text{cm}$ for PNC with MWCNTs and $1.1 \times 10^4 \Omega\text{cm}$ for PNC with SWCNTs are both lower than $1.25 \times 10^6 \Omega\text{cm}$, and $10^6 \Omega\text{cm}$, respectively, the values reported in literature [82].

REFERENCES

-
- [1] H. I. Aaronson, G. Spanos, R. A. Masamura, R. G. Vardiman, D. W. Moon, E. S. K. Menon and M. G. Hall, *Materials Science and Engineering B*, 32 (1995) 107-123.
 - [2] Y. Yan, S. J. Pennycook, J. Dai, R. P. H. Chang, A. Wang, T. J. Marks, *Applied Physics Letters*, 73 (1998) 2585-2587.
 - [3] M. A. McCoy, R. W. Grimes, W. E. Lee, *Philosophical Magazine A*, 76 (1997) 1187-1201.
 - [4] S. Takeuchi, K. Suzuki, K. Maeda, and H. Iwanaga, *Philosophical Magazine A*, 50 (1985) 171-178.
 - [5] J. F. John, S. Mahurin, S. Dai, M. J. Sepaniak, *Journal of Raman Spectroscopy*, 41 (2010) 4-11.
 - [6] M. Gobelt, R. Keding, S.W. Schmitt, B. Hoffmann, S. Jackle, M. Latzel, V. V. Radmilovic, V. R. Radmilovic, E. Spiecker and S. Christiansen, *Nano Energy*, 16 (2015) 196-206.
 - [7] E. Spiecker, V. R. Radmilovic, U. Dahmen, *Acta Materialia*, 55 (2007) 3521-3530.
 - [8] A. van der Drift, *Philips Research Reports*, 22 (1967) 267-288.
 - [9] P. Smereka, X. Li, G. Russo, and D. J. Srolovitz, *Acta Materialia*, 53 (2005) 1191-1204.
 - [10] E. C. Garnett, W. Cai, J. J. Cha, F. Mahmood, S. T. Connor, M. G. Christoforo, Y. Cui, M. D. McGehee and M. L. Brongersma, *Nature Materials*, 11 (2012) 241-249.
 - [11] R. E. Smallman, R. J. Bishop, *Modern Physical Metallurgy and Materials Engineering*, Butterworth-Heinemann, Oxford, UK 1999, p. 101.
 - [12] V. V. Radmilovic, J. Kacher, E. R. Ivanovic, A. M. Minor and V. R. Radmilovic, *Crystal Growth & Design*, 16 (2016) 467-474.
 - [13] V. V. Radmilovic, M. Gobelt, S. Christiansen, E. Spiecker, V. R. Radmilovic, *Advanced Functional Materials*, 2016, Submitted.

-
- [14] K. A. Afanasyev, F. Sansoz, *Nano Letters*, 7 (2007) 2056-2062.
- [15] T. Filleter, S. Ryu, K. Kang, J. Yin, R. A. Bernal, K. Sohn, S. Li, J. Huang, W. Cai and H. D. Espinosa, *Small*, 8 (2012) 2986-2993.
- [16] L. Liu, D. Shen, G. Zou, P. Peng and Y. Zhou, *Scripta Materialia*, 114 (2016) 112-116.
- [17] G. J. R. Rockland, *Acta Materialia*, 15 (1967) 277-286.
- [18] G. C. Kuczynski, *Transactions of the Metallurgical Society of AIME*, 185 (1949) 169-178.
- [19] H. Park, Y. C. Joo, D. Y. Kim, J. T. Park, J. K. Kim, N. M. Hwang, *Journal of Applied Physics*, 95 (2004) 5515-5521.
- [20] J. R. Greer, R. A. Street, *Acta Materialia*, 55 (2007) 6345-6349.
- [21] D. A. Porter, K. E. Esterling, M. Y. Sherif, *Phase transformations in metals and alloys*, 3rd edition, CRC Press, Taylor & Frances, Boca Raton, USA, 2009, p. 310.
- [22] T-B. Song, Y. Chen, C-H. Chung, Y. Yang, B. Bob, H-S. Duan, G. Li, K-N. Tu, Y. Huang, Y. Yang, *ACS Nano*, 8 (2014) 2804-2811.
- [23] S. Iwama, K. Hayakawa, *Japanese Journal of Applied Physics*, 20 (1981) 335-340.
- [24] Y. Suzuki, H. Kikuchi, and N. Koshizuku, *Japanese Journal of Applied Physics*, 27 (1988) L1175-1178.
- [25] W. F. Egelhoff and I. Jacob, *Physical Review Letters*, 62 (1989) 921-924.
- [26] P. Bedrossian, B. Poelsema, G. Rosenfeld, L. C. Jorritsma, N. N. Lipkin, and G. Comsa, *Surface Science*, 334 (1995) 1-9.
- [27] W. C. Elliott, P. F. Miceli, T. Tse, P. W. Stephens, *Physical Review B*, 54 (1996) 17938-17942.
- [28] B. D. Yu and M. Scheffler, *Physical Review Letters*, 77 (1995) 1095-1098.
- [29] J. Vrijmoeth, H. A. van der Vegt, J. A. Meyer, E. Vlieg, and R. J. Behm, *Physical Review Letters*, 72 (1994) 3843-3846.
- [30] E. M. Perassi, J. C. Hernandez-Garrido, M. S. Moreno, E. R. Encina, E. A. Coronado, and P. A. Midgley, *Nano Letters*, 10 (2010) 2097-2114.
- [31] M. J. Hytch and A. M. Minor, *MRS Bulletin*, 39 (2014) 138-146.
- [32] P. M. Jones, G. M. Rackham, J. W. Steeds, *Proceedings of the Royal Society of London A*, 354 (1977) 197-222.
- [33] A. Armigliato, R. Balboni, G. P. Carnevale, G. Pavia, D. Piccolo, S. Frabboni, A. Benedetti, A. G. Cullis, *Applied Physics Letters*, 82 (2003) 2172-2174.
- [34] K. Usuda, T. Numata, T. Irisawa, N. Hirashita, S. Takagi, *Materials Science and Engineering B*, 124-125 (2005) 143-147.
- [35] F. Uesugi, A. Hokazono, S. Takeno, *Ultramicroscopy*, 111 (2011) 995-998.
- [36] M. J. Hytch, E. Snoeck, R. Kilaas, *Ultramicroscopy*, 74 (1998) 131-146.
- [37] M. J. Hytch, F. Houdellier, F. Hue and E. Snoeck, *Nature*, 453 (2008) 1086-1089.
- [38] Collaboration with C. Ophus of National Center for Electron Microscopy, Molecular Foundry, Lawrence Berkeley National Lab, Berkeley, USA.
- [39] S. De, T. M. Higgins, P. E. Lyons, E. M. Doherty, P. N. Nirmalraj, W. J. Balu, J. J. Boland, J.N. Coleman, *ACS Nano*, 3 (2009) 1767-1774.
- [40] L. Hu, H. Wu, Y. Cui, *MRS Bulletin*, 36 (2011) 760-765.
- [41] X-Y. Zeng, Q-K. Zhang, R-M. Yu, and C-Z. Lu, *Advanced Materials*, 22 (2010) 4484-4488.
- [42] B. Park, I-G. Bae and Y. H. Huh, *Scientific Reports*, 6 (2016) 19485.
- [43] F. Guo PhD Thesis, *Material and Process Engineering of Printed Semitransparent*

Organic Solar Cells and Advanced Multi-junction Architectures, Friedrich Alexander University, Erlangen-Nuremberg, Germany, 2015.

- [44] D. Angmo, H. F. Dam, T. R. Andersen, N. K. Zawacka, M. V. Madsen, J. Stubager, F. Livi, R. Gupta, M. Helgesen, J. E. Carlé, T. T. Larsen-Olsen, G. U. Kulkarni, E. Bundgaard and F. C. Krebs, *Energy Technology*, 2 (2014) 651-659.
- [45] S. B. Walker and J. A. Lewis, *Journal of the American Chemical Society*, 134 (2012) 1419-1421.
- [46] F. Guo, N. Li, V. V. Radmilovic, V. R. Radmilovic, M. Turbiez, E. Spiecker, K. Forberich and C. J. Brabec, *Energy & Environmental Science*, 8 (2015) 1690-1697.
- [47] W. Chen, M. P. Nikiforov and S. B. Darling, *Energy & Environmental Science*, 5 (2012) 8045- 8074.
- [48] N. Li, T. Stubhan, J. Krantz, F. Machui, M. Turbiez, T. Ameri and C. J. Brabec, *Journal of Materials Chemistry A*, 2 (2014) 14896-14902.
- [49] S-H. Zhang, Z-Y. Jiang, Z-X. Xie, X. Xu, R-B. Huang and L-S. Zheng, *Journal of Physical Chemistry B*, 109 (2005) 9416–9421.
- [50] F. Guo, N. Li, F. Fecher, N. Gasparini, C. O. Ramírez Quiroz, C. Bronnbauer, Y. Hou, V. V. Radmilovic, V. R. Radmilovic, E. Spiecker, K. Forberich and C. Brabec, *Nature Communications*, 6 (2015) 7730.
- [51] L-M. Chen, Z. Xu, Z. Hong and Y. Yang, *Journal of Materials Chemistry*, 20 (2010) 2575–2598.
- [52] G. Wranglén, *Electrochimica Acta*, 2 (1960) 130-143; A. M. S. El Din and G. Wranglén, *Electrochimica Acta*, 7 (1962) 79-90.
- [53] V. Germain, J. Li, D. Inger, Z. L. Wang and M. P. Pileni, *Journal of Physical Chemistry B*, 107 (2003) 8717-8720.
- [54] C. Lofton and W. Sigmund, *Advanced Functional Materials*, 15 (2005) 1197-1208.
- [55] A. I. Kirkland, D. A. Jefferson, D. G. Duff, P. P. Edwards, I. Gameson, B. F. G. Johnson and D. J. Smith, *Proceedings of the royal society of London series A - Mathematical physical and engineering sciences*, 440 (1993) 589-609.
- [56] J. Fang, H. You, P. Kong, Y. Yi, X. Song and B. Ding, *Crystal Growth & Design*, 7 (2007) 864-867.
- [57] G. Zhang, S Sun, M. N. Banis, R. Li, M. Cai and X. Sun, *Crystal Growth & Design*, 11 (2011) 2493-2499.
- [58] S. Schmitz and F. E. Brenker, *Astrophysical Journal*, 681 (2008) L105-L108.
- [59] A. Courty, A. I. Henry, N. Goubet and M. P. Pileni, *Nature Materials*, 6 (2007) 900-907.
- [60] Z. Jiang, Y. Lin and Z. Xie, *Material Chemistry and Physics*, 134 (2012) 762-767.
- [61] M. P. Pileni, *Nature Materials*, 2 (2003) 145-150.
- [62] J. Yang, H. Wang, H. Zhang, *Journal of Physical Chemistry C*, 112 (2008) 13065-13069.
- [63] J. Zhang, H. Liu, P. Zhan, Z. Wang, N. Ming, *Advanced Functional Materials*, 17 (2007) 1558-1566.
- [64] E. Ivanovic, N. Nikolic, V. R. Radmilovic, *Journal of Serbian Chemical Society*, 80 (2015) 107-113.
- [65] R. E. Smallman, R. J. Bishop, In *Modern Physical Metallurgy and Materials Engineering*; Butterworth-Heinemann: Oxford, 1999, pp. 101.
- [66] R. S. Wagner, *Acta Metallurgica*, 8 (1960) 57-60.

-
- [67] D. R. Hamilton, R. G. Seidensticker, *Journal of Applied Physics*, 31 (1960) 1165-1168.
- [68] J. W. Faust, H. F. John, *Transactions of the Metallurgical Society of AIME*, 233 (1965) 230-233.
- [69] M. Supova, G. S. Martynkova, and K. Barabaszova, *Science of Advanced Materials*, 3 (2011) 1–25.
- [70] G. Mittal, V. Dhand, K. Y. Rhee, S-J. Park and W. R. Lee, *Journal of Industrial and Engineering Chemistry*, 21 (2015) 11-25.
- [71] R. A. Vaia and H. D. Wagner, *Materials Today*, 7 (2004) 32-37.
- [72] A. Jorio, P.A. Pimenta, A. G. Souza Filho, R. Saito, G. Dresselhaus and M. S. Dresselhaus, *New Journal of Physics*, 5 (2003) 139.
- [73] S. Osswald, M. Havel and Y. Gogotsi, *Journal of Raman Spectroscopy*, 38 (2007) 728-736.
- [74] M. S. Dresselhaus, G. Dresselhaus, R. Saito, and A. Jorio, *Physical Reports*, 409 (2005) 47-99.
- [75] A. G. Souza Filho, A. Jorio, G. G. Samsonidze, G. Dresselhaus, M. A. Pimenta, M. S. Dresselhaus, A. K. Swan, M. S. Unlu, B. B. Goldberg and R. Saito, *Physical Review B: Condensed Matter*, 67 (2003) 035427.
- [76] H. Wilhelm, M. Lelaurain, E. Mcrae and B. Humbert , *Journal of Applied Physics*, 84 (1998) 6552-6558.
- [77] J. H. Lehman, M. Terrones, E. Mansfield, K. E. Hurst and V. Meunier, *Carbon*, 49 (2011) 2581–2602.
- [78] A. C. Ferrari, J. C. Meyer, V. Scardac, C. Casiragh, M. Lazzeri, F. Mauri, S. Piscanec, D. Jiang, K. S. Novoselov, S. Roth and A. K. Geim, *Physical Review Letters*, 97 (2006) 187401.
- [79] N. Ferralis, R. Maboudian and C. Carraro, *Physical Review Letters*, 101 (2008) 156801.
- [80] V. V. Radmilovic, C. Carraro, P. S. Uskokovic, V. R. Radmilovic, *Polymer Composites*, 2016, DOI: 10.1002/pc.24079.
- [81] C. A. Charitidis, E. P. Koumoulos, M. Giorcelli, S. Musso, P. Jagadale and A. Tagliaferro, *Polymer Composites*, 34 (2013) 1950-1960.
- [82] Y. Li, T. Yu, T. Pui, P. Chen, L. Zheng and K. Liao, *Composites Science and Technology*, 71 (2011) 1665-1670.
- [83] M-T. Le and S-C. Huang, *Sensors and Materials*, 27 (2015) 617–624.
- [84] J. N. Coleman, U. Khan U, W. J. Blau and Y. K. Gunko, *Carbon*, 44 (2006) 1624–1652.
- [85] Z. Zhang, W. Zhang, D. Li, Y. Sun, Z. Wang, C. Hou, L. Chen, Y. Cao and Y. Liu, *International Journal of Molecular Sciences*, 16 (2015) 2239-2251.
- [86] S. Stankovich, D. A. Dikin, G. H. B. Dommett, K. M. Kohlhaas, E. J. Zimney, E. A. Stach, R. D. Piner, S. T. Nguyen and R. S. Ruoff, *Nature*, 442 (2006) 282-286.

6. Conclusions and Future Outlook

Based on experimental results presented in Chapter 4 and discussion of the main contributions of this thesis presented in Chapter 5, the following conclusions can be drawn:

- The polyol reduction synthesis method has produced AgNWs with average diameter (thickness) of 132.34 ± 32.16 nm. Focused Ion Beam (FIB) technique in combination with high resolution transmission electron microscopy (HRTEM) has been employed in order to elucidate the mechanisms of solid-state wetting and welding which occur during AgNWs annealing prior to AZO film deposition. It has been elucidated that pentagonal cross-sectional morphology of AgNWs has a dominant effect on the formation of nanowelds, as well as on nucleation and diffusion direction of Ag atoms between two NWs in contact. It was determined that crystal lattice distortion, measured by atomic columns displacement, is non-uniform, ranging from 0 to ± 1 unit cell, between each of the five twin segments of the AgNW. The welding process between two AgNWs in contact, as a consequence of complete solid-state wetting, starts with diffusion of Ag atoms from the NW in contact via corner (small radius of curvature) and continues with homoepitaxial attachment of Ag atoms on 100 facets of other NW (large radius of curvature). This geometric relation between two AgNWs in contact, has been supported by electron tomography of welded AgNWs with average diameter ~ 30 nm, where it is unambiguously evident that AgNW in contact via corner (small radius of curvature) supplies the welded zone with Ag atoms, consistent with Ostwald ripening. The welded zone, consisting of attached Ag atoms, grows, extending out epitaxially to the neighboring twin segments. Crystallographic orientation of the welded zone is identical to the crystallographic orientation of the twin segments of the NW on which the material is attached. This is supported by the distribution of orientation calculated from electron diffraction maps of AgNWs and welded zone. Distributions of residual strain and rotation angle have been also calculated using diffraction maps of AgNWs, which showed that the after welding, ϵ_{xx} , ϵ_{yy} , and ϵ_{xy} , ranged from -2 to 2% while the rotation angle range was in the

range of -2 to 2° . These findings contribute to a better understanding of solid-state wetting and welding mechanisms that occur during annealing and the role NW morphology has in these processes, which in turn can lead to the development in optimization of NW networks for the application as transparent electrodes in optoelectronic devices, primarily flexible solar cells. Possible future research in this field could include: kinetics temperature dependent study and simulation of AgNW solid-state wetting for establishing accurate growth model as well as exploration of how alternative welding routes (plasmonic welding, electric resistance welding, etc.), affect essential optoelectronic and thermo-mechanical properties as well as structural stability of AgNWs when compared to the conventional thermally induced welding.

- Tandem organic bulk heterojunction (BHJ) solar cells, both double and triple junction were a subject of microstructural characterization with the aim of morphology elucidation. AgNWs utilized as transparent electrodes in tandem organic solar cells exhibited best properties, based on FoM, for ~ 100 nm network thickness, $9 \Omega/\text{sq}$ sheet resistance at 18.7% area coverage. In the double junction OSC, processed entirely from solution and triple junction OSC, processed mostly from solution, AgNW networks exhibited large variations in thickness, as expected for non-continuous films as well as indirect contact with ZnO layers through PVP capping layer thereby increasing resistance of device. Other layers exhibited mostly uniform thickness, with no interdiffusion occurring between the layers, as confirmed by EDS analysis, which favorably affects the overall power conversion of the devices deposited on glass with efficiencies of 5.43 % for the triple junction OSC where sub-cells were coupled in series-parallel connection and 5.81% for the double junction OSC where sub-cells were coupled in series connection. For both tandem OSC, layer thicknesses obtained from analyzing TEM/STEM images exhibit discrepancy when compared to results obtained from profilometry measurements, which is expected as TEM/STEM characterization provides a far greater resolution which means the thickness measurement results are more accurate. Future investigations regarding these tandem OSC could include: optimizing processing in order to ensure optimal layer thicknesses and interface morphology (surface roughness) for maximum

performance, elucidating a way of decreasing porosity of P_Ag electrode, thereby increasing adhesion to the substrate and finally, incorporating novel nanostructures like Ag dendrites as transparent electrodes.

- In the research of Ag dendrites, it was demonstrated that they possess, not just twins and stacking faults running parallel to the {111} broad dendrite surface, but also randomly distributed twin domains. These domains are irregular in shape, heterogeneous in size distribution and are related to each other by in-plane 60° rotations around the $\langle 111 \rangle$ direction, perpendicular to the broad dendrite surface. Defects present in the structure serve as heterogeneous nucleation sites for dendrite growth via ledge growth assisted mechanism. Branches growing out of the trunk cannot occur without twinning of the {111} plane of the trunk. The growth directions of the trunk and branches are not close to $\langle 111 \rangle$ as one would expect, because of twinning and stacking fault formation on {111} planes. Instead, they are close to $\langle 112 \rangle$ direction and maintained by breaking dendrite facets into thermodynamically stable 111 and 200 steps and structural ledges of different length. Future work regarding Ag dendrites could include optimizing synthesis in order to assure high aspect ratios which are required for these structures to be a competitive transparent electrode choice in solar cell applications.
- A very simple and inexpensive solution processing method has been employed in the production of PNC thin films. Nature of carbon nanofillers and PNC has been elucidated by Raman spectroscopy while microstructure and morphology was characterized by TEM. Although small loading of nanofillers was not enough to reach a percolation threshold, which was desirable, PNC have exhibited superior properties compared to those of pristine polymer, with PNC with graphene as nanofiller exhibiting highest values. Mechanical properties like reduced modulus and hardness were increased from 5.7 ± 0.1 GPa and 169 ± 3 MPa, respectively, for pure PVB polymer to 9.44 ± 0.44 GPa and 242.98 ± 22.35 MPa, respectively, for PNC with graphene as the nanofiller. Simultaneously, addition of nanofiller to PVB matrix did not substantially lower optical transmittance as this value decreased from 92% for pure PVB to 84% for PNC with graphene as nanofiller, at 550 nm. This

difference can possibly be even smaller as variations in transmittance can originate from different factors and the deconvolution of the effects of these factors is a challenging task. This research presents a simple processing route of PNC which utilizes small amounts of nanofiller providing a low cost material with superior properties with a wide range of potential applications, one of which could be encapsulation, i.e. protective surface layers for solar cells. Future work regarding these PNC might include: varying nanofiller loading and achieving optimal dispersion through optimizing processing methods, in order to attain superior mechanical properties without affecting optical transmittance as well as testing PNC for permeability of oxygen and moisture as protection of solar cells against these factors is the main assignment of encapsulation/surface protection layers.

Biography

Vuk V. Radmilović was born 19.11.1984 in Belgrade. He graduated from the Faculty of Technology and Metallurgy, University of Belgrade in 2010 and in the same year enrolled in doctoral studies at the Department of Materials Science, Faculty of Technology and Metallurgy, University of Belgrade, under the mentorship of prof. dr Petar Uskoković. Since February 2011 he is employed at the Innovation Center of the Faculty of Technology and Metallurgy and was elected as a junior researcher in May 2011 and as a research associate in October 2014. He is involved in the project from the Serbian Ministry of Education, Science and Technological Development entitled “Synthesis, processing and applications of nanostructured multifunctional materials with defined properties”, record number III 45019.

Vuk V. Radmilović has been a co-author on 15 scientific papers and 20 conference proceedings and has given invited talks at universities in Serbia, Germany and Switzerland.

Research Visits

02/2016–02/2016	Characterization of silver nanostructures for optoelectronic applications, Centre des Materiaux, Mines ParisTech, Corbeil-Essones, France.
10/2014–12/2014	Characterization of nanocomposites for optoelectronic applications and processing and characterization of organic solar cells, CENEM and IMEET, Friedrich Alexander University, Erlangen, Germany.
05/2012–06/2012	Solar cell processing and characterization, Civil and Environmental Engineering Department, University of Perugia, Terni, Italy.

Awards and scholarships

11/2015	Embassy of France/French Institute of Serbia scholarship for scientific mobility, Franco-Serbian cooperation for the fight against climate change.
9/2015	YUCOMAT conference best oral presentation
9/2013	YUCOMAT conference best poster

Прилог 1.

Изјава о ауторству

Потписани VUK RADMILOVIĆ

број индекса 4066/2010

Изјављујем

да је докторска дисертација под насловом

TRANSPARENTNI NANOKOMPOZITNI FILMOVI ZA PRIMENU U PLASTIČNOJ ELEKTRONICI

TRANSPARENT NANOCOMPOSITE FILMS FOR PLASTIC ELECTRONICS APPLICATIONS

- резултат сопственог истраживачког рада,
- да предложена дисертација у целини ни у деловима није била предложена за добијање било које дипломе према студијским програмима других високошколских установа,
- да су резултати коректно наведени и
- да нисам кршио ауторска права и користио интелектуалну својину других лица.

Потпис докторанда

У Београду, 22.09.2016



Прилог 2.

Изјава о истоветности штампане и електронске верзије докторског рада

Име и презиме аутора VUK RADMILOVIĆ

Број индекса 4066 / 2010

Студијски програм INŽENJERSTVO MATERIJALA

Наслов рада TRANSPARENTNI NANOKOMPOZITNI FILMOVI ZA PRIMENU U PLASTIČNOJ ELEKTRONICI
TRANSPARENT NANOCOMPOSITE FILMS FOR PLASTIC ELECTRONICS APPLICATIONS

Ментор DR PETAR USKOKOVIĆ

Потписаник VUK RADMILOVIĆ

Изјављујем да је штампана верзија мог докторског рада истоветна електронској верзији коју сам предао за објављивање на порталу **Дигиталног репозиторијума Универзитета у Београду**.

Дозвољавам да се објаве моји лични подаци везани за добијање академског звања доктора наука, као што су име и презиме, година и место рођења и датум одбране рада.

Ови лични подаци могу се објавити на мрежним страницама дигиталне библиотеке, у електронском каталогу и у публикацијама Универзитета у Београду.

Потпис докторанда

У Београду, 22.09.2016



Прилог 3.

Изјава о коришћењу

Овлашћујем Универзитетску библиотеку „Светозар Марковић“ да у Дигитални репозиторијум Универзитета у Београду унесе моју докторску дисертацију под насловом: *TRANSPARENTNI NANOKOMPOZITNI FILMOVI ZA PRIMENU U PLASTICNOJ ELEKTRONICI*

TRANSPARENT NANOCOMPOSITE FILMS FOR PLASTIC ELECTRONICS APPLICATIONS

која је моје ауторско дело.

Дисертацију са свим прилозима предао/ла сам у електронском формату погодном за трајно архивирање.

Моју докторску дисертацију похрањену у Дигитални репозиторијум Универзитета у Београду могу да користе сви који поштују одредбе садржане у одабраном типу лиценце Креативне заједнице (Creative Commons) за коју сам се одлучио/ла.

1. Ауторство
2. Ауторство - некомерцијално
3. Ауторство – некомерцијално – без прераде
4. Ауторство – некомерцијално – делити под истим условима
5. Ауторство – без прераде
6. Ауторство – делити под истим условима

(Молимо да заокружите само једну од шест понуђених лиценци, кратак опис лиценци дат је на полеђини листа).

Потпис докторанда

У Београду, 22. 09. 2016

